UNIVERSITÀ DEGLI STUDI DI PADOVA

Department of Industrial Engineering

Ph.D. course in Industrial Engineering

Curriculum: Materials Engineering

XXXV cycle

Doctoral dissertation

Complex architectures of Si-infiltrated Polymer-Derived Ceramics: computational design and hybrid additive manufacturing

Coordinator: Prof. Paolo Sgarbossa

Supervisor: Prof. Alberto Ortona

Co-supervisor: Prof. Paolo Colombo

Ph.D. candidate: Marco Pelanconi

I hereby declare that the contents and organization of this dissertation constitute my own original work and does not compromise in any way the rights of third parties, including those relating to the security of personal data.

Marco Pelanconi
Padova, February 22th 2023

To my parents and my sister,
constant sources of support and inspiration.

Abstract

The thesis introduces a novel hybrid additive manufacturing approach for the fabrication of complex cellular architectures, made of silicon-infiltrated polymer-derived ceramics, with fine resolution and smaller details than those achievable with other ceramics additive manufacturing approaches.

The process involves the 3D printing of a porous polymeric preform through the selective laser melting of polyamide powders combined with preceramic polymer infiltration and pyrolysis. The optimized combination of the printing parameters allows to fabricate discs with controlled relative density of 52%. Polycarbosilane was used to infiltrate the preform and to obtain the polymer-to-ceramic conversion into amorphous SiOC/SiC ceramics. Despite the high shrinkage of ~25%, the parts maintained their pristine shape without distortion or macrocracks. Few cycles of infiltration and pyrolysis were used to increase the relative density from 30% to 90%. The final densification was achieved with liquid silicon infiltration, producing the crystallization of the ceramic phase. Crystalline βSiC and Si composed the final nearly fully dense (98.3%) ceramic part with a volume fraction of 45% and 55%, respectively. The final Si-βSiC ceramic disc had a biaxial strength of 165 MPa.

The process was expanded to the production of geometrically-complex architectures thanks to the development of a computational design tool. It allows the generation of cellular structures with tunable topology and a quick parametrization of the geometrical quantities. The cellular architectures of the rotated cube and the gyroid with 25 mm diameter, 44 mm height and 67% of geometric macroporosity were generated and used for the fabrication.

The process was extended to the production of a wide range of polymer-derived ceramics, using different preceramic polymers. Polycarbosilane, polycarbosiloxane, polysilazane and furan resin were respectively used for the fabrication of SiC, SiOC, SiCN and C ceramics. The final densification was achieved with an optimized liquid silicon infiltration treatment on four different ceramics. The components had a final diameter of 19 mm and height of 33 mm and maintained their complex shape. The Si-βSiC ceramics, obtained with a reactive silicon infiltration, had a maximum true density of 3.173 g/cm^3, with apparent density of 2.966 g/cm^3 and a relative density of 93.5%. βSiC, RB-βSiC and Si composed the material with 38%, 58% and 4% of volume fractions, respectively. A maximum compressive strength of 25 MPa was achieved by these architectures, which is more than twice than what found in literature. Also, a superior oxidation resistance at high temperature was assessed. Furthermore, the Si-βSiC parts were manufactured with (i) much smaller features (e.g., gyroid surface thickness of 0.185 mm) than those achievable using binder jetting and (ii) denser features (95.7%) than those obtainable through the replica method.

Contents

Research motivation

The development of Advanced Ceramics for high temperature applications has experienced significant growth, thanks to their use in the aerospace, military, energy management industries, automotive and biotechnology. These classes of materials offer unmatched properties that cannot be provided by steels. Non-oxide ceramics, in comparison with oxides, are well-suited to be used in extreme environments and in applications that require to bear significant loads. Recently, the increasing application demand of advanced ceramics has required manufacturing technologies with high-speed, low-cost, high-performance, complex-shaped parts. The new challenge is to build advanced ceramic parts through additive manufacturing (AM), to exploit the excellent properties of these materials combined with the possibility to obtain complex architectures, which are not achievable with the traditional manufacturing approaches.

To date, there are still many challenges and basic scientific issues in the fabrication of such ceramics by AM. The current main disadvantage is that high resolution cannot be achieved in complex ceramic architectures (e.g., cellular structures). Powder-based methods have the difficulty of removing the support material after printing, especially when highly intricate structures with small pores are produced. For stereolithography the main drawback is the opacity of the powders, which does not allow high powder packing. Filament extrusion techniques currently do not allow sufficient geometric freedom to produce 3D highly intricate structures. Not all the ceramic AM techniques are best suited to produce complex cellular ceramic architectures. In addition, regardless of the used technology, the ceramic preforms are coarse in resolution with respect to the traditional approaches, coarse in the surface quality, low in mechanical strength and low in density.

By analyzing the final application, a proper design of the architecture topology can result in structures with optimized properties for specific applications. However, such structures can contain large numbers of geometrical details, which are impossible to generate with traditional software. Therefore, it is currently crucial to develop more appropriate generation tools.

The aim of this thesis is to introduce a novel hybrid Additive Manufacturing process for the fabrication of complex architectures made of silicon-infiltrated polymer-derived ceramics. The objective is to produce nearly fully dense and net-shape SiSiC ceramics directly from the preceramic precursor, without the need of ceramic powders and avoiding several process-related challenges. Further aim is to develop a parametric computational design tool for the generation of complex structures, such as cellular porous architectures made by strut or surfaces, with high engineerable topology and quick tunability.

Thesis overview

The thesis consists of five chapters:

1. Introduction: this chapter offers an overview of advanced ceramics and additive manufacturing approaches commonly used to produce non-oxide ceramics. A brief description of the engineering design evolution, along with the design of complex architectures, is given to provide the basic knowledge necessary to understand the computational design approach. The chapter also introduces the additive manufacturing of cellular ceramic architectures with its limitation and prospects.

2. Process development: this chapter introduces and describes the new hybrid additive manufacturing approach for the fabrication of Si-infiltrated polymer-derived ceramics. The proposed method exploits the 3D printing of polymer powders combined with polymer infiltration and pyrolysis and liquid silicon infiltration. The materials characterization was performed during all stages of the process through different methods of analysis. The results were compared with the literature.

3. Parametric computational design of cellular structures: this chapter describes the development of a new parametric computational design method for cellular architectures. The proposed approach uses a library of purpose-built algorithms and scripts that allow to generate structures with different features and functionalities, depending on the user's requirements and on the application.

4. Production of a wide range of complex ceramic architectures: this chapter describes the fabrication of complex ceramic architectures through the proposed hybrid additive manufacturing process and with the use of the developed design tools. Various preceramic polymers were used to produce different polymer-derived ceramics, which were then compared under different aspects, including ceramic yield, density, composition, microstructure, mechanical strength, and oxidation resistance. In conclusion, reactive silicon infiltration was performed into different ceramic preforms to obtain fully dense and net-shape Si-βSiC ceramics with superior mechanical strength and oxidation resistance, compared to the literature.

5. Conclusions and prospects: this chapter concludes the thesis by summarizing the work carried out and underlying the major findings. A perspective on the needed next steps and further improvements is given.

The work described in this thesis is based upon the following journal publications:

- Pelanconi, M., Rezaei, E., & Ortona, A. (2020). Cellular ceramic architectures produced by hybrid additive manufacturing: A review on the evolution of their design. Journal of the Ceramic Society of Japan, 128(9), 595-604. https://doi.org/10.2109/jcersj2.20071

- Pelanconi, M., Ortona, A. (2021). Review on the Design Approaches of Cellular Architectures Produced by Additive Manufacturing. In: Meboldt, M., Klahn, C. (eds) Industrializing Additive Manufacturing. AMPA 2020. Springer, Cham, pp. 52–64. https://doi.org/10.1007/978-3-030-54334-1_5

- Pelanconi, M., Colombo, P., & Ortona, A. (2021). Additive manufacturing of silicon carbide by selective laser sintering of PA12 powders and polymer infiltration and pyrolysis. Journal of the European Ceramic Society, 41(10), 5056-5065. https://doi.org/10.1016/j.jeurceramsoc.2021.04.014

- Pelanconi, M., Bianchi, G., Colombo, P., & Ortona, A. (2022). Fabrication of dense SiSiC ceramics by a hybrid additive manufacturing process. Journal of the American Ceramic Society, 105(2), 786-793. https://doi.org/10.1111/jace.18134

In this thesis, part of the material was collected during a research period abroad at the Mechanical Engineering and Materials Technology Institute (MEMTi) at the University of Applied Sciences and Arts of Southern Switzerland (SUPSI), where Professor Alberto Ortona (supervisor) is head of the Hybrid Materials Laboratory, Department of Innovative Technologies (DTI).

1

Introduction

1.1 Advanced ceramics

In recent years, the development of Advanced Ceramics for high temperature applications has experienced significant growth, thanks to their use in the aerospace, military and defense, energy management industries, automotive, biotechnology, communication, and chemical processing. Advanced ceramics or technical ceramics are inorganic, non-metallic, crystalline materials of rigorously controlled composition and highly engineered microstructure. They are manufactured with detailed regulation from highly refined raw materials, giving unique or superior functional attributes[1–4]. This class of materials offers unmatched properties that cannot be provided by steels. For this reason, they are used for the design of components operating at temperature above 1000°C, such as industrial burners, solar absorbers, heat exchangers, heat storage systems, and energy plants[5,6]. Such apparatuses and materials suffer high thermal and oxidative stresses during their operation, and therefore they must meet several requirements, including good strength, high temperature resistance, high thermal shock resistance, and oxidation resistance[7,8]. Figure 1 shows the mechanical strength as a function of the maximum operating temperature for different families of materials: metals, polymers, ceramics and composites[9].

Advanced ceramics are gathered in two macro categories: oxides and non-oxides. Oxides, or better metal oxides, are a combination of a metallic element with oxygen. The most common technical oxide ceramics are alumina (Al_2O_3), zirconia (ZrO_2) and silica (SiO_2) along with its silicates. Non-oxide ceramics are a combination of different elements with

several other elements like carbon, nitrogen, and boron. The most common non-oxide ceramics are silicon carbide (SiC), tungsten carbide (WC), boron carbide (B_4C), silicon nitride (Si_3N_4), aluminum nitride (AlN), and zirconium diboride (ZrB_2).
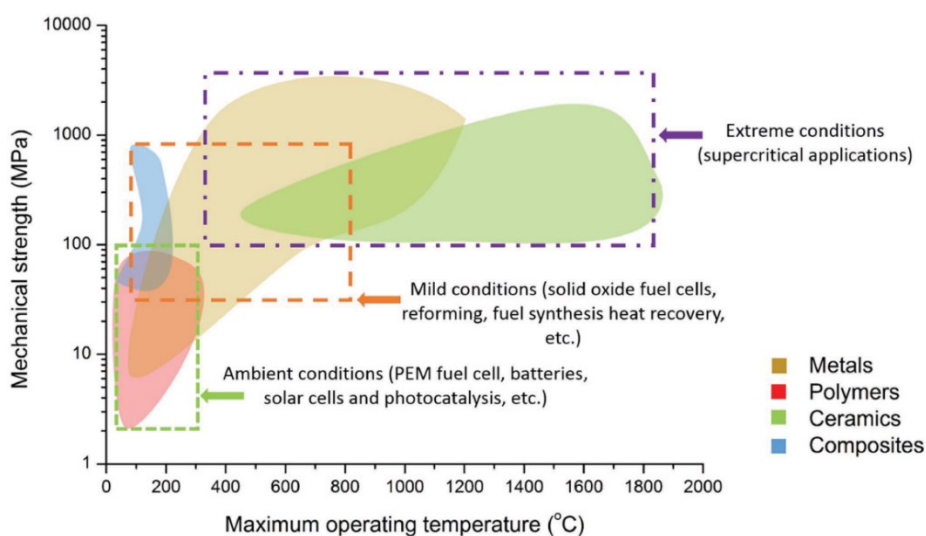

Figure 1. Mechanical strength as a function of the maximum operating temperature for different families of materials: metals, polymers, ceramics and composites[9].

Non-oxide ceramics, in comparison with oxides, are well-suited to be used in extreme environments and in applications that require to bear significant loads. They are characterized by higher working temperatures, higher mechanical strength and toughness, and a much better thermal shock resistance. They offer incredibly high corrosion and oxidation resistance, high thermal conductivity, and low values of thermal expansion. These properties are difficult and expensive to achieve because non-oxides rarely exist in nature and the raw materials must be synthesized artificially. The chemical bonds between oxygen atoms and metallic atoms are mainly ionic bonds, while in non-oxides are generally covalent bonds with strong bonding. Therefore, non-oxide ceramics are generally more difficult to melt and sinter than normal oxides, because of the higher temperatures and the inert atmospheres necessary to their sintering. For example, carbides are prepared at temperatures ranging 1000°C to 2800°C and they are used in key industrial applications[10].

The traditional manufacturing technique of the most common non-oxide ceramic, i.e., silicon carbide, consists in the sintering process or in the preparation of a ceramic preform (usually carbon[11–13]) which is subsequently infiltrated through one of the following processes: chemical vapor deposition (CVD) or infiltration (CVI)[14–16], polymer impregnation and pyrolysis (PIP)[17–19] and liquid silicon infiltration (LSI)[20–23]. Then the part is machined to obtain its final shape. Recently, the increasing application demand of advanced ceramics have required high-speed, low-cost, high-performance, complex-shaped part manufacturing technologies, generating attention and investments from different industrial and research sectors.

1.2   Additive manufacturing of non-oxide ceramics

A significant opportunity for manufacturing advanced ceramic materials is represented by additive manufacturing (AM), also called rapid prototyping[24,25]. AM is the industrial production name for 3D printing, which is a computer-controlled process that creates three dimensional objects through the deposition of materials in layers. Ceramics additive manufacturing has always been a step behind the techniques utilizing polymers and metals, due to their lower attractivity on the market. Lately, ceramic artefacts have been also produced, adapting the equipment developed for polymers and metals. The reason lays in the need of ceramic net-shape complex components for high-tech systems. Compared to the conventional production processes, AM of ceramics[26–28] offers several technological advantages, such as high-efficiency, rapid manufacturing processes, fabrication of geometrically-complex parts, net-shape components produced without the need of additional machining and avoiding secondary processing, shortening of development cycle, cost reduction, and unique properties due to the use of highly engineered design[29–32]. Nowadays, AM of ceramics is leading to the opening of new application areas and to new generation components, such as catalysts, adsorbers, porous burners and reactors, heat dissipator and high temperature heat exchangers[33–38]. However, great progress has been made to date for the additive manufacturing of oxide ceramics[39–45] and less so for the additive manufacturing of non-oxide ceramics[46–48].

In recent years, the AM of non-oxide ceramics is mainly focused on the production of reaction-bonded silicon carbide (RB-SiC or SiSiC) ceramics. SiSiC also known as siliconized silicon carbide or silicon infiltrated silicon carbide, is widely used in several engineering applications where endurance and thermal stability is required[33,49,50]. The new challenge is to build SiSiC parts through AM[51–54], to exploit the excellent properties of this material combined with the possibility to obtain geometrically-complex architectures[55–57], that are not obtainable with the traditional manufacturing approaches (reaction sintering, hot pressing sintering, pressureless sintering, and other techniques). Several components have been successfully manufactured by combining 3D printing with reactive silicon infiltration. This process involves the infiltration of a carbon (C) porous preform with molten silicon (Si), at a temperature exceeding its melting point (1414°C)[58,59], to obtain their reaction into SiC. The drawbacks of this approach are the low relative density, low mechanical strength, and coarse resolution of the parts, compared to the traditional techniques. Several studies have been performed to investigate the nature of the residual porosity after the reactive silicon infiltration, and it was found that the infiltration process is not controlled by viscous flow but by the reaction at the infiltration front. The reaction between C and Si causes the formation of a dense surface, which might limit subsequent infiltration from the liquid, leading to the presence of residual porosity in the part[60,61].

At present, almost all AM-based non-oxide ceramics are produced through a multi-steps procedure, due to the high sintering temperature of the non-oxide ceramics. The process comprises two steps: (1.2.1) preparation of the ceramic preform and (1.2.2) densification of the preform.

1.2.1 Preparation of the ceramic preform (or green body)

The standard approach for 3D printing of ceramics is based on feedstock consisting of ceramic particles and organic polymers (binder) formed through low temperature melting/solidification of the latter. Once the green body is produced, it undergoes a two-step heat treatment to first remove the organic polymer (debinding) and then to pyrolyze or sinter the ceramic particles to consolidate the part. The ceramic green body is produced using different AM technologies which differ according to the raw material used: powder, wire, sheet, paste, slurry, or ink.

Two main AM methods are used for non-oxide ceramics and they both work with powders:

- Indirect selective laser sintering (iSLS)[54,62–70] which exploits the mixing of a ceramic powder with a binding polymeric powder[71–73].

- Binder jetting (BJ)[51,52,74–79] which exploits the deposition of a liquid polymeric binder over a ceramic powder bed by an ink jet head[80,81].

Figure 2 shows the schematic of the iSLS and BJ technologies.
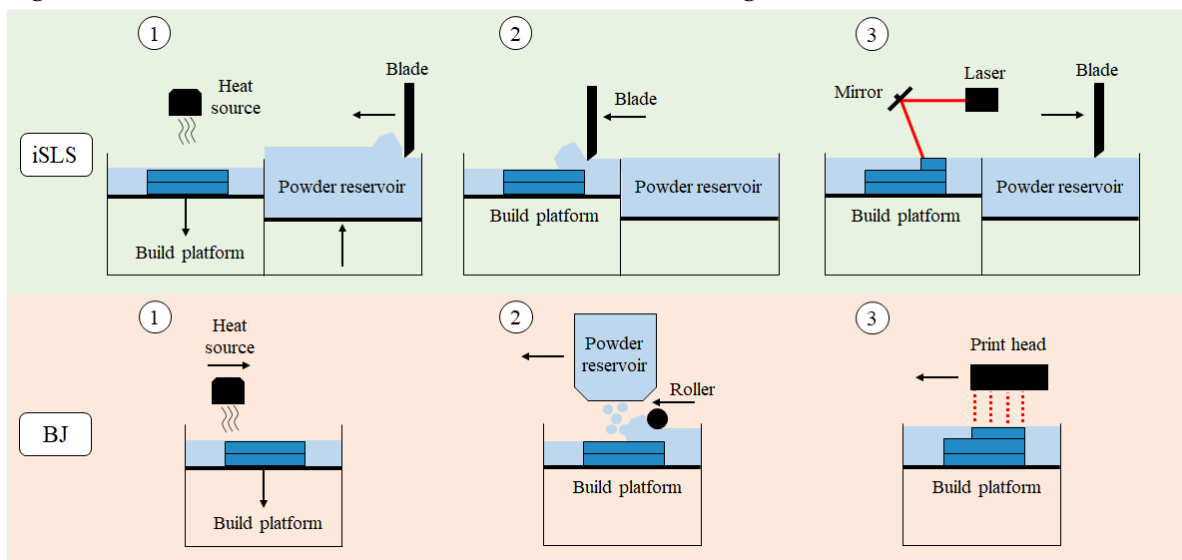

Figure 2. Schematic of SLS and BJ additive manufacturing technologies. iSLS steps: (1) powder heating and new powder deposition; (2) powder layering of a specific thickness by the blade; (3) selectively fusion of the binding powder by the laser beam (driven by motorized mirrors). BJ steps: (1) powder layer heating; (2) new powder deposition and layering of a specific thickness by the roller; (3) selective jetting of the liquid binder from the print head over the ceramics powder bed.

BJ and iSLS techniques require a particular understanding of the ceramic powder's properties, especially its flowability and bulk density, which are influenced by the geometrical properties of the powder (shape and particle size distribution)[72,73,80,81]. In addition to the powder, the choice of the binder is important. For example, for the production of silicon carbide component, with BJ technology the most used binder is the phenolic resin[51,74–79] which is a precursor of carbon, and with iSLS technology the phenolic[62] and epoxy[63,70] resins are commonly used. However, for iSLS some interesting researches were reported investigating the use of boron carbide[48] or silicon powders[54] as binders.

In addition, by using high power laser beams, the selective laser sintering technology can also be used to directly sinter the ceramic powders. Ceramics parts could therefore be formed, sintered, and densified in one step. This technique is called direct selective laser sintering (dSLS) and it is like selective laser melting for metals. Nevertheless, local heating results in stress, micro-cracks, porosities, poor surface quality, poor resolution, and high energy consumption. Accordingly, the dSLS is used only for oxides ceramics, which have lower sintering temperature (< 2000°C) with respect to non-oxides (> 2000°C).

Recently, other technologies have been used for the manufacturing of non-oxide ceramics, including fused deposition modelling (FDM)[82–85], laminated object manufacturing (LOM)[86], stereolithography (SLA)[58,87–94], robocasting[53,95,96], fused filament fabrication (FFF) or extrusion free forming (EFF)[59,97], and direct ink writing (DIW)[98–101]. However, results comparable with iSLS and BJ were documented only in a few cases.

Instead, an interesting approach has been recorded on the direct additive manufacturing of preceramic polymers, as alternative to the elaborate processing of ceramic powders. The preceramic polymers, or ceramic precursors, are polymeric compounds that are converted into ceramics through pyrolysis (700°C-1100°C) in an oxygen-free environment. The ceramics produced are called polymer derived ceramics (PDCs). See paragraph 1.2.3 for more details.

1.2.2   Densification of the preform

Regardless of the used technology, the produced ceramic preforms are low in matrix strength and high in porosity, and they require densification. Several densification technologies have been used for processing ceramic preforms, including polymer impregnation and pyrolysis (PIP), liquid silicon infiltration (LSI), reactive melt infiltration (RMI) or reactive infiltration (RI), chemical vapor infiltration (CVI), chemical vapor deposition (CVD), cold isostatic pressing (CIP) and hot isostatic pressing (HIP)[14–23].

PIP and LSI processes are the main methods used for the fabrication of silicon carbide-based advanced ceramics. They are typically combined with additively manufactured preforms because they allow to maintain the geometric shape of the parts.

PIP method involves the infiltration of a porous ceramic preform with a liquid preceramic polymer (see paragraph 1.2.3 for more details) followed by pyrolysis, to obtain the polymer-to-ceramic conversion. Figure 3 shows the schematic of the PIP process in which the liquid preceramic polymer infiltrates the porosity of the preform and then it is converted into ceramic through pyrolysis.
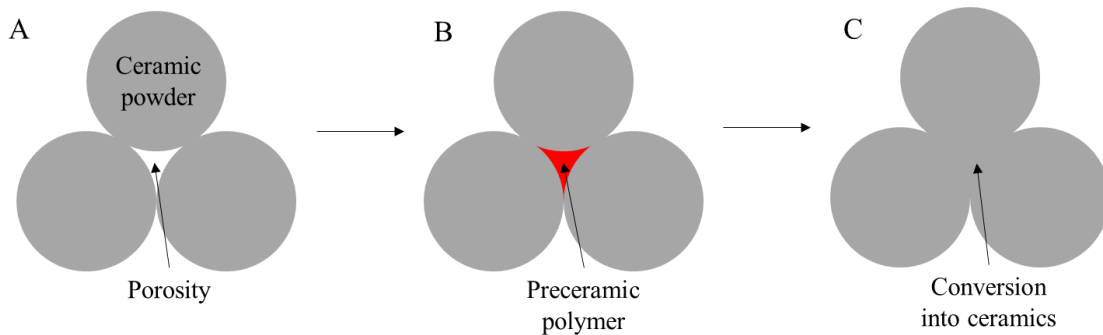

Figure 3. Schematic of the PIP process. (A) porous ceramic preform; (B) infiltration with liquid preceramic polymer; (C) polymer-to-ceramic conversion through pyrolysis.

LSI method involves the infiltration of a porous ceramic preform (usually carbon) with molten silicon at a temperature exceeding its melting point. The LSI infiltration can be reactive[102,103] if there is chemical interaction between the metal and the preform, i.e., Si (liquid) + C (solid) → SiC (solid). Figure 4 shows the schematic of the reactive silicon infiltration process into a carbon preform.
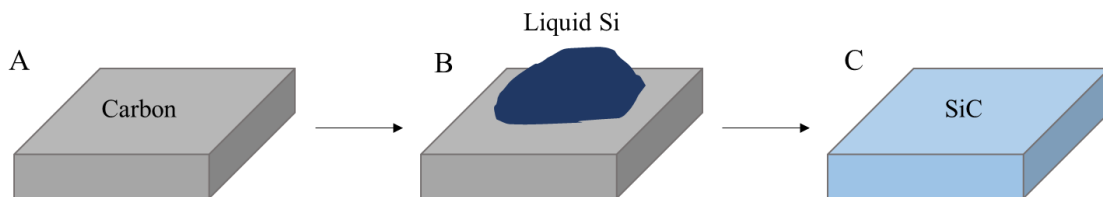

Figure 4. Schematic of the reactive silicon infiltration process. (A) porous carbon preform; (B) infiltration with molten silicon at temperature exceeding its melting point; (C) reaction bonded silicon carbide part.

During the reaction between silicon and carbon[104–107], the key factors contributing to the rapid densification of the material are the evaporation state of the molten Si, the exothermic effect during the infiltration/reaction process and the volume increases induced by the conversion of carbon into SiC. In general, the initial stage of SiC production involved diffusion-reaction producing nano-SiC, whereas the latter stage involved dissolution-precipitation producing coarse SiC. Some progresses have also been made at the numerical level by simulating the mechanism of infiltration, the reaction of Si into C channels and the Si-C interface formation.

The infiltration of molten silicon[108–112] were explained by the theory of spontaneous capillary infiltration. According to Washburn's model, capillary infiltration of liquid Si into porous preforms is explained by the assumption that the pore medium is a constant capillary[113]:

$$h_i{}^2 = r \cdot \gamma \cdot cos\theta \cdot (2 \cdot \eta)^{-1} \cdot t_i \qquad \text{Eq. 1}$$

where h_i represents the infiltrated depth, r the pore radius, γ the surface tension, θ the wetting angle between fluid and solid, η the fluid viscosity and t_i the infiltration time. The following are the literature data for the infiltration properties of liquid silicon at 1600°C: γ = 0.82 N·m^{-1}, θ = 10°, η = 0.7 mPa·s.

The basic principle is the need to have hollow channels for the silicon to flow before it reaches new regions of carbon and reacts with them. Therefore, studying the reactive silicon infiltration is of primary importance to improve the processing technique and its final product[105–107]. <u>What drives the entire process and its success, is the preparation of the ceramic preform and its microstructure.</u> The biggest drawback of the LSI technique is that a certain amount of unreacted residual silicon is always present in the final microstructure.

Advantages and disadvantages of the two main techniques used for the densification of advanced ceramic produced by AM are summarized in Table 1.

	Advantages	Disadvantages
PIP	• Formed at a relatively low temperature (700°C-1100°C). • Good control of the microstructure and composition. • Complex and net-shapes fabrication. • Different types of preceramic polymers can be used.	• Residual porosity in the preform (due to the ceramic yield of the polymer used) which can lead to low mechanical properties. • Long fabrication times are required because of multiple infiltration-pyrolysis cycles. • Higher costs than melt infiltration.
LSI	• Short production time. • Very low residual porosity. • In situ reaction and formation are possible. • Complex and net-shapes fabrication. • Low cost.	• Residual silicon in the preform (which affects the maximum service temperature). • Presence of unreacted carbon is possible. • If there are fibers, they can be damaged by the high temperature of molten silicon (>1414 °C).

Table 1. Advantages and disadvantages of PIP and LSI densification methods[102,103].

As shown in Figure 5, the research in the additive manufacturing of SiC-based advanced ceramics has increased over the past 20 years[114].
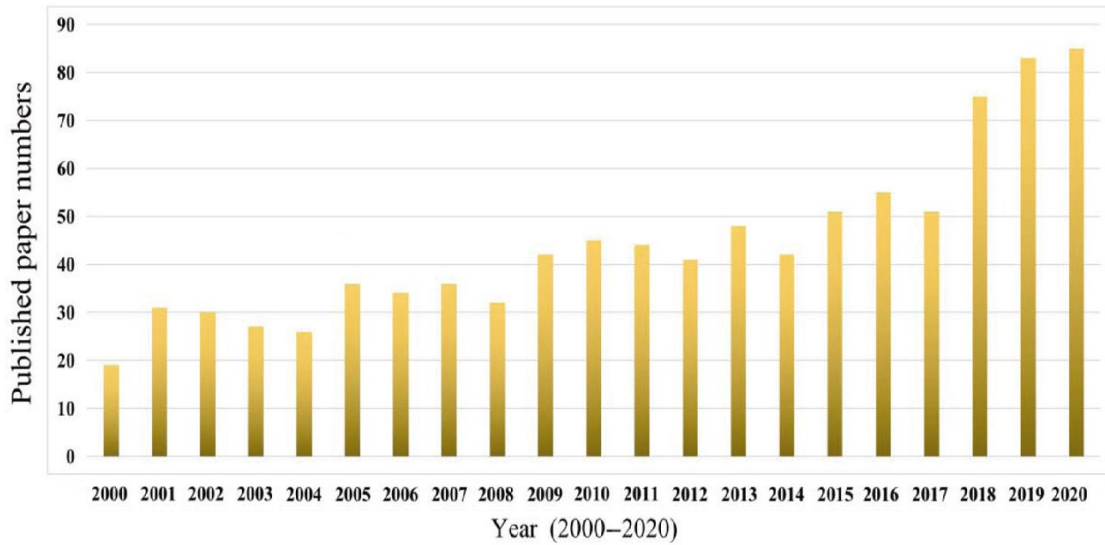

Figure 5. Published papers on the AM of SiC-based ceramics from the Web of Science database from 2000.01 to 2020.12[114].

However, there are still many challenges and basic scientific issues especially in the mechanical strength and relative density of the parts, compared to the traditional manufacturing methods[114]. Figure 6 shows the comparison.
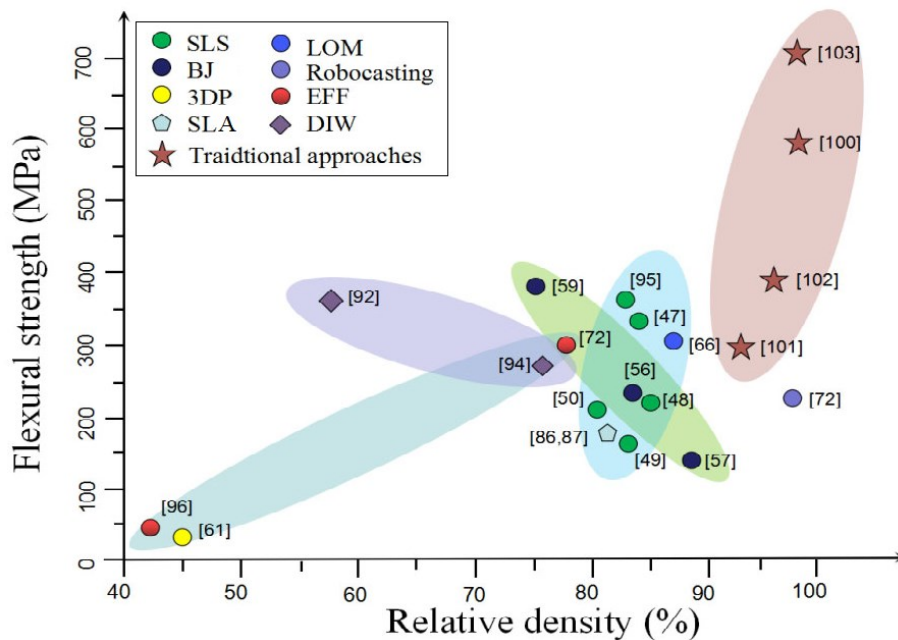

Figure 6. Comparison of the mechanical strength and relative density of SiC-based ceramics prepared by various AM technologies and densification methods (PIP, LSI, CVI, CVD) compared to those prepared by traditional methods[114].

1.2.3 Preceramic polymers used for 3D printing and densification

In the early 1960s, the production of non-oxide ceramics starting from molecular precursors was reported[115,116]. Silicon-based polymer derived ceramics (PDCs) have been synthesized directly by the pyrolysis of organosilicon polymers. Ten years later[117], for the first time the polymer to ceramic transformation of polysilazanes, polysiloxanes, and polycarbosilanes was performed to produce ceramic parts. A comprehensive review on preceramic polymers was reported by P. Colombo, G. Mera, R. Riedel and G. D. Sorarú[118].

The polymer precursors represent inorganic/organometallic systems that provide ceramics with a tailored chemical composition and a closely defined nano-structural organization by proper thermal treatment (curing and thermolysis processes under a controlled atmosphere). The PDCs route is an emerging chemical process as attested by the increasingly commercial development of preceramic polymers to produce near-net shapes in a way not known from other techniques[119]. Moreover, PDCs are additive-free ceramic materials possessing excellent oxidation and creep resistance up to exceptionally high temperatures. The ceramics produced include silicon carbide (SiC), silicon oxycarbide (SiOC), silicon nitride (Si_3N_4), silicon oxynitride (Si_2N_2O) and others[30,118,120–123].

The molecular structure and type of the preceramic polymer influences not only the composition but also the number of phases as well as the phase distribution and the microstructure of the final ceramic produced. Thus, the macroscopic chemical and physical properties of PDCs can be varied and adjusted to a huge extent by the design of the molecular precursor. Therefore, synthesis of preceramic polymers is one of the key issues in the field of PDCs. An oversimplified general formula of an organosilicon polymer suitable as a precursor for the synthesis of ceramics is presented in Figure 7.
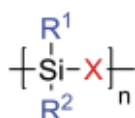

Figure 7. General oversimplified representation of the molecular structure of preceramic organosilicon compounds[118].

There are two important parameters to modify and design the preceramic compound on the molecular level: the group (X) of the polymer backbone and the substituents (R^1 and R^2) attached to silicon. The variation of X results in different classes of Si-based polymers such as poly(organosilanes) with X=Si, poly(organocarbosilanes) with X=CH2, poly(organosiloxanes) with X=O, poly(organosilazanes) with X=NH, and poly(organosilylcarbodiimides) with X=[N=C=N] (see Figure 8). By changing the functional groups R^1 and R^2 at the silicon atoms, the chemical and thermal stability as well as the solubility of the polymer, their electronic, optical, and rheological properties can be modified and adjusted.

Usually, hydrogen or aliphatic or aromatic organic side groups R are attached at the silicon atoms. In particular, the solubility, the thermal stability, and the viscosity as a function of the temperature are important features for the further processing of the polymers.
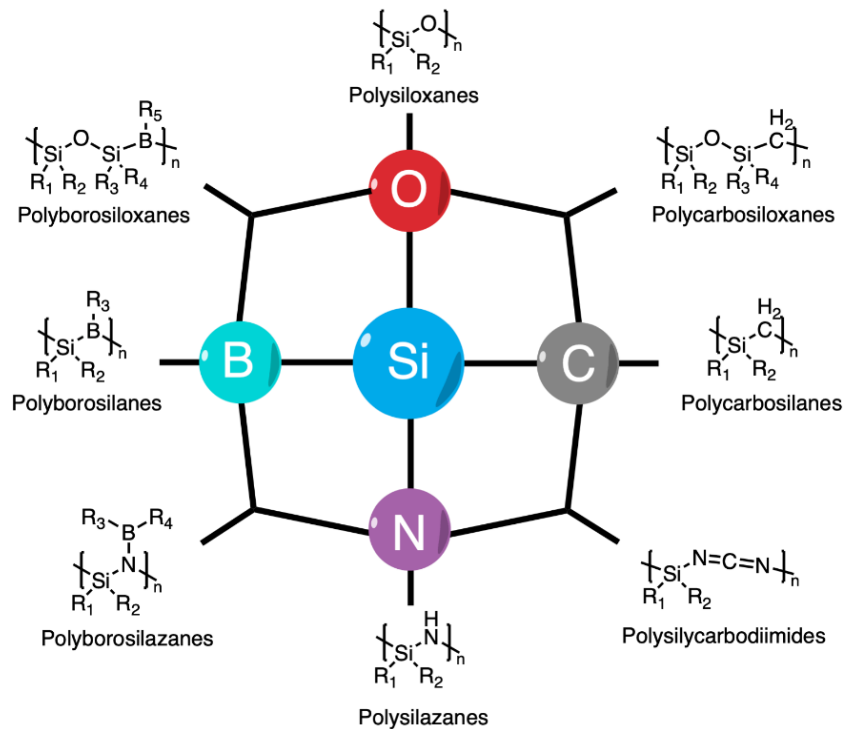

Figure 8. Main classes of Si-polymer as precursors for ceramics[118].

The traditional method to prepare ceramics involves powder technology, which, however, requires the presence of additives and significantly constrains technical applications. In the case of the PDCs, it is possible to produce ceramic fibers, layers, coatings, or composite materials starting from preceramic polymers, which cannot be easily obtained using the powder technology. In principle, preceramic polymers can be processed or shaped using conventional polymer-forming techniques, such as polymer infiltration pyrolysis, injection molding, coating from solvent, extrusion, or resin transfer molding.

Recently, an interesting and innovative approach have been recorder on the additive manufacturing of preceramic polymers as alternative approach to the elaborate processing of ceramic powders into AM. Preceramic polymers are directly used with SLA[88,90–94], DIW[99–101] and FFF[83–85] techniques in the formulation of slurry and paste, while with BJ and iSLS they are used as binders or in the infiltration process[75–79]. The common purpose is to form a solid object through the crosslinking of the preceramic polymer. Then the polymer-to-ceramic conversion is obtained with pyrolysis in a separate step.

The relatively low synthesis temperature (lower energy consumption) of 1100°C–1300°C to produce PDCs is of economic interest, in comparison with classical ceramic powder processing technology, which requires 1700°C–2000°C to sinter covalent Si_3N_4- and SiC-based ceramics.

The polymer-to-ceramic conversion (see Figure 9) occurs with gas release, isotropic volume shrinkage (20–30%, linear shrinkage) and formation of porosity (micro and macro). This typically leads to large defects, such as cracks or pores, which make the direct conversion of a preceramic part to a dense ceramic virtually unachievable. In addition, each preceramic polymer has its own conversion yield, called ceramic yield, which can be easily measured with the thermal gravimetric measurements.
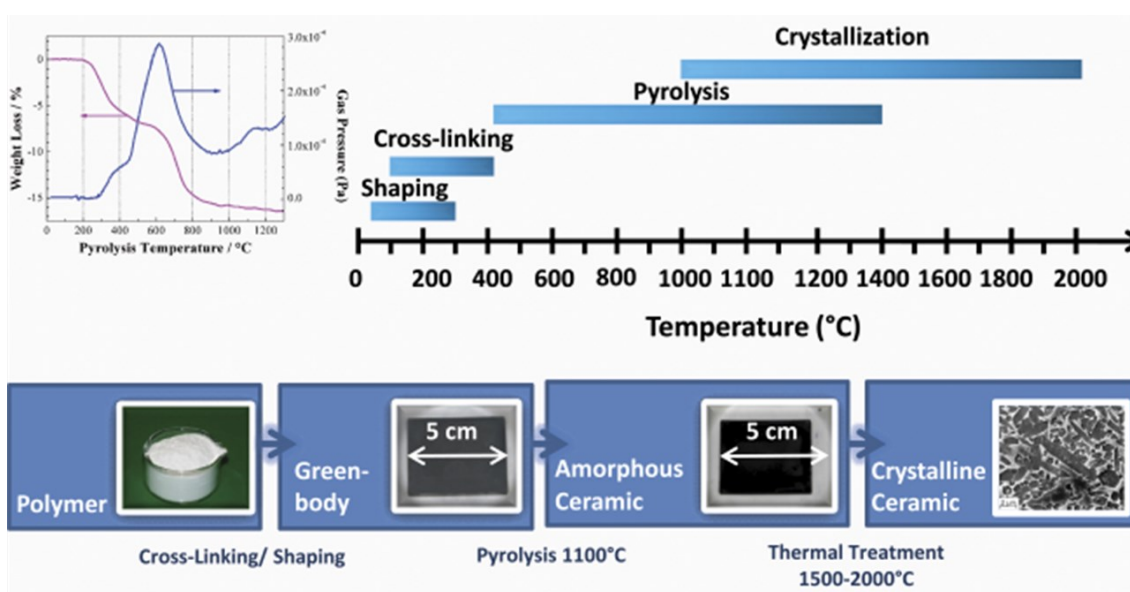

Figure 9. Thermogravimetric analysis of a preceramic polymer decomposition and microstructural evolution with pyrolysis temperature[118].

Because of their physical–chemical and functional properties as well as their ability of being shaped using a wide variety of processing methods, PDCs have been proposed for application in several key fields. For examples, information technology, transport, defense, energy as well as environmental systems, biomedical components and micro- or nano-electromechanical systems. In recent years, they were employed to produce structural ceramics for high-temperature applications, also for fibers, ceramic matrix composites, coatings, high porous components, and micro components.

1.3 Evolution of engineering design

The very big advantage of the additive manufacturing is that it allows the production of structures with different morphologies starting from a three-dimensional (3D) Computer-Aided Design (CAD) file[39,124,125]. The new generation 3D printing technologies allows fabricating complex shapes with micro-scale details. It is demonstrated that a proper design of the topology can result in structures with optimized properties for specific applications[126–128]. However, such structures can contain large numbers of geometrical details, which are impossible to generate with standard CAD packages[129]. In general, traditional CAD tools are not able to perform quick and efficient design of large and complex structures with fine details. Nowadays, the modeling of these complex structures is based on the so-called computational design.

1.3.1 Computational design Vs. Traditional CAD

Figure 10 shows the difference between the effort needed to generate a traditional CAD model and then to make changes to the model, in comparison with the effort needed to develop a computational design tool and then to make changes to the model. In the CAD environment the operator cannot always work fast, and to modify the topology of an object he must repeat the commands using the same effort and time of the first building. Therefore, the process is not automated. In computational design, the very large effort is done at the beginning of the work for the development/setup of the tool. In this phase, all the geometric quantities which describe the object are defined with parametric values. Then, each modification of the topology is very fast and takes place by modifying the numerical values of the parameters. The object is automatically re-generated with the new topology without any new effort by the operator. This is the immense benefit of computational design, which allows to be highly productive for design automation, mass customization and most importantly part optimization. For example, the practical consequence is the immediate coupling with simulations: the designed model can be simulated to predict its behavior (mechanical, thermal, electrical, etc.) and then rapidly modified based on simulation results. For example, aerodynamic optimization of race car components can greatly benefit from the use of computational design coupled with simulations.
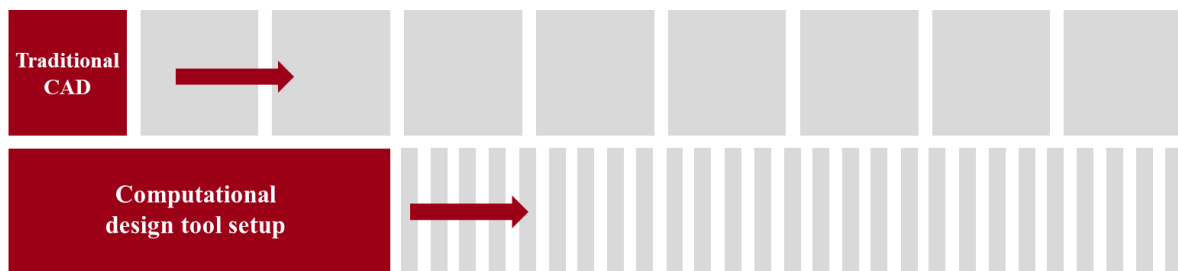

Figure 10. Traditional CAD Vs. Computational design tool setup: effort to create and make changes to the model.

Figure 11 shows the principle of the computational design approach. The process starts with the definition of the general inputs which will define the modeling of the structure, such as geometrical parameters, base geometry, mesh constraints, simulation inputs, scan data and so on. As previously described, the fundamental part of the process is the development of the core design tool, which can be done by means of algorithms, scripts, and codes, in many different software environments, such as Grasshopper, Matlab and others. The output of the process is the 3D final geometry generated by using the inputs into the design tool.
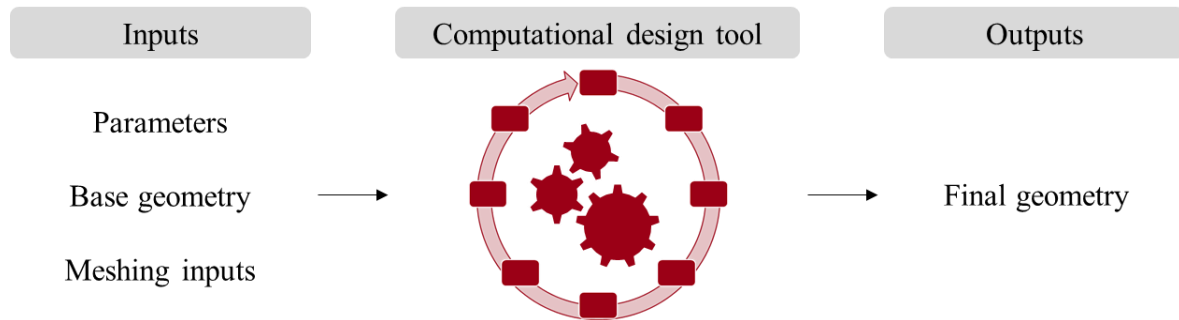

Figure 11. Computational design process: inputs definition, algorithm design and output results.

1.3.2 Design of cellular architectures

Cellular materials have become of great interest for various research fields in recent years. Also called metamaterials or lattices structures, they are any material engineered to have a property that is not found in natural materials and they are made from assemblies of multiple elements. Cellular architectures are usually arranged in repeating patterns called unit-cells, at different scales level (from nm to m) depending on the application. They derive their properties not only from the properties of the base materials, but also from their designed topology. Their precise shape, geometry, size, orientation, and arrangement give them the ability to manipulate the properties of their base material. This leads to benefits that go beyond what is possible with conventional materials[130,131]. Figure 12 shows two examples of cellular architectures.
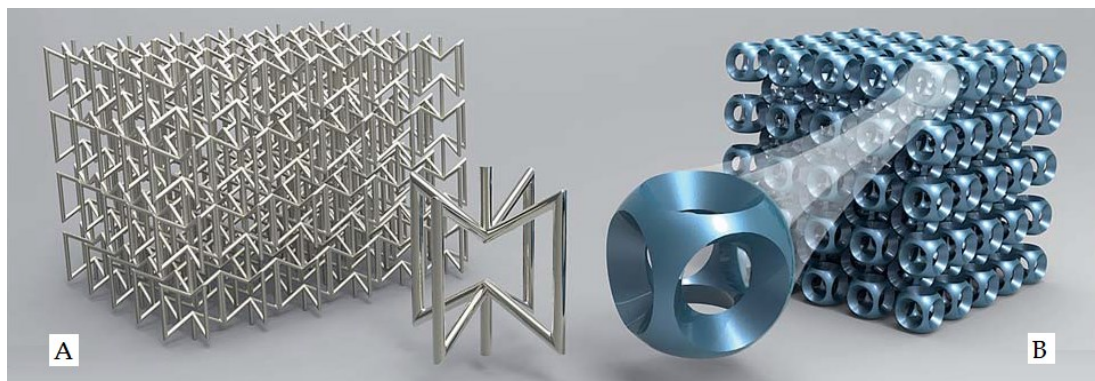

Figure 12. Examples of cellular architectures: (A) typical lattice structure made of struts hexagonal unit cells and (B) Bucklicrystal structure presented by the Bertoldi group[130,131].

Open-cell cellular structures[132] can be idealized as a network of edges (i.e., struts) belonging to interconnected polyhedra filling the space. In nature, they exist in different foams[133]. Unlike foams, lattices have an ordered 3D structure consisting of an interconnected network of repeatable dimensional arrangements[134] called "unit cells". Several types of unit cell can be designed[57], including octet, cube, hexagon, tetrakaidekahedron. The arrangement of the cells can be controlled through several parameters, such as cell size, cell type and orientation. Numerous studies have been carried out to evaluate their effects when varying one parameter at a time both experimentally and numerically[135]. The common goal of these research was to obtain a trade-off between heat transfer and pressure drop[136] in energy applications. Furthermore, macro porous lattices were characterized for their high porosity that favors heat transfer, radiation propagation, pressure drop and fluid dispersion[137]. The convective heat transfer was investigated[138] by varying average cell size and cells number, demonstrating that the increase of volume fraction of cells generates an increase in the heat transfer[139], because of the larger heat transfer area. Nowadays cellular materials (polymeric, metallic and ceramic) are produced and employed in different technological fields[140].

1.4 Additive manufacturing of cellular ceramic architectures

AM of complex ceramic architectures[57,141,142] has strongly increased in the last years due to the technology advancements both in the equipment and the constituent materials[25,26,28]. Among the non-direct manufacturing techniques available, the best improvements were obtained thanks to the development of dedicated 3D printing equipment. They can handle liquid or solid beds in a better way to achieve high parts resolution with high packing.

1.4.1 Methods and applications

The acceleration in parts production started first with the most common oxide-based ceramics[143]. For those materials several components have been successfully manufactured for biomedical applications (bones, teeth)[144,145], heterogeneous catalysis[6,146], concentrated solar energy[147], water filters[148], heat management[8,34], porous burners[49,149], automotive[150]. These components were produced mainly by stereolithography[39,90,151]. This technique is successful for many oxide powders because of their favorable optical characteristics.

Non oxide ceramics are difficult to process in this way because such ceramic powders are in general opaque, absorbing or reflective against UV light, not allowing proper photocuring of the photopolymer. Few examples of non-oxide ceramic green forming by stereolithography are present in the literature[152].

Only a few examples exist of stereolithography of photocurable slurries in which silicon carbide powders were dispersed[87,88]. On the other hand, several works have been carried out on stereolithography 3D printing of silicon carbide parts using preceramic precursor mixed with photocurable polymers[91,93,120,121].

Other techniques, hybridizing additive manufacturing for polymers with conventional processing routes for ceramics have been also developed[46,153,154]. They include polymer template 3D printing followed by replica[55,154], 3D printing of a polymer template followed by polymer infiltration and pyrolysis[99,101], 3D printing by binder jetting followed by polymer infiltration and pyrolysis[51,52,75], chemical vapor deposition/infiltration[38,74,76] or reactive silicon infiltration[58,59,79]. There is also an interesting application employing selective laser sintering on dry silicon carbide-silicon powders beds. Silicon is used as binding phase for the silicon carbide powders. It is further converted by reaction bonding into silicon carbide by providing extra carbon to the preform[54]. These techniques have all advantages and disadvantages. Among the advantages, some of them are easy to use and already industrialized, such as the replica method[124] and some of them can realize high precision parts and complex architectures.

Figure 13 shows a cellular lattice structure made of silicon infiltrated silicon carbide ceramic and produced by the replica process. The picture shows the use of the component as a porous media for a burner during combustion at 1400°C.
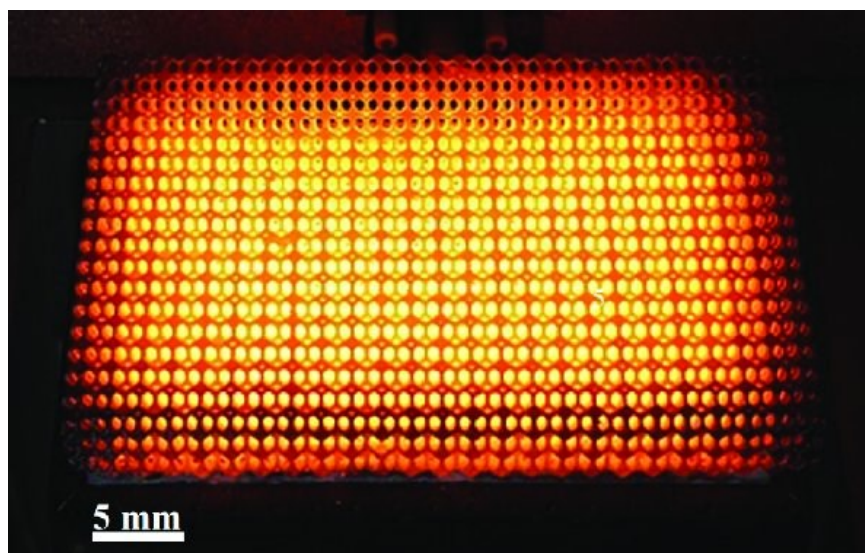

Figure 13. Porous media combustion through a silicon carbide cellular lattice. Temperature up to 1400°C. Emission of short-wave infrared radiation (1.7 μm)[57,141].

1.4.2 Limitations and prospects

Regarding the disadvantages, in the replica approach it is not possible to achieve high resolution in complex ceramic architectures, and parts (e.g., struts of cellular structures) are hollow. For direct stereolithography of photocurable polymers and ceramics powders, the main drawback is the opacity of the powders, which does not allow for high powder packing. Powder-based methods have the difficulty of removing the support material after printing especially when highly intricate structures with small pores are produced. And the green part is very fragile. Filament extrusion techniques currently do not allow sufficient geometric freedom to produce 3D highly intricate structures. Therefore, not all the ceramic AM techniques are best suited to produce complex porous ceramic architectures.

In addition, despite the unique forming capabilities of AM technology in fabricating advanced ceramics, their performance is far from meeting application requirements, particularly in aerospace. Several factors contribute to this, especially the microstructure, the material composition, and the interfacial bonding between the preform with the infiltration phase. Accordingly, AM-based advanced ceramics parts will require a focus on the following aspects[29–32,114,155]:

a. Densification: a fundamental understanding of the influence of infiltration and interface, reaction, content, and composition on the material properties is needed in respect of the AM technique. For example, in the LSI process, the common goal is to produce fully dense parts with high ceramic content with respect to residual silicon.

b. Strengthening: improving the mechanical performance of the material by controlling the defects and the porosity and by increasing the volume fraction of the reinforced phase. The current approaches produce very poor mechanical quality of the parts with respect to the traditional manufacturing processes (see Figure 6).

c. Structural and functional design: at present, a variety of structures such as lattices structures, topological structures, surfaces structures, and other novel structures are increasingly used to design structural solutions for polymer and metal AM. However, the structural design of additively manufactured advanced ceramics is still rare.

d. Simulation: development and implementation of numerical models on the forming and reaction mechanism during infiltration and validation through experimental activities on different preforms.

e. New applications: expanding the sectors for advanced ceramics by producing new materials and structures. Then AM-based ceramics could have a significant impact on a wide range of applications, such as propulsion, power generation, chemical processing, medical implants and opening new ones.

2

Process development

This chapter aims to describe the process developed in this thesis work for the fabrication of nearly fully dense, net-shape silicon infiltrated silicon carbide components. This novel hybrid additive manufacturing approach allows to overcome several processing problems that have been found in other AM techniques for ceramics. The big advantage is the possibility of manufacturing Si-βSiC ceramics directly from the preceramic precursor, without the need of adding ceramic powder to the infiltrating solution.

The part of this chapter is published in:

- Journal of European Ceramic Society in August 2021 as "Pelanconi, M., Colombo, P., & Ortona, A. (2021). Additive manufacturing of silicon carbide by selective laser sintering of PA12 powders and polymer infiltration and pyrolysis. Journal of the European Ceramic Society, 41(10), 5056-5065." Note: the flexural strength (see section 2.3.4) was calculated using f=1 in Eq. 9. https://doi.org/10.1016/j.jeurceramsoc.2021.04.014

- Journal of the American Ceramic Society in February 2022 as "Pelanconi, M., Bianchi, G., Colombo, P., & Ortona, A. (2022). Fabrication of dense SiSiC ceramics by a hybrid additive manufacturing process. Journal of the American Ceramic Society, 105(2), 786-793." Note: the flexural strength (see section 2.3.4) was calculated using f=1 in Eq. 9. https://doi.org/10.1111/jace.18134

2.1 Process overview

The new hybrid approach exploits the 3D printing of polymer powders combined with polymer infiltration and pyrolysis, and liquid silicon infiltration. The process involves the use of Selective Laser Melting (SLM) technology for the preparation of a polyamide preform with high microporosity, to achieve a subsequent high infiltration rate using a liquid preceramic polymer. Pyrolysis at 1000°C is then used to obtain the polymer-derived ceramic and five PIP cycles are performed to increase the relative density of the part. The final densification is achieved though infiltration with molten silicon at 1600°C to produce a fully dense ceramic part. Figure 14 shows the schematic of the process.
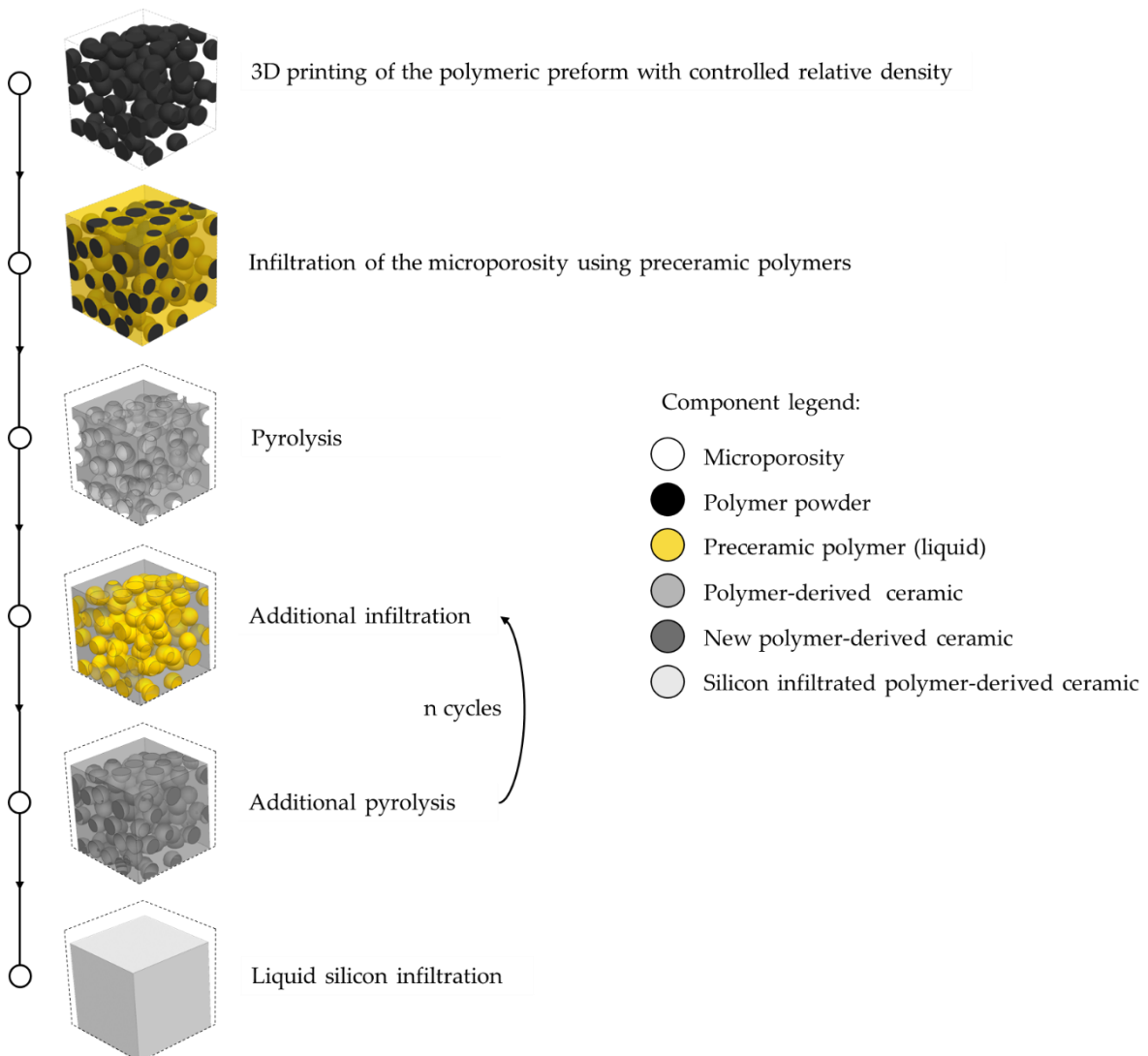
Figure 14. Overview of the novel hybrid AM process developed in this thesis work and schematic of the material microstructure at the different stages of the process.

2.2   3D printing of the polymeric preform with controlled relative density

SLM is a layer-by-layer AM technology that builds objects by solidifying their slices (cross-sections) through selectively material melting. It allows to customize the printing parameters and their combinations to control the melting rate of the polymer powders. The first aim of the work was to prepare a polymeric preform with tunable and controlled relative density.

2.2.1   Selective Laser Melting of PA12 powders

The production of the polymeric preform was performed using a commercially available SLM 3D printer (Sintratec KIT, Sintratec AG, Brugg, Switzerland) with a low-power laser beam driven by motorized mirrors (laser wavelength blue: 445 nm, diode laser power: 2.3W, spot size: 250 μm, max laser speed: 1000 mm/s, speed in z: 11 mm/h, in-plane resolution ≈ 250 μm). The printing process was performed in air involving three main phases:

- Pre-processing: the 3D CAD model of the object is sliced into two-dimensional cross-sections, the printing parameters are defined and uploaded in the machine. The chamber and the powder bed are heated to reach and maintain a uniform temperature within the PA12 sintering window (see Figure 16), to minimize the energy required for the melting.

- Processing (see Figure 15): the build platform is lowered by a pre-set distance (layer thickness) and the delivery platform is uplifted. Then, the recoating blade deposits a new powder layer. Finally, the laser traces the component cross-section providing thermal energy to melt the powders selectively. The process is repeated until printing the whole volume.

- Post-processing: natural cooling of the chamber and removing of the 3D printed part. The non-melted powder around the part is removed using compressed air.
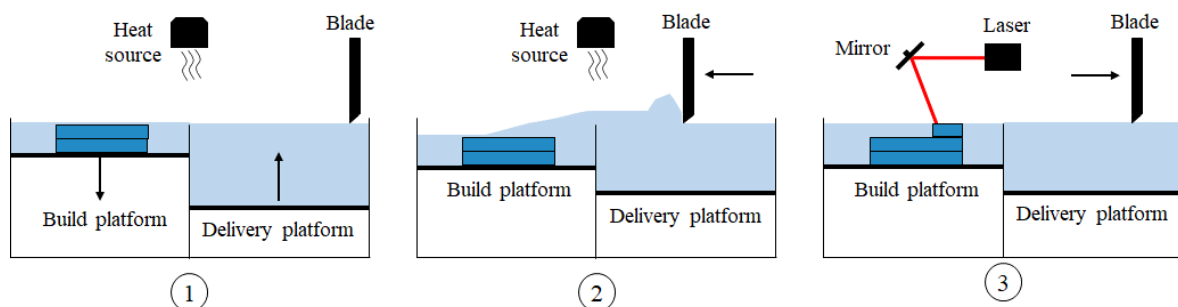

Figure 15. Schematic of the SLM technology for polymers: (1) lowering of the build platform (by a fixed layer thickness) and uplift of the delivery platform, meanwhile the chamber temperature is regulated by a heat source; (2) deposition of a new powder layer by the blade and heating of the new powder layer; (3) selectively melting of the polymer powders by the laser beam (driven by motorized mirrors).

Black spherical powders (D50: 60 μm) of polyamide 12 (PA12, Sintratec AG, Brugg, Switzerland) were used for the 3D printing. PA12 is a thermoplastic and semicrystalline-crystalline material with the formula $[-(CH_2)_{11}C(O)NH-]_n$ suitable for processing with the SLM technique, with a density of 1.0 g/cm³. The thermal behavior of PA12 was evaluated by differential scanning calorimetry (DSC) using a thermal analysis system (TGA/DSC 3+, Mettler-Toledo GmbH, Greifensee, Switzerland). The data were recorded with the STARe software package (Thermal Analysis Software, Mettler- Toledo GmbH, Greifensee, Switzerland). The powder was heated and cooled in air (flow rate of 50 mL/min; heating/cooling rate (*HR*) of 10 °C/min) up to 220°C to determine its sintering window. Four tests were performed and Figure 16 shows the average curve of the specific power (*SP*) as a function of temperature.
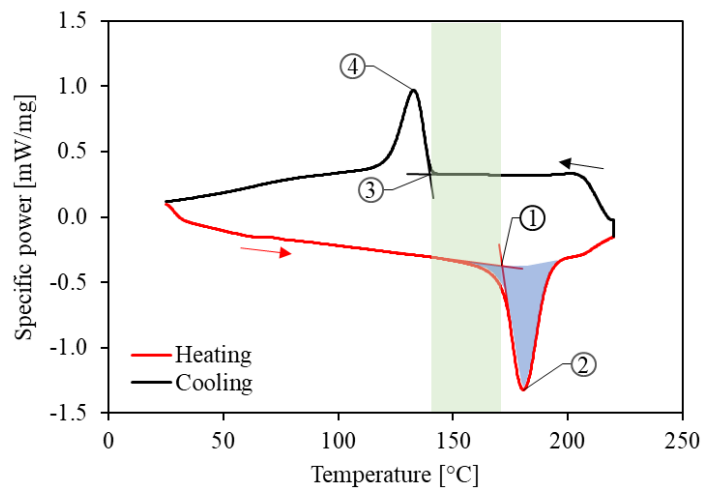
Figure 16. DSC plot of the heating and cooling of PA12 in Air. (1) onset of melting at 171°C; (2) melting point at 181°C; (3) onset of crystallization at 140°C; (4) crystallization point at 133°C. The green area is the sintering window between 140°C and 170°C. The blue area is the enthalpy of melting.

Figure 16 shows the DSC data recorded for PA12 in Air. The material exhibited a sintering window between the onset of crystallization at 140°C and the onset of melting (*T$_m$*) at 171°C. This range defined the temperatures at which the 3D printer must operate. The melting temperature peak occurred at 181°C. The thermal analysis system also provided two useful quantities related to the material:

- the melting enthalpy (*hf*) of 86.94 Jg⁻¹, by integrating the red curve between 150°C and 200°C (blue area) and dividing by the heating rate of 0.167 °C/s.

- the specific heat capacity (*cp*), which is temperature dependent and can be calculated with the following the equation:

$$cp \left[\frac{J}{g \cdot °C} \right] = \frac{SP \left[\frac{W}{g} \right]}{HR \left[°\frac{C}{s} \right]}$$

Eq. 2

2.2.2   Experimental campaign

The aim of this experimental campaign was to select the proper printing parameters to control the relative density. The printing parameters affect the melting rate of the powders and thus the microporosity (φ) of the material. Fully or partially melting influences the microstructure morphology and the final properties of the component, such as the relative density (p_{rel}) and mechanical strength (σ). Poor melting leads to low relative density and vice versa. Figure 17 shows the schematic of the melting stages during SLM 3D printing. By regulating the supplied energy density, it is possible to increase the enthalpy of the powder bed and therefore the melting rate, with subsequent control on the relative density of the final part.
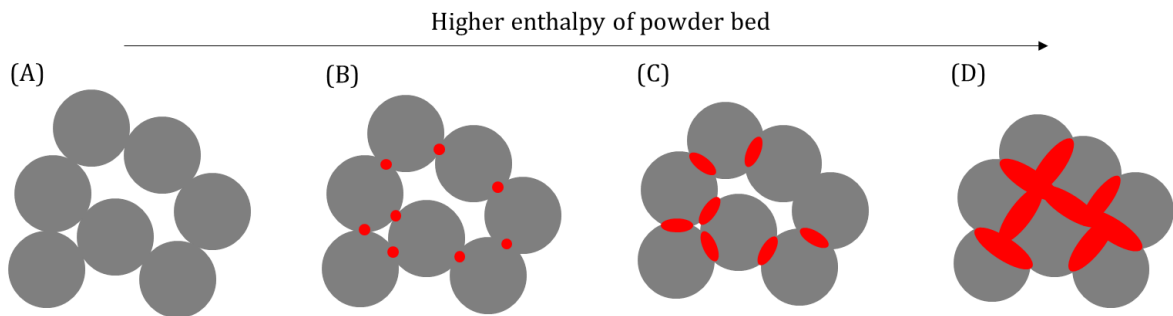
Figure 17. Schematic of the melting stages during 3D printing with SLM technology. Red shapes indicate the bonding bridges. (A) no permanent bonding between particles; (B) very slight bonding and melting allowing 3D printing of the part with very low relative density and mechanical strength; (C) little more melting with consequent increasing of the relative density and mechanical strength; (D) fully melting of the powder bed leading to a fully dense part with high mechanical strength.

Figure 18 shows the optical view of the surface of two different 3D printed samples. The difference between a partially melted part with microporosity (Figure 18-A) and a fully melted part with no microporosity (Figure 18-B) is visible.
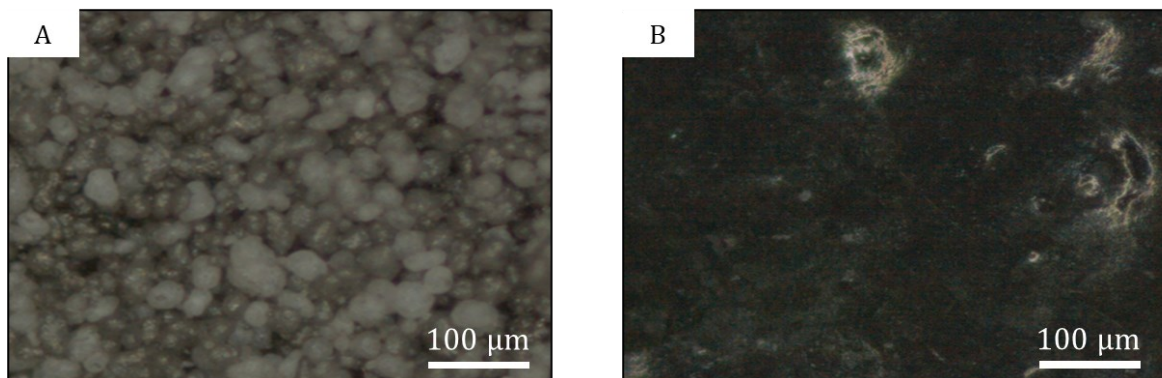

Figure 18. Optical imagines of the different melting rate of the PA12 powders: (A) partially melted material with microporosity; (B) fully melted material without microporosity.

Table 2 shows the ranges of the "open parameters" of the Sintratec KIT, which can be varied and combined to control the energy density supplied to the powder bed and the relative density of the 3D printed object.

Parameter	Unit	Default range	Screening result
Laser speed (v)	mm/s	1-1000	600-1000
Layer thickness (z)	μm	50-500	100-200
Powder surface temperature (T_b)	°C	20-180	155-170
Chamber temperature	°C	20-150	140
Hatching spacing (y_h)	μm	1-500	250
Number of perimeters	-	0-3	1
Perimeters offset	μm	1-500	100
Hatching offset	μm	1-500	120

Table 2. Ranges of the open parameters of Sintratec KIT, and screening results.

In a preliminary analysis, a screening DoE method was used (Design-Expert 10.0, Stat-Ease, Minneapolis, MN 55413, USA) to reduce the parameters range as shown in the table. Results of the preliminary tests showed that the laser speed (v), layer thickness (z) and powder surface temperature (T_b) had the higher influence on the relative density of the 3D printed parts. These parameters were chosen for the optimization DoE analysis to find the combination that allowed manufacturing low relative density preforms with excellent quality and resolution, easy to clean and to handle. High porosity of the part is essential for its subsequent infiltration with liquid preceramic polymer and to obtain a high ceramic content after pyrolysis.

In the optimization DoE, laser speed (600-1000 mm/s), layer thickness (100-200 μm) and powder surface temperature (155-170°C) were simultaneously changed to investigate their influence on two responses: the relative density and the quality of the 3D printed polymeric preforms. Parallelepipeds (8×6×3 mm³) were printed and characterized. A total number of 72 print jobs were performed with three replicas for each sample.

The relative density was calculated with the following equation:

$$\rho_{rel} = \frac{\rho^*_{calc}}{\rho_{PA12}} \qquad \qquad Eq.\ 3$$

where ρ_{PA12} is the true density of the PA12 powder and ρ^*_{calc} is the apparent (or bulk) density calculated by the ratio between the weight and the measured volume of the sample. The sample quality was rated with a score from 1 (insufficient) to 5 (excellent), by evaluating the size of the sample with respect to the size of the CAD model, shape distortion, cracks, and delamination.

Figure 19-A and -B depict the perturbation of the relative density and the parts quality by varying the individual parameters, showing that both responses increased with the decreasing of v and z. Vice versa responses increased with the increasing of the T_b. Therefore, low values of relative density were obtained with the combination of lower T_b and higher v and z, while for the high-quality response was the opposite. Figure 19-C shows that the relative density was affected by the interaction between v and T_b: increasing v resulted in a relative density decreasing with higher influence at 170°C. Figure 19-D shows that the quality was affected by the interaction between v and z: decreasing v resulted in a quality increasing with higher influence at 200 µm. Figure 19-E shows that the quality was affected by the interaction between T_b and z: increasing T_b resulted in a quality increasing with higher influence at 200 µm. Figure 19-F shows a 3D plot of the relative density as a function of v and T_b at $z = 100$ µm, showing that low values of relative density were obtained with higher laser speed and lower temperature. High values of relative density were obtained in the opposite corner.
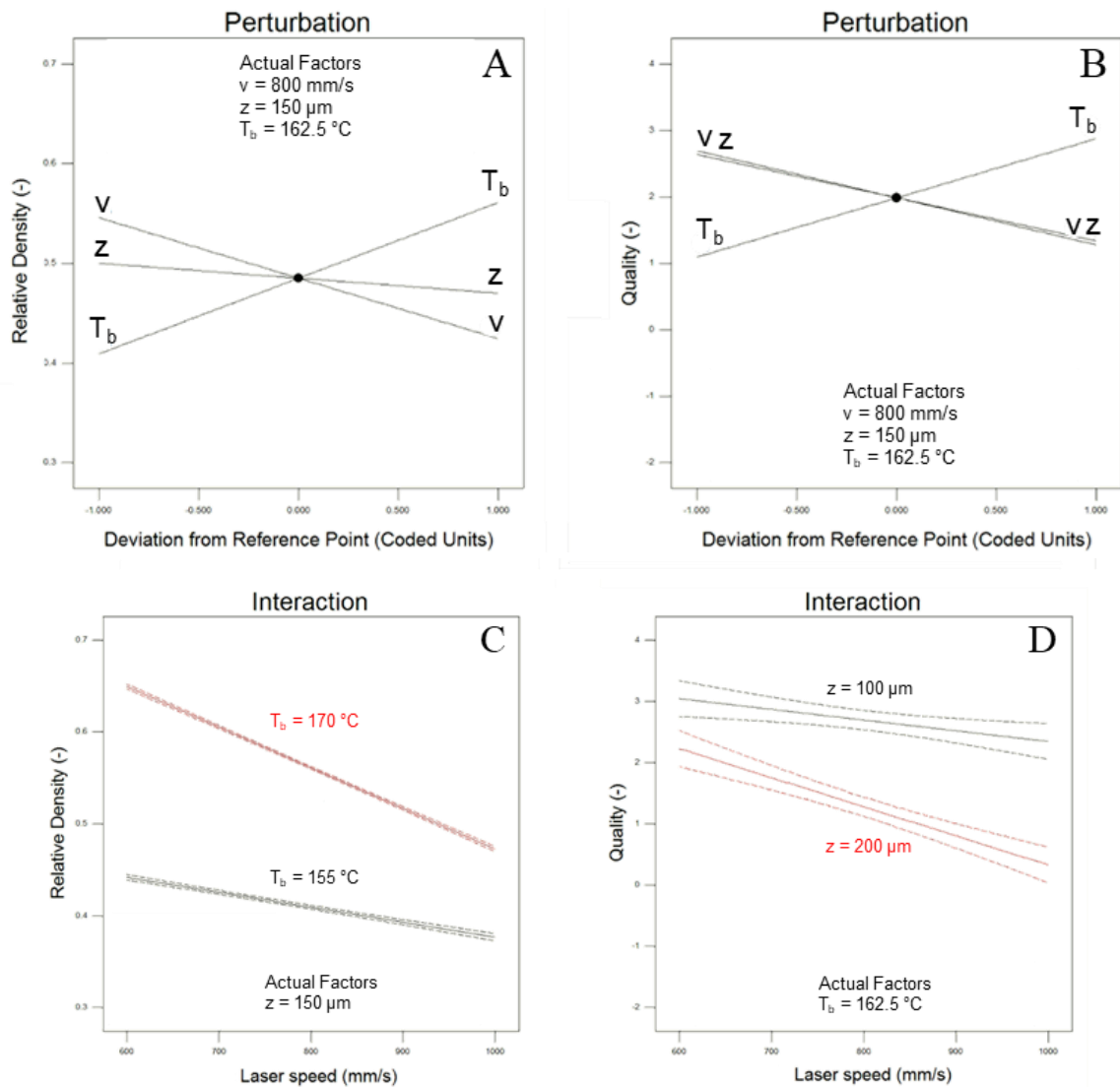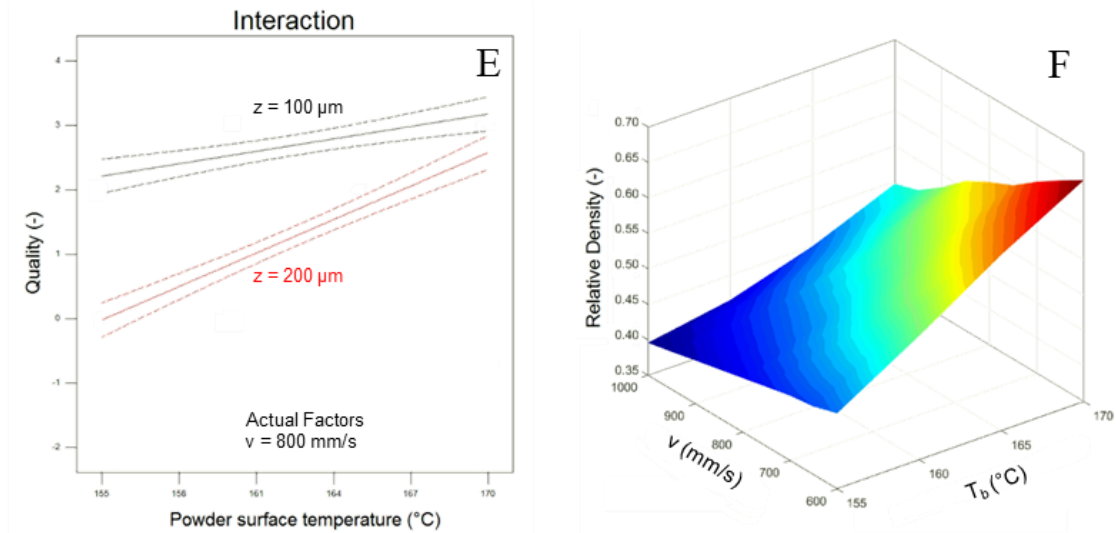
Figure 19. Optimization DoE results: (A) relative density and (B) quality as a function of the individual parameters; (C) relative density as a function of the interaction between laser speed and powder surface temperature; (D) quality as a function of the interaction between laser speed and layer thickness; (E) quality as a function of the interaction between powder surface temperature and layer thickness; (F) 3D plot of the relative density as a function of the laser speed at different powder surface temperature at a layer thickness of 100 μm.

Figure 20 shows the results obtained for the 3D printed 72 specimens in terms of relative density as a function of laser speed, at different powder surface temperature and layer thickness values of 100 μm (Figure 20-A) and 200 μm (Figure 20-B).
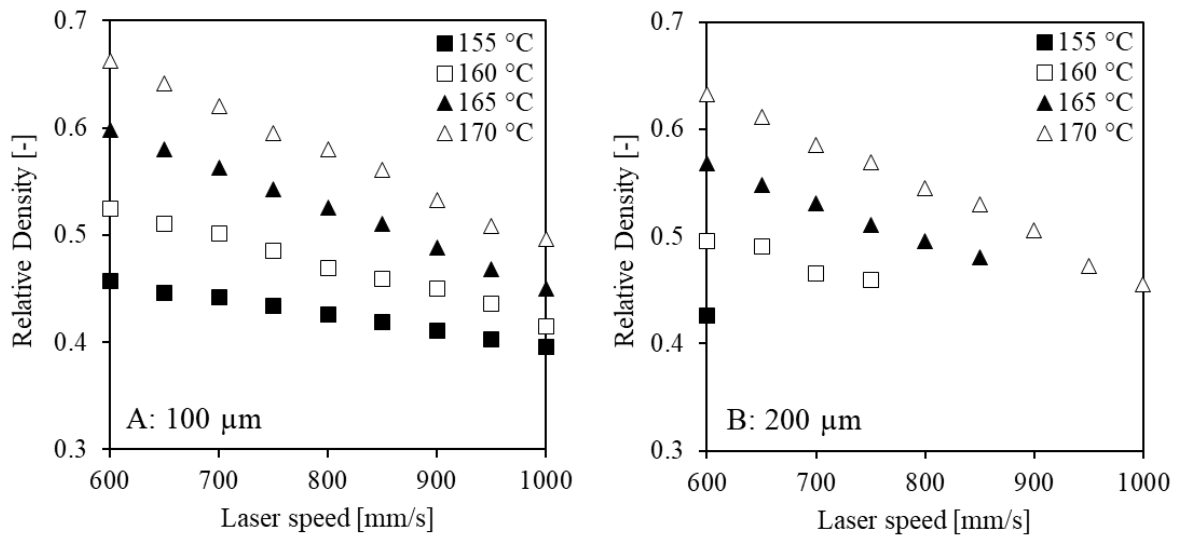
Figure 20. Relative density of the PA12 3D printed preforms at different combination of laser speed, powder surface temperature values and layer thickness of: (A) 100 μm; (B) 200 μm. Average standard deviation for the relative density of each test: ±0.02. Table 3 reports the data recorded.

As expected, the highest relative density of 0.66 was obtained with the lower laser speed of 600 mm/s, the higher temperature of 170°C and the smaller layer thickness of 100 μm. This combination of printing parameters allows to provide more thermal energy during printing and consequently to obtain a higher melting degree of the PA12 particles.

Conversely, the relative density decreased with increasing laser speed and decreasing temperature until reaching the lower value at 0.40 with a 100 μm layer thickness. In general, the relative density decreased with a layer thickness of 200 μm (Figure 20-B), but this led to a significant decrease in the mechanical strength and handleability of the parts. Indeed, with the temperature of 155°C and laser speed higher than 600 mm/s, the prints failed due to insufficient energy for melting (missing dots in Figure 20-B). Table 3 summarizes the data of the 3D printing results.

2.2.3   Melting energy calculation

In a laser melting process, the control of the thermal conditions during printing is a fundamental requirement for producing object with high quality and properties. The parameters, summarized in Table 2, are the printing inputs for the operator and they can be quantitatively correlated to the energy provided to the PA12 powder. Such quantity is the applied energy density (*AED*) and it was calculated by the following equation[156–160]:

$$AED\left[\frac{J}{mm^3}\right] = \frac{P[W] \cdot S[-]}{y_h[mm] \cdot v[mm/s] \cdot z[mm]} \qquad Eq.\ 4$$

where P is the laser power of 2.3 W, S is the scan count of 1, y_h is the scan hatching spacing of 0.25 mm, v is the laser speed, z is the layer thickness.

Figure 21-A shows the relative density and microporosity as a function of the applied energy density, at different combination of powder surface temperature values and at different layer thickness. Results showed that samples with relative density from 0.40 to 0.65 can be obtained using both layer thicknesses. The difference was in the quality of the samples: with a layer thickness of 100 μm the quality was higher and with a layer thickness of 200 μm the quality was lower (see Figure 19-D and -E) due to the low energy density that was provided to melt the material. As expected, the *AED* increased with decreasing of the laser speed at a constant temperature value, due to the laser beam providing more energy to the powder by staying on it for longer times. With smaller layer thickness the *AED* was higher because the volume taken into consideration was smaller at the constant power (Figure 21-B).

The applied energy density was compared to the theoretical melt energy (*TME*), which is the energy required to melt a given material[156–160]. The TME calculation was performed assuming that it was equal to the energy needed to heat up the PA12 from the powder surface temperature to its melting onset temperature, by the following equation:

$$TME \left[\frac{J}{mm^3}\right] = \left[cp \cdot (T_m - T_b) + h_f\right] \cdot \rho_{PA12} \cdot pf \qquad Eq.\ 5$$

where *cp* is the specific heat capacity of PA12, T_m is the melting onset temperature, T_b is the powder surface temperature, *hf* is the enthalpy of melt, *p* is the PA12 true density and *pf* is the assumed packing factor of 0.418[156].

Table 3 summarizes the data obtained for the applied energy density and the theoretical melt energy calculations. The comparison of these two quantities was done by calculating the energy melt ratio (*EMR*)[156–160], which is the ratio between the applied energy density (*AED*) during the laser melting process and the theoretical melt energy (*TME*), using the following equation:

$$EMR \ [-] = \frac{AED \left[\frac{J}{mm^3}\right]}{TME \left[\frac{J}{mm^3}\right]} = \frac{\frac{P \cdot S}{y_h \cdot v \cdot z}}{\left[C_p \cdot (T_m - T_b) + h_f\right] \cdot \rho_{PA12} \cdot pf} \qquad Eq.\ 6$$

If the *EMR* coefficient is equal to 1 it means that the minimum amount of energy is applied to melt the material, if *EMR* < 1 the energy applied is less and the material will not melt, while if *EMR* > 1 the energy applied is higher than the minimum necessary for melting.

Figure 21-C shows that *EMR* increased with the increasing of the powder surface temperature for both layer thicknesses. The trends were quite similar but, by increasing the temperature, the *EMR* increased more using a layer thickness of 100 μm. The EMR decreased by increasing the layer thickness because of the larger amount of material that must be melted. With all the parameters combination, the *EMR* was higher than 1, meaning that at least the minimum amount of energy for melting was applied during each 3D printing test.

In addition, an important result was provided by the dashed lines in Figure 21-C, which are referred to the non-printable samples. It was observed that with *EMR* < 1.60 the print job failed due to insufficient applied energy density, leading to non-melting of the powders. These tests correspond to the same values missing from Figure 20-B and to the red data reported in Table 3. Exception for the combination of *v* = 650 mm/s, T_b = 155°C and *z* = 200 μm, which was unprintable despite having an EMR of 1.69.

Instead, very high-quality samples were produced with EMR > 3. As expected, the higher *EMR* value was obtained with z = 100 μm, T_b = 170°C and v = 600 mm/s, producing samples with the highest relative density of 0.66.
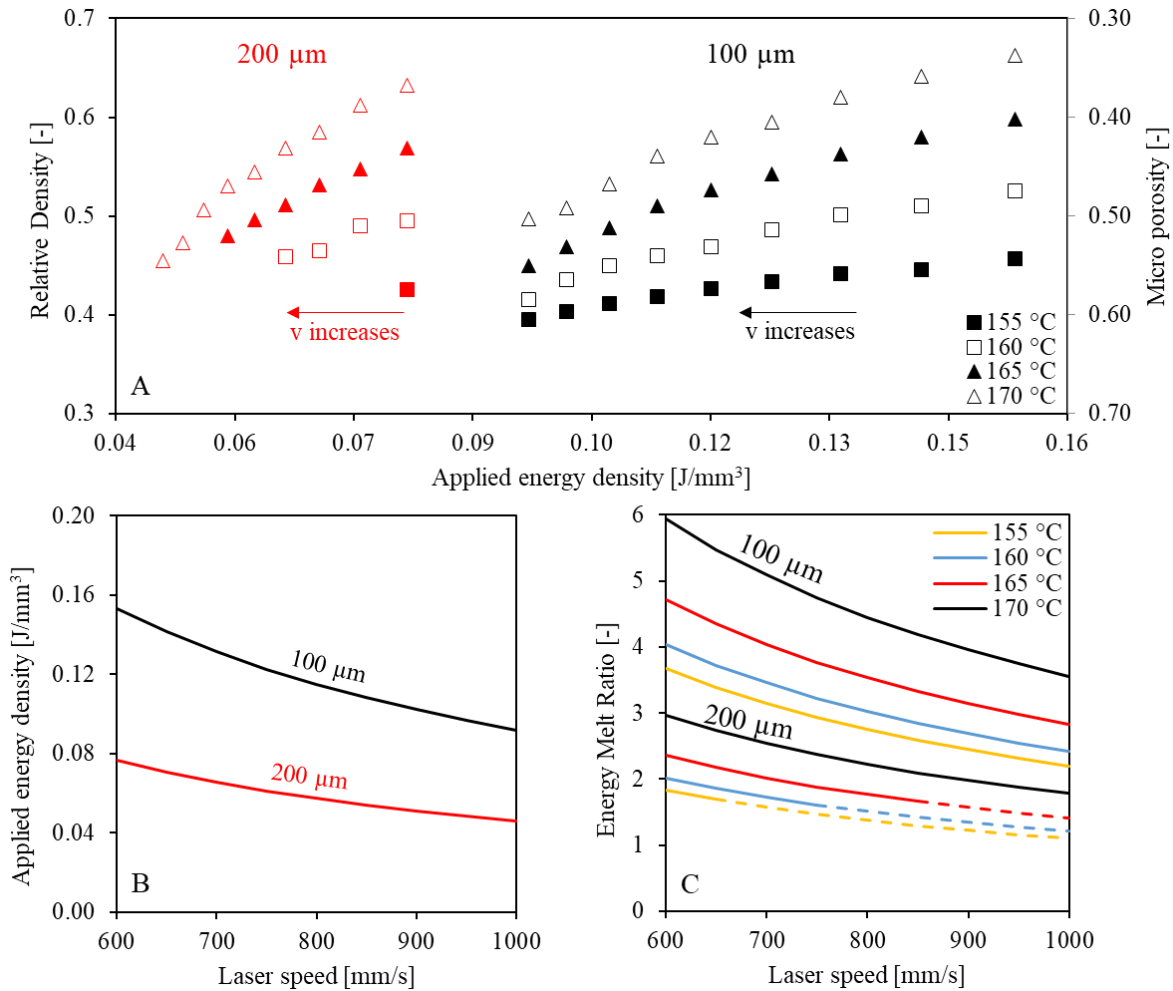

Figure 21. SLM energy calculation: (A) relative density and micro porosity as a function of the applied energy density at different temperature and layer thickness; (B) applied energy density as a function of laser speed and layer thickness; (C) energy melt ratio at different combination of laser speed, powder surface temperature values and layer thickness (dashed lines are referred to non-printable parts). Table 3 reports the data calculated.

Table 3 summarizes the data of all the experimental 3D printing tests and the melting energy calculations.

	z = 100 μm				z = 200 μm			
v	p_{rel} [-] at				p_{rel} [-] at			
mm/s	155°C	160°C	165°C	170°C	155°C	160°C	165°C	170°C
600	0.46	0.52	0.60	0.66	0.43	0.50	0.57	0.63
650	0.45	0.51	0.58	0.64	-	0.49	0.55	0.61
700	0.44	0.50	0.56	0.62	-	0.47	0.53	0.59
750	0.43	0.49	0.54	0.59	-	0.46	0.51	0.57
800	0.43	0.47	0.53	0.58	-	-	0.50	0.55
850	0.42	0.46	0.51	0.56	-	-	0.48	0.53
900	0.41	0.45	0.49	0.53	-	-	-	0.51
950	0.40	0.44	0.47	0.51	-	-	-	0.47
1000	0.40	0.42	0.45	0.50	-	-	-	0.46

	z = 100 μm				z = 200 μm			
v	EMR [-] at				EMR [-] at			
mm/s	155°C	160°C	165°C	170°C	155°C	160°C	165°C	170°C
600	3.67	4.03	4.71	5.93	1.83	2.02	2.36	2.97
650	3.39	3.72	4.35	5.48	1.69	1.86	2.17	2.74
700	3.14	3.46	4.04	5.09	1.57	1.73	2.02	2.54
750	2.93	3.23	3.77	4.75	1.47	1.61	1.88	2.37
800	2.75	3.02	3.53	4.45	1.38	1.51	1.77	2.22
850	2.59	2.85	3.33	4.19	1.29	1.42	1.66	2.09
900	2.45	2.69	3.14	3.96	1.22	1.34	1.57	1.98
950	2.32	2.55	2.98	3.75	1.16	1.27	1.49	1.87
1000	2.20	2.42	2.83	3.56	1.10	1.21	1.41	1.78

v	AED [J/mm³] at			TME [J/mm³] at			
mm/s	100 μm	200 μm		155°C	160°C	165°C	170°C
600	0.153	0.077		0.042	0.038	0.033	0.026
650	0.142	0.071					
700	0.131	0.066					
750	0.123	0.061					
800	0.115	0.058					
850	0.108	0.054					
900	0.102	0.051					
950	0.097	0.048					
1000	0.092	0.046					

Table 3. Comprehensive data of all the experimental 3D printing results and the melting energy calculations. Red data are referred to the non-printable parts (see dashed lines in Figure 21-C).

2.2.4 Optimal preform: 3D printing and microstructure characterization

The experimental campaign allowed to define the optimal parameters for the 3D printing of the polymer preform to be subsequently infiltrated and converted into a ceramic component. The selected optimal parameters which <u>allowed to obtain the lower relative density value combined with very good parts quality</u> were the following:

- Laser speed of 848 mm/s.

- Layer thickness of 100 μm.

- Powder surface temperature of 166°C.

This combination allowed to 3D print solid parts with a relative density of 0.52 ± 0.02 and very high quality, easy to clean and to handle. The true density of the PA12 was 1.0 g/cm^3 and the apparent density was of 0.52 ± 0.02 g/cm^3. The applied energy density was 0.108 J/mm^3 and the energy melt ratio was 3.365.

For the purposes of the thesis project, discs-shaped preforms were then produced with a diameter of 30 ± 0.40 mm and thickness of 6 ± 0.10 mm. The discs with a relative density of 0.52 had mass of 2.298 ± 0.127 g. A total number of 45 samples were 3D printed in view of the several infiltrations. Figure 22 shows the optical images of two PA12 discs printed with different parameters: (A) sample printed with the selected optimal parameters and (B) sample with lower relative density but poor quality. Delamination and slipping of the layers during the printing process can be observed in Figure 22-B, while Figure 22-A showed no defects.
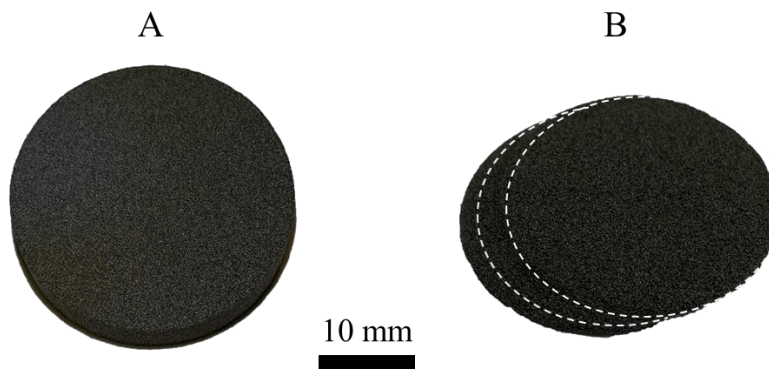
Figure 22. Optical images of two PA12 discs printed with: (A) optimal parameters showing no defects; (B) lower relative density but poor quality due to delamination and layer slipping during the printing process.

Scanning electron microscopy (SEM) analyses (JSM-6010PLUS/LA, Jeol Ltd., Japan) were conducted to investigate the microstructure of four PA12 samples with different relative density, as shown in Table 4. Sample 3 is the one manufactured with the optimal parameters. Figure 23 shows the SEM micrographs of the samples' fracture surface.

Sample	v	z	T_b	p_{rel}
-	mm/s	μm	°C	-
1	1000	100	155	0.40
2	600	200	155	0.43
3	848	100	166	0.52
4	600	100	170	0.66

Table 4. Relative density of four PA12 samples produced using different combinations of the printing parameters. Sample 3 is the one manufactured with the optimal parameters previously identified.
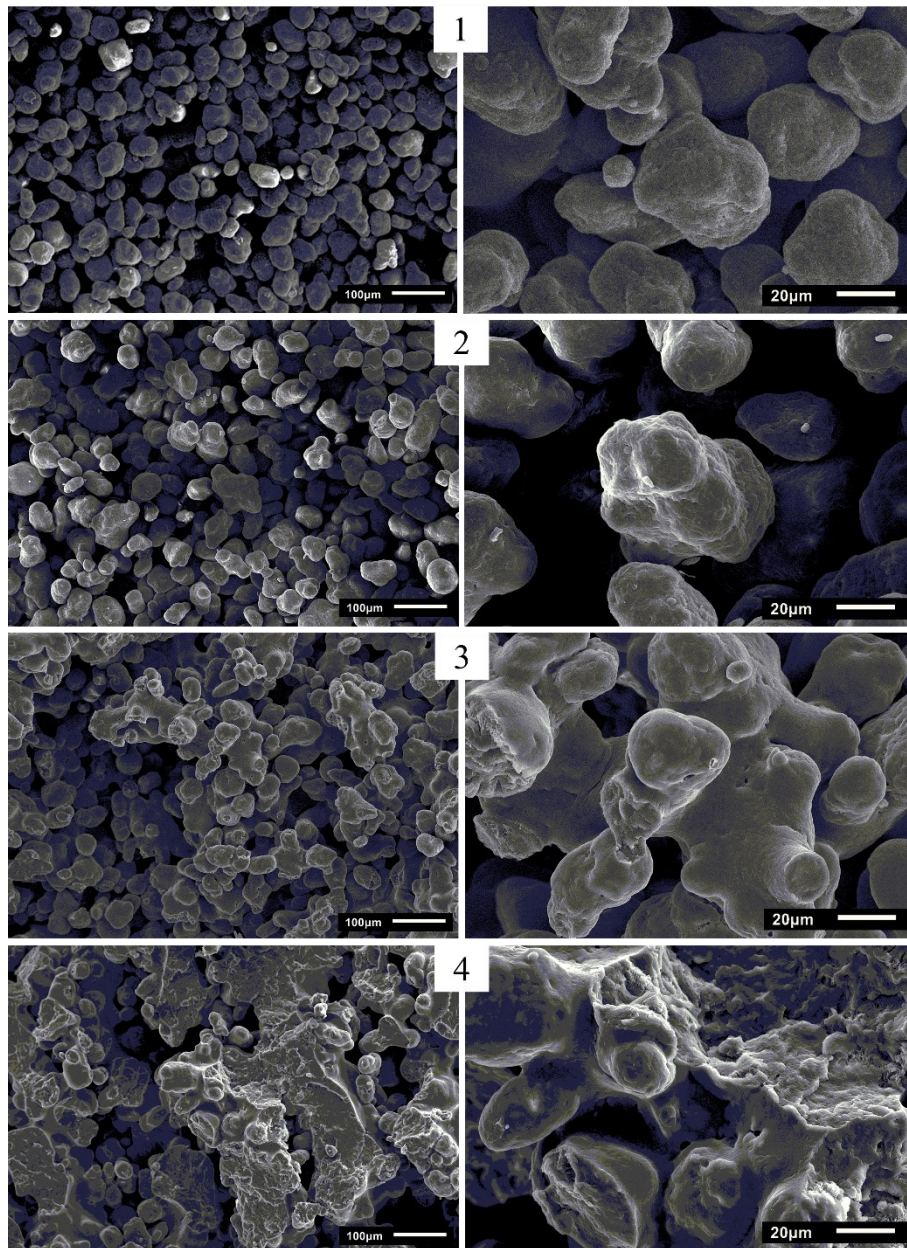
Figure 23. SEM micrographs with two magnifications of the fracture surface of PA12 samples with different relative density: (1) 0.40, (2) 0.43, (3) 0.52 and (4) 0.66. Table 4 reports the printing parameters.

As expected, the microstructure of the samples was affected by the melting rate of the PA12 during SLM. In sample 1, the particles were separated, and few small agglomerates can be observed. The material relative density was 0.40. In sample 2, more agglomerates of particles can be observed, and the relative density was slightly higher at 0.43. The relative density of sample 3 was about 10% higher, and many large agglomerates were visible. Sample 4 shows that the particles were more melted and large agglomerates were visible all over the fracture surface. Furthermore, the different fracture behavior of the four samples can be observed by the figures with higher magnification: (i) the fracture of samples 1 and 2 was characterized by the separation of the particles without any breakage of the agglomerates; (ii) the fracture of samples 3 and 4 was characterized by the breakdown of the agglomerates. This was due to the energy that holds the particles together (higher in samples 3 and 4) which was related to the energy applied for melting the powders.

The relative density of the sample 3 (0.52) was also measured thanks to the combination of SEM micrographs with a purpose-built script using MATLAB R2020 (MathWorks. Natick, Massachusetts, USA). The algorithm calculates the relative density by separating the pixels of the SEM images according to their color. Four tests were performed and Figure 24-A shows one of them as example: black/dark area represents the 3D printed PA12, and the light grey area represents the pores that were filled with the resin used to incorporate the samples. Figure 24-B shows the image elaborated by the software: black area represents the 3D printed PA12, and white area represents the pores. The approach was found to be relatively accurate as the relative density obtained from the elaborated images was of 0.54 ± 0.04 while the calculated one was of 0.52 ± 0.02.
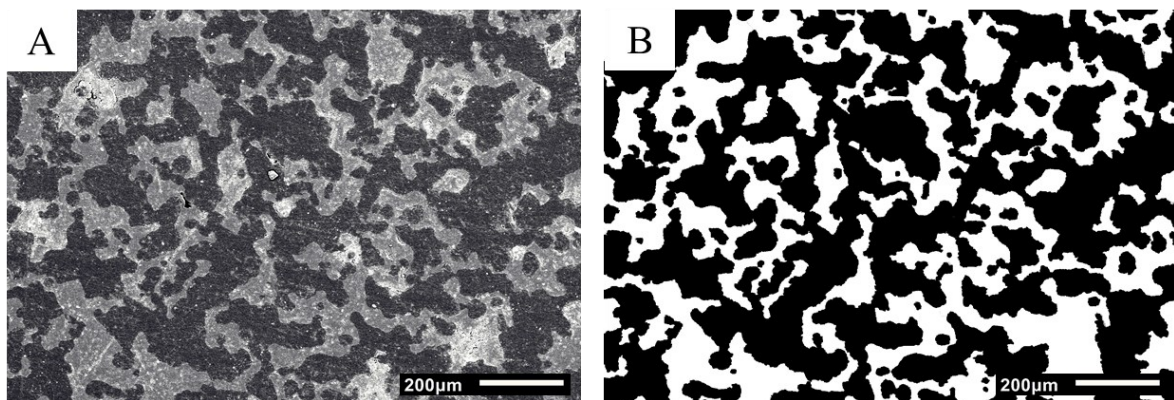
Figure 24. SEM micrographs of the incorporated fracture surface of sample 3: (A) black/dark area represents the 3D printed PA12, and the light grey area represents the pores that were filled with the resin used to incorporate the samples; (B) elaborated image using MATLAB: black area represents the 3D printed PA12, and white area represents the pores.

Another investigation on the porosity of the 3D printed samples was performed using the SEM apparatus. Figure 25 shows the micrographs of the fracture surface of the sample 4 (see Table 4) with two different magnifications:

- In Figure 25-A, the horizontal layering of the microstructure can be observed by using lower magnification. This was due to the nature of the printing process which uses a layer-by-layer approach. In the SEM analysis, it was possible to distinguish each layer and to measure it, resulting of 100 μm in this case. The fracture was characterized by separation of the layers by the breakdown of the agglomerates. These allowed to observe the porosity between the polymeric particles (interparticle porosity), which was produced by the combination of the printing parameters. This characteristic was observed in all the samples independent on the printing parameters used. The main difference was the height of the printed layer that can change from 100 μm to 200 μm, and the breakdown or not of the agglomerates.

- In Figure 25-B, the SEM micrographs with even higher magnification shows the intraparticle porosity. This image was taken on the fracture surface of a single agglomerate of sample 4. It shows the microporosity within the PA12 particle. Based on this result, by using the combination of the chosen printing parameters, not only an interparticle porosity is produced, but also a porosity of the agglomerates themselves was achieved. The subsequent infiltration step will benefit from this, as a better infiltration of the agglomerates can significantly increase the conversion yield into ceramics. However, this aspect should be better investigated as this type of porosity seems to form in polymers by fracture with plastic deformation.
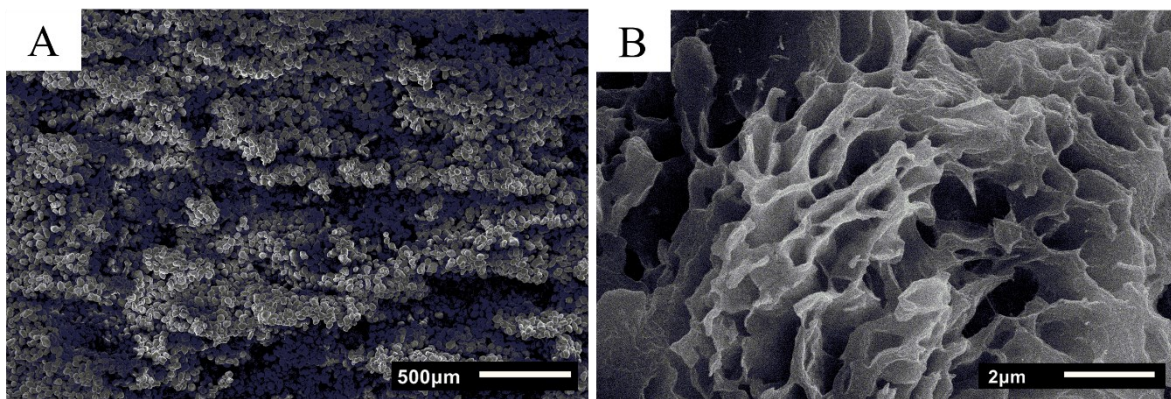
Figure 25. SEM micrographs of the fracture surface of a PA12 sample with two different magnifications: (A) interparticle porosity; (b) intraparticle porosity.

Mercury intrusion porosimetry (MIP) tests (PoreMaster 60, Anton Paar Switzerland AG, Buchs, Switzerland) were performed to evaluate the bulk porosity, the open pore size distribution, and the pore volume. Analyses were performed by using a pressure range from 0.0014 MPa to 414 MPa.

Figure 26 shows the porosimetry results of the PA12 samples previously presented in Table 4. The pore size distribution was plotted against the cumulative pore volume (Figure 26-A) comparing the four specimens. Two common behavior patterns can be observed. The first pore size range (10-45 μm) was attributed to the inter-agglomerate porosity present between the PA12 melted regions generated by SLM. The second pore size range (0.004-0.5 μm) comprised the intra-agglomerate porosity present within the individual melted regions. The results showed that the microstructure of the samples was characterized by similar pore size distributions, but different amounts of pores. This means that the melting rate of the PA12 particles influenced the number of pores and not their size[161].

It is clear from Figure 26-B that the inter-agglomerate porosity of the samples was controlled by the SLM conditions, while the intra-agglomerate porosity was negligible. Figure 26-C shows the comparison between the relative density obtained from the porosimetry analyses and the one calculated. The result showed no appreciable differences between the respective values.
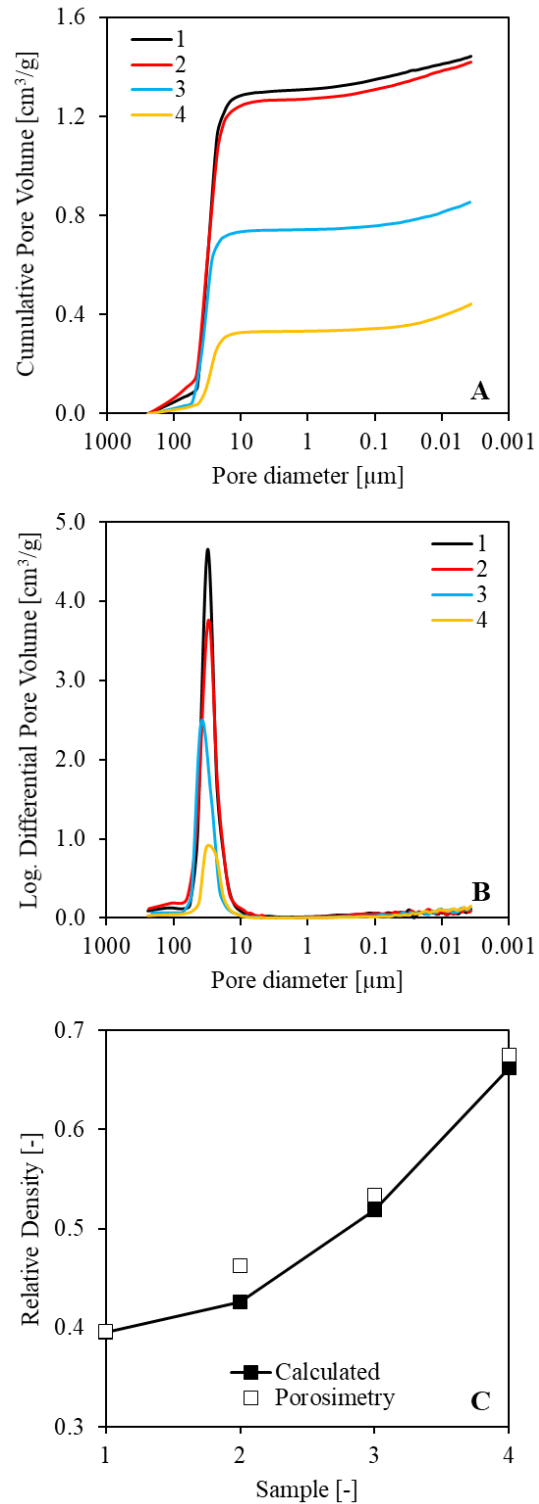
Figure 26. Porosimetry of PA12 samples (see Table 4): (A) cumulative pore volume and (B) log. differential pore volume as a function of the pore diameter; (C) calculated vs. measured relative density of the samples.

2.3 Polymer Infiltration and Pyrolysis

The development of the polymer-to-ceramic conversion involved three phases: (1) the evaluation of the thermal behavior of the ceramic precursor in combination with the preform material; (2) the development of the apparatus and the strategy to infiltrate the preforms; (3) the implementation of the heat treatment to pyrolyze the infiltrated samples and thus produce the ceramic part. The aim was to prepare a ceramic component with high relative density through several PIP cycles.

2.3.1 Thermal behavior of the starting materials

The obtained 3D printed disc-shaped preforms with relative density of 0.52 ± 0.02 were infiltrated using the allylhydridopolycarbosilane (AHPCS) preceramic polymer (StarPCS™ SMP-10, Starfire Systems Inc, Glenville, NY, USA). Polycarbosilane (PCS), $[SiH(CH_3)CH_2]_n$, derived from polydimethylsilane, has been widely explored as matrix resin for C/SiC composite. AHPCS derives from the addition to the PCS of an allyl group, which is a substituent with the structural formula $H_2C=CH-CH_2R$, where R is the rest of the molecule. It consists of a methylene bridge ($-CH_2-$) attached to a vinyl group ($-CH=CH_2$)[162]. AHPCS has been reported to have a compositional formula $[Si(CH_2CH\ CH_2)_2CH_2]_x[SiH_2CH_2]_{n-x}$. Recently, AHPCS has been used instead of PCS for the following reasons: relatively air-stability, it is liquid at room temperature and solvent-free, it is less viscous and hence better porosity penetration[163–165].

AHPCS is the precursor of SiC and in this project was used for the infiltration of the preforms and to yield the final ceramic after the thermal treatment. In the liquid state, its density is 0.998 g/cm^3 and the dynamic viscosity is $0.04–0.1$ Pa·s at 25°C. Amorphous SiC forms when pyrolyzing at 850-1200°C in inert atmosphere, with a 72–78% of theoretical ceramic yield. Nanocrystalline βSiC forms at temperature higher than ~1250°C.

The behavior of the starting materials as a function of temperature was evaluated by Thermogravimetry (TGA) and Differential Scanning Calorimetry (DSC) using a thermal analysis system (TGA/DSC 3+, Mettler-Toledo GmbH, Greifensee, Switzerland), to understand the effect of the pyrolysis. The data were recorded with the STARe software package (Thermal Analysis Software, Mettler- Toledo GmbH, Greifensee, Switzerland). PA12, AHPCS and PA12 infiltrated with AHPCS (named PA12 + AHPCS) were tested in inert atmosphere using Argon (flow rate: 50 mL/min; heating rate: 10°C/min) up to 1000°C. The combination of the two materials, PA12 + AHPCS, was obtained by infiltrating a PA12 sample with relative density of 0.52 with AHPCS (one infiltration cycle). Three analyses were conducted for each material.

Figure 27-A-F shows the TGA/DSC plots recorded for samples PA12, AHPCS and PA12 + HPCS in Argon. PA12 (Figure 27-A-B) underwent the melting between 175 and 220°C without weight change, and the decomposition between 280 and 500°C with a 99% weight loss. At 1000°C the carbon residue was 1% of the initial weight. The melting peak occurred at 190°C. AHPCS (Figure 27-C-D) cross-linked between 100 and 400°C with 15% weight loss due to the loss of oligomers, and the polymer-to-ceramic transformation occurred between 440 and 1000°C, with an additional 10% weight loss. At 1000°C, the SiC residue (ceramic yield) was 75% of the initial weight. A cross-linking peak was visible at 239°C[19,166,167]. It is essential that the preceramic polymer crosslinks before the melting of the PA12 otherwise the shape of the object is lost.

The curve for sample PA12 + AHPCS (Figure 27-E-F) showed melting of PA12 and cross-linking of AHPCS between 100 and 280°C, with 2% weight loss due to the release of AHPCS oligomers. PA12 decomposed between 280 and 520°C, and AHPCS underwent ceramization between 520 and 1000°C, with an additional 8% weight loss. At 1000°C, the total residue was 47% of the initial weight. The melting peak for PA12 occurred at 191°C, the cross-linking peak for AHPCS at 250°C and the decomposition peak for PA12 at 410°C. By analytically summing the two separate contributions according to the following equation, the PA12 + AHPCS ceramic yield should be 37 %:

$$y_{PA12+AHPCS} = \frac{Mi_{PA12} \cdot y_{PA12} + Mi_{AHPCS} \cdot y_{AHPCS}}{Mi_{PA12} + Mi_{AHPCS}} \qquad Eq.\ 7$$

where $y_{PA12+AHPCS}$ is the yield of PA12 + AHPCS, Mi_{PA12} and Mi_{AHPCS} are the initial weights of PA12 and AHPCS respectively, y_{PA12} and y_{AHPCS} are the individual yields of the two materials (1% and 75% respectively). However, from the TGA results the yield was 47%, 10% higher than calculated. This increase could be attributed to the precursor that could remain on the surface as coating and to the portion of PA12 in direct contact with AHPC (see section 2.3.3), according to microstructural investigations by SEM.
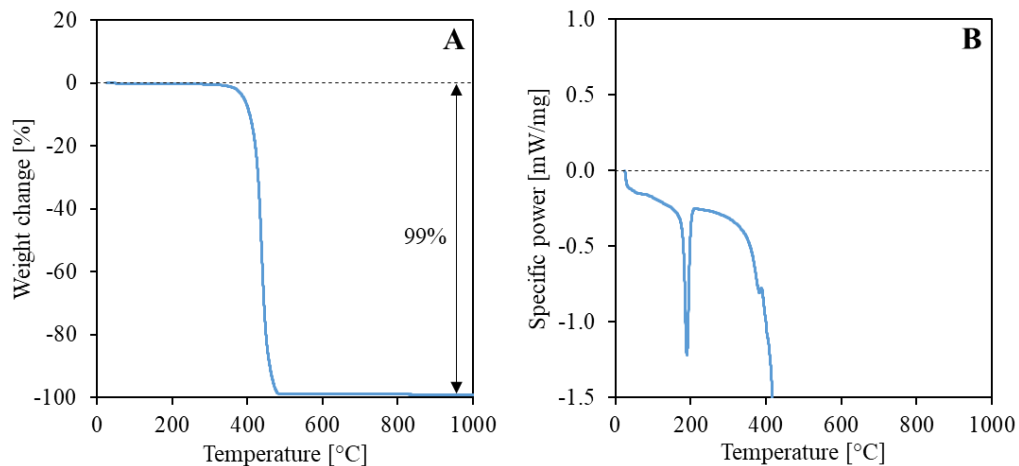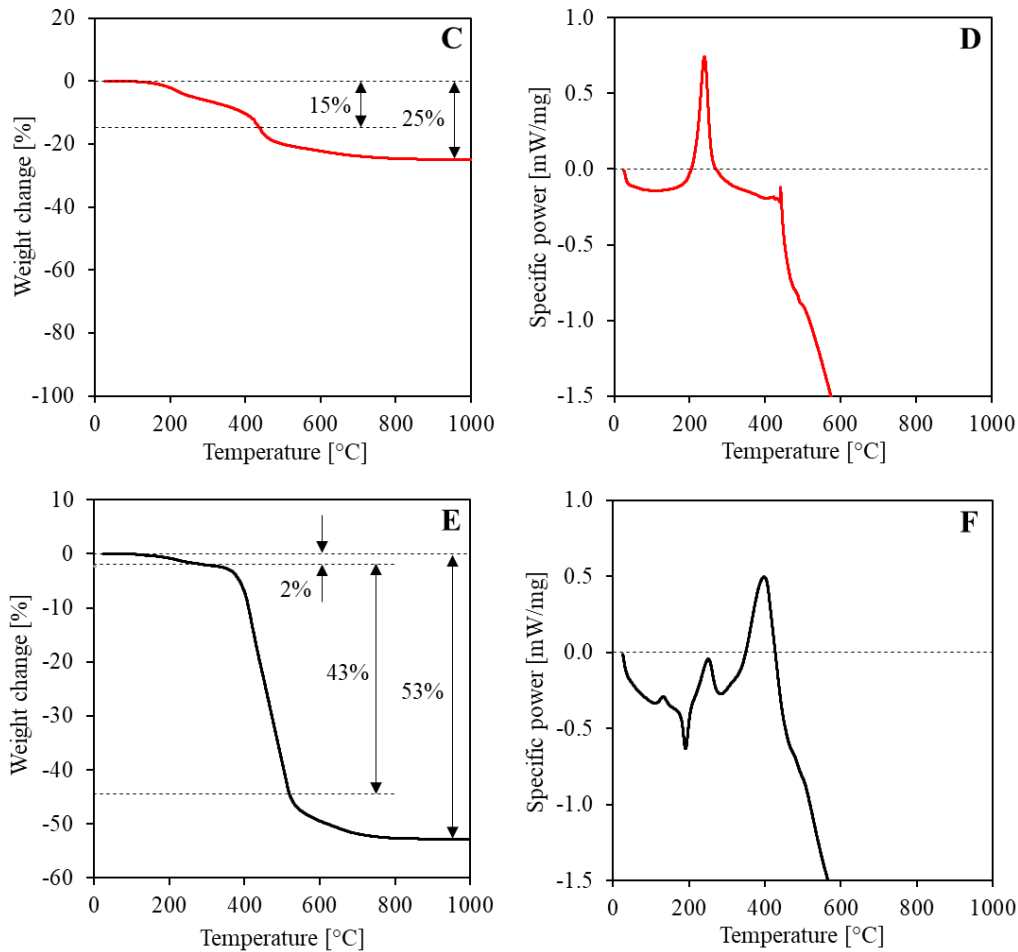
Figure 27. TGA/DSC analysis: (A)-(B) TGA-DSC plot for PA12 in Argon; (C)-(D) TGA-DSC plot for AHPCS in Argon; (F)-(F) TGA-DSC plot for PA12 + AHPCS in Argon (sample infiltrated one time).

2.3.2 Polymer-to-ceramic conversion and densification

The infiltrations were performed in light vacuum at room temperature with a purpose-built apparatus. This apparatus is a hermetic container at which bottom is poured the polymer, it allows infiltrating samples of various size, by controlling pressure and time. The infiltration process involves four phases (see Figure 28): (i) the specimen, hanging outside the polymer into the thigh container, is degassed at room temperature (RT) for 60 seconds; (ii) the sample is dipped into AHPCS and held for 60 seconds; (iii) atmospheric pressure is restored and the sample keeps into the polymer for further 60 seconds; (iv) the sample is re-emerged. Then the excess polymer is drained through a rotary system for uniform drying. The last phase of the process was fundamental to produce a high-quality object without shape distortions. The use of longer infiltration times did not lead to significant gains on the infiltration rate (the ratio between the volume occupied by the precursor and the volume of the pores) and quality of the final parts.
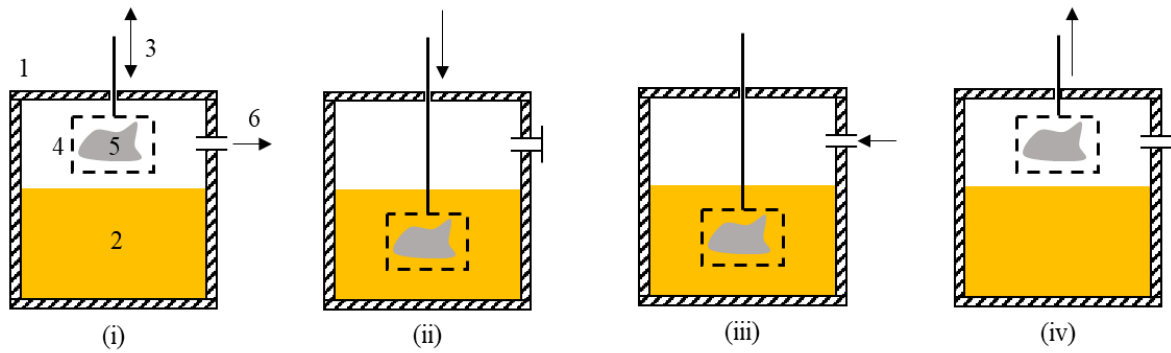
Figure 28. Infiltration apparatus: (1) hermetic pressure chamber; (2) liquid preceramic polymer; (3) z-axis piston; (4) porous crucible; (5) sample; (6) vacuum aspiration. Procedure steps: (i) sample degassing; (ii) sample dipping; (iii) restoring of the atmospheric pressure; (iv) sample re-emerging.

After infiltration, samples underwent heat treatment in high purity flowing Argon (99.99%, 30 L/h) using a vertical retort furnace (SPS01, Keos Srl, Concorezzo, IT). The thermal cycle included three ramps: (i) from RT to 500°C with a heating rate of 80°C/h; (ii) from 500 to 960°C with a heating rate of 51°C/h; (iii) a dwell of 1 hour at 960°C [*]; (iv) natural cooling to RT. Figure 29 shows the optical images of the PA12 samples as printed (A), the obtained ceramic disc after infiltration and pyrolysis (B) and the ceramic parts obtained using preforms with different relative densities (C).
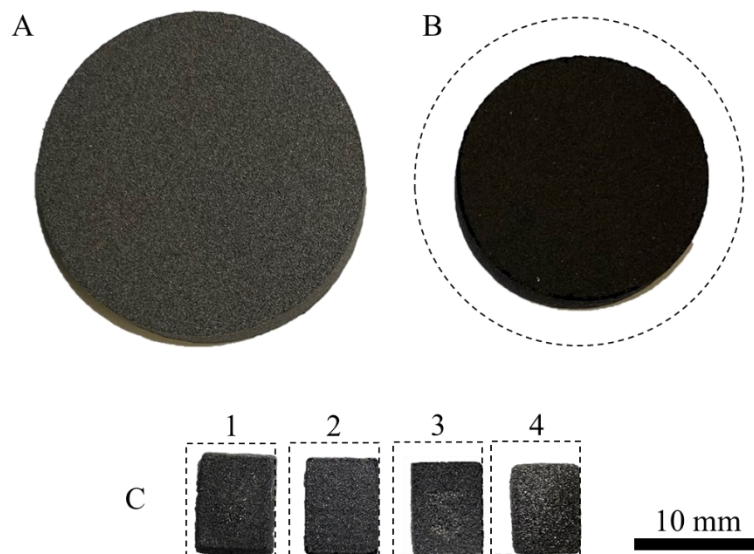
Figure 29. Optical images of: (A) PA12 sample printed with the selected parameters (relative density of 0.52 before infiltration); (B) ceramic part after the first pyrolysis; (C) ceramic parts obtained after the first pyrolysis of PA12 samples printed at different relative density values (see Table 5).

---

[*] This temperature was chosen considering that the maximum service temperature of the furnace was 1000°C. Higher pyrolysis temperature would have led to the production of a crystalline polymer-derived ceramic.

Infiltration and subsequent pyrolysis of the PA12 discs resulted in the fabrication of amorphous silicon oxycarbide / silicon carbide (SiOC/SiC) porous ceramic samples without shape distortion and macroscopic cracks. The composition of the produced ceramic was assessed, and it is presented in the paragraph 2.3.3. Before pyrolysis, the 3D printed samples had a diameter 30 ± 0.40 mm and height of 6 ± 0.10 mm. Then, the pyrolyzed ceramic discs had a diameter of 23 ± 0.25 mm and a height of 5 ± 0.10 mm. As shown in Figure 29-B, a linear shrinkage of 24% was observed during pyrolysis. This value is correlated to the infiltration rate, to the relative density of the preform and to the ceramic yield of the AHPCS polymer. Figure 29-C and Table 5 show the correlation.

Figure 29-C shows the ceramic parts obtained after the first pyrolysis of PA12 samples printed at different relative density values. Table 5 reports the effect of the printing parameters on the relative density (before infiltration) and on the linear shrinkage after the first pyrolysis. Sample 3 is the one manufactured with the optimal parameters previously identified. As result of the pyrolysis, the preform with the lower relative density achieved the lower shrinkage. This means that during infiltration, it was possible to fill more volume with the AHPCS and then to obtain a higher volumetric fraction of the ceramic phase after pyrolysis, resulting in a lower shrinkage. Increasing the relative density of the polymeric preform decreases the infiltrated volume and consequently the shrinkage of the ceramic part increases.

By regulating the printing parameters, it is therefore possible to control the size of the ceramic part, and this can be very interesting to produce components with high resolution and with very small feature (e.g., struts), such as complex cellular architectures.

Sample	v	z	T_b	p_{rel} as printed	Linear shrinkage
-	mm/s	μm	°C	-	%
1	1000	100	155	0.40	5
2	600	200	155	0.43	15
3	848	100	166	0.52	24
4	600	100	170	0.66	28

Table 5. Relative density (before infiltration) of four PA12 samples produced using different combinations of the printing parameters, and their linear shrinkage after the first polymer infiltration and pyrolysis.

The pyrolysis of the selected PA12 preform (#3) produced a ceramic part with relative density of 0.30 ± 0.02 after the first pyrolysis. This is mainly due to the PA12 degradation that produced pores inside the part and to the ceramic yield of the AHPCS precursor.

To increase the relative density and to obtain the maximum densification of the ceramics, the samples were re-infiltrated six times with liquid AHPCS and then re-pyrolyzed after each infiltration.

Mercury intrusion porosimetry (MIP) tests (PoreMaster 60, Anton Paar Switzerland AG, Buchs, Switzerland) were performed to evaluate the relative density of the parts after each PIP cycle. Analyses were performed by using a pressure range from 0.0014 MPa to 414 MPa.

Table 6 reports the measured weight of the ceramic parts after each PIP cycle and their relative density measured with porosimetry. The results are also appreciable in Figure 30. During the second cycle, the gain in weight was about 40% due to the filling of the larger pores left by the PA12 degradation. Increasing the number of cycles, the weight gained increased but with a lower rate. During the last cycle, the gain was much lower than in the other cases and consequently the relative density slightly increased. This behavior was due to the strong decrease in the size of the pores present in the sample, which then became very difficult to infiltrate. The final ceramic part, after seven infiltration and pyrolysis cycles, had a relative density of 0.90 ± 0.01, meaning that the material was not fully dense. Micropores and microcracks were still present. By performing seven PIP cycles, the apparent density of the ceramic components tripled.

PIP cycle	Weight	Gain in weight	Rel. density	Apparent density
-	g	%	-	g/cm^3
1	1.65	-	0.30	0.72
2	2.30	40	0.59	1.42
3	2.72	65	0.71	1.71
4	2.99	81	0.79	1.90
5	3.18	93	0.82	1.97
6	3.32	101	0.85	2.04
7	3.42	107	0.90	2.16

Table 6. Mercury intrusion porosimetry results in terms of measured weight, relative density, and apparent density values of the ceramic parts after each PIP cycle. The gain in weight is calculated with respect to sample after the first pyrolysis.

The density of the material was also measured by means of a gas pycnometer, using Helium (Ultrapyc3000, Anton Paar QuantaTec Inc., Florida, USA). Analyses were performed by using a pressure target of 18 psi. A bulk sample piece and sample powder were used for obtaining the apparent and true density values, respectively. Eight tests were performed for each sample.

Table 7 reports the measured apparent density, true density, and relative density values of the ceramic parts after six and seven PIP cycles obtained with Helium pycnometer analysis. A slight difference (< 2%) between the relative density measured with mercury intrusion porosimetry and the one measured with helium pycnometer was observed.

PIP cycle	Apparent density	True density	Rel. density	Rel. density (MIP)
-	g/cm³	g/cm³	-	-
6	2.043 ± 0.001	2.403 ± 0.014	0.85 ± 0.005	0.85
7	2.209 ± 0.001	2.403 ± 0.015	0.92 ± 0.005	0.90

Table 7. Helium pycnometer results in terms of apparent density, true density, and relative density values of the ceramic parts after six and seven PIP cycle.

Figure 30 shows the comparison between the relative density obtained from the mercury porosimetry analyses with the one calculated using Eq. 8, where p is the true density of the amorphous polymer-derived ceramic and p^*_{calc} is the apparent density calculated by the ratio between the weight and the measured volume of the SiOC/SiC sample.

$$\rho_{rel} = \frac{\rho^*_{calc}}{\rho_{SiOC/SiC}}$$

Eq. 8

The difference between the calculated and the measured values could be attributed to the uneven bottom and top surfaces of the sample and to the excess material attached to the external surface after the pyrolysis, which cannot be removed to avoid altering subsequent infiltrations. The measured true density of the SiOC/SiC was 2.403 g/cm³, in accordance with the literature for the pyrolyzed amorphous SiC[19,163,168] of 2.35-2.49 g/cm³.
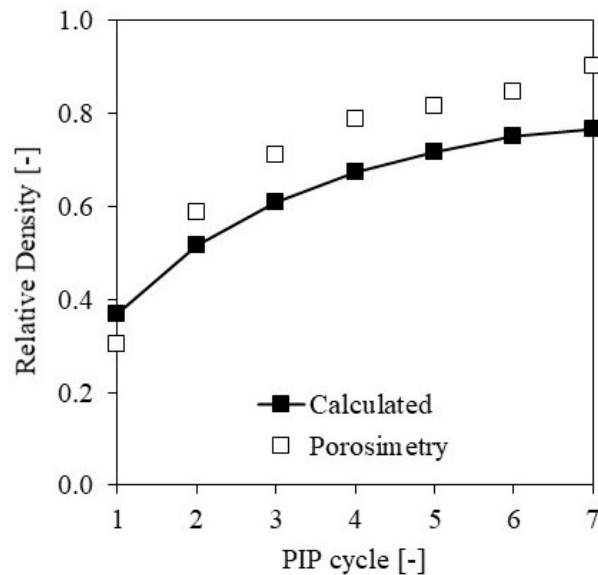
Figure 30. Mercury intrusion porosimetry results for the relative density of the SiOC/SiC samples as a function of the PIP cycle compared with the calculated values.

2.3.3 Microstructure characterization after each PIP cycle

Scanning electron microscopy (SEM) analyses (JSM-6010PLUS/LA, Jeol Ltd., Japan) were conducted to investigate the microstructure of the produced ceramic discs. Surface compositional analysis on the samples was carried out using the Energy Dispersive X-ray Analysis (EDX) probe attached to the SEM. Samples were fractured and incorporated using phenolic resin (black/dark areas). Figure 31 shows the SEM images of the polished fracture surface of the SiOC/SiC samples after each PIP cycle.
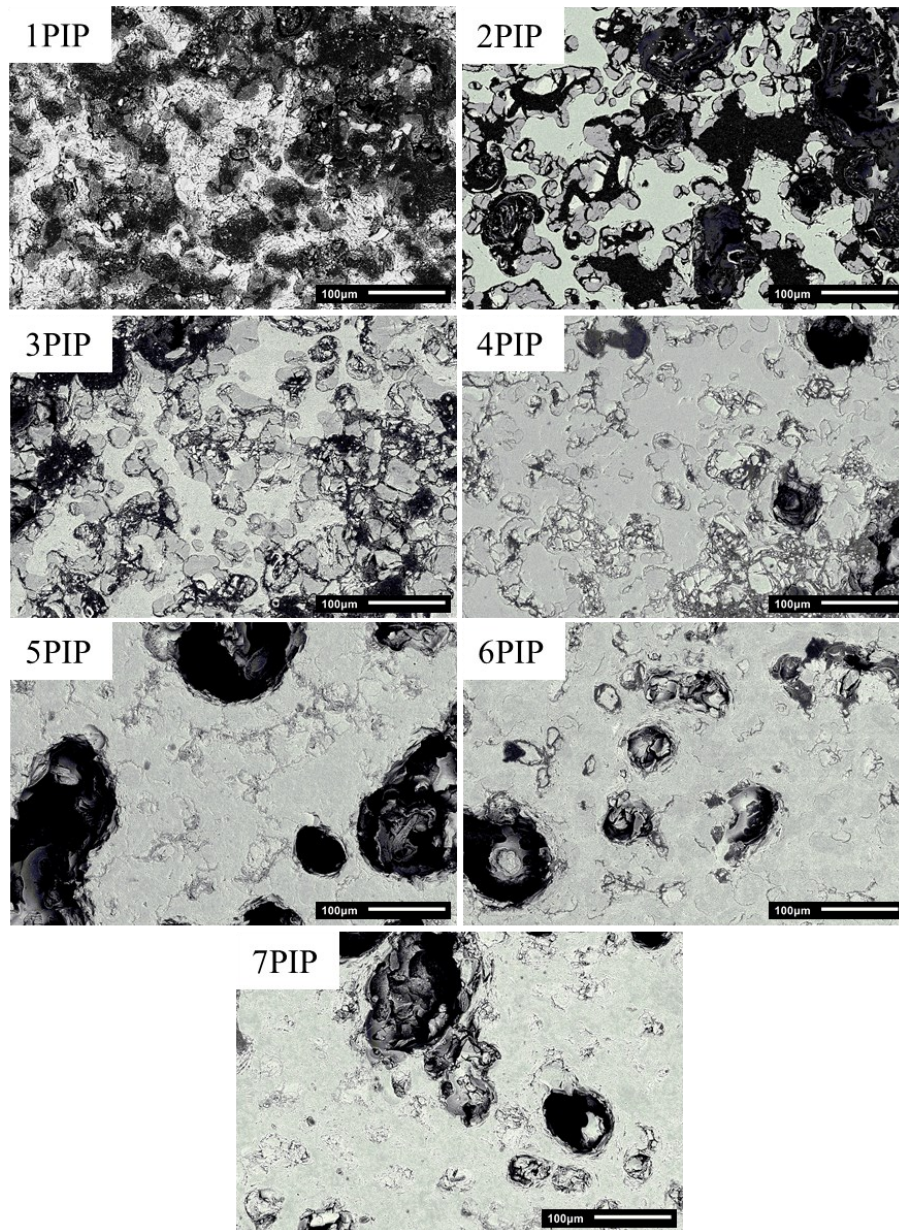
Figure 31. SEM micrographs of the fracture surface of SiOC/SiC samples after each PIP cycle: black/dark area represents the pores, the dark grey area is the SiOC, and the light grey area is the SiC.

By analyzing the composition of the samples, three different phases were found:

(i)   the black/dark area represents the pores that were in many cases filled with the resin used to incorporate the samples.

(ii)   the dark grey area is the SiOC produced by the pyrolysis of AHPCS which was directly in contact with the PA12 particles (i.e., the one deriving from the first infiltration). The main cause of the oxygen presence was the evolution of CO/CO_2 from the decomposition of PA (amide group CO-NH) which introduced oxygen in the SiC matrix[85,169]. Furthermore, the polymeric preform was not dried before processing, and humidity was present at their surface[170]. This was confirmed by a 22% oxygen content in the dark grey phase after EDX analysis (see Table 8), therefore attributable to a SiOC phase. silicon oxycarbide is a fully amorphous ceramic material. A very negligible amount of free carbon was detected by XRD (Figure 42) derived from the PA12 pyrolysis.

(iii)   the light grey area is the SiC produced by the pyrolysis of AHPCS incorporated in subsequent infiltration (cycles 2–7). It had a low oxygen content (9%) attributable to the subsequent infiltrations, which were performed in air (literature confirmed that a certain amount of oxygen is always present in the matrix, caused by its incorporation during polymer synthesis[171]).

Table 8 shows the summary of the composition results for different samples. This composition was found in all the samples from 1 PIP to 7 PIP. The large standard deviation is due to the large prevalence of SiC despite the presence of SiOC. Especially after four PIP cycles, the SiC phase covered the SiOC phase.

Area	Phase	C	O	Si
-	-	atom%	atom %	atom %
black/dark	C (resin)	88 ± 5.7	12 ± 6.4	0 ± 0.0
dark grey	SiOC	62 ± 0.7	22 ± 1.8	16 ± 4.6
light grey	SiC	67 ± 11.7	9 ± 3.2	24 ± 4.9

Table 8. EDX result of the compositions of the three areas of the SiOC/SiC samples.

Several strategies could be adopted in order to reduce the presence of oxygen and to obtain only a SiC phase: (i) in the printing phase by drying the powder before printing, printing in an oxygen-free environment or by using a polymer powder with less (or none) oxygen content; (ii) in the PIP phase by drying the preform before processing, drying the infiltrated preform before each pyrolysis cycle, infiltrating the preform in an oxygen-free environment or avoiding the incorporation of oxygen during polymer synthesis (supplier task).

An image analysis (with the tool used in Figure 24) was performed to further distinguish and quantify the three phases in the SEM images. Figure 32 shows the obtained results in terms of volume fraction against PIP cycle. Samples possessed the three phases in different volumetric fractions. After the first PIP cycle the porosity was 70% according to the mercury porosimetry (see Table 6), the SiOC and SiC phases had a volume fraction of 13% and 17% respectively. As expected by increasing the PIP cycle the porosity decreased and the solid phase increased. After seven cycles the volume fraction was 10% and 90% respectively. Figure 32 shows two different results in the material composition between the samples from 1PIP to 4PIP and the samples from 5PIP to 7PIP. In the first case, a slight increase of the SiOC phase was observed from 13% to 16% meaning that during each infiltrations a very low amount of oxygen is trapped into the preform. The SiC phase increased from 17% to 63%. Samples 5PIP, 6PIP and 7PIP showed a different composition due to the large prevalence of SiC despite the presence of SiOC. SiC increased from 79% to 87% and SiOC occupied only 2% of the total volume. This was due to the SiC phase that covered the SiOC, making difficult to see it during the SEM analysis. However, no large oxygen contamination appeared to have been introduced after the first infiltration cycle, indicating that processing of the AHPCS polymer in air is possible and the oxygen content in the first cycle was related to the PA12 conversion.
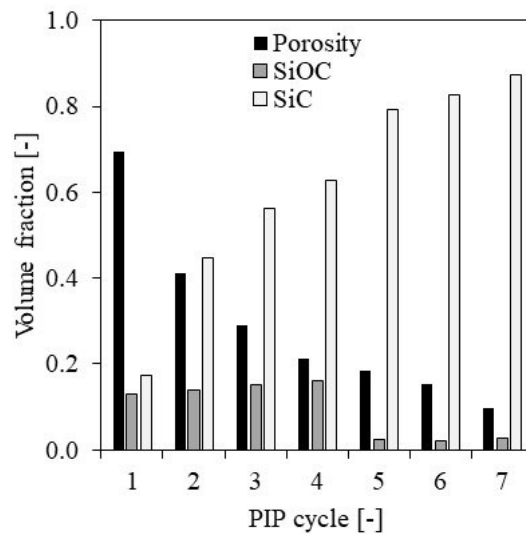
Figure 32. SEM image analysis of the SiOC/SiC samples: volume fraction of the porosity (resin, black areas), SiOC (dark grey areas) and SiC (light grey areas) as a function of the PIP cycle.

Mercury intrusion porosimetry (MIP) tests (PoreMaster 60, Anton Paar Switzerland AG, Buchs, Switzerland) were performed to evaluate the bulk porosity, the open pore size distribution, and the pore volume after each PIP cycle. Analyses were performed by using a pressure range from 0.0014 MPa to 414 MPa. Figure 33 reports the porosimetry results of the SiOC/SiC samples taken from the fractured ceramic discs. The pore size distribution is plotted against the cumulative pore volume (Figure 33-A) for seven specimens.

The final cumulative volume decreased with increasing of the PIP cycles and accordingly the relative density increased, but the behavior of the samples was clearly different. The microporosity of sample 1PIP was bimodal: larger pores from 0.1 to 60 μm (derived from the PA12 degradation) exist together with smaller pores from 0.004 to 0.05 μm (derived from the precursor yield conversion). The two distributions were also distinguishable by observing the changes in the curve slope. Sample 1PIP was the only one that had small pores in large quantity, while the other samples contained only larger pores (Figure 33-B). This means that the second PIP cycle enabled filling the smaller pores and reducing the amount of the larger ones. As observed in samples 5PIP, 6PIP and 7PIP, the microstructure was characterized by several pores in the 50-100 μm size range. This is because of capillarity and surface tension, or by the physical impossibility of the polymer to reach those pores.
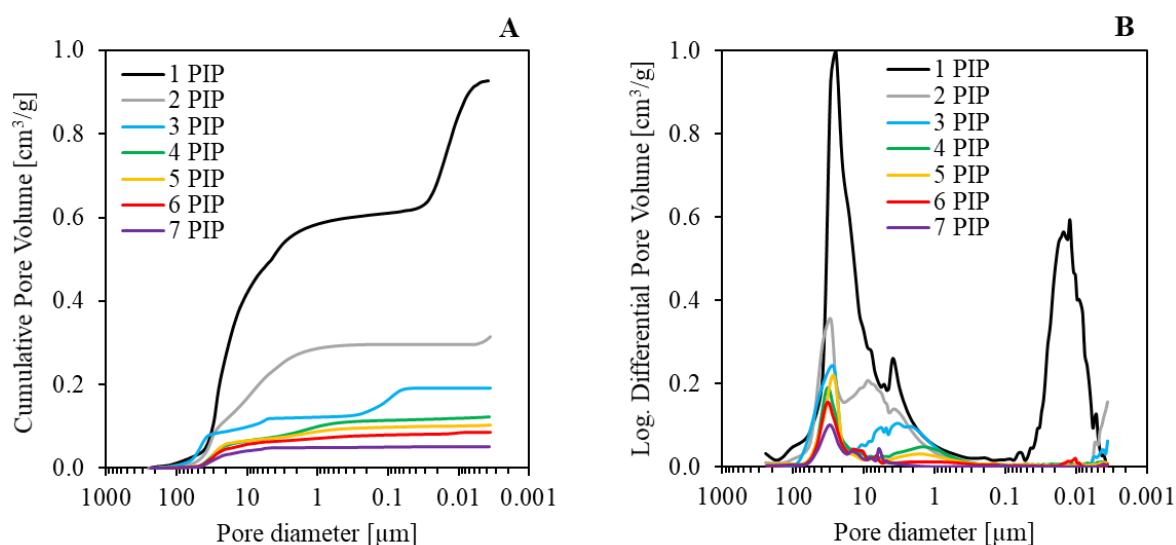
Figure 33. Mercury intrusion porosimetry results of the SiOC/SiC samples after each PIP cycle: (A) cumulative pore volume and (B) log. differential pore volume as a function of the pore diameter.

The specific surface area (*SSA*) of the samples as a function of the number of infiltrations was quantified by MIP. It was observed that after the first conversion, the sample had an SSA that exceeded many of the literature catalytic supports[172,173]. This was due to the high presence of small pores from 0.004 to 0.05 μm. In a future work could be interesting to produce advanced catalytic supports by combining this fabrication method with surface coating, to increase reactivity during catalysis. In addition, the production of templates with high-geometric surface area (such as cellular architectures) could be a further advantage.

PIP	-	1	2	3	4	5	6	7
SSA	m²/g	103.6	18.9	6.7	3.7	2.3	2.0	0.5

Table 9. Specific surface area (SSA) of the samples as a function of the number of infiltrations by MIP.

2.3.4 Mechanical properties

The mechanical strength of the ceramic samples was evaluated through biaxial flexural tests (Zwick Z050, Zwick GmbH & Co.KG, Ulm, Germany) employing the ball-on-three-balls (B3B) setup with stainless steels balls of 13 mm diameter[174,175]. Tests were performed at strain rate of 10^{-3} s^{-1} and a cell load of 5 kN (KAP-S, AST, Dresden, Germany) was used to record the reaction force. The disc (diameter of 23 ± 0.25 mm and height of 5 ± 0.10 mm) was placed at the center of the three balls and pre-loaded with a force of 2.5 N. A Poisson's ratio of 0.2 was assumed. Five samples were tested for each PIP cycle. In the B3B test, the maximum flexural stress (σ) appears in the center of the specimen on the opposite side of the loading ball (see Figure 34-A). The strength is given by the following equation[174]:

$$\sigma_f^* = f \cdot \frac{F}{h^2} \qquad \text{Eq. 9}$$

where σ_f^* is the apparent flexural strength (of fracture) of the material, F is the maximum fracture load, h the thickness of the specimen and f is a dimensionless factor which depends on the thickness of the specimen (h), the radius of the specimen (R), the Poisson's ratio of the tested material (v_p) and the support radius (Ra) calculated with the radius of the support balls (Rb) as follow:

$$R_a = \frac{2\sqrt{3}}{3} \cdot R_b = \frac{2\sqrt{3}}{3} \cdot \frac{13\ mm}{2} = 7.51\ mm \qquad \text{Eq. 10}$$

The factor f was obtained using Eq. 11 and Figure 34-B:

$$f\left(\frac{h}{R}, \frac{R_a}{R}, v_p\right) = \left(\frac{5}{23.25/2}, \frac{7.51}{23.25/2}, 0.25\right) = (0.43, 0.65, 0.25) = 1.3 \qquad \text{Eq. 11}$$
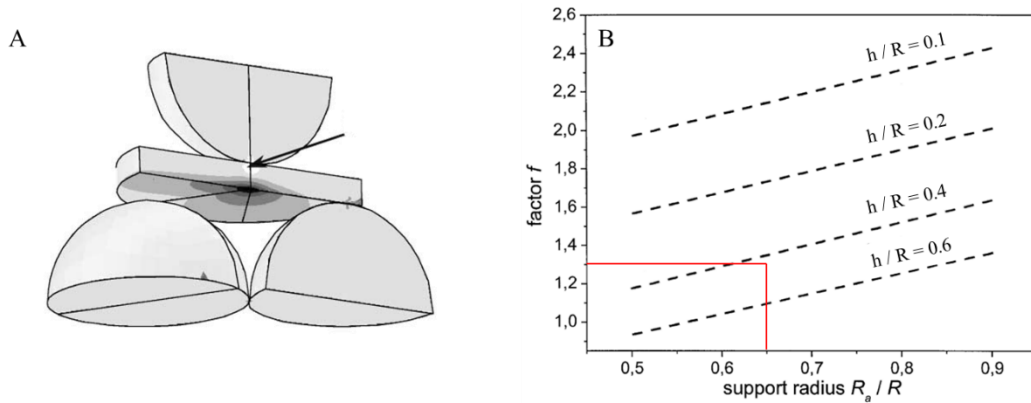
Figure 34. B3B flexural test[174]: (A) schematic of the assembly in section view (the arrow indicates the contact area between support balls and the disc); (B) Factor f versus the ratio of Ra/R for Poisson of 0.25. The curves refer to different ratios of thickness to disc radius h/R. The red lines indicate this case study.

Stress-strain curves of the SiOC/SiC samples after each PIP cycle are shown in Figure 35-A. In general, the stress increased with increasing strain until the maximum strength was reached, after which the specimens collapsed with brittle fracture. As a result of the fracture, the samples were split into three almost-equal parts. It can be observed that increasing the number of PIP cycles increased the fracture stress and decreases the strain of the samples. Samples pyrolyzed up to three times showed about the half of the maximum stress of the other samples. In Figure 35-B and -C, the strength and elastic modulus of the samples as a function of their relative density are shown respectively. The relative density and the average strength increased with increasing the PIP cycles. After the first pyrolysis the strength was very low (9.14 ± 0.62 MPa), increasing to a more than three times higher value (31.09 ± 2.63 MPa) after seven PIP cycles. After the fourth cycle, the increase rate of the relative density was lower meaning that the infiltration was reduced by the drag force of the remaining small pores. Closed pores cannot be filled (see Figure 31-7PIP) and after the last cycle, the relative density was still 0.90 showing the limits of PIP processing[16,166,167,176].
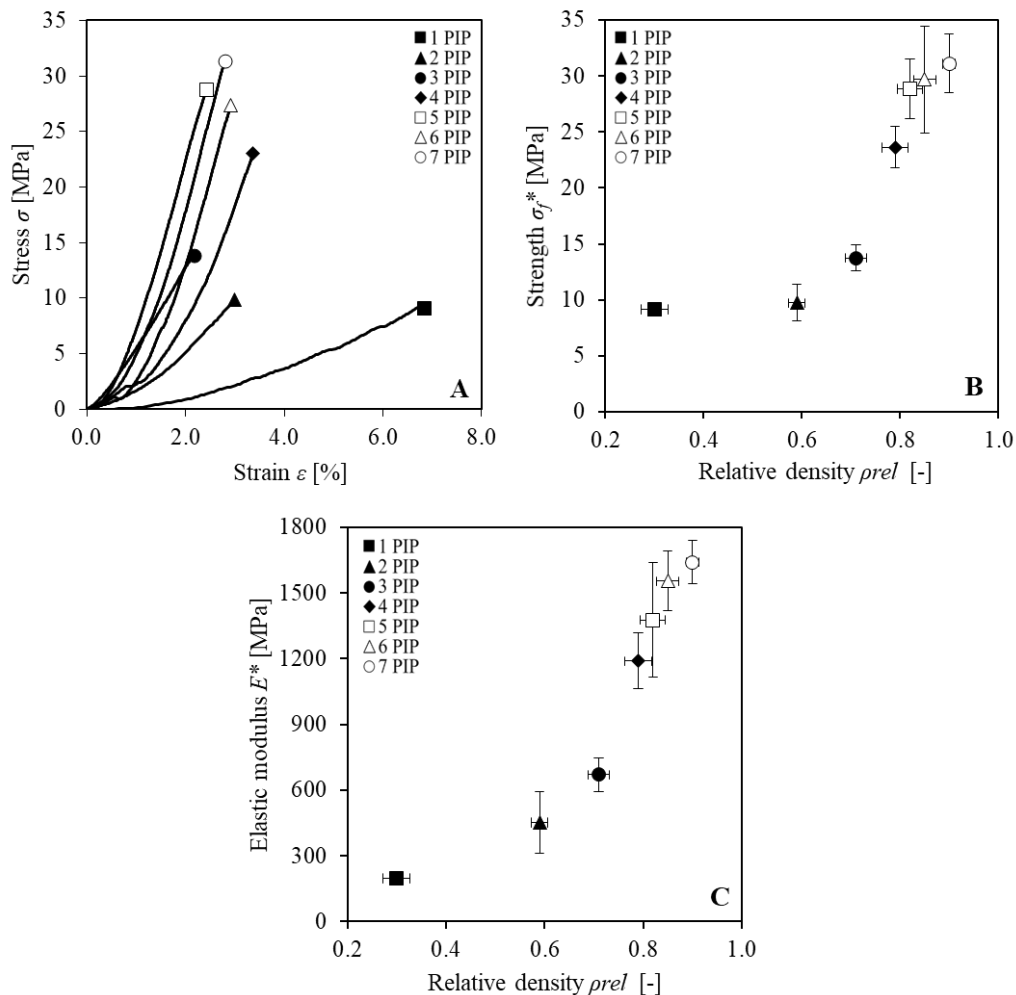
Figure 35. Mechanical test results for the SiOC/SiC samples after each PIP cycle: (A) flexural stress-strain curves; (B) average flexural strength as a function of the relative density; (C) average elastic modulus as a function of the relative density. Table 10 reports the data recorded.

The values of the elastic modulus (Figure 35-C) had a similar trend as that of the strength plot. The large error bars can be attributed to the uneven bottom and top surfaces of the sample. Also, the distribution of micro voids and microcracks due to shrinkage after heat treatment and the layer-by-layer building approach had an influence. The relative flexural strength ($\sigma_{f,rel}$) can be calculated with the ratio between the apparent flexural strength and the flexural strength of the dense material:

$$\sigma_{f,rel} = \frac{\sigma_f^*}{\sigma_f} \qquad\qquad Eq.\ 12$$

According to the literature and to the Ashby's materials database (ANSYS Granta EduPack 2022 R2, ANSYS, Pittsburgh, PA, USA), the flexural strength (σ_f) of the amorphous SiC was taken to be 200 MPa and the true density between of 2.403 g/cm³ (measured in this work).

Table 10 summarizes the data of all the experimental B3B tests and strength calculation.

PIP	-	1	2	3	4	5	6	7
$p_{rel.MIP}$	-	0.30 ±0.02	0.59 ±0.02	0.71 ±0.02	0.79 ±0.03	0.82 ±0.03	0.85 ±0.02	0.90 ±0.01
p^*	g/cm³	0.72	1.42	1.71	1.90	1.97	2.04	2.16
E^*	MPa	198 ±12	452 ±141	670 ±78	1189 ±128	1376 ±262	1554 ±136	1640 ±97
σ_f^*	MPa	9.14 ±0.62	9.73 ±1.65	13.75 ±1.14	23.61 ±1.85	28.83 ±2.66	29.67 ±4.75	31.09 ±2.63
$\sigma_{f,rel}$	-	0.046 ±0.003	0.049 ±0.008	0.069 ±0.006	0.118 ±0.009	0.144 ±0.013	0.148 ±0.024	0.155 ±0.013

Table 10. Comprehensive data of all the experimental B3B mechanical test results and strength calculations.

A numerical analysis on the mechanical properties of the SiOC/SiC discs was performed by using the fundamental predictive model of porous mechanical response of Gibson-Ashby[140,177,178]. It provides useful insight into the anticipated mechanical response of a proposed additively manufactured component. The mechanical properties of porous structures were successfully modelled in many cases by simple relationships derived by considering a regular cubic structure, which deforms by beam bending (the case of foams) or by beam stretching (the case of lattices). Basically, the difference is that a foam is less stiff than a lattice of the same relative density due to their different cell's configurations. The flexural strength of open-cell structures can be predicted by the Gibson-Ashby model using two different equations: Eq. 13 for the bending-dominated structures and Eq. 14 for the stretch-dominated structures.

$$\frac{\sigma_{f,B}^*}{\sigma_f} = C \cdot \rho_{rel}^{\frac{3}{2}} \qquad\qquad Eq.\ 13$$

$$\frac{\sigma_{f,S}^*}{\sigma_f} = C \cdot \rho_{rel} \qquad\qquad Eq.\ 14$$

where σ_f^* is the calculated flexural strength, the subscript B indicates the bending and the subscript S indicates the stretching, σ_f is the flexural strength of the material, p_{rel} is the relative density and C is a constant of proportionality established both by experiment and by numerical computation, which ranges from 0.1 to 1.

Figure 36 shows the flexural strength and the relative flexural strength as a function of the relative density for the tested samples after each PIP cycle, compared with the Ashby-Gibson predictive numerical models. The predicted red and blue areas were obtained by changing the factor C in Eq. 13 and Eq. 14, respectively. Eq. 12 was used to build the chart of the relative strength in Figure 36-B.
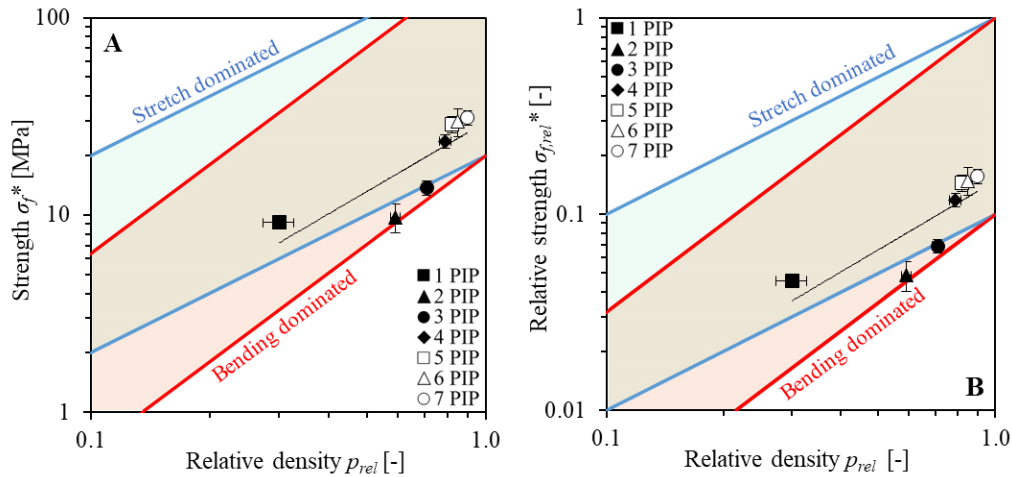
Figure 36. (A) flexural strength and (B) rel. flexural strength as a function of the relative density for the tested samples after each PIP cycle, compared with the Ashby-Gibson predictive numerical models. Red and blue areas represent the bending-dominated behavior (foams) and the stretch-dominated behavior (lattices) respectively. The predicted ranges were obtained by changing the factor C from 0.1 to 1 in Eq. 13 and in Eq. 14.

As expected, the ranges for both strength and relative strength produced higher values for stretch-dominated structures and lower values for bending-dominated structures (blue and red areas respectively). The materials tested in this study are located within both areas except for the samples 2PIP and 3PIP which fall only in the bending area and outside the stretch area. As expected, the black trend line of the measures is similar to the bending-dominated structures. These materials were produced using SLM technology without a control on the geometrical configuration of the microstructure, i.e., the configuration of the pores is random. Stretch-dominated structures such as lattices are composed by an ordered arrangement of a specific designed unit cells, which is not this case.

Figure 37 shows an Ashby chart of the flexural strength vs. density. It compares the mechanical properties of the materials in this study, along with the dense ceramic and with other ceramics. The chart shows the produced amorphous SiC discs after each PIP cycle (red points with relative density in brackets) and the dense amorphous SiC (brown point). The flexural strength of the dense amorphous SiC was taken to be 200 MPa and the density of 2.403 g/cm^3 (measured in this work). Materials properties for dense crystalline SiC (yellow points), i.e., thermally treated at temperature higher than 1500°C., were obtained from the software Granta EduPack 2022 R2 (ANSYS, Pittsburgh, PA, USA). Other groups of materials were taken from literature as reported in Table 8. They were produced using different manufacturing techniques, especially uniaxial isostatic pressure, and then pyrolyzed up to 1000°C or sintered above 1000°C with different dwell time. The proposed comparison in Table 8 was made considering the testing method and the dimensions of the tested samples. Results showed that the produced materials can be compared to the literature values both for density and strength. As expected, in general the strength increases with the increasing of the density for all the materials taken into consideration. This increasing was observed also through the very different slopes of the materials families. Material #7 showed the highest strength increasing with very low increasing of the density, demonstrating the high influence of the ceramic powder size in the pressing method. On the contrary, the materials of this work had relatively high strength increasing but related to a very high increasing of the density. The values obtained after 7 PIP cycles are in the range of the other SiC ceramics found in literature and thermally treated at a temperature around 1000°C. Material #7 produced a strength (67 MPa) two times higher with respect to sample 7PIP (31.09 MPa) due to the raw materials used, the fabrication method and sintering temperature of 1500°C. Sample 1 PIP had a much higher flexural strength (9.14 MPa) than those achieved by other materials with higher density (see all the strength data below 10 MPa). By considering the effective volume and the defects population, the bending strength results coming from different testing methods can be compared. In general, *B3B* tests show the smallest effective volumes and therefore highest strength values compared to 3- and 4-point bending[175,179]. This means that the material developed in this study should possess a lower strength than the SiC ceramics reported in literature, when tested with 3- or 4-point bending. The difference is certainly attributable to the proposed fabrication method which clearly is disadvantaged compared to pressing and sintering. The reported literature materials were all fabricated through uniaxial isostatic pressure of α- or β-SiC powders (with the addition of bonding agents or fillers) as starting materials and then sintered at temperature higher than 1000°C (except in case #2 and #5). However, their strength and density can be compared with the materials produced in this work in which no ceramic powders were used.
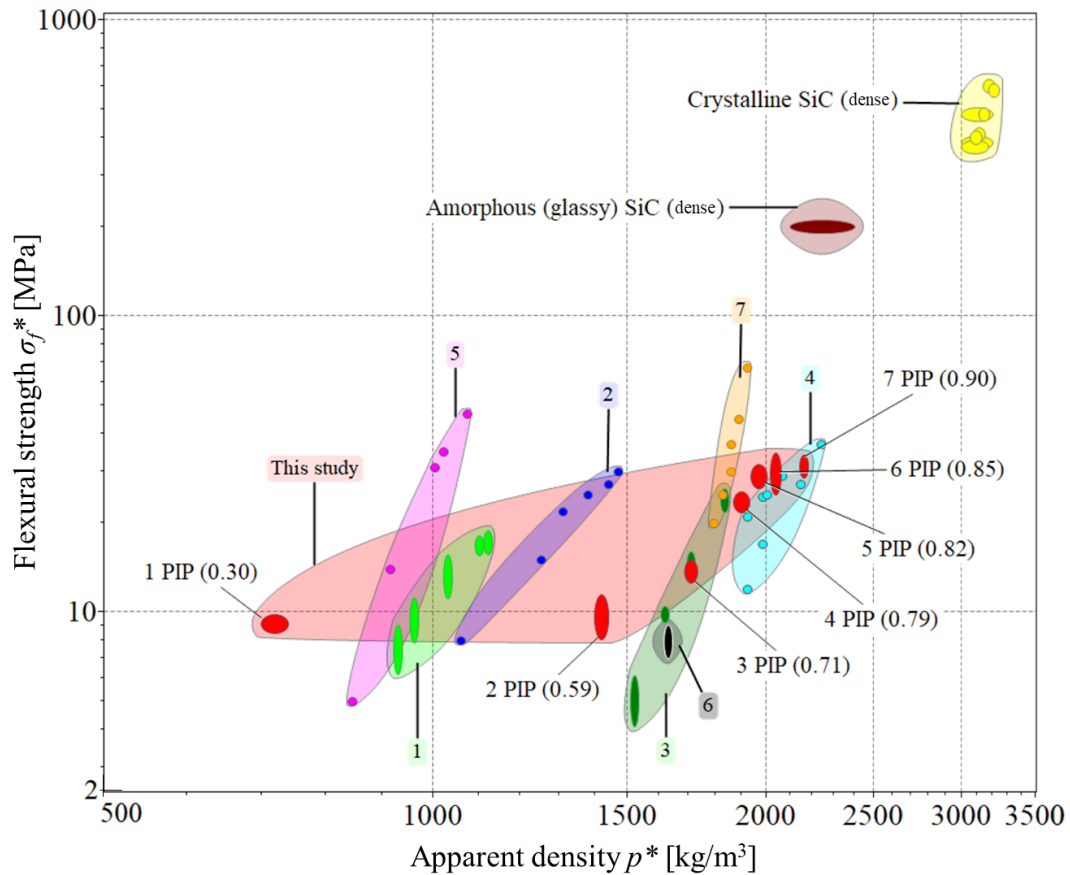
Figure 37. Ashby chart of the flexural strength against the density for SiC ceramics. The chart compares the fabricated structure against other materials. Materials properties for crystalline SiC (yellow points) were obtained from the software Granta EduPack 2022 R2 (ANSYS, Pittsburgh, PA, USA). The red area represents the experimental results of the SiOC/SiC discs after each PIP cycle with the relative density in brackets. The flexural strength of the dense amorphous SiC was taken to be 200 MPa and the measured density was 2.403 g/cm³ (brown point). Other groups of materials were taken from literature. Table 11 reports the data.

Table 11 shows the comparison between SiC ceramics fabricated by different methods as reported in Figure 37.

Fabrication method	Pyr/sint temp.	Note	φ	p^*	σ_f^*	Test type	Sample size	Ref	#
-	°C	-	%	kg/m³	MPa	-	mm³	-	-
		1 PIP	70	720	9.14				
		2 PIP	41	1420	9.73				
		3 PIP	29	1710	13.75				
SLM + PIP	960°C (1h@T_{max})	4 PIP	21	1900	23.61	B3B	d23 h5	This study	
		5 PIP	18	1970	28.83				
		6 PIP	15	2040	29.67				
		7 PIP	10	2160	31.09				

Method	Temperature	Condition	Porosity	Density	Strength	Test	Dimensions	Ref	#
Pressing then sintering	1300	1h@T$_{max}$	62	1030	13				
	1300	3h@T$_{max}$	61	1100	17				
	1300	5h@T$_{max}$	60	1120	17	3p	6x8x36	[180]	1
	1200	3h@T$_{max}$	66	960	10				
	1100	3h@T$_{max}$	68	930	8				
Pressing then pyrolysis	900	1h@T$_{max}$	37	1062	8	4p	6x8x60	[181]	2
			27	1250	15				
			25	1312	22				
			20	1375	25				
			18	1437	27				
			17	1468	30				
Pressing then sintering	1400	4h@T$_{max}$	53	1519	5	3p	3x4x36	[182]	3
	1450		59	1623	10				
	1500		47	1710	15				
	1550		43	1833	24				
Pressing then sintering	1300 (3h)	10 wt.% bond phase. 3h@T$_{max}$	40	1920	12	3p	5x6x36	[183]	4
			38	1984	17				
			33	2144	27				
			30	2240	37				
		15 wt.% bond phase. 3h@T$_{max}$	40	1920	21				
			38	1984	24				
			38	2000	25				
			36	2064	29				
Cold pressure then pyrolysis	800	Bond content: 1h@T$_{max}$	52	845	5	4p	4x5x35	[184]	5
			48	915	14				
			43	1003	31				
			42	1021	35				
			39	1074	47				
Pres.+sint.	1400	2h@T$_{max}$	49	1630	8	4p	2x2x25	[185]	6
Pressing then sintering	1500	Avg. particle size: 7, 17, 18, 28, 43, 45. 1h@T$_{max}$	40	1920	67	4p	3x4x35	[186]	7
			41	1888	45				
			42	1856	37				
			42	1856	30				
			43	1824	25				
			44	1792	20				

Table 11. Comparison of the porosity, density, and flexural strength of SiC ceramics fabricated with different methods. 3p and 4p indicate the 3-point and 4-point bending tests respectively. Column # indicates the group number in Figure 37.

2.3.5 Oxidation tests

TGA analyses (TGA/DSC 3+, Mettler-Toledo GmbH, Greifensee, Switzerland) were carried out in Air at atmospheric pressure to determine the oxidation behavior of the produced ceramic materials. Samples taken from the fractured discs after each PIP cycle were tested with a heating rate of 10°C/min up to 1200°C. Figure 38 shows the oxidation behavior of the ceramic specimens. Two trends were observed: active oxidation of carbon and passive oxidation of silicon carbide. The conditions adopted in this work should cause oxidation according to the reactions[7,187–190]:

$$C_{(s)} + O_{2(g)} \rightarrow CO_{2(g)} \qquad\qquad Eq.\ 15$$

$$2SiC_{(s)} + 3O_{2(g)} \rightarrow 2SiO_{2(s)} + 2CO_{(g)} \qquad\qquad Eq.\ 16$$
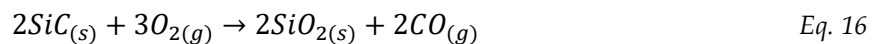
Oxidation first occurred on the material's surface exposed to air. C oxidations was higher in sample 1PIP and 2PIP, which had free carbon at the surface due to PA12 residue and more SiOC. This was confirmed by their mass loss. From 3PIP the loss of carbon by active oxidation was hindered by SiC passive oxidation and SiO$_2$ layer formation on the surface. Oxygen progressed much slower by diffusion into the formed SiO$_2$ and in the SiC denser core. Another factor was the relationship between the relative density and the geometric surface area of the interconnected pores (open porosity). After the first pyrolysis, the material was highly porous (70%) and by carrying out several PIP cycles, the porosity decreased due to the filling

Figure 38. Oxidation tests of the produced SiOC/SiC samples: microporosity vs. weight change at 1200°C. The geometric surface area of the sample is indicated near the points.

of the open pores, and moreover some interconnections among pores were eliminated. Consequently, the geometric surface area was reduced allowing less material to be exposed to the oxidation. The weight loss of sample 1PIP corresponded to the amount of the carbon that was oxidized. As the relative density of the material increased, the amount of exposed surface area decreased and the carbon remained trapped inside a SiC matric, while the SiC oxidized and added mass to the material due to its passive oxidation. This can be observed also in the SEM results (Figure 31): by increasing the number of PIP cycles, the products of the first pyrolysis were totally covered by the new SiC phase, resulting in the trapping of carbon inside the matrix. Therefore, SiOC and C that were first on the surface oxidized and this prevails over the oxidation of SiC (black data points), while after they were embedded by the new SiC phase with increasing number of infiltrations and were no longer at the surface, the passive oxidation of SiC prevailed (red data points) leading to a mass gain.

2.4 Liquid Silicon Infiltration

The final densification of the material was achieved via liquid silicon infiltration (LSI) of the solid amorphous SiOC/SiC network with the aim to produce Si-infiltrated SiC. During LSI at high temperature, the ceramic phase crystallizes and shrinks allowing for a full infiltration by the molten Si. The notable result was the possibility to obtain almost fully dense ceramic parts. The LSI process was performed on the 6PIP samples instead of the 7PIP to have a comparison between the two methods. Before LSI, the discs had a diameter of 23 ± 0.25 mm and a height of 5 ± 0.10 mm.

2.4.1 Final densification

Silicon grains (HQ1, Sicerma, Erkelenz, Germany) with a grit size of 0.2–2.0 mm were used to perform LSI of the ceramic discs. Tests were carried out in vacuum atmosphere (10^{-2} mbar) at 1600°C[†] for 1h using a graphite resistor furnace (XGRAPHITE 2200, XERION GmbH, Berlin, DE), with a heating rate of 20°C/min. At this temperature the crystallization of the SiC phase into βSiC (αSiC is formed at temperature exceeding 1700°C) and the degradation of the SiOC phase were expected.

Figure 39 shows the section-view schematic of the crucible used for the infiltrations. The sample (F) was placed on top of a cylinder-shaped graphite foil (D) which contained the silicon grains (E). A graphite foil base (B) coated with boron nitride (C) was used to support the cylinder. This configuration was placed into a graphite crucible (A). At >1414°C the silicon melts and infiltrates the graphite foil cylinder which then allows the spontaneously infiltration of the samples. Diffusion of the molten silicon and capillarity forces of the open pore channels system drive the process. The boron nitride coating was used for its low wettability with Si which allowed to avoid Si spreading into the crucible. The amount of Si was calculated considering five times the weight of the graphite cylinder and one time the sample weight. Eight samples can be infiltrated in the same crucible.
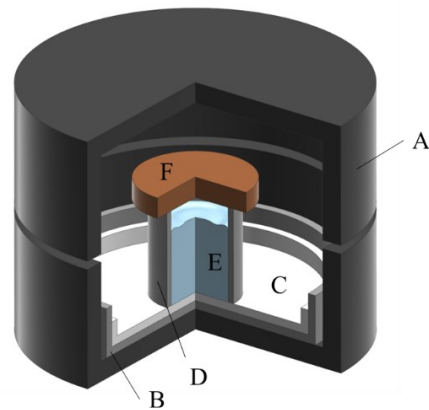
Figure 39. Section-view schematic of the crucible used for LSI: (A) graphite crucible; (B) graphite foil base; (C) boron nitride coating; (D) cylinder-shaped graphite foil; (E) silicon grains; (F) sample.

[†] Typical temperature for LSI[102,103], i.e., temperature exceeding the silicon melting point of 1414°C.

Three different tests were performed to better understand the process and to investigate and characterize the different produced microstructures.

Sample 6PIP+LSI: the ceramic after six PIP cycle was infiltrated with molten silicon. The aim was to perform thermal treatment at 1600°C and Si infiltration in one time. Before this treatment the polymer-derived SiOC/SiC had only been pyrolyzed up to 1000°C. Therefore, the in-situ formation of βSiC, the shrinkage of the part and weight loss due to the SiOC decomposition were expected. The Si infiltration could benefit as SiC should shrinks during the process generating pores accessible for the silicon infiltration. Large gain in weight and relative density were expected.

Sample 6PIP+TT: the ceramic after six PIP cycle was thermally treated (TT) under the previous mentioned LSI conditions but without Si infiltration. The aim was to study the effect of the higher temperature treatment on the SiOC/SiC. The in-situ formation of βSiC and SiOC decomposition were expected with a possible shrink of the part. Also, formation of pores and huge embrittlement were expected. Non-maintenance of the shape also possible.

Sample 6PIP+TT+LSI: the ceramic after six PIP cycle was thermally treated under the previous mentioned LSI conditions but without Si infiltration and then, with another thermal cycle, it was infiltrated with molten silicon. Basically, this was the Si infiltration of the sample 6PIP+TT. It is obvious that the result of this test depends on the outcome of the first thermal treatment. If after the first thermal treatment the part remains in shape and produce higher microporosity, then the infiltration might benefit, in terms of gain in weight and relative density. However, the silicon residue would be evident.

The three tests were performed as above mentioned and Table 12 reports the obtained results. The table provides a comparison of the produced materials with the starting one (sample 6PIP). The density of the produced materials was measured by means of a gas pycnometer, using Helium (Ultrapyc3000, Anton Paar QuantaTec Inc., Florida, USA). Bulk sample pieces and samples powder were used for obtaining the apparent and true density values, respectively. Eight tests were performed for each material. The determination of the volumetric fractions of SiC and Si was performed using the following equation:

$$\rho_{SiSiC} = V_{SiC} \cdot \rho_{SiC} + V_{Si} \cdot \rho_{Si} \qquad \text{Eq. 17}$$

where ρ_{SiSiC} is the true density of the SiSiC measured with gas picnometry, V_{SiC} and V_{Si} are the volumetric fractions of SiC and Si respectively, ρ_{SiC} and ρ_{Si} are the theoretical densities of βSiC (3.210 g/cm^3) and Si (2.329 g/cm^3) respectively.

Sample	-	6PIP	6PIP+LSI	6PIP+TT	6PIP+TT+LSI
Weight	g	3.32 ± 0.10	2.33 ± 0.19	2.07 ± 0.09	4.24 ± 0.12
Gain in weight	%	-	-30	-38	105 (*)
Linear shrink	%	-	6.9	7.4	- (*)
Ceramic type	-	SiOC/SiC	Test failed: material not infiltrated with silicon. Material properties not measured.	βSiC	Si-βSiC
Apparent density	g/cm³	2.043 ± 0.001		1.527 ± 0.036	2.672 ± 0.015
True density	g/cm³	2.403 ± 0.014		3.206 ± 0.099	2.718 ± 0.015
Relative density	-	0.847 ± 0.005		0.476 ± 0.040	0.983 ± 0.011
Residual porosity	%	15.3		52.4	1.7
SiOC/SiC (amorph.)	vol%	100		-	-
βSiC content	vol%	-		100	45
Si content	vol%	-		-	55

*Table 12. Liquid silicon infiltration results of the ceramic sample after 6 PIP cycles with AHPCS precursor (6PIP), the 6PIP sample after LSI at 1600°C (6PIP+LSI), the 6PIP sample heated at 1600°C without Si infiltration (6PIP+TT) and the 6PIP sample after thermal treatment at 1600°C followed by LSI at 1600°C (6PIP+TT+LSI). Gain in weight and linear shrinkage are referred to the 6PIP sample. * value referred to the 6PIP+TT sample.*

Sample 6PIP+LSI showed that the samples 6PIP cannot be directly infiltrated with silicon at 1600°C. The sample gave a weight loss of 30% and a linear shrinkage of 6.9%. The silicon did not infiltrate the parts and only dirtied the lower face of the material. Also, the sample 6PIP+TT gave a similar weight loss of 38% and a similar shrinkage of 7.4%. The explanation for the high weight loss must be sought by investigating the SiC and SiOC phases of the 6PIP material.

The SiC phase present in the network was derived by its precursor, therefore an increase of the pyrolysis temperatures from 1000°C to 1600°C led to its crystallization and to a slight weight loss (< 5% due to its ceramic yield) according to literature[118]. In addition, SiC ceramics can withstand much higher temperature (> 2000°C) with very good stability. Therefore, the huge weight loss of 30% cannot be addressed to the SiC phase.

The SiOC phase present in the network was derived by the conversion of the AHPCS in contact with the PA12 due to its content of oxygen and to the humidity (see Table 8 and Figure 32). Silicon oxycarbide was shown in various studies to undergo phase separation at temperature beyond 1200°C and its glassy matrix is continuously evolving in the temperature range between 1200-1600°C[191–193]. At 1600°C, the silica has already reacted with carbon to form SiO and CO (Eq. 18), then depending on the relative ration between SiO and C, crystalline SiC can be formed (Eq. 19)[195]. In general, over 1500°C, SiOC ceramics display weight loss due to carbothermal reduction, where silica reacts with carbon in a two-step reaction under evaporation of CO.

After complete consumption of the segregated carbon phase, SiO_2 can directly react with SiC resulting in a complete decomposition of the material (Eq. 20)[196,197].

$$SiO_{2(s)} + C_{(s)} \rightarrow SiO_{(g)} + CO_{(g)} \qquad \text{Eq. 18}$$

$$SiO_{(g)} + 2C_{(s)} \rightarrow SiC_{(s)} + CO_{(g)} \qquad \text{Eq. 19}$$

$$2SiO_{2(s)} + SiC_{(s)} \rightarrow 3SiO_{(g)} + CO_{(g)} \qquad \text{Eq. 20}$$
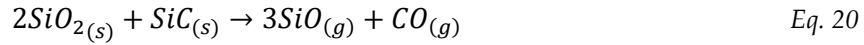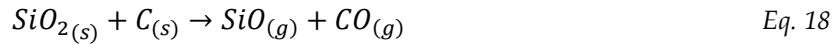
Therefore, the weight loss can be addressed to the SiOC phase. To better investigate this behavior, a TGA analysis was performed on the SiOC/SiC network with respect to the SiC precursor between 1000°C and 1600°C. The tests were carried out in inert atmosphere using an Argon flow rate of 20 mL/min and heating rate of 20°C/min. The temperature of 1600°C was hold for 20 minutes (limit of the TGA equipment) to partially reproduce the thermal treatment of the LSI process. Figure 40-A shows the weight change with respect to the temperature and Figure 40-B shows the weight change within 20 minutes at 1600°C. TGA showed that between 1000°C and 1600°C, the SiC precursor (AHPCS) alone had a weight loss of about 2%. After 20 minutes at 1600°C, the weight loss was of 3%. As expected, and in accordance with literature, the weight loss of AHPCS alone was very low. The SiOC/SiC ceramic (6PIP) had a weight loss of about 7.5% at 1600°C. Holding at this temperature for 20 minutes, a 16% increase in the weight loss was observed. This result confirmed that the mass loss was due to SiOC and in agreement with the literature started above 1200°C. As a comparison, in sample 6PIP+TT case (see Table 12) the sample was hold at 1600°C for 1h and the final weight loss was of 38% (15% higher than TGA). The results agreed well, and the slope of the blue curve could be expected to decrease over time.
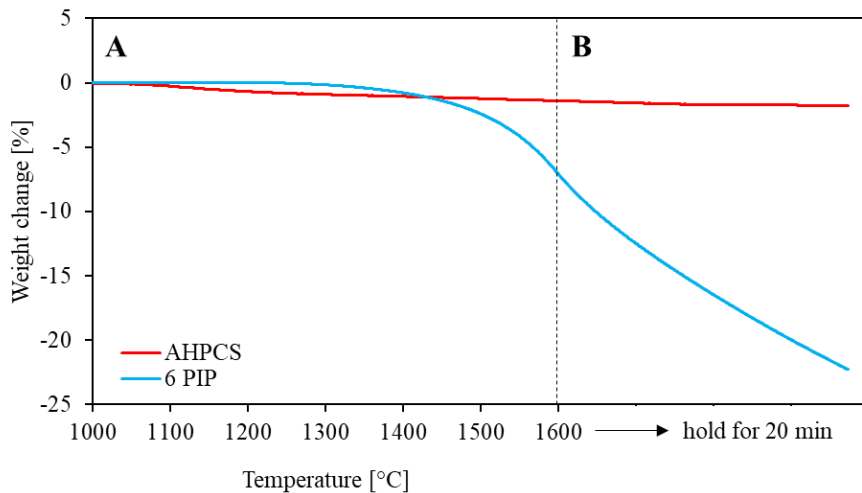
Figure 40. TGA analysis of the AHPCS alone (red curve) and the 6PIP sample (blue curve): (A) from 1000°C to 1600°C; (B) holding the temperature of 1600°C for 20 minutes.

This result led to the conclusion that, in the 6PIP+LSI case (in Table 12), the silicon did not infiltrate the material due to the simultaneously SiOC transformation and to its products (SiO, CO and SiC crystals). The large amount of vapors produced by the phase decomposition of the SiOC acted as an obstacle to the penetration of the silicon inside the pores of the material. Furthermore, the silicon could have had a low wettability over the new phases. In a future work these aspects must be investigated because no useful material was found in the literature.

Sample 6PIP+TT (in Table 12) was the demonstration of what has just been explained and its testing was useful to avoid any possible influence of the silicon in the 6PIP+LSI case. As expected, sample 6PIP+TT gave a weight loss of 38% due to the SiOC phase decomposition. It was about 8% higher than that of 6PIP+LSI samples due to the absence of silicon dirt on the bottom surface. Despite the high mass loss and the shrinking of about 7.4%, the part maintained its pristine shape, with no shape distortion or macrocracks. However, the part was very fragile, just by handling it. The non-infiltrated sample, after heating at 1600°C, had an apparent density of 1.527 ± 0.036 g/cm^3 and a true density of 3.206 ± 0.099 g/cm^3, in very good agreement with the theoretical density of SiC (3.210 g/cm^3) and indicating the very limited presence of residual carbon in the material. The relative density was 0.476 ± 0.040 g/cm^3 and the residual porosity was, therefore, ~52.4vol%. X-ray diffractometer (XRD) analysis (see Figure 42) of the sample demonstrated that amorphous SiC crystallized into βSiC at 1600°C, but a residual amorphous phase was also detected and confirmed by SEM (see Figure 43). Probably, the non-complete crystallization of the material allowed to guarantee a minimum mechanical stability of the piece.

Sample 6PIP+TT+LSI (in Table 12) produced a ceramic part without change of size and shape distortion with respect to sample 6PIP+TT, with a weight gain of about 105%. The final SiSiC discs had an apparent density of 2.672 ± 0.015 g/cm^3, a true density of 2.718 ± 0.015 g/cm^3, and a relative density of 0.983 ± 0.011. The residual porosity was, therefore, only ~1.7 vol%. A complete infiltration of the part was performed by the molten silicon, resulting in an almost fully dense part. XRD and SEM (see Figure 42 and Figure 43 respectively) were carried out to assess the phase assemblage and the microstructure of the produced SiSiC ceramic. It was shown that in this case the SiC completed its crystallization and no amorphous phase was detected. This means that the full transformation of the SiC took place in contact with the molten silicon. As expected, a large amount of residual silicon of about 55% was present in the material.

Figure 41 shows a schematic of the microstructure evolution during the thermal treatment at high temperature and the subsequent liquid silicon infiltration (TT+LSI) process. The figure shows a pore into the ceramic matrix. The porous and amorphous SiOC/SiC is produced by pyrolysis at 1000°C (A), and it is then thermally treated at 1600°C (B). During this step, SiOC decomposition occurred with its mass loss, and SiC starts crystallizing into βSiC and shrinks. This combined effect produces an increase in porosity of over 50%, opening the way to the infiltration by molten silicon. At the end of the thermal treatment, the SiC does not complete its crystallization, and a residual amorphous phase is present. With the second cycle, the liquid silicon infiltration starts into large pores (C), and it proceeds inside increasingly smaller pores, while the SiC phase simultaneously continues to crystallize. Then, the silicon infiltrates almost all the porosity of the material and it allows the fully crystallization of the βSiC (D).
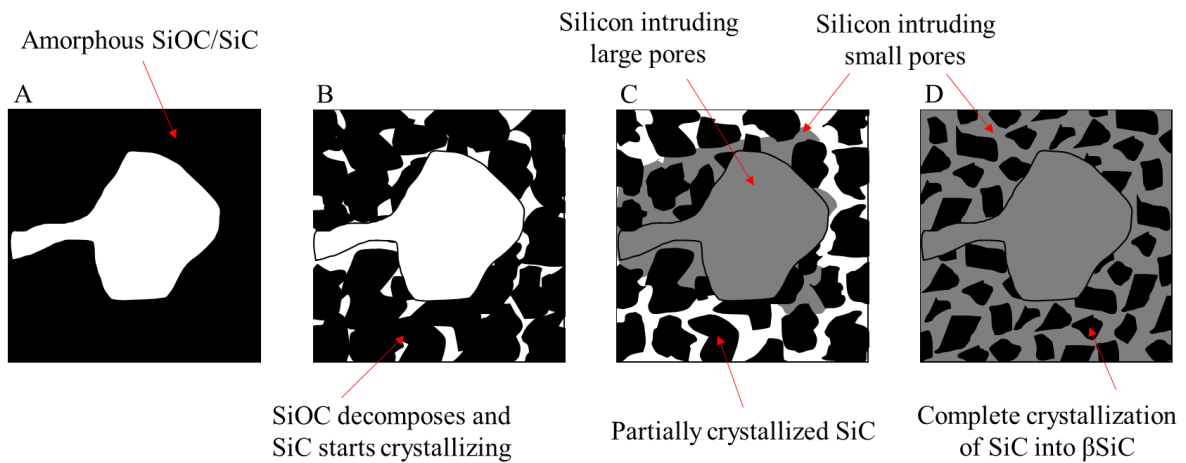
Figure 41. Schematic of the microstructure evolution during TT+LSI process. A pore into the ceramic matrix was represented: (A) porous and amorphous SiOC/SiC network produced by PIP at 1000°C; (B) SiOC decomposition and initiation of SiC crystallization generating a large porosity; (C) silicon infiltrates the large pore and SiC continues to crystallize into βSiC that allows for the infiltration of the smaller pores by molten silicon; (D) silicon infiltrates almost all pores and the SiC completes its crystallization.

The silicon does not react with any other elements. There is only a very negligible amount of free carbon inside the preform. This means that the process does not produce βSiC by reaction bonding, which consists in the formation of SiC by reaction between carbon or graphite powder with silicon. Rather the process produces βSiC by in-situ formation (or a sort of nucleation assisted crystallization) because the process does not involve the use of ceramic powders. The formation of the SiC crystals is directly derived from the transformation of the preceramic polymer into amorphous ceramic with PIP, and then into insoluble micro-crystals with LSI.

2.4.2 Phases assessment

The phase assemblage of the parts was investigated on sample powder, using an X-ray diffractometer (D8 Advance, Bruker Italia Srl, Milano, IT) with Cu(kα) radiation, from 10° to 80°, 0.05°/step, 2 s/step. The Match! *S*oftware package (Crystal Impact GbR, Bonn, Germany) was used for a semi-automatic phase identification, supported by data from the PDF-2 database (ICDD-International Centre for Diffraction Data, Newtown Square, PA, USA). Figure 42 shows the results obtained on the samples 6PIP (black curve), 6PIP+TT (blue curve) and 6PIP+TT+LSI (red curve).

The phase assemblage of the sample after pyrolysis (black line, 6 PIP) was comprised by totally amorphous SiC and a very limited amount of graphitic carbon. The SiOC was not visible by XRD due to the low amount compared to the SiC phase. The XRD analysis of the sample heat treated at 1600°C without Si infiltration (blue line, 6PIP+TT) demonstrated that amorphous SiC crystallized into βSiC at 1600°C. As expected, the result showed only the SiC phase, which appears to comprise by smaller crystallites (broader peaks) with respect to that formed during the Si infiltration and containing some stacking faults (shoulder at ~33.9°), as well as some residual amorphous phase. The silicon infiltrated sample (red line, 6 PIP+TT+LSI) also showed the presence of Si, besides well crystallized βSiC and some graphitic carbon. The amorphous SiC phase therefore appears to have been eliminated from the sample infiltrated with Si, demonstrating that Si have a crucial role on the fully crystallization of the SiC.
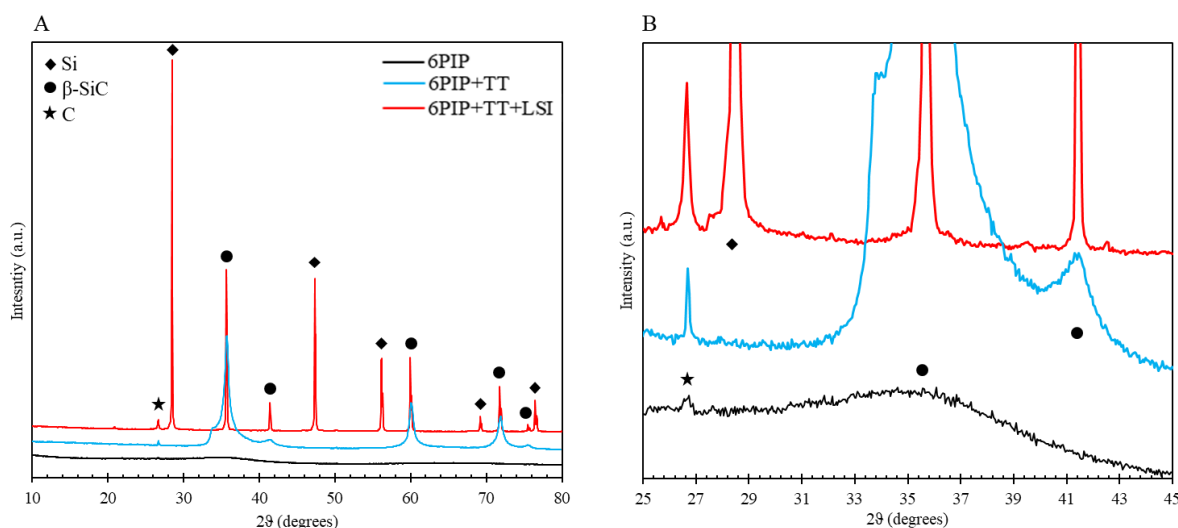
Figure 42. XRD patterns of the sample after pyrolysis (black line, 6 PIP), the non-Si infiltrated sample (blue line, 6 PIP+TT) and the silicon infiltrated sample (red line, 6 PIP+TT+LSI). (A) full graph between 10° and 80° and (B) magnification between 25° and 45°.

2.4.3 Microstructure characterization

Figure 43 shows the SEM images with different magnifications of the fracture surface of the βSiC sample after thermal treatment at 1600°C (6PIP+TT) and the Si-βSiC sample after thermal treatment at 1600°C followed by LSI at 1600°C (6PIP+TT+LSI).

Figure 43. SEM micrographs with different magnification of the βSiC sample after thermal treatment at 1600°C without Si infiltration (6PIP+TT) and the SiSiC sample after thermal treatment at 1600°C followed by LSI at 1600°C (6PIP+TT+LSI).

Sample 6PIP+TT shows the incomplete crystallization of the SiC phase (dark grey areas) and the absence of Si in the material pores. The compact light grey area is the SiC and the dark area are the pores filled with the resin used to incorporate the sample. The black areas are other very large pores not filled with the resin. SEM micrographs with higher magnifications and EDX mapping are provided in the Figure 44. The EDX mapping of composition of the 6PIP+TT sample showed that in addition to carbon and silicon there were traces of oxygen due to the pores or residuals of the SiOC decomposition. Carbon, silicon, and oxygen were found with atoms fraction of 64%, 30% and 6% respectively. The result demonstrated that the complete transformation of amorphous SiC into βSiC occurred in contact with the molten Si (case 6PIP+TT+LSI), which while infiltrating the pores raises the temperature very quickly during the reaction, favoring crystallization (see the process schematic in Figure 41).
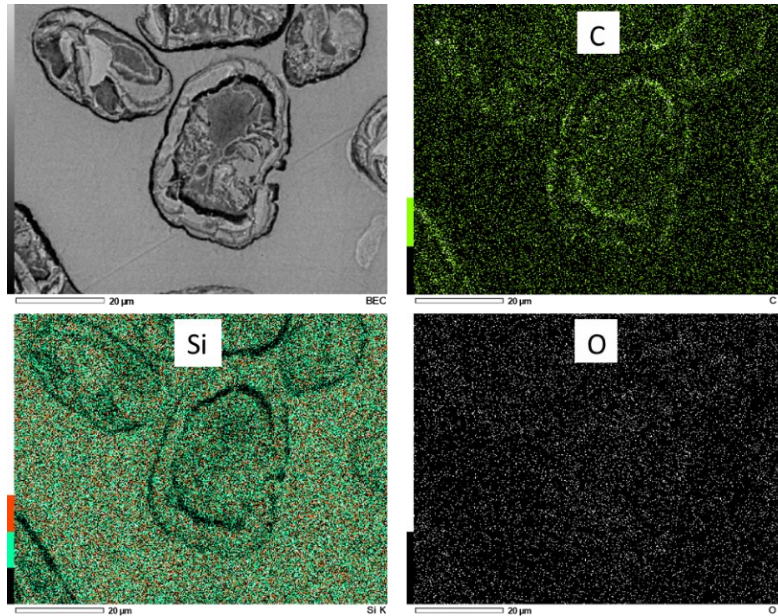
Figure 44. EDX mapping of the βSiC sample (6PIP+TT): C, Si and O were present in the network.

Sample 6PIP+TT+LSI shows the full crystallization of the amorphous polymer-derived SiC matrix into the βSiC phase. The faceting of the crystals' boundary (dark grey areas), and the full infiltration by the Si phase (light grey areas) were observed. After LSI at 1600°C, the SiC phase appeared to have shrunk by about 53 vol% with respect to 6PIP microstructure, as assessed by image analysis, due to the crystallization and SiOC decomposition. This phenomenon occurred during the thermal treatment, enabling for a complete infiltration of the part by the molten silicon, resulting in an almost fully dense ceramic part. EDX mapping of the composition was carried out to distinguish and quantify the phases (see Figure 45). Results confirmed that C and Si were the only elements present in the network (porosity was not identifiable, only ~1.7 vol%). The atoms fractions for C and Si were of 46% and 54% respectively. Using Eq. 17, the calculated density was 2.735 g/cm^3, in very good agreement with the measured true density value of that sample (2.718 ± 0.015 g/cm^3).
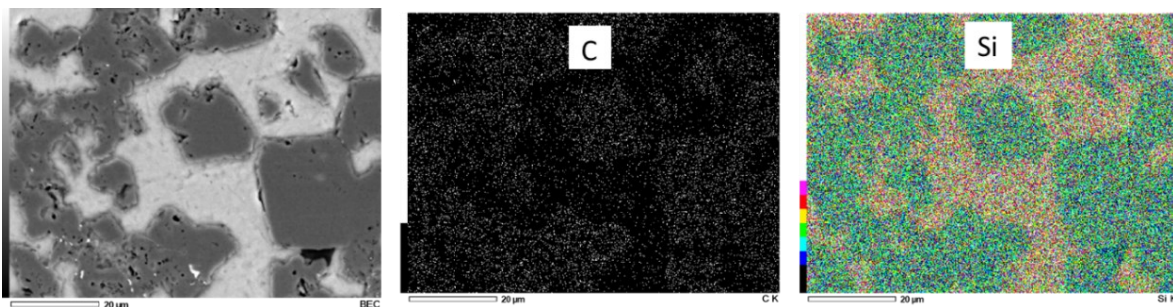
Figure 45. EDX mapping of the Si-βSiC sample (6PIP+TT+LSI): C and Si were the only elements present in the network.

2.4.4 Mechanical properties

The mechanical strength of the samples was evaluated through B3B biaxial flexural tests with the same method presented in the paragraph 2.3.4. In general, the stress increased with increasing strain until the maximum strength was reached, after which the specimens collapsed with brittle fracture. As a result of the fracture, the samples were split into three almost-equal parts. The maximum flexural stress reached by the Si-βSiC sample was 165 ± 9.45 MPa. Figure 46-B shows the biaxial flexural strength of the samples as a function of their relative density. As expected, the average strength and the relative density increased with increasing of the number of PIP cycles. After the first pyrolysis the strength was very low (7 ± 0.48 MPa), increasing to a more than three times higher value (23 ± 3.66 MPa) after six PIP cycles. The samples after LSI showed a significant increase both in strength (more than seven times) and relative density (98.3%). The values of the elastic modulus (Figure 46-C) had a similar trend as that of the strength plot. The maximum elastic modulus reached by the SiSiC samples was 2.66 ± 0.09 GPa. The large error bars can be attributed to the uneven bottom and top surfaces of the sample.
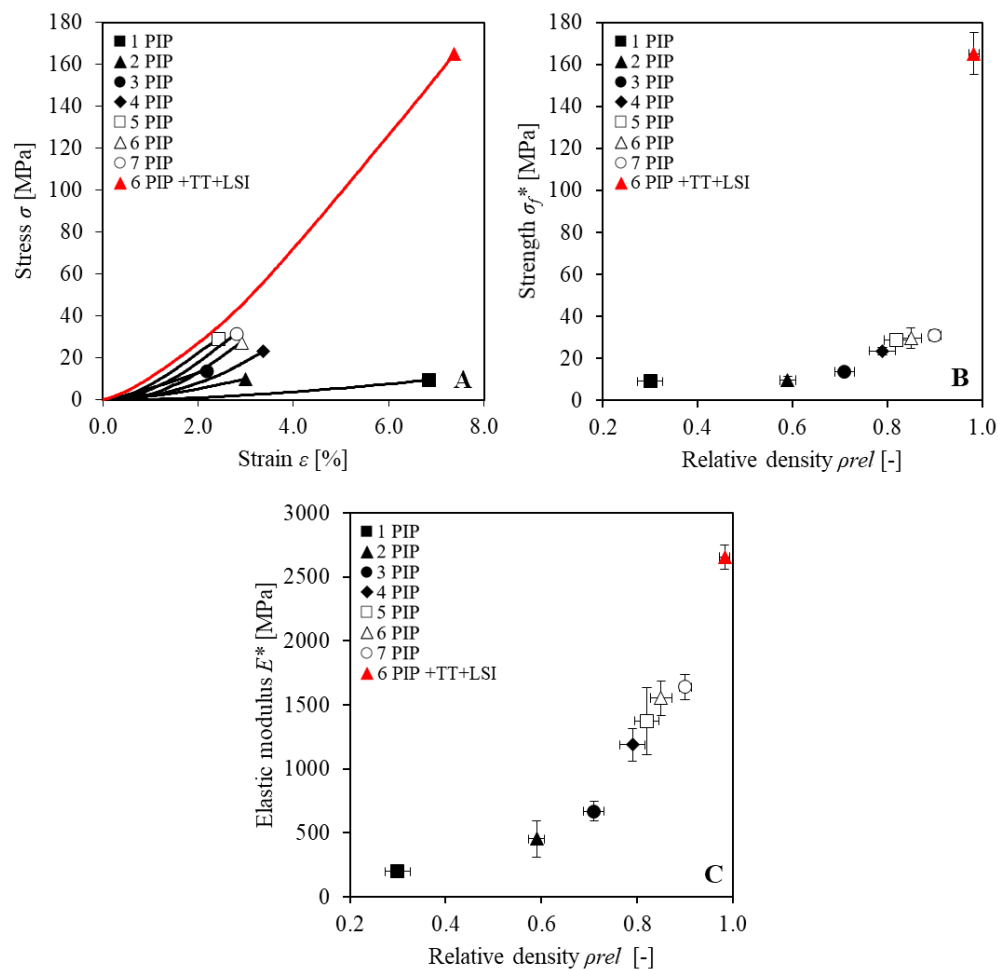
Figure 46. Mechanical test results for the SiOC/SiC samples and Si-βSiC samples: (A) flexural stress-strain curves; (B) average flexural strength and (C) average elastic modulus as a function of the relative density.

Table 13 shows the comparison between SiSiC ceramics fabricated by different AM technologies combined with LSI. In all these cases, a reactive silicon infiltration (RSI) was performed, meaning that free carbon was present in the matrix before silicon infiltration (by means of powders mixture, PIP, or other methods) which then reacted with the silicon to form SiC. This allows to reach higher SiC content with respect to the Si phase which has lower mechanical strength. In general, the material produced in this work can be compared with literature values, although many materials are twice as strong. The difference is attributable to the silicon content in the produced material, which is higher (two to eight times) than in the other ceramic materials. Furthermore, the βSiC phase of the produced materials was directly obtained by pyrolyzing the precursor at 1600°C, which is a huge mechanical disadvantage compared to the strength of α- and βSiC powders used in the literature works.

However, the strength of the material developed in this work could be further increased through the optimization of the process, for example, by increasing the volume fraction of SiC with respect to the Si phase. This could be achieved, for instance, either by infiltrating the preform with AHPCS containing also SiC particles (especially for the first PIP cycle) or by infiltrating the preform with phenolic resin (for the last PIP cycle) in order to generate crystalline SiC through the reaction between residual C (derived from the pyrolysis of the phenolic resin) and molten Si provided by LSI, or by printing a bed comprised of both PA12 and SiC particles thereby generating a preform already containing a high amount of crystalline silicon carbide phase.

Fabrication method	True density	Relative density	Si content	Strength	Test type	Sample size	Ref.
-	g/cm³	-	vol%	MPa	-	mm³	-
SLM+PIP+LSI	2.718	0.983	54.1	165	B3B	d23, h5	This study
iSLS + LSI	3.06	~1	16.4	162	4p	3x4x45	[54]
iSLS + LSI	2.69	-	-	200	3p	-	[70]
iSLS + LSI	2.64	~1	65	220	4p	3x4x50	[134]
ROB + LSI	2.94	0.979	22.9	224	4p	4x5x47	[53]
BJ + LSI	2.49	0.91	41	245	4p	3x4x50	[78]
iSLS+CIP+LSI	2.96	0.94	7	292-348	3p	3x4x35	[62]
EFF + LSI	-	-	-	300	3p	4x3x36	[59]
LOM + LSI	2.60	-	-	315	4p	2x3x22	[86]
BJ + LSI	3.05	~1	15-25	358-380	B3B	d10, h2	[52]

Table 13. Comparison between SiSiC ceramic samples fabricated by different AM technologies combined with LSI: iSLS = indirect selective laser sintering, ROB = robocasting, BJ = binder jetting, CIP = cold isostatic pressure, EFF = extrusion free forming, LOM = laminated object manufacturing. 3p and 4p indicate the 3-point and 4-point bending tests respectively. For this work was taken the 6PIP+TT+LSI sample in Table 12.

Figure 47 shows the Ashby chart (Granta EduPack 2022 R2, ANSYS, Pittsburgh, PA, USA) of the flexural strength against the density. It compares the mechanical properties of the material in this study, along with its dense ceramic and with other ceramics. The chart shows the same materials of the Figure 37 with the addition of the SiSiC ceramics presented in the Table 13. Results showed that the produced ceramics can be compared to the literature values both for density and strength. The values obtained after 6PIP+TT+LSI are in the range of the other SiSiC ceramics produced by additive manufacturing in literature. The lower strength is attributable to the fabrication methods which differ from the one used in this work, especially for the reactive infiltration technique. The common objective of research on ceramics will be to get as close as possible to the strength and density of the same material produced with traditional techniques (yellow area).
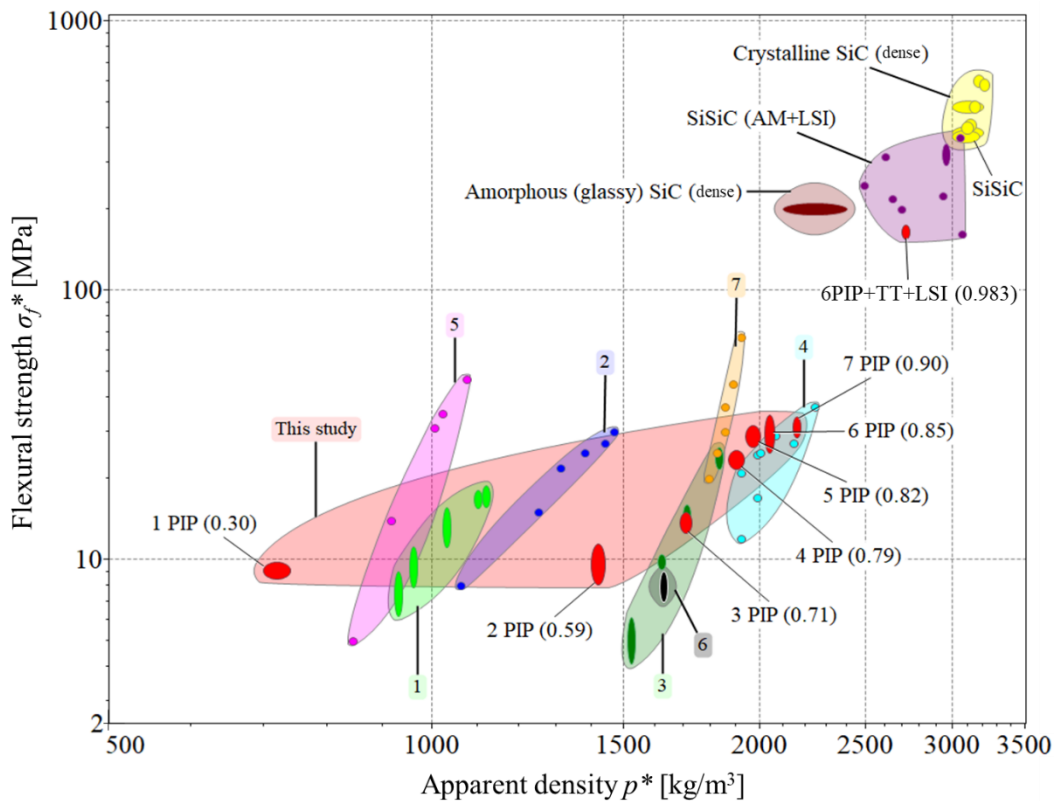
Figure 47. Ashby chart of the flexural strength against the density for SiC and SiSiC ceramic samples. The chart compares the fabricated structure against other materials. Materials properties for crystalline SiC (yellow points) were obtained from the software Granta EduPack 2022 R2 (ANSYS, Pittsburgh, PA, USA). The red area represents the experimental results of the amorphous SiC discs after each PIP cycle and the Si-βSiC after 6PIP+TT+LSI with the relative density indicated in brackets. The flexural strength of the dense amorphous SiC was taken to be 200 MPa and the measured density was 2.403 g/cm³ (brown point). Other groups of materials were taken from literature and reported in Table 11 and Table 13.

2.5 Results summary and discussion

A novel hybrid fabrication approach based on additive manufacturing to produce nearly fully dense, net-shape SiC and SiSiC components was introduced. The work was focused on the development of the process, and the microstructure and mechanical properties of the produced components were assessed. This hybrid method exploits the selective laser melting of a polymeric preform combined with few cycles of polymer infiltration and pyrolysis, followed by liquid silicon infiltration. Thanks to 3D printing, it is possible to produce any shape and to maintain the micro details after the polymer-to-ceramic transformation. This occurs through the choice of the printing parameters, which allows to control the relative density of the printed part. Accordingly, the infiltration rate and the shrinkage after the first pyrolysis cycle (~24%.) can be controlled. The final densification is achieved via liquid silicon infiltration of the solid amorphous SiC network derived from the pyrolysis of the preceramic precursor. During silicon infiltration at high temperature, the SiC phase crystallizes and shrinks allowing for a full infiltration by the molten silicon, producing the final Si-βSiC ceramic component without shape distortion. Crystalline βSiC and Si composed the final nearly fully dense (98.3%) ceramic part with a volume fraction of 45% and 55%, respectively. The final biaxial strength of 165 MPa can still be increased through further optimization of the process.

2.5.1 Strength of the developed process

The notable result was the possibility to obtain almost fully dense ceramic parts, with the crystalline βSiC phase, directly derived from the preceramic precursor, without the use of ceramics powder. This can overcome several processing problems that have been found in other additive manufacturing techniques for ceramics, and it can be seen as an alternative approach to binder jetting and direct ink writing, to produce templates to be further processed by silicon infiltration.

The developed process has three significant advantages:

- Technology: this method uses the selective laser melting of thermoplastic powders, which is a technique with very high maturity and low cost, compared to almost all ceramics approaches. Increasing the resolution of the equipment can lead to a huge increase in the control of the relative density of the component. Consequently, an object with higher microporosity can lead to higher infiltration efficiency and then to a lower number of PIP cycles. A higher control on the shape and shrinkage of the material can be achieved during all stages of the process. Furthermore, the process makes used of the PIP and LSI, which are consolidated and well-known techniques that have been used in the field of ceramics for more than 30 years.

- **Material**: the process is very flexible in reference to the material to be produced. In principle, it is possible to produce any ceramic material starting from its preceramic polymer. It will be enough to infiltrate the 3D printed preform with the selected preceramic polymer to produce a wide variety of different ceramic materials. The only constraint is that the preceramic must crosslink before the PA12 melting, i.e., around 155°C. Adding an agent that promotes cross linking can easily solve this issue. The production of different ceramics using this method is presented in the paragraph 4.3.

- **Structure**: the manufacturing approach can be extended to the fabrication of components possessing more complex (e.g., cellular) architectures, leading to parts with (i) much smaller features (e.g., pores) than those achievable using binder jetting, and (ii) denser struts than those obtainable through the replica method of structures manufactured by digital light processing. The computational design of complex cellular architectures and their fabrication using the developed process are presented in the chapter 3 and 4 respectively.

2.5.2 Weakness and possible improvements

Despite the developed process has several advantages with respect to other methods for ceramics, there are some aspects that can be improved:

- **Material composition after PIP**: the oxygen content produced in the first conversion could be reduced or eliminated. First, by using a polymer powder without oxygen content instead of PA12. Several other strategies could be adopted, such as drying the powder before printing, printing in an oxygen-free environment, drying the preform before processing, drying the infiltrated preform before each pyrolysis cycle, and infiltrating the preform in an oxygen-free environment.

- **Material composition after LSI**: the volume fraction of the βSiC phase must be increased with respect to the residual Si phase. Ideally the latter should be eliminated. This could be achieved, for instance, either by infiltrating the preform with AHPCS containing also SiC particles (especially for the first PIP cycle) or by infiltrating the preform with phenolic resin (for the last PIP cycle) in order to generate crystalline SiC through the reaction between residual C (derived from the pyrolysis of the phenolic resin) and molten Si provided by LSI, or by printing a bed comprised of both PA12 and SiC particles thereby generating a preform already containing a high amount of crystalline SiC phase. Consequently, the volume fraction increasing of the βSiC phase will lead to a huge increase of the industrial interest of the material, due to higher strength and resistance to higher temperature. This investigation is presented in the paragraph 4.4.2.

- <u>PIP process</u>: the number of polymer infiltration and pyrolysis cycles must be reduced to save time and costs. This means that a relative density of about 0.85-0.90 must be achieved with fewer PIP cycles than the current ones (6-7 respectively). Stating that the infiltration technique is already being optimized, two strategies can be adopted. (i) By using a 3D printer with a higher resolution will allow to produce a microstructure with finer details, leading to the possibility of generating polymer preforms with much higher microporosity. Consequently, the first PIP will generate a preform with higher relative density with respect to the current 0.30. (ii) By using raw materials with higher ceramic yield both for the 3D printed powder and for the preceramic polymers. However, component thickness can play a significant role in the number of infiltration and pyrolysis cycles.

- <u>Thermal treatments</u>: during PIP the material is infiltrated and pyrolyzed at 1000°C several times until reaching a high relative density. While during silicon infiltration the material is heated at 1600°C. Scientifically it would be better to directly perform a treatment at 1600°C during the PIP. The two processes were performed by two different furnaces (see paragraph 2.3.2 and 2.4.1 respectively) for a practical issue. The pyrolysis oven was suitable for the digestion of vapors and smoke coming from the conversion of preceramics and its maximum temperature was 1000°C. Instead, the other oven was used only for silicon infiltration to avoid dirtying the graphite resistors which are very expensive. Furthermore, the material treated at 1600°C is very fragile, therefore it needs a high relative density before heating, otherwise it would collapse. For these reasons the two processes were separated. Ideally, a single oven could reduce process times and directly produce the crystalline βSiC phase.

Some weaknesses were investigated, and some improvements were implemented in the process. These progresses are presented in chapter 4.

3

Parametric computational design of cellular structures

This chapter aims to describe the development of a new parametric computational design method for cellular architectures. The proposed approach uses a library of purpose-built algorithms and scripts that allow to generate structures with different features and functionalities, depending on the user's requirements. <u>The structures shown in all the figures of this chapter have been designed and generated with the developed design tools.</u>

The part of this chapter is published in:

- Journal of the Ceramic Society of Japan in September 2020 as "Pelanconi, M., Rezaei, E., & Ortona, A. (2020). Cellular ceramic architectures produced by hybrid additive manufacturing: A review on the evolution of their design. Journal of the Ceramic Society of Japan, 128(9), 595-604.". https://doi.org/10.2109/jcersj2.20071

- Industrializing Additive Manufacturing: Proceedings of AMPA2020 (Springer Nature Book) in September 2020 as "Pelanconi, M., Ortona, A. (2021). Review on the Design Approaches of Cellular Architectures Produced by Additive Manufacturing. In: Meboldt, M., Klahn, C. (eds) Industrializing Additive Manufacturing. Proceedings of AMPA2020. Springer, Cham, pp. 52–64.". https://doi.org/10.1007/978-3-030-54334-1_5

3.1   Cellular architectures overview

Porous cellular ceramics are used in many different engineering industrial fields, such as high temperature application, catalyst, protection systems, weight saving applications, thermal storage, and composites[7,49,198–201]. They are employed exploiting their properties related to the material and to the morphology. Additive manufacturing made it possible to produce these structures that previously could not be fabricated with conventional manufacturing methods. AM allows to fabricate metal, plastic and ceramic objects starting from a 3D computer aided drafting (CAD) file[202] and it has opened the doors to the generation of more and more complex CAD models. A proper design of the morphology can result in structures with optimized properties for specific applications[126–128].

Cellular porous architectures are very complex in their morphology because of the large numbers of geometrical details, and for this reason they are impossible to generate with standard CAD packages[129]. In recent years, the need to develop special design tools was recorded. All the new generation design approaches for cellular architectures are based on the Ashby and Gibson[140] simplified model of foams, in which the unit cell is assumed as "cube like". The arrangement of cubic unit cell forms a lattice structure. Their idea of using cubic lattice structures was introduced to explain the behavior of foams, with analytical models, in terms of pressure drop, heat and mass transfer, and stiffness[132,203,204]. Compared to random foams, lattice structures are regular and reproducible. They offer more design freedom, which results in structures with enhanced properties and novel functionalities[205].

In this thesis work, the development of new design tools was focused on lattice-based structures and triply periodic minimal surface-based structures. The tools are based on a parametric computational design approach. Figure 48 shows the different families and sub-families of cellular architectures that can be generated with the tools.
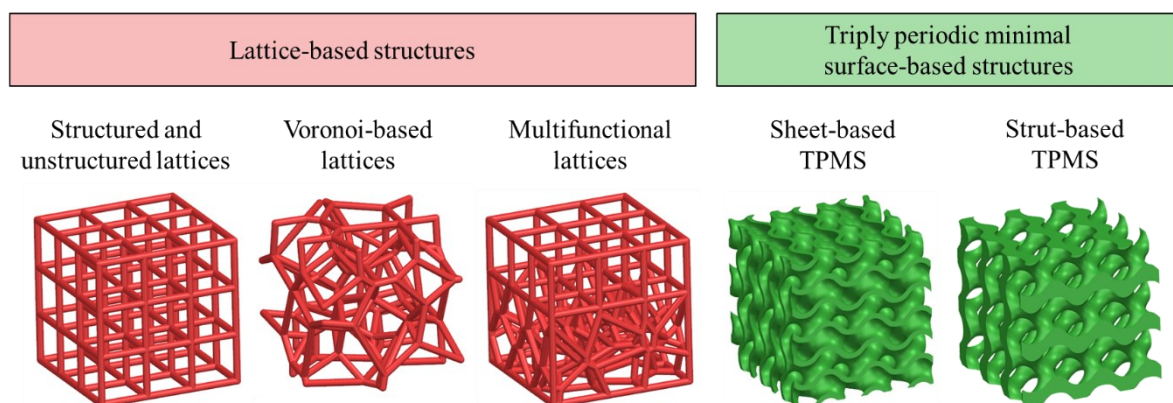
Figure 48. Design solutions for cellular architectures produced by additive manufacturing: lattice-based structures (structured and unstructured lattices, Voronoi-based lattices, and multifunctional lattices) and triply periodic minimal surface based-structures (sheet-based TPMS and strut-based TPMS).

3.2 Lattice-based structures
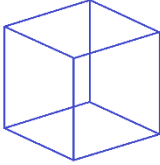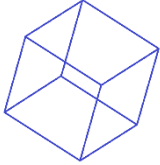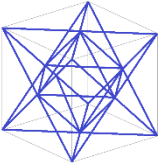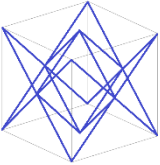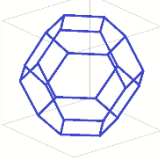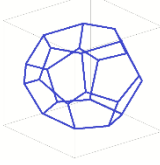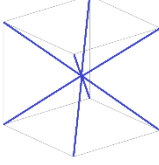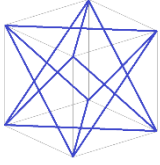
A lattice-based structure consists of an arrangement of cells composed by struts, which are connected one to another by nodes. The architecture construction takes place from the unit cell. There are unit-cells, with periodic boundaries, that can fill the space forming a lattice structure. The lattice can be made by polyhedra (e.g., cubic, dodecahedron, etc.) or by a combination of them (e.g., Weaire-Phelan[206] and octet truss). By replicating the unit-cell in three directions, a lattice structure is generated.

3.2.1 Structured and unstructured lattices

Structured lattices are periodic arrangement of cells with homogeneities in the volume, meaning that they have constant cell size, constant cell orientation and constant strut diameter (constant relative density in the whole volume). In many cases, unstructured lattices are preferred with respect to structured ones. This is due to the possibility to have components with heterogeneities, such as variable cell size, variable cell orientation and variable strut diameter (and thus variable relative density).

For both these structures, a parametric numerical tool was developed by using Grasshopper that runs within the Rhinoceros 3D software (McNeel, Seattle, Washington, USA). Grasshopper is a visual programming language environment that allows creating programs by dragging components onto a canvas. The outputs to these components are then connected to the inputs of subsequent components. Grasshopper is primarily used to build generative algorithms, but its advanced uses include parametric modelling for structural engineering[207], parametric modelling for architecture and fabrication[208], lighting performance analysis for eco-friendly architecture and building energy consumption[209].

The developed algorithm contains a library of several purpose-built unit cells made up of lines (Table 14), such as straight cube, rotated cube, hexagonal, octet-truss, tetrakaidecahedron, weaire-phelan, start, cross, tesseract, vintiles, diamond and honeycomb. In addition to these cells, the code can manage any other type of cell.

Cube	Rotated Cube	Hexagonal	Octet-truss
Tetrakaidecahedron	Weaire-Phelan	Star	Cross
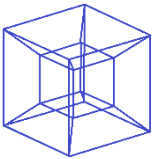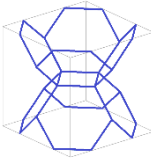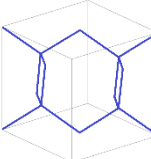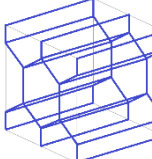
Tesseract	Vintiles	Diamond	Honeycomb

Table 14. Library of several purpose-built unit cells made up of lines for lattice-based structures designed using Grasshopper.

The desired lattice unit cell is selected and replicated in the space until filling the volume of the desired size and shape. The array of lines is then converted into a 3D triangular mesh, created using Cocoon add-on[210], which uses a direct implementation of the Marching Cubes algorithm[211]. This component allows, through the triangulation of the space, to give a thickness to a line, giving as input the distance from it (the radius of the strut). The output of the tool is a STL file that can be processed immediately for 3D printing. Figure 49 shows the design steps of the developed tool for lattice-based structures.
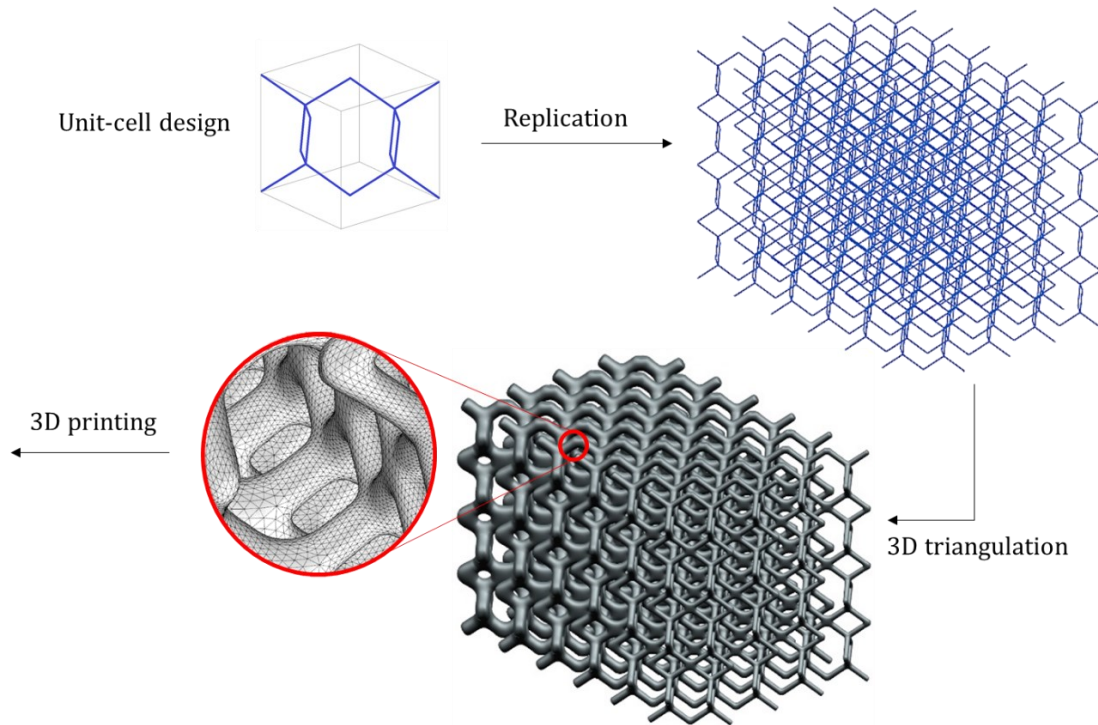
Figure 49. Design steps for structured and unstructured lattice structures using the developed parametric numerical tool using Grasshopper[142]. The strut radius gradient of the 3D triangulated mesh is visible.

The algorithm allows the generation of lattices structures of any shape, with a quick parametrization of the geometrical quantities: cells type, cells size, orientation, struts diameter, gradient for struts diameter, sample size and shape. The algorithm has several advantages with respect to traditional CAD modeling: the generation time is much shorter, the generation is automatic, it allows visualization of the structure after each step, and it allows properties calculation (surface area, volume, relative density, etc.).

Figure 50 shows some examples of complex cellular architectures developed with this tool. Figure 50-A shows a rotated cubic lattice and Figure 50-B shows a tetrakaidekahedron lattice both with constant cell size and strut diameter. Figure 50-C shows a rotated cube lattice with variable strut diameter along one direction, and Figure 50-D shows an octet lattice with variable cell size and variable strut diameter both along the vertical direction.
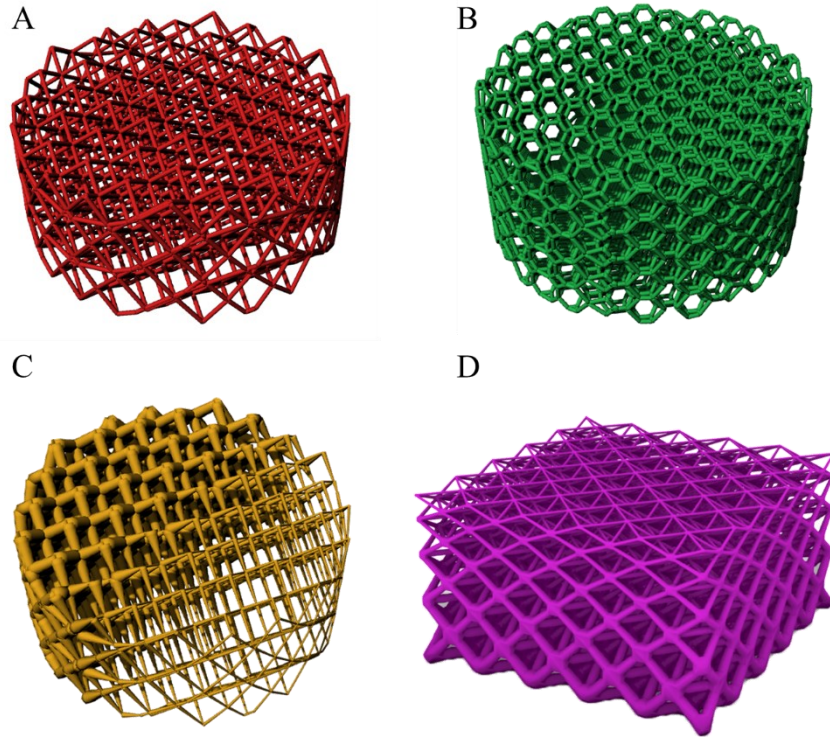
Figure 50. Example of lattice structures generated with the developed codes. (A) rotated cubic lattice and (B) tetrakaidekahedron lattice both with constant cell size and strut diameter. (C) rotated cube lattice with variable strut diameter along one axis. (D) octet lattice with variable cell size and variable strut diameter along Z-axis.

Figure 51 shows a rotate cubic lattice used in a thermo-fluid dynamic simulation environment with the purpose to improve the performance of a heat exchanger system.
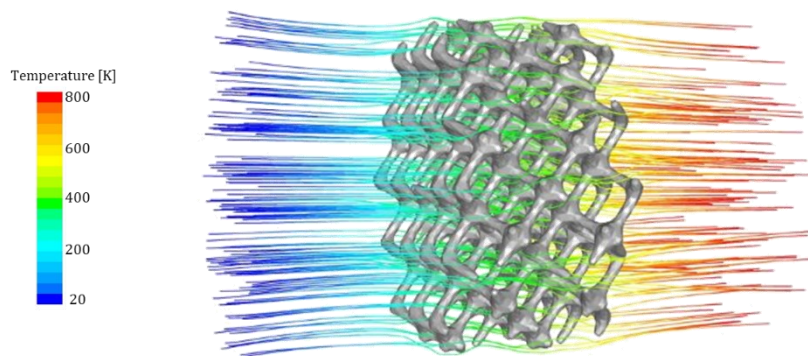
Figure 51. Results of a computational thermo-fluid dynamic simulation of a rotated cubic lattice used to increase the temperature of a cold fluid into a tubular heat exchanger system. Simulation performed in the framework of another project[8].

Figure 52 shows the developed Grasshopper flowchart for the design of lattice-based structures. The schematic shows different modules which represent the design steps for the generation of the 3D final structure useful for the 3D printing. The parametric tool allows to change several features to modify the topology of the lattice in very few seconds. Furthermore, the code allows the calculation of several quantities during generation, such as cell volume, number of cells, geometric surface area, solid volume, porosity, and others.
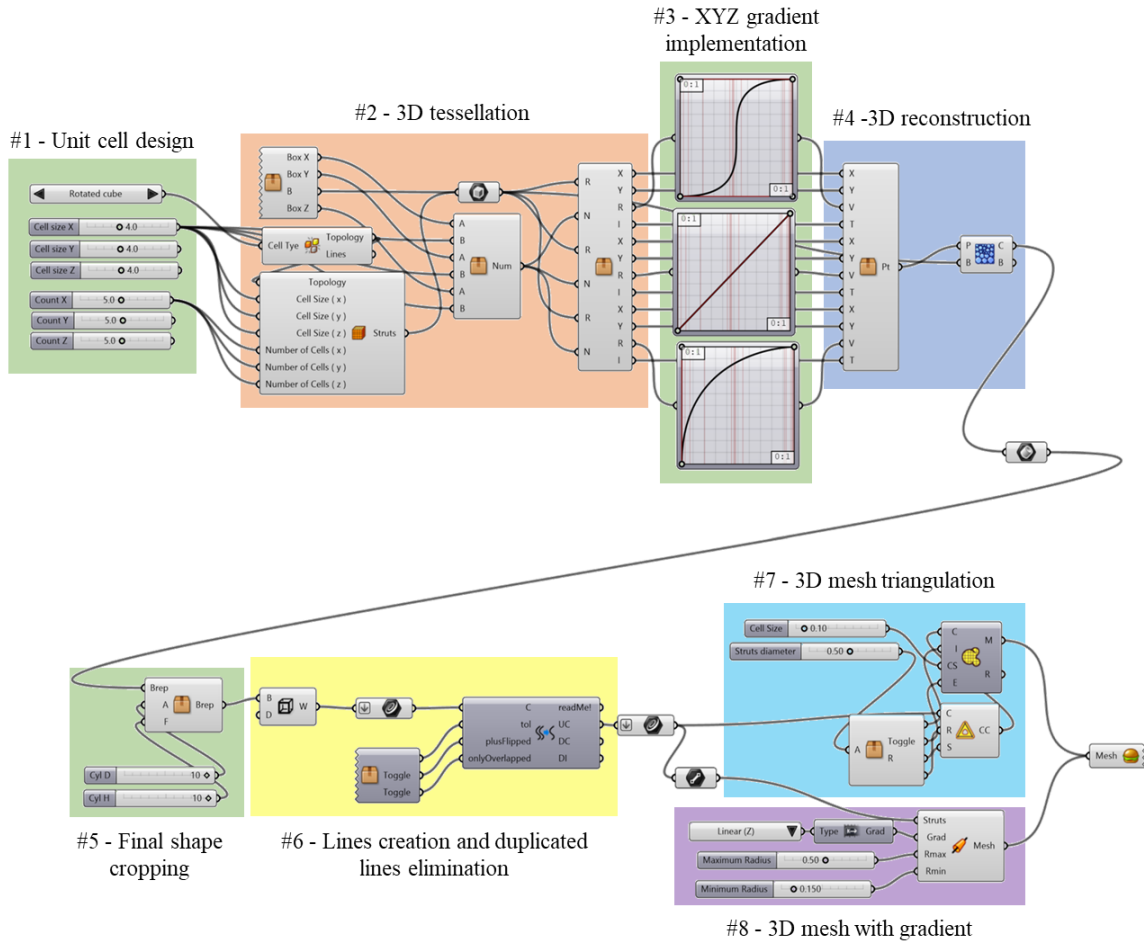
Figure 52. Grasshopper flowchart developed in this work for the generation of lattice architectures. The schematic shows different modules which represent the design steps. The first green box #1 contains the parameters which can be easily varied to change the topology of the lattice (cell type and cell size) or can be used to create a new unit cell. The orange box #2 replicates the cell in the 3D space through a tessellation script (the commands were compressed in several clusters to improve the visualization). The second green box #3 allows the implementation of a gradient along the three axes by following different purpose-built mathematical functions (graphs show three examples). The blue box #4 re-creates the 3D tessellation after the gradient implementation. The third green box #5 allows to generate the final shape and size of the part and crop it with the 3D array of cells. The yellow box #6 creates the lines from the solid of each cell and then eliminates the duplicated lines that are created when the cell is replicated in the space. The light blue box #7 generates the 3D mesh triangulation with constant strut diameter. The purple box #8 generates the 3D mesh triangulation with variable strut diameter.

3.2.2 Voronoi-based lattices

The need to represent a random foam, instead of periodic arrangement of the regular lattices, with an engineerable structure has led to the development of a new algorithm based on the Voronoi 3D tessellation[212]. Voronoi structures are obtained by partitioning space into zones based on the distance from a specific set of points. There are several algorithms to obtain Voronoi diagrams. To create a Voronoi tessellation, first the desired enclosure is populated with a set of seed points. Based on these points, the space is then partitioned into small cells, called Voronoi cells. Each cell contains the space around a seed point that is closer to that seed than any other one. The edges of each cell are subsequently converted into solid struts. The code, realized into Grasshopper (McNeel, Seattle, Washington, USA) using Rhinoceros for the visualization, allows the generation of Voronoi-based lattices of any shape (Figure 53-a) with a parametrization of the following geometrical quantities: mean cells size, struts diameter, gradient for struts diameter, and sample size. The code was further developed allowing the implementation of a cells size gradient along one or more directions (Figure 53-b): the cells size changes starting from one value and arriving at another, even with more variations. In this way, it is possible to generate a lattice with different porosities in different regions of its volume.
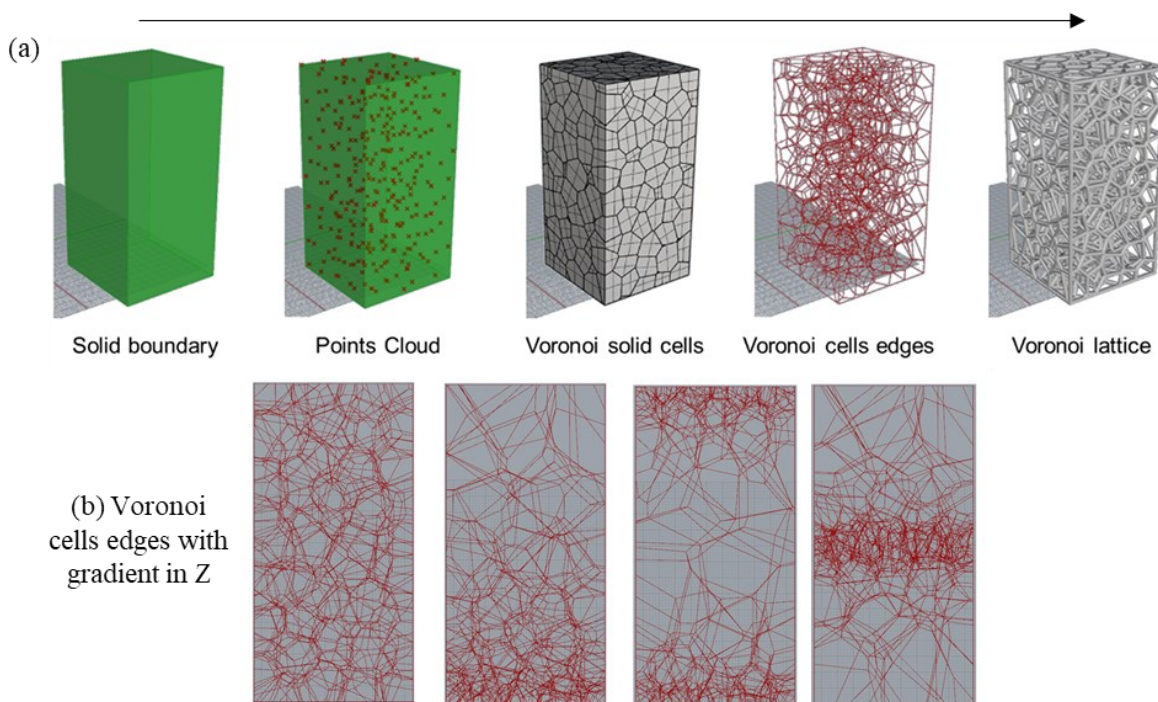
Figure 53. (a) Design steps of the Voronoi-based lattice tool and (b) 2D visualization of different Voronoi structures (edges of the cells) with variable cells size along Z axis. These structures were generated with the developed codes of this work[142].

3.2.3 Multifunctional lattices

Additive manufacturing allows producing very complex geometry. This means that different components, which perform different functions, can be fabricated together in one piece with the combination of the features. In this thesis, a novel design method of multifunctional cellular architectures was developed, enabling to generate structures with morphological variations. This provides a component with different features and functionalities in its own volume, depending on its requirements. The purpose-built Grasshopper algorithm allows to generate structures with different cell types in the same volume. There is a gradient between a cell type and another, made up of Voronoi 3D tessellation. The flexibility of Voronoi tessellation can be employed to join different structures. Figure 54 shows a 2D representation of a multi-lattice produced with this approach. The 3D solid is generated with the same method presented in the paragraph 3.2.1. The fabrication of such complex parts thanks to additive manufacturing can significantly improve the performance of several components. For example, in the fluid-dynamic technologies, it will be possible to control the fluid mixing in specific regions of the system by placing straight cells (e.g., cubic) or oriented cells (e.g., tetrakaidekahedron) and increasing/decreasing the velocity of the fluid to control the pressure drop and the turbulence of the flow. Also, in mechanical engineering could be possible to have a control on the deformation in different regions of the same volume.
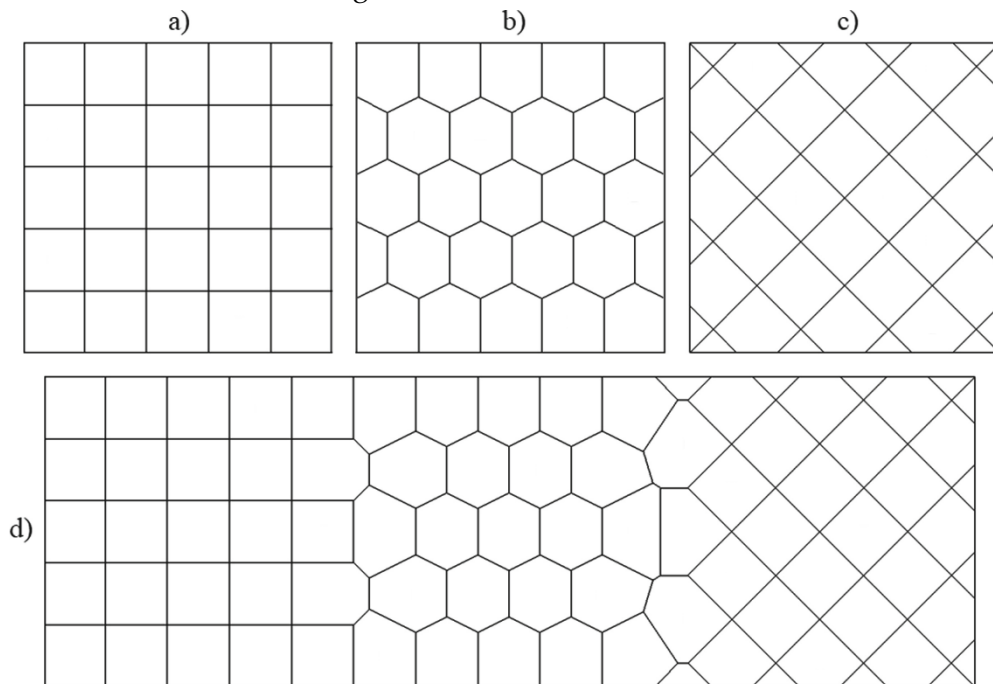
Figure 54. Multifunctional cellular architectures design: a) quad lattice; b) hexagonal lattice; c) rotated quad lattice; d) multi-lattice structure consisting of quad, hexagonal and rotated quad cells. The 3D solid is generated with the same method presented in the paragraph 3.2.1. These structures were generated with the developed codes of this work[142].

3.3 Triply periodic minimal surfaces-based structures

Additively manufactured cellular structures made up of struts elements are mainly employed for their high porosity, permeability[213] and thermal properties[214,215]. In applications where the objective is to maximize the surface area of a component (for example catalytic substrates), these structures are not the best solution. In recent years, a new kind of structures is emerging, as an outstanding solution for constructing porous cellular architectures, based on minimal surfaces[216]. A minimal surface is a surface that is locally area-minimizing, e.g., a small piece has the smallest possible area for a surface spanning the boundary of that piece. Minimal surfaces necessarily have zero mean curvature (the sum of the principal curvatures at each point is zero). Minimal surface topologies have been known for over a century and have been observed in nature in soap films and butterfly wings[217,218]. Fascinating are minimal surfaces that have a crystalline structure, in the sense of repeating themselves in three dimensions, named triply periodic minimal surface (TPMS)[219–221]. More and more research attention has been played to TPMS involving multiple engineering disciplines, including lightweight materials[222–225], composites[226–229], heat exchangers[230–232], catalytic supports[6], filters for water treatment[233–235] and many others. Compared with other kinds of structures, TPMS porous structures have three significant merits:

- The whole structure can be precisely expressed by mathematical functions. Basic performances, such as porosity or volume specific surface areas can be directly controlled by adjusting the function parameters.

- The surfaces of TPMS are very smooth, without sharp edges or junctions as the lattice structures. Furthermore, the TPMS porous structures are highly interconnected with non-tortuous pores, which could be an important advantage for several applications.

- The surface of the TPMS divides space into two interwoven domains, which could be interesting as heat exchangers architectures. Moreover, the high surface area to volume ratio provides a wider spread in catalyst applications[6].

TPMS can be designed by using two different approaches[236], as shown in Figure 55:

1) Strut-based structure: one domain is filled with solid material and the other is left empty (void domain). The resulting structure is a lattice made up of struts, i.e., as the previous presented structures but with a TPMS unit cell.

2) Sheet-based structure: the surface is thickened of a desired value, forming two separate empty domains, which are infinite and intertwined, but not interconnected. The resulting structure is a warped sheet with a constant thickness.

To the purpose of creating structures with higher geometrical surface area than lattices, a new parametric computational design approach based on TPMS was developed. The 3D numerical tool was developed in Grasshopper using Rhinoceros for the visualization. It allows the generation of TPMS-based structures of any shape, with a parametrization of the following geometrical quantities:

- Cells size

- Surface thickness or strut diameter for sheet- and strut-based structures respectively

- Gradient of the cell size in the same volume

- Gradient of the surface thickness or strut diameter in the same volume

- Sample size

- Sample shape

The architecture construction takes place from a single surface (the unit cell) that is designed by plotting the approximation of the mathematical functions which define its topology. As example, the following equations show the functions used to design three different TPMS[237], namely Gyroid (GY), Crossed Layers of Parallels (CLP) and Primitive (P).

$$GY = \sin x \cdot \cos y + \sin y \cdot \cos z \cdot \sin z \cdot \cos x \qquad \text{Eq. 21}$$

$$CLP = \sin z \cdot \sin y - 0.4 \cdot (\sin x \cdot \cos z \cdot \cos y) \qquad \text{Eq. 22}$$

$$P = \cos x + \cos y + \cos z \qquad \text{Eq. 23}$$

Figure 55 shows the different approaches for creating sheet- or strut-based TPMS structures from the surface unit cell.
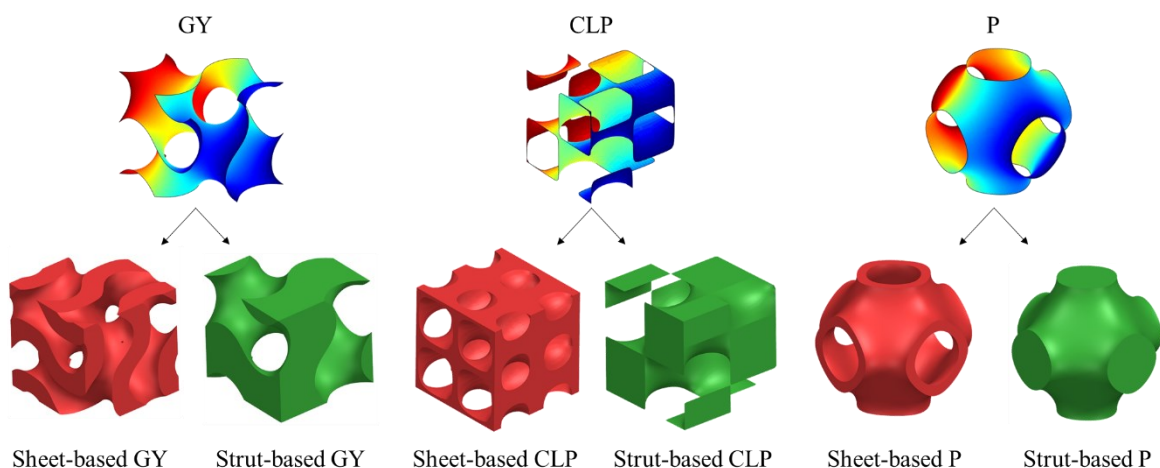
Figure 55. Different approaches for creating sheet- or strut-based TPMS structures from the surface unit cell of the Gyroid (GY), Crossed Layers of Parallels (CLP) and Primitive (P). These structures were generated with the developed codes of this work.

Figure 56 shows the six steps used for the generation of TPMS structures into Grasshopper.
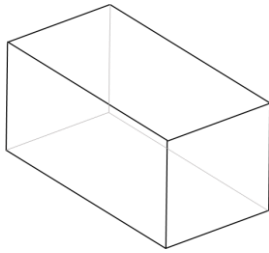
(i) the domain is designed, and the shape and size of the object is chosen.
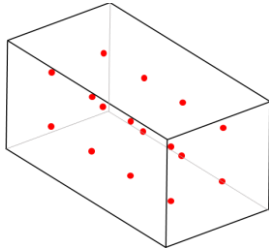
(ii) a $\mathbb{R}^3$ cloud of points is precisely introduced into the domain with a specific distance between points (constant or with a gradient) which represent the center of the unit cells.
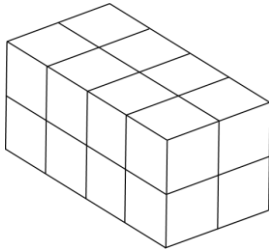
(iii) an arrangement of 3D voxels is generated by using the Voronoi tessellation[238] (if the points are at the same distance from each other the voxels will all be of the same size, if the points are placed at different distances from each other the voxels will be of different sizes).
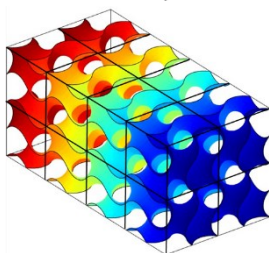
(iv) the previously designed unit cell of the TPMS is introduced inside each 3D voxel generating an arrangement of surfaces. The size of the TPMS cell is equal to the voxel size.
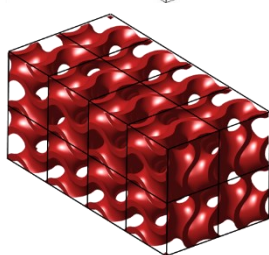
(v) this stage involves a mesh module, which converts the surface structure to a solid mesh, with the possibility to generated gradient in the surface thickness (same 3D triangulator meshing method presented in the paragraph 3.2.1).

(vi) the final stage involves the modeling of the final shape by cropping the two volumes together. A 3D sphere was generated in this case.

Figure 56. Design steps for TPMS structures using Grasshopper.

Figure 57 shows some examples of TPMS designed by introducing a gradient into the structures, by means of a sheet/strut thickness variation or cells size variation in the same volume. The gradient can be designed in terms of fast or slow variation. The thickness gradient is applied in the step (v) in Figure 56, by setting the volume fraction in the two sides of the volume. While the cells size gradient is applied in the step (ii) in Figure 56, by changing the distance between the cell center points.
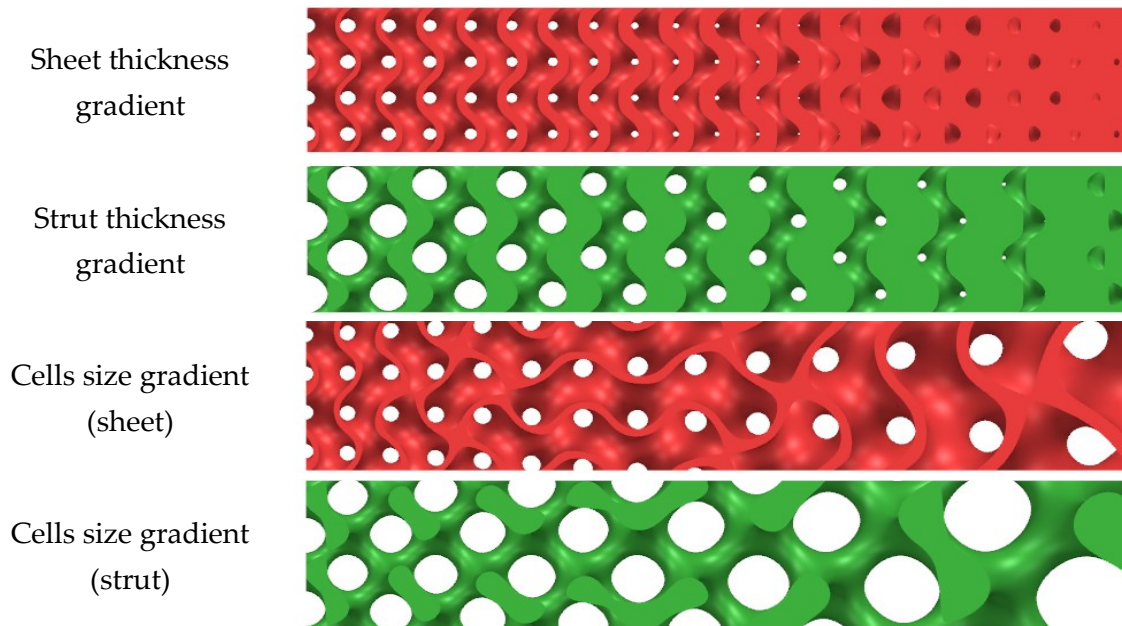
Figure 57. Design example of TPMS with gradient in the sheet/strut thickness and gradient in the cell size. These structures were generated with the developed codes of this work.

Figure 58 shows an example of the potential of the developed code for designing complex component, such as new generation heat exchangers, consisting of a TPMS Gyroid core with a cells size gradient from the inlet to the outlet.
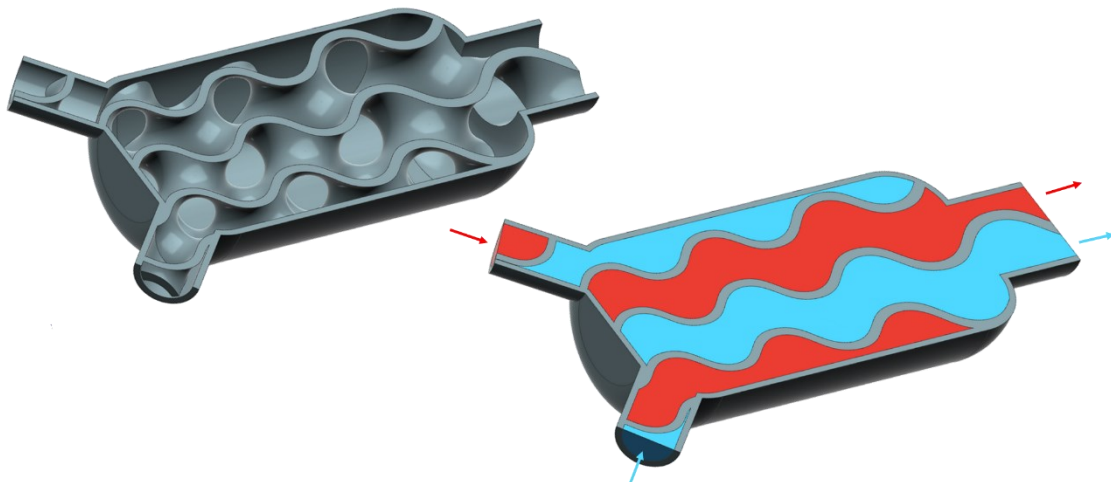
Figure 58. Section views of a new generation heat exchanger with TPMS gyroid structure designed with the developed codes of this work: architecture (grey), the hot fluid (red) and the cold fluid (blue).

3.4   Results summary and discussion

The strategy of designing a component has always been influenced by its manufacturing. The advent of AM has allowed conceiving components by their function and no longer by their manufacture. This benefit allows improving the components' performances and the fabrication of geometrically complex parts such as cellular structures. The structured and unstructured lattices approach is based on the replication of a desired unit-cell in the space, followed by the gradient implementation, and the Boolean cropping to obtain the desired final shape. With the Voronoi approach is possible to generate random foams and engineered Voronoi lattice. These structures exhibit scattered properties, and they can be used when randomness is needed. The multi-lattice approach, based on the Voronoi tessellation, allows to generate structure with different morphologies in a single volume. It can be used to join different lattices and generate very geometrically-complex components. The TPMS design approach consists in the creation of surface-based components with high mechanical properties and very high surface area compared with lattice structures.

3.4.1   Strength of the developed design tools

The developed tools allow to generate virtually any type of geometry with very fine details. Furthermore, the high control on the geometric parameters and on the 3D mesh allows to create very precise and smooth surface. The big advantage of the tools is the automation on the creation of the structure: once the Grasshopper model is built, the operator has only to choose the parameter and the computer done the whole generation effort to achieve the final structure. Moreover, the very quick possibility to change the topology of the cellular structure is a huge advantage with respect to traditional CAD software (see Figure 10). The developed computational design tolls can be easily coupled with the simulation of the component behavior (mechanical, thermal, fluid dynamic, etc.) and therefore, the possibility of quickly modify the geometric parameters of the component becomes fundamental. The purpose will be to modify the topology of the structure and then to investigate the enhancing of the performance through simulations, for example by using a trial-and-error approach. Figure 59 shows that using the computational design tool it is possible to quickly modify the geometric parameters to generate different lattice configurations. The design tools[141,142] presented in this work were employed to design components for catalytic supports[5] and heat exchangers[239].
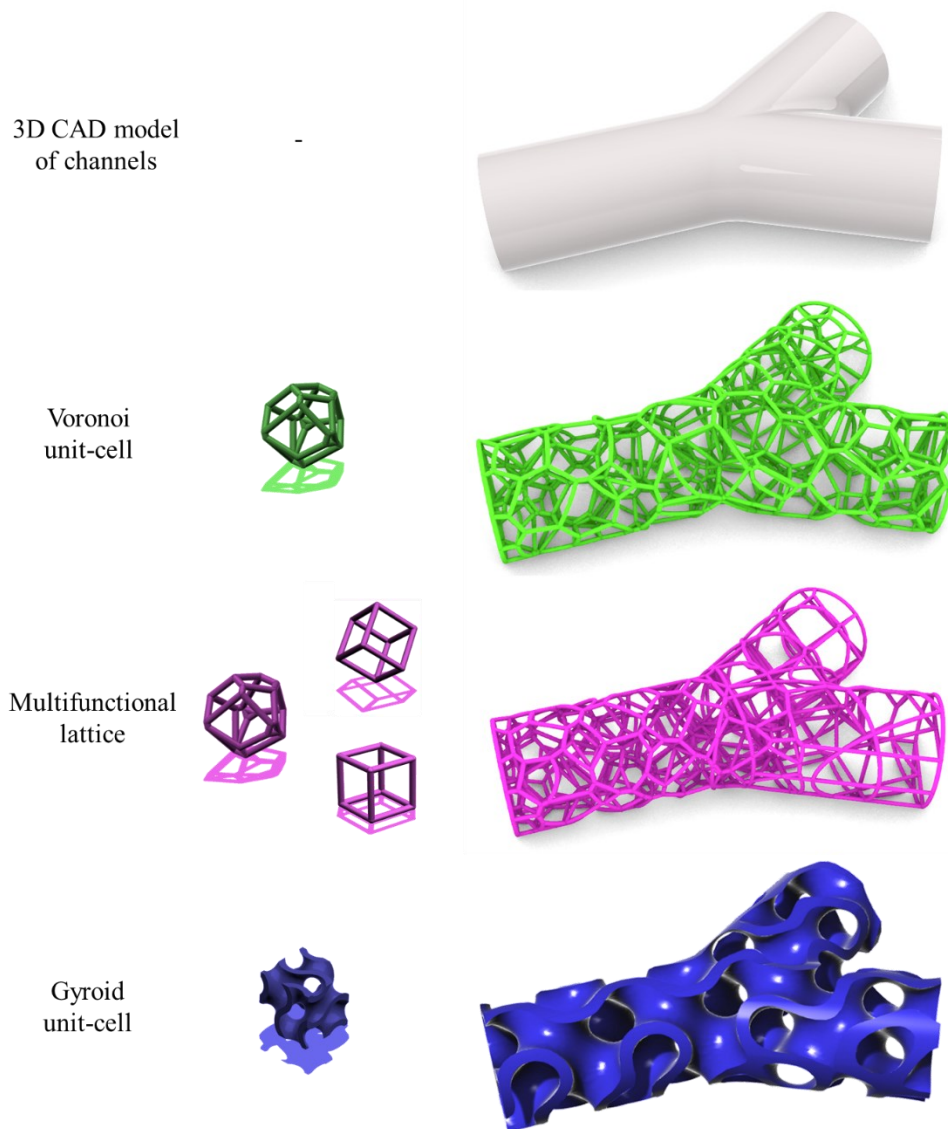
Figure 59. The developed computational tools used for the design of channels with different topologies: Voronoi lattice, multifunctional lattice (from Voronoi to rotated cube and straight cube) and gyroid-based structure. The figure shows the possibility of quickly modify the geometric parameters of the component to generate the models.

3.4.2 Weakness of the developed design tools

The most challenging part of the design process is the creation of the Grasshopper code. This phase is very complex and at the same time it is the most important part, because the final shape of the component depends on it. This step is usually longer than generating a CAD model with traditional software. Furthermore, these tools require adequate computational power (processors and RAM) to generate the part in a short time.

4

Production of a wide range of complex ceramic architectures

This chapter aims to describe the fabrication of complex architectures through the proposed hybrid additive manufacturing process. As demonstrated above, the process allows the use of any preceramic polymer for the infiltration and pyrolysis. In this chapter, various preceramic polymers were used to produce different polymer-derived ceramics. Finally, silicon infiltration was performed into different ceramic preforms to obtain fully dense and net-shape Si-infiltrated SiC ceramics of different types.

4.1   Design of the architectures

Two different complex architectures were generated through the computational design approach: one based on lattice (Figure 60-RC) and the other based on TPMS (Figure 60-GY) using the tools presented in the paragraph 3.2.1 and 3.3 respectively.
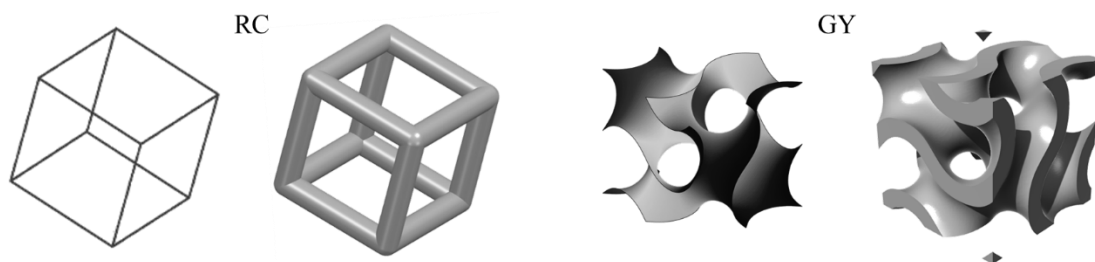
Figure 60. Unit-cell of the rotated cube (RC) from the lines to the solid model, and unit-cell of the Gyroid (GY) from the surface to the solid model.

The aim of the design was to generate two cylindrical structures with very different topologies, one made by struts (RC) and the other made by surfaces (GY), but maintaining the same geometric properties, such as solid volume, geometric surface area and geometric porosity (or macroporosity). This was achieved by using two different unit-cell sizes (C_S) and thickness of the struts or surface (t). Table 15 summarizes the geometric properties of the two structures and Figure 61 shows their 3D computational models.

Architecture name	-	RC	GY
Unit cell type (C_t)	-	Rotated cube	Gyroid
Unit cell size (C_S)	mm	2.9	6.8
Struts diameter or surface thickness (t)	mm	1.1	1.0
Sample diameter (D)	mm	25.0	25.0
Sample height (H)	mm	44.0	44.0
Geometric surface area (GSA)	cm^2	204.9	203.0
Solid volume (V_s)	cm^3	7.1	7.2
Total volume occupied (V_{tot})	cm^3	21.5	21.5
Specific geometric surface area ($SGSA$)	1/m	950.8	942.3
Geometric (macro) porosity (φ_M)	%	67	67

Table 15. Comparison between the geometric properties of the two designed cylindrical models: rotated cube (RC) and gyroid (GY).
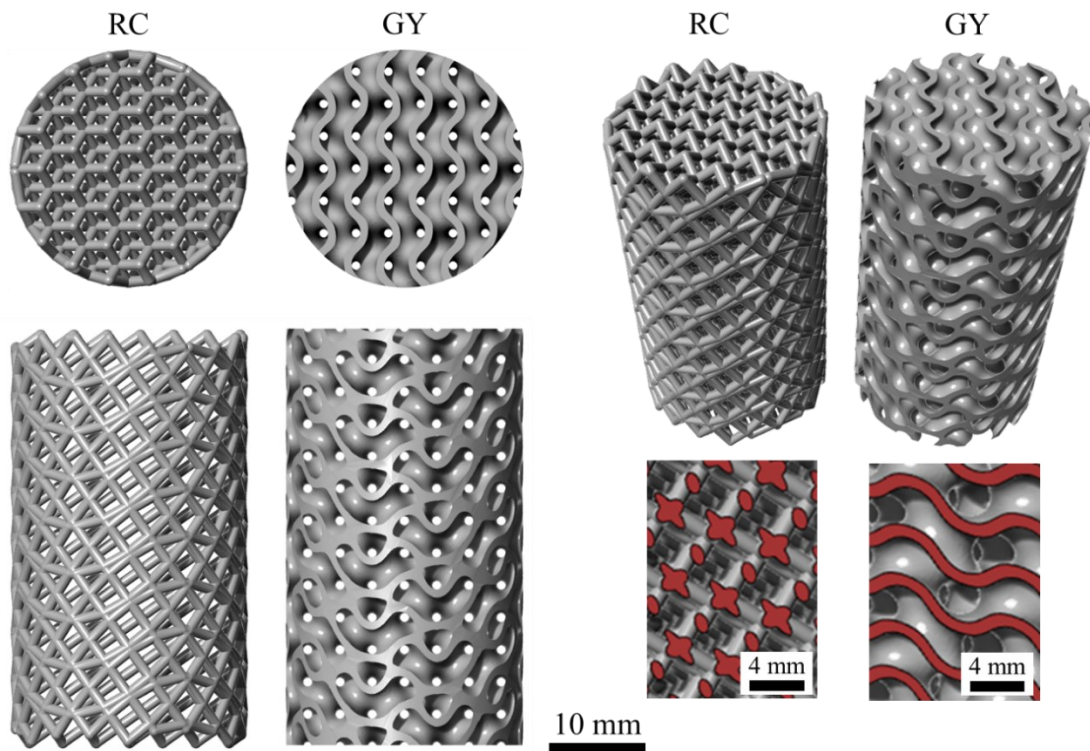
Figure 61. Computational models of the rotated cube (RC) and gyroid (GY) architectures in different views. The red surfaces are the section views of the parts.

4.2 Selective Laser Melting of the complex-shaped preforms

The complex-shaped design models were 3D printed with the same method presented in the paragraph 2.2.4, by using the same material (polyamide 12) and the same printing parameters: laser speed of 848 mm/s, layer thickness of 100 μm and powder surface temperature of 166°C. A total number of 160 samples were printed in view of subsequent testing. Figure 62-A shows the optical images of the architectures during the layer-by-layer 3D printing of the cross-section and Figure 62-B shows the fabricated polymeric parts.
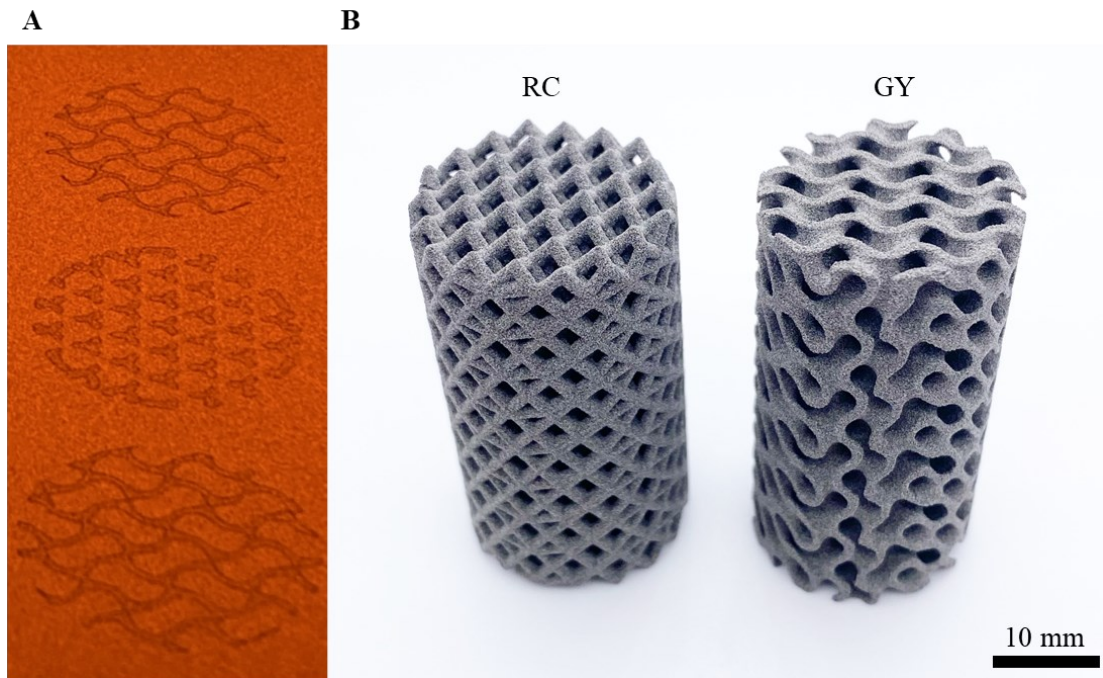
Figure 62. Optical images of the samples during the 3D printing (A) and the cellular polymeric samples as produced (B).

The combination of the printing parameters allowed to 3D print the complex architectures with a relative density of 0.56 ± 0.04 and very high quality, and the samples were easy to handle and to clean despite the complicated geometry. In accordance with the computational models, the final PA12 preforms had a diameter of 25 ± 0.47 mm, a height of 45 ± 0.64 mm and a mass of 4 ± 0.43 g. The measured struts diameter of the RC structures was 1.1 ± 0.018 mm, and the surface thickness of the GY structures was 1.0 ± 0.015 mm. The same parameters combination allowed to reach a relative density of 0.52 when printing discs (see paragraph 2.2.4). This means that the cross-section size has an influence on the microporosity of the part. This can be attributed to the path of the laser beam during the 3D printing. With samples processing a small thickness, the laser passes rapidly near the just melted powder, supplying further energy in a short time, which results in an over melting of the previous path, and therefore a lower amount micropores. Conversely, when samples have a larger thickness, the laser takes longer to pass near the just fused areas, and it does not influence the melting of the previous path.

4.3   Polymer Infiltration and Pyrolysis

As demonstrated in the chapter 2, the process flexibility allows to use any preceramic polymer for the infiltration and pyrolysis. Therefore, the obtained 3D printed complex-shaped preforms were infiltrated by using four commercial liquid preceramic polymers to produce different polymer-derived ceramics after pyrolysis. The aim was to compare the performance of the different ceramics in terms of ceramic yield, density, mechanical strength, and oxidation resistance. PIP was performed using the same equipment and methods presented in the paragraph 2.3.2. Table 16 shows the four solvent-free preceramic polymers used, which had similar viscosity and density.

AHPCS	Full name:	Allylhydridopolycarbosilane
	Commercial name:	StarPCS™ SMP-10
	Supplier:	Starfire Systems Inc, NY, USA
	Polymer-derived ceramic:	Silicon Carbide (SiC)
PCSO	Full name:	Polycarbosiloxane
	Commercial name:	MS-154
	Supplier:	EEMS-LLC, NY, USA
	Catalyst added:	CLC-PB055 (EEMS-LLC, NY, USA) 1%wt
	Polymer-derived ceramic:	Silicon Oxycarbide (SiOC)
PSN	Full name:	Polysilazane
	Commercial name:	Durazane 1800
	Supplier:	Merck KgaA, Darmstad, DE
	Polymer-derived ceramic:	Silicon Carbonitride (SiCN)
FUR	Full name:	Furanic resin (or carbon thermosetting resin)
	Commercial name:	Furolite 100
	Supplier:	TransFurans Chemicals, Geel, BE
	Catalyst added:	HM 1448 (WIZ chemicals, Dairago, IT) 5%wt
	Polymer-derived ceramic:	Carbon (C)

Table 16. Preceramic polymers used for the fabrication of different polymer-derived ceramics.

In the cases of PCSO and FUR, the addition of a catalyst was needed to promote the crosslinking of the preceramic polymer before the complete melting of the PA12 preform, and to maintain the object shape. A planetary centrifugal mixer (Thinky Mixer ARE-250, Thinky, USA) was used to mix the preceramic polymer with its catalyst at 700 rpm for 3 minutes. The samples after infiltrations with PCSO, PSN and FUR underwent a pre-cure treatment in a static furnace at 145°C for 2 hours before pyrolysis. This step was found to be crucial to promote the crosslinking of the preceramic polymer, and to maintain the shape of the part after pyrolysis.

4.3.1 Thermal behavior of the preceramic polymers

The behavior of the preceramic polymers as a function of the temperature was evaluated by Thermogravimetry (TGA). Tests were carried out in inert atmosphere using Argon (flow rate of 50 mL/min and heating rate of 10°C/min) up to 1000°C to investigate their behavior during pyrolysis. PCSO, PSN and FUR were tested after the pre-curing treatment at 145°C. AHPCS was tested as produced by the supplier. Figure 63 shows the results.
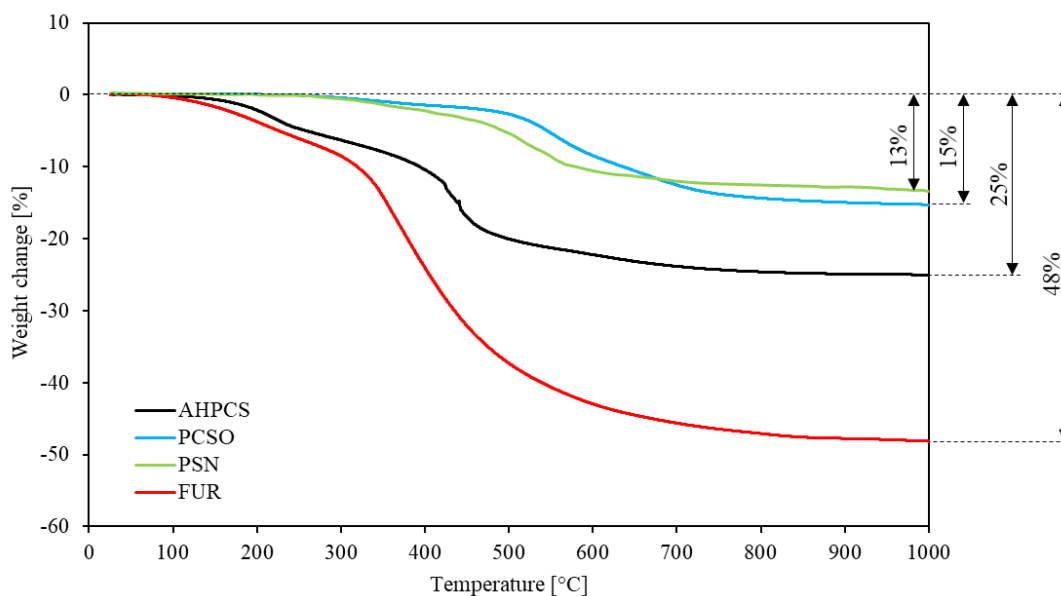
Figure 63. TGA analysis of the four preceramic polymers up to 1000°C: SiC precursor (AHPCS, black curve), SiOC precursor (PCSO, blue curve), SiCN precursor (PSN, green curve) and C precursor (FUR, red curve).

The four preceramic polymers showed three different behaviors. PCSO and PSN had about the same trend: up to 200°C no weight loss was observed due to the pre-curing treatment that provided stability to the material. A negligible weight loss was observed during the complete crosslinking of the polymers up to 350°C. Then, the polymer-to-ceramic conversion produced a higher weight loss for PSN up to 650°C. After this temperature an opposite behavior was observed with an increase of the weight loss for the PCSO. At 1000°C, the final ceramic residues of the SiOC and SiCN were 85% and 87% respectively. According to [240], the pre-crosslinking of the PSN produced a higher yield with respect to the not crosslinked one (10-15% lower)[241]. AHPCS behavior (black curve) cross-linked between 100-400°C with 10% weight loss due to the release of oligomers, and the polymer-to-ceramic transformation occurred above 400°C, with an additional 15% weight loss. At 1000°C, the SiC residue was 75% of the initial weight. FUR showed a difference behavior despite being pre-cured similarly to PCSO and PSN. A 10% weight loss was observed between 150-300°C due to the complete crosslinking of the polymer. Then the transformation into amorphous carbon produced an additional weight loss of about 38%, with a final C residue of 52%. All yields obtained agreed with the literature[85,241–243].

4.3.2 Polymer-to-ceramic conversion and densification

The 3D printed architectures were infiltrated with the selected preceramic polymers and then pyrolyzed at 960°C to produce their respective ceramic materials. Three additional infiltration and pyrolysis cycles were performed for their densification. Except for the Carbon parts (Furan resin as preceramic polymer) which underwent one cycle less, due to the clogging of the lattice cells (see Figure 68 for more information). 20 samples were produced for each different ceramics (10 for the RC and 10 for the GY). The AHPCS, PCSO, PSN and FUR preceramic polymers are precursor for the following ceramic materials: SiC, SiOC, SiCN and C respectively. A small amount of oxygen is always present in the matrix of polymer-derived ceramics due to the PA12 degradation (see to paragraph 2.3.3). Figure 64-A shows the difference between the 3D printed parts with the SiC ceramic generated after the conversion. Despite the high linear shrinking of about 21-25% (same for the discs) the parts kept their designed shape for all the preceramics used. No macrocracks or shape distortion were observed. No optical differences were observed between the SiC, SiOC and SiCN ceramics, and all had a dull black color (Figure 64-B), while the C structures showed instead a shiny grey color (Figure 64-C). The size of the samples was almost the same, while the mass was different, both after the conversion and after the various densification cycles.
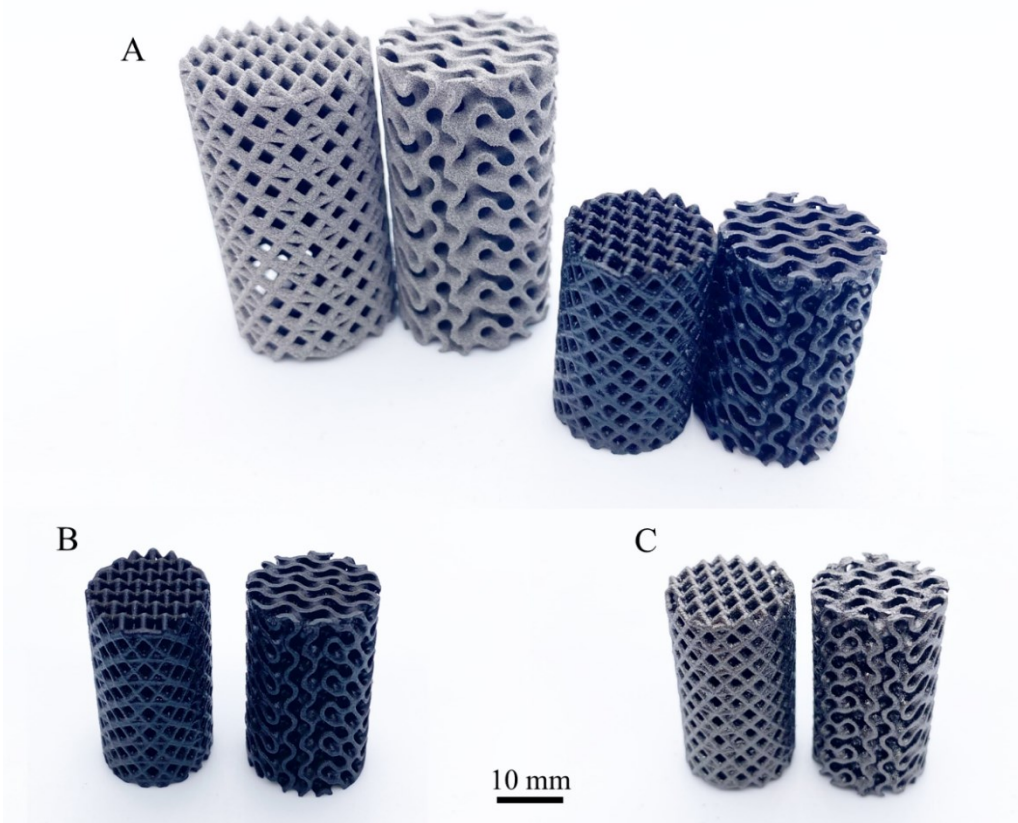
Figure 64. Optical images of the samples after PIP: (A) comparison between the 3D printed sample with the SiC sample after conversion; (B) SiC, SiOC and SiCN samples showed no optical differences, and all were dull black; (C) C sample showed a shiny grey color.

Table 17 reports the measurements performed on the produced ceramic parts. Helium pycnometry and mercury intrusion porosimetry were used to assess the true density, the apparent density and the relative density of the materials. Eight tests were conducted for each material. The mass variation was recorded with a precision balance (0.1 mg resolution).

Polymer-derived ceramic	-	SiC	SiOC	SiCN	C
Preceramic polymer	-	AHPCS	PCSO	PSN	FUR
Ceramic yield of the polymer	%	75	85	87	52
True density (after final pyrolysis)	g/cm^3	2.403	2.301	2.278	1.921
Relative density (1 PIP)	-	0.483	0.534	0.384	0.411
Relative density (2 PIP)	-	0.601	0.702	0.588	0.570
Relative density (3 PIP)	-	0.726	0.831	0.702	0.652
Relative density (4 PIP)	-	0.798	0.925	0.781	-
Apparent density (last PIP)	g/cm^3	1.917	2.127	1.778	1.251
Weight (1 PIP)	g	4.525	3.985	3.370	2.794
Weight (2 PIP)	g	5.638	5.237	5.161	3.881
Weight (3 PIP)	g	6.806	6.199	6.166	4.433
Weight (4 PIP)	g	7.479	6.898	6.855	-
Cumulative weight gain (2 PIP)	%	24.58	31.42	53.15	38.93
Cumulative weight gain (3 PIP)	%	50.39	55.56	82.96	58.66
Cumulative weight gain (4 PIP)	%	65.26	73.09	103.41	-
Diameter	mm	19.48	18.58	19.88	19.17
Height	mm	34.28	33.97	35.15	34.46
Strut diameter of RC	mm	0.850	0.821	0.866	0.839
Surface thickness of GY	mm	0.773	0.747	0.788	0.763
Linear shrinkage (1PIP)	%	22.75	25.33	21.24	23.69

Table 17. Comprehensive data of the experimental measurements on the produced polymer-derived ceramic samples with helium pycnometry and mercury intrusion porosimetry.

The measured true densities (Figure 65-A) were in accordance with the values found in literatures for the same amorphous ceramics[118,120,192,244]. After the first conversion the relative density of the ceramics was different due to (i) the different infiltration rate, which depends on the wettability of the liquid preceramic polymers on the PA12 surface, and (ii) their different ceramic yields. Also, the subsequent infiltrations resulted in a different relative density increase for the same reasons. The linear shrinkage developed only in the first conversion, as expected, leading to the production of cylindrical ceramic samples with ~19 mm diameter and ~34 mm height. The struts diameter and surfaces thickness shrunk accordingly. In subsequent PIP cycles, no shrinking was observed, and the structures maintained their shape and size. The results were better examined thanks to Figure 65.

Figure 65-B-C-D shows the comparison of the relative density, sample weight and cumulative weight gain after each PIP cycle. These charts offered an important comparison with the yield of the preceramics polymers presented in Figure 63. At the first conversion, the SiCN had the lowest relative density (0.384) despite the yield of PSN alone being the highest (87%). This means that probably the infiltration of the PA12 preform with PSN was not efficient due to not good wettability. However, in the subsequent cycles, the SiCN achieved the highest increase in terms of relative density (+50%) and mass (+103%), according to its yield, indicating that PSN had a good wettability on the SiCN surface. After the first conversion, the SiOC sample reached the highest elative density (0.534) due to the high yield of the PCSO (85%) and probably to its good wettability with the PA12 surface. After 4 PIP cycles the increase of relative density and mass were of 42% and 73% respectively. SiOC reached the highest relative density of 0.925. SiC showed a similar behavior to SiOC but with a lower yield. As expected, C showed in general the lowest yield.
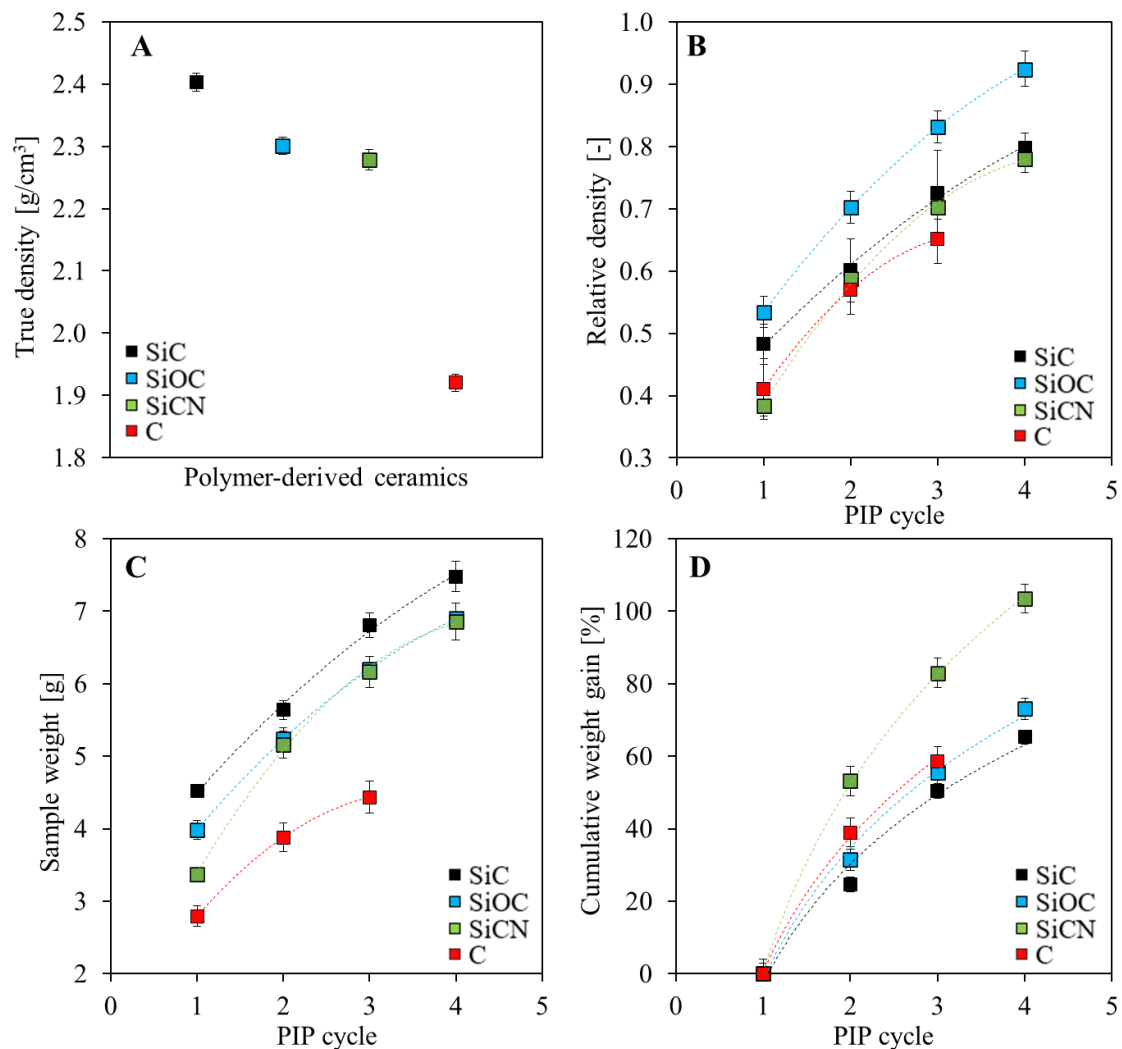
Figure 65. Measurements on the produced polymer-derived ceramic samples: (A) true density; (B) relative density, (C) sample weight and cumulative weight gain (D) as a function of the PIP cycle.

4.3.3 Phases assessment

The phase assemblage of the ceramic parts was investigated on sample powder, using an X-ray diffractometer (D8 Advance, Bruker Italia Srl, Milano, IT) with Cu(kα) radiation, from 10° to 80°, 0.05°/step, 2 s/step. The Match! *S*oftware package (Crystal Impact GbR, Bonn, Germany) was used for a semi-automatic phase identification, supported by data from the PDF-2 database (ICDD-International Centre for Diffraction Data, Newtown Square, PA, USA).

Figure 66 shows the results obtained on the SiC (black curve), SiOC (blue curve), SiCN (green curve) and C (red curve) ceramic samples. The analysis of the phases was difficult due to the absence of crystallinity; indeed, the materials were all totally amorphous. All the measurements agreed with the trends reported in the literature. The phase assemblage of the SiC ceramics (black curve) was comprised by totally amorphous SiC and a very limited amount of graphitic carbon. The phase assemblage of SiOC comprised amorphous carbon and SiO_2. The curve for SiCN was in agreement with the Si_3N_4 record and a slight amount of carbon. C showed the presence of amorphous carbon. Negligible traces of SiO_2 were found in all the ceramics, which can correspond to the SiOC peak (according to literature[192]) produced with the first pyrolysis (see paragraph 2.3.3 for more details).
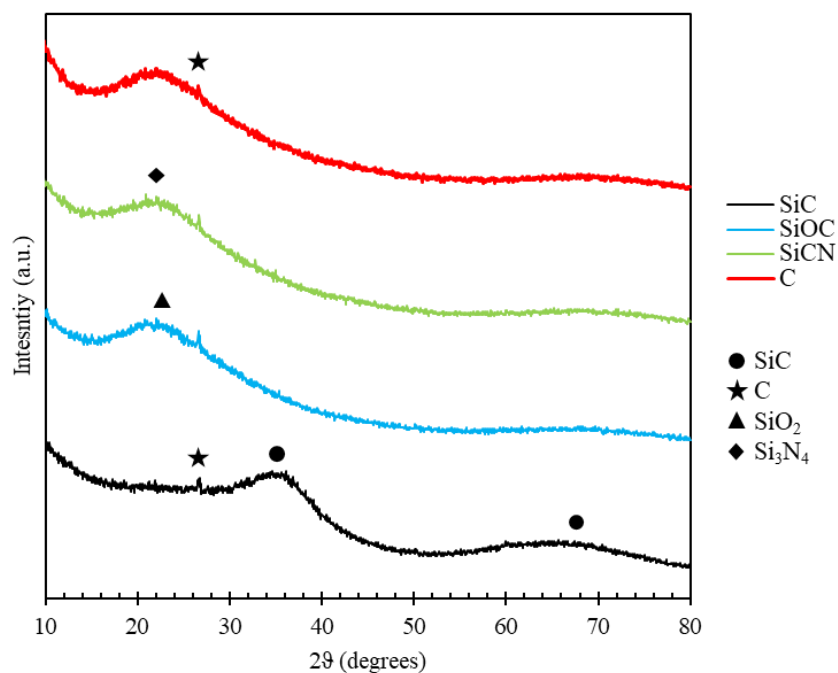
Figure 66. XRD analysis of the polymer-derived ceramic samples: SiC (black curve), SiOC (blue curve), SiCN (green curve) and C (red curve).

4.3.4   Microstructure characterization

Scanning electron microscopy analyses (JSM-6010PLUS/LA, Jeol Ltd., Japan) were conducted to investigate the microstructure of the four ceramic architectures. The samples were fractured, and they were incorporated using a phenolic resin. The surfaces were polished before SEM. The materials were observed after the last PIP cycle. Figure 67 shows the micrographs of the different ceramics. Black/dark grey areas are the pores of the materials. The light grey area is the ceramic phase.
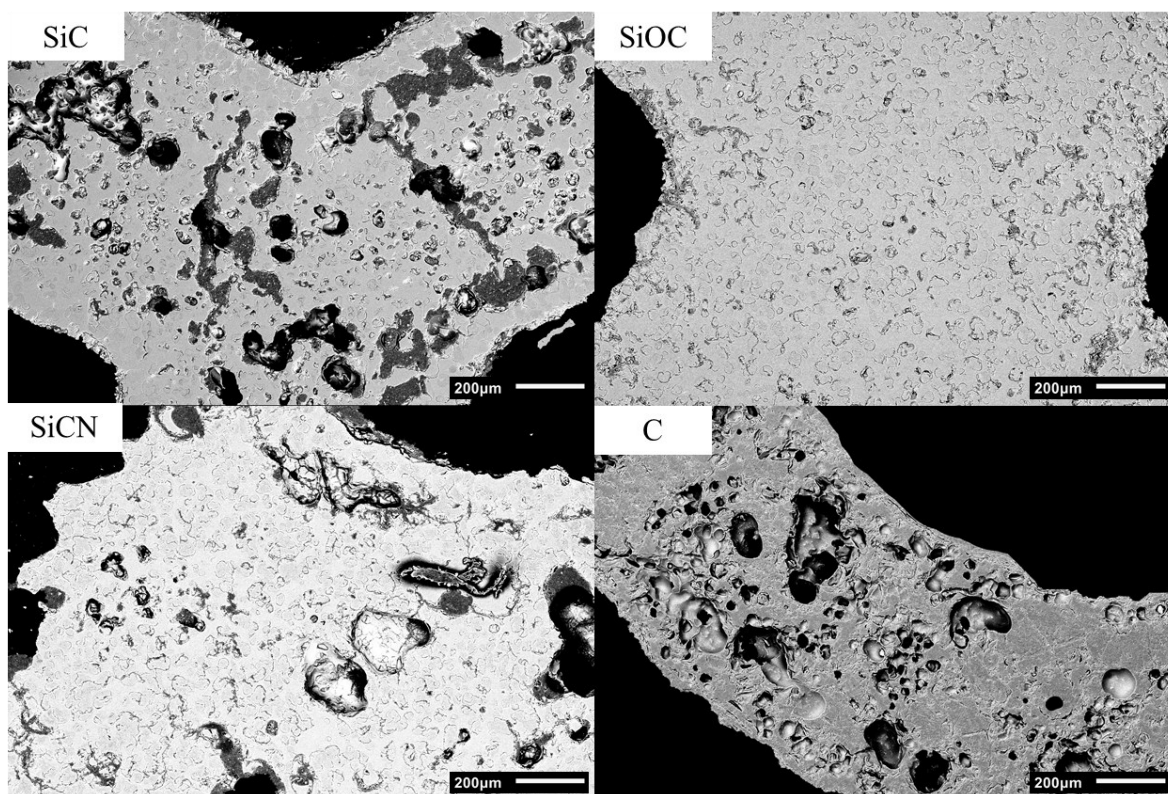
Figure 67. SEM micrographs of the fracture surfaces of the produced polymer-derived ceramics samples.

The SiC ceramics showed high compactness but also a high level of microporosity (Table 18 summarizes the porosity results). Several cracks were observed in the material and pores in the range of 10-100 µm can be detected. The SiOC ceramics after 4 PIP cycles had the highest level of compactness, with an almost fully dense solid phase. The microporosity in the materials was very low with pores of size < 10 µm. The SiCN as well as the SiC samples possessed high porosity. In this case larger pores were occasionally observed in the microstructure. The C ceramics showed the highest level of porosity with pores larger than 100 µm. The microstructure was also characterized by the presence of smaller pores (< 10 µm).

Figure 68 shows the mercury intrusion porosimetry results performed to evaluate the relative density of the parts after each PIP cycle and their pore size and distribution. Analyses were performed by using a pressure range from 0.0014 MPa to 414 MPa.
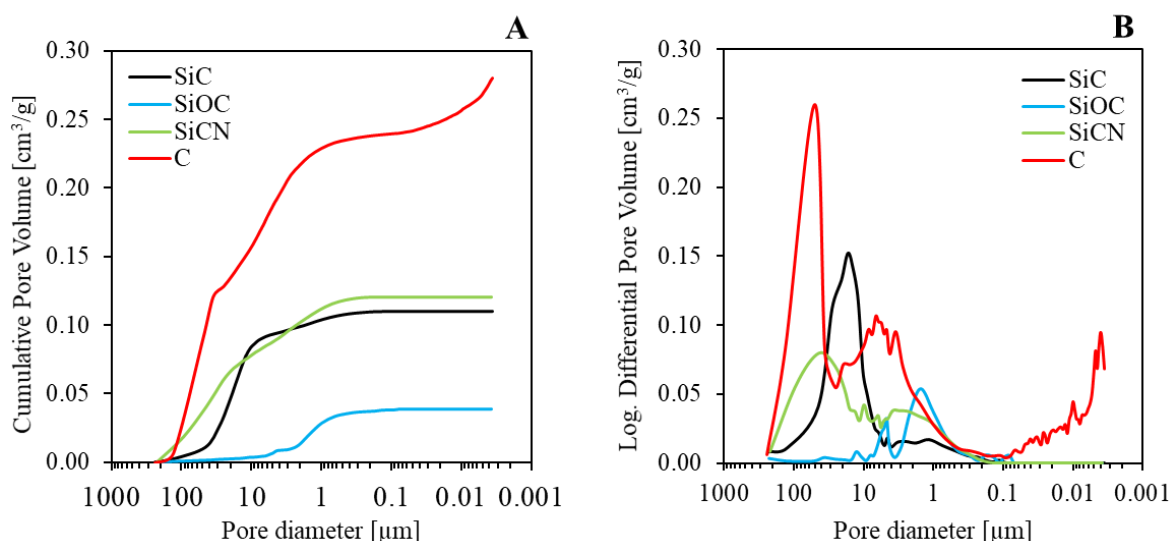
Figure 68. Mercury intrusion porosimetry analysis of the produced polymer-derived ceramics samples: (A) cumulative pore volume and (B) log differential pore volume as a function of the pore diameter.

The MIP analyses confirmed the SEM results. The SiC ceramics (black curve) contained a prevalence of pores in the range of 100 to 10 µm. The high slope in Figure 68-A and the high peak in Figure 68-B showed a large prevalence of 20 µm pores, which corresponds to an interparticle porosity of 17.4%. The SiOC ceramics (blue curve) possessed a bimodal microstructure with several 5 µm pores and a prevalence of smaller pores in the range of 2 to 0.5 µm. The SiCN ceramics (green curve) had pores in the range of 200 to 1 µm. A large prevalence of 50 µm pores corresponds to an interparticle porosity of 16.4% and the total porosity was 22.0%. The C ceramics (red curve) was comprised by a three-modal structure with large pores between 200 and 30 µm (peak at 60 µm), medium pores between 30 and 0.5 µm (peak at 6 µm) and small pores between 0.1 and 0.004 µm (peak at 0.005 µm). Furan resin was the only preceramic polymer used in this work which produced a structure containing nanopores. Table 18 summarizes the porosity results for the four types of ceramic samples produced.

		SiC	SiOC	SiCN	C
Interparticle porosity	%	17.4	2.2	16.4	24.0
Intraparticle porosity	%	2.8	5.2	5.6	10.8
Total porosity	%	20.2	7.4	22.0	34.8

Table 18. Mercury intrusion porosimetry analysis of the produced polymer-derived ceramics samples: interparticle, intraparticle and total porosity.

4.3.5 Mechanical properties

The mechanical strength of the ceramic samples was evaluated through uniaxial quasi-static compression tests (Zwick Z050, Zwick GmbH & Co.KG, Ulm, Germany). Tests were performed at strain rate of 10^{-3} s^{-1} and a cell load of 50 kN (KAP-S, AST, Dresden, Germany) was used to record the reaction force. The cylindrical sample (~19 mm diameter and ~34 mm height) was placed at the center of the plates and pre-loaded with a force of 5 N. Ten samples were tested for each type. Before testing the top and bottom surfaces of the cylinders were machined for flattening. Figure 69 shows the resulting stress-strain curves of the four materials according to the two types of architectures.
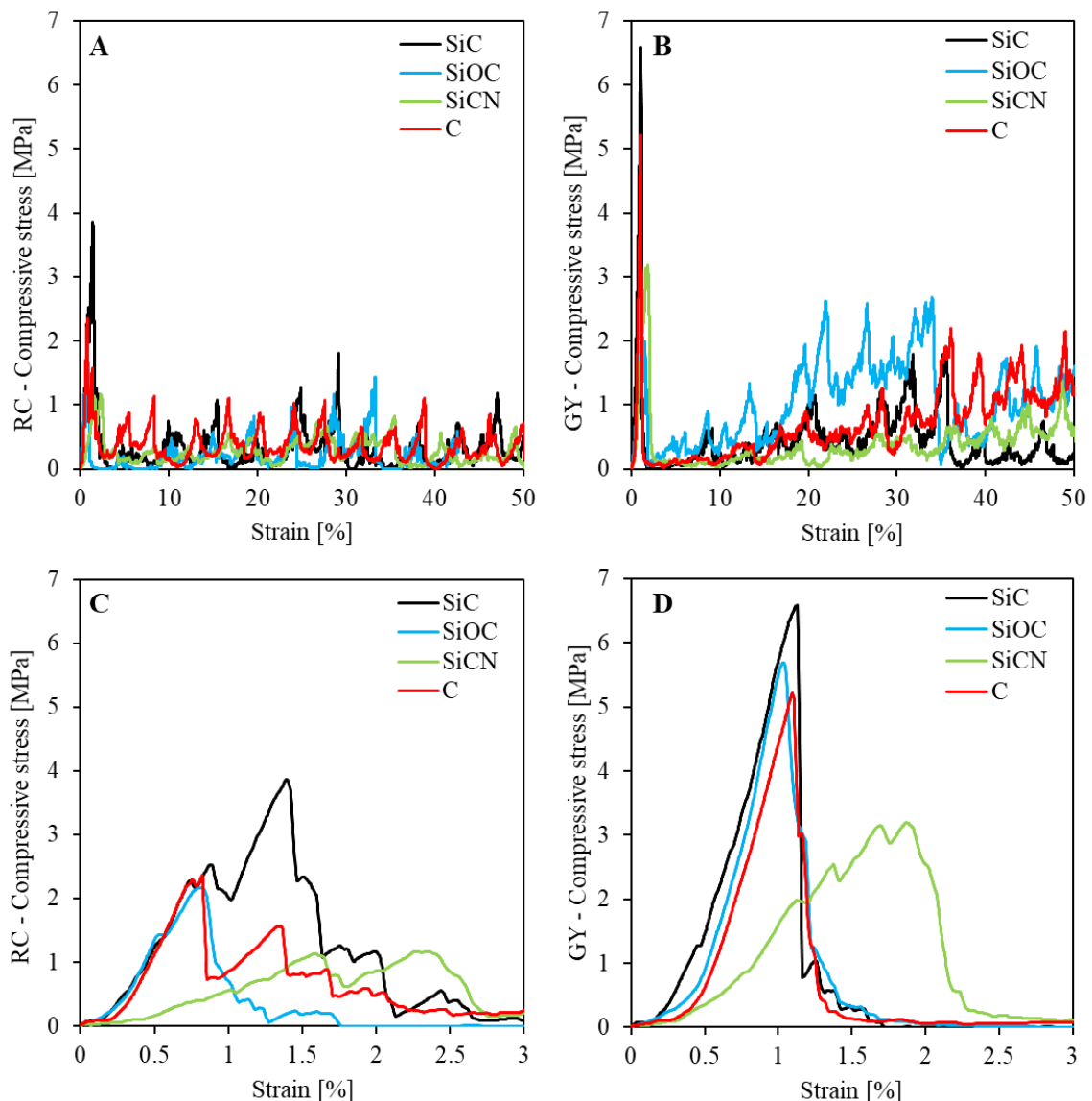
Figure 69. Mechanical compression tests results of the produced SiC, SiOC, SiCN and C ceramics samples. (A-B) Stress-strain curves up to 50% deformation and (C-D) stress-strain curves with a magnification up to 3% deformation for the RC and GY structure respectively.

The trend typical of the cellular structures under compression was observed. Both RC and GY are bending-dominated structures[245–247]. Figure 69-A and -B show that the stress-strain curves for the RC and GY had a similar trend but with different magnitude. Both structures showed the fragile behavior typical of ceramics. At the very beginning of the tests (see higher magnification in Figure 69-C and -D), the maximum stress was reached for all the ceramics at a strain between 0.8% and 2.4%. The SiCN ceramics reached the maximum stress with a higher deformation than the other ceramics. In general, once the first major crack in the architecture was created, it propagated into the various cells of the lattice leading to a stepwise behavior. This means that once the material fractured with the maximum force, it did not collapse but continued to support the load thanks to its cellular structure. This can be seen from the continuous compressive stress that was sustained up to 50% deformation. Considering that between RC and GY of the same material there was no difference in terms of relative density, this allowed to directly compare the two geometries. In general, the geometry of the gyroid supported about twice as much load as the rotated cube. Furthermore, at large deformations (>20%) the GY structure offered greater strength, thus leading to a lower propagation of cracks than for the RC one. Figure 70 helps to understand the fracture behavior of the different architectures. The RC lattice after the first fracture (45° oriented) continued to fragment with a crack propagation at an almost constant rate cell after cell. The crack propagated in the direction of the struts. Instead, the GY after the first fracture (also in this case 45° oriented) continued to support the load and proceeded with a slower crack propagation. In both cases, the collapse of the structure occurred by propagation of the initial crack through the cells of the structure, and indeed the cells remained intact in the opposite side of the fractured part.
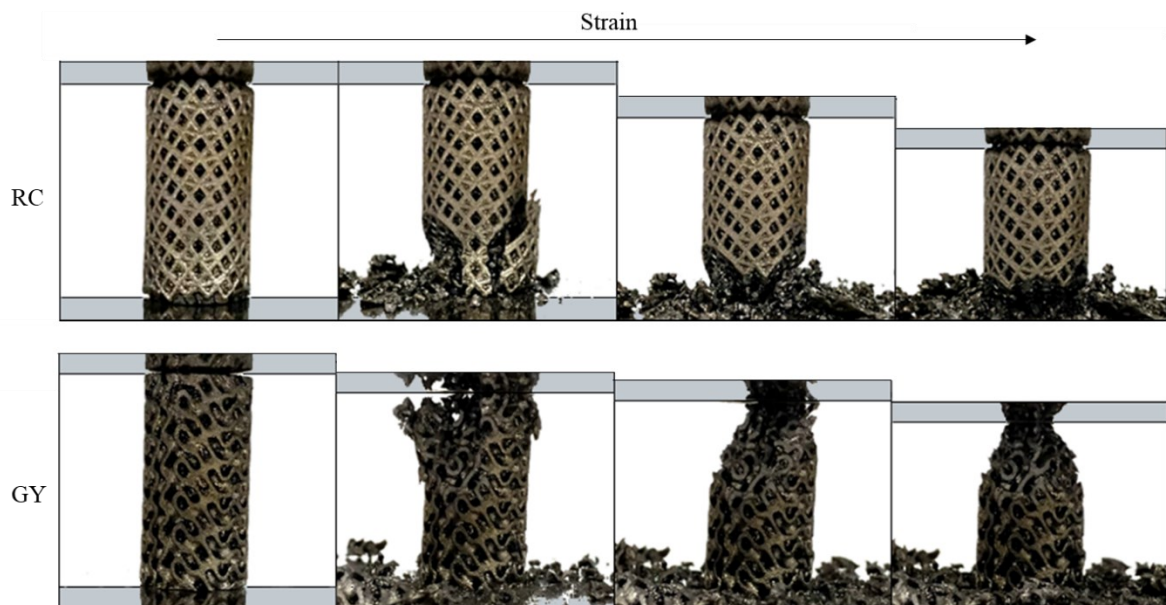
Figure 70. Optical views during the compression tests at increasing strain rate of the polymer-derived SiC ceramic samples of the RC and GY architectures.

Figure 71-A and -B show the comparison of the produced materials and structures in terms of maximum compressive strength against their true density and relative density. Results showed that there is not a direct relation between the compressive strength with the true density and relative density. This means that the quality and type of the produced phase played the main role in the mechanical performances. The principal example is the C ceramic, which were produced with one PIP cycle less than the other samples. It had a 17% lower true density and 30% lower relative density than SiOC, but it possessed about the same compressive strength for both architectures. The C ceramic samples had also a 50% and 38% higher strength with respect to the SiCN ones for the RC and GY respectively. The SiC ceramics had the highest strength of 3.7 ± 0.2 MPa and 7.1 ± 0.5 MPa for the RC and GY respectively. In general, the sample with the GY architecture showed a higher compression strength than the RC ones, due to the presence of a continuous surface which is structurally less fragile, and better supports the load with respect to thin struts.
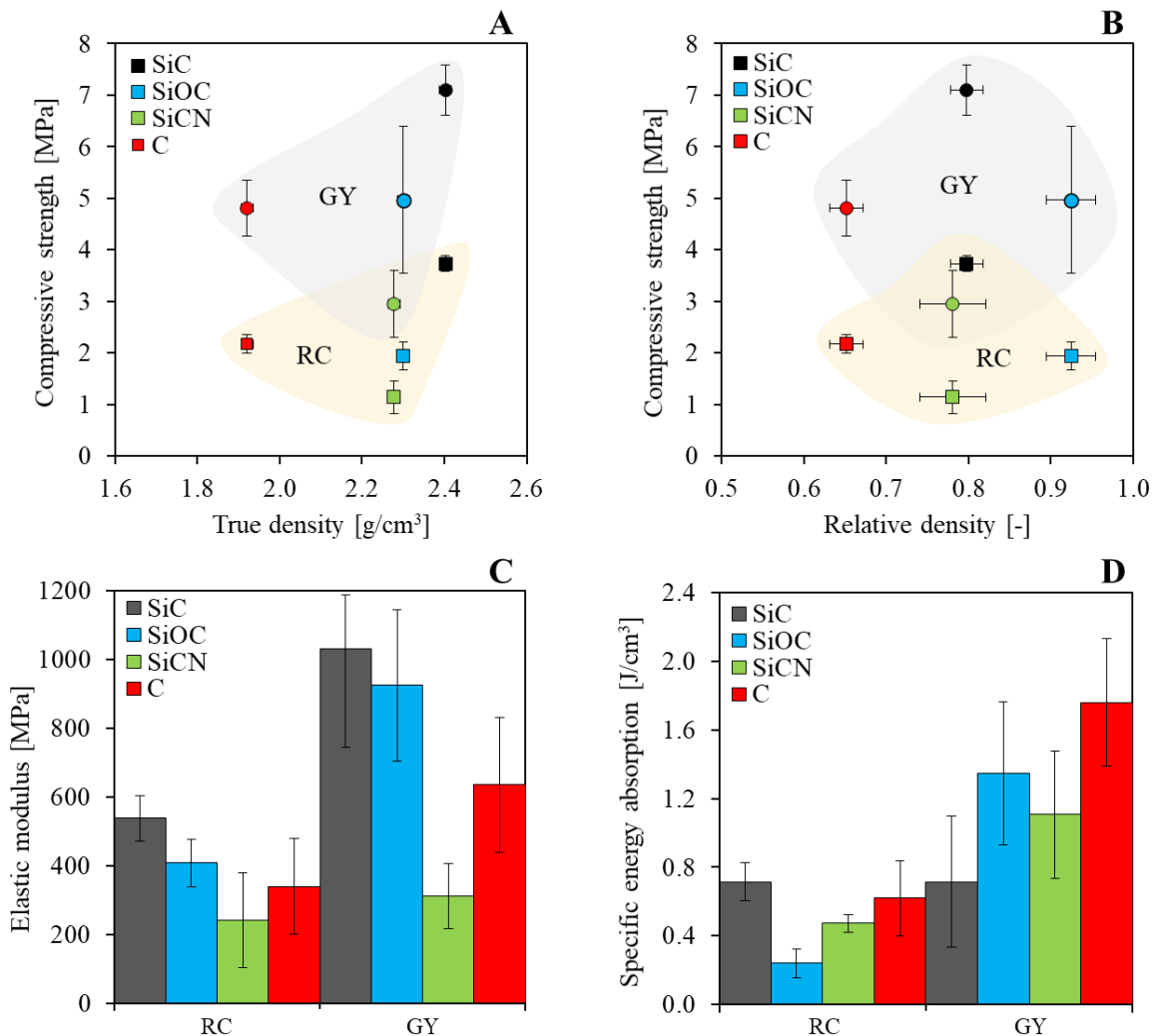
Figure 71. Mechanical compression test results for the produced SiC, SiOC, SiCN and C samples. (A-B) Maximum compressive strength against the true density and the relative density. (C-D) Estimated elastic modulus and specific energy absorption for the different materials and architectures.

Figure 71-C shows the estimation of the elastic modulus for the produced ceramics and architectures. The measurement of the elastic modulus for ceramic materials is very complex due to their fragile nature. For this reason, the data shown are an estimation and are useful only to compare the structures. The calculation is based on the slope of the stress-strain curve before the break. The large error bars can be attributed to the random cracking of the lattice cells. The values of the elastic modulus had, to a great extent, a similar trend as that of the strength plot. In general, the modulus of the GY structures was double that of RC, except for the SiCN ceramics which were similar. Considering that the relative density was the same for the two architectures of the same ceramics, the results means that the geometry of the lattice played an important role on the mechanical performance. The trend showed that the SiC ceramics had the highest value of 538 MPa and 1031 MPa for the RC and GY respectively. The SiCN showed the lowest values.

Figure 71-D shows the specific energy absorption of the different materials and architectures. The calculation of the integral in the stress-strain curve was performed up to 50% of the strain. The large error bars can be attributed to the random cracking of the lattice cells, and this behavior is more evident for the GY structures. As expected, in general the GY structure absorbed higher energy with respect to the RC of the same materials, in accordance with strength and modulus, except for the SiC architectures which absorbed the same energy, meaning that for this ceramic there was no influence of the geometry on the energy absorption (at the same relative density). The SiOC ceramics had the most significant influence of the architecture on the energy absorbed, with a 550% times increase from RC to GY. The maximum specific energy of 1.759 J/cm^3 was absorbed by the C gyroid, because of its nanopores structure (pores acted as a block for the crack propagation).

Table 19 summarizes the data of the compression tests of the ceramic samples.

Arch.	Material	Maximum load	Compressive strength	Elastic modulus	Specific energy absorption (ε=50%)
[-]	[-]	[N]	[MPa]	[MPa]	[J/cm^3]
RC	SiC	953 ± 281	3.7 ± 0.2	538 ± 66	0.716 ± 0.113
	SiOC	551 ± 76	1.9 ± 0.3	408 ± 69	0.241 ± 0.084
	SiCN	360 ± 92	1.1 ± 0.3	241 ± 138	0.474 ± 0.052
	C	621 ± 38	2.2 ± 0.2	340 ± 140	0.621 ± 0.219
GY	SiC	1924 ± 321	7.1 ± 0.5	1031 ± 156	0.716 ± 0.380
	SiOC	1361 ± 356	5.0 ± 1.4	925 ± 220	1.346 ± 0.415
	SiCN	932 ± 216	3.0 ± 0.6	311 ± 95	1.106 ± 0.372
	C	1378 ± 152	4.8 ± 0.5	635 ± 197	1.759 ± 0.369

Table 19. Comprehensive data of the compression tests results of the SiC, SiOC, SiCN and C samples.

4.3.6   Oxidation tests

The oxidation of SiC ceramics at high temperature proceeds following two different behaviors. Passive oxidation (Eq. 24) in which a layer of silicon dioxide forms on its surface and it occurs at oxygen partial pressures around one bar. The SiO_2 dense layer on the surface of SiC acts as an anti-oxidation protective layer[248,249]. The other mechanics is active oxidation (Eq. 25) in which a loss of mass is observed at pressures lower than one bar due to the formation of a gaseous phase of SiO[250].

The oxidation chemistry of SiOC ceramics involves a weight loss (Eq. 26) and also produces a weight gain (Eq. 24)[251,252]. Additionally, the carbothermal reduction and decomposition of the SiOC ceramics occurs according to Eq. 18, Eq. 19 and Eq. 20.

The oxidation of SiCN ceramics comprises formation of silicon nitride, silicon carbide and carbon (Eq. 27). Also, Si_3N_4 reacts with oxygen and forms a silicon oxynitride scale, which further oxidizes and converts into SiO_2 (Eq. 28 and Eq. 29)[240,253–255]. The produced SiC can further reacts according to Eq. 24 and Eq. 25.

The oxidation of C ceramics (and the residual free carbon present in the other ceramics) at high temperature proceeds according to Eq. 26.

$$2\ SiC\ (s) + 3\ O_2\ (g) \rightarrow 2\ SiO_2\ (s) + 2\ CO\ (g) \qquad \textit{Eq. 24}$$

$$2\ SiC\ (s) + O_2\ (g) \rightarrow SiO\ (g) + CO\ (g) \qquad \textit{Eq. 25}$$

$$C\ (s) + O_2\ (g) \rightarrow CO_2\ (g) \qquad \textit{Eq. 26}$$

$$Si_3N_4\ (s) + 3C\ (s) \rightarrow 3SiC\ (s) + 2N_2\ (g) \qquad \textit{Eq. 27}$$

$$4Si_3N_4\ (s) + 3O_2\ (g) \rightarrow 6Si_2N_2O\ (s) + 2N_2\ (g) \qquad \textit{Eq. 28}$$

$$2Si_2N_2O\ (s) + 3O_2\ (g) \rightarrow 4SiO_2\ (s) + 2N_2\ (g) \qquad \textit{Eq. 29}$$
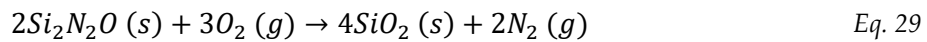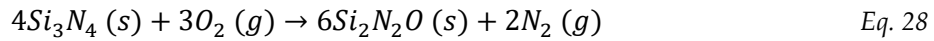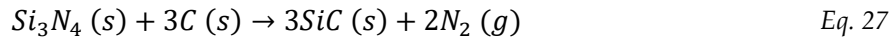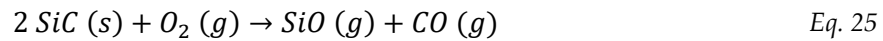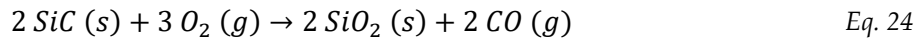
During oxidation, discerning between the reactions or the extent to which one or another takes place is not a trivial matter. One cannot assess to what extent each of these reactions has proceeded from only an analysis of the weight change upon oxidation. Furthermore, residual free carbon is present in all the materials (according to XRD analysis in Figure 66) and its reaction (Eq. 26) can have an important role in the oxidation.

Oxidation tests were performed at 1500°C in steady air in a standard furnace (LHT 08/18, Nabertherm GmbH, Germany) for 1, 2 and 4 hours cumulatively. The heating rate was 20°C/min. Between each oxidation cycle at high temperature, samples were weighted with a precision balance (0.1 mg resolution) to record mass variations.

Figure 72 shows the test results in terms of weight change against the oxidation time.
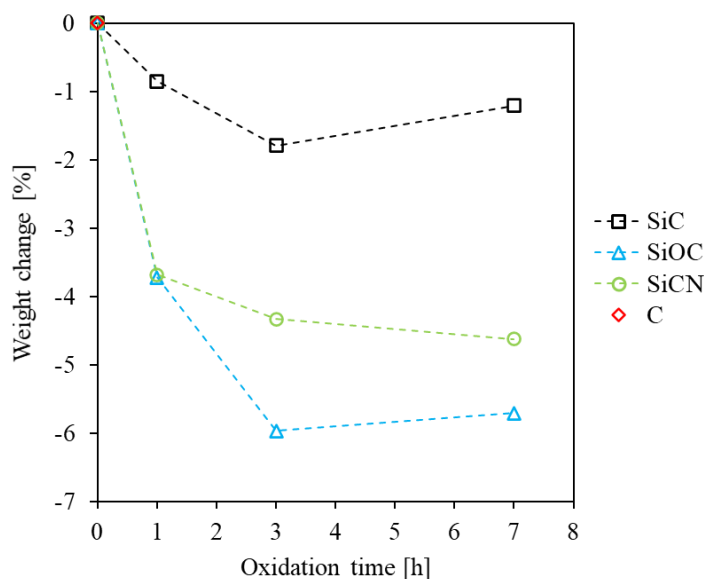
Figure 72. Oxidation tests of the polymer-derived ceramic samples at 1500°C for 1h, 2h and 4h cumulatively: weight change against the oxidation time. The C ceramics completely disappears after 1 hour of oxidation.

In general, the weight loss of the polymer-derived ceramics produced in this work had similar results with the literature, which shows a limited weight loss[251].

All the ceramics suffered a mass loss already after the first hour of oxidation and C ceramics completely disappeared due to CO_2 formation. The same behavior was observed after 3 hours but with a lower loss rate for all the cases. Then after 7 hours SiC and SiOC ceramics produced a slight weight gain while the SiCN mass loss increased. The data suggest that the mass gain or loss was due to the rates of oxidation of the excess carbon versus the oxidation of the main ceramic phase (SiC, SiOC and SiCN). Probably, initially the carbon oxidation initially predominates for its presence on the surface, leading to a higher mass loss. The SiOC ceramics possessed the highest content of C (according to Figure 66) and thus the highest loss with respect to SiC and SiCN. In addition, it probably suffered carbothermal reduction. After 7 hour, a silica-like surface formed on the SiOC produced an increase of mass. The SiC ceramics showed the best oxidation resistance probably due to a lower content of residual carbon and the formation of a passivating silica barrier at the surface of the material (Eq. 24). This silica layer slowed diffusion of oxygen into the bulk and, therefore, inhibited oxidation from proceeding rapidly throughout the entire material. The SiCN mass loss continued according to the reactions in Eq. 24 to Eq. 29.

In general, these very slight variations in mass suggested a very high resistance to oxidation of the materials produced. However, further investigations are needed to confirm the results, such as by using a larger mass of materials for testing (to increase the surface area for the oxidation), XRD, SEM and Raman spectrometry before and after the oxidation to evaluate the oxidation products.

Figure 73 shows the optical images and the micrographs of the polymer-derived ceramics before and after the oxidation at high temperature. The optical images of the non-oxidazed samples (0h) were taken from other fractured pieces and they are not the same piece as the oxidized ones. The C ceramics derived from the furan resin was not included in the figure due to its complete decomposition.

An optical difference between the initial samples with respect the oxidized samples was observed, with the latter ones having a grey color of the surface. High magnification imaging allowed to assess that this color was due to the formation of glassy components on the surface (the above mentioned SiO_2 layer). This formation was more evident in SiC and SiOC, in accordance with their mass gain.
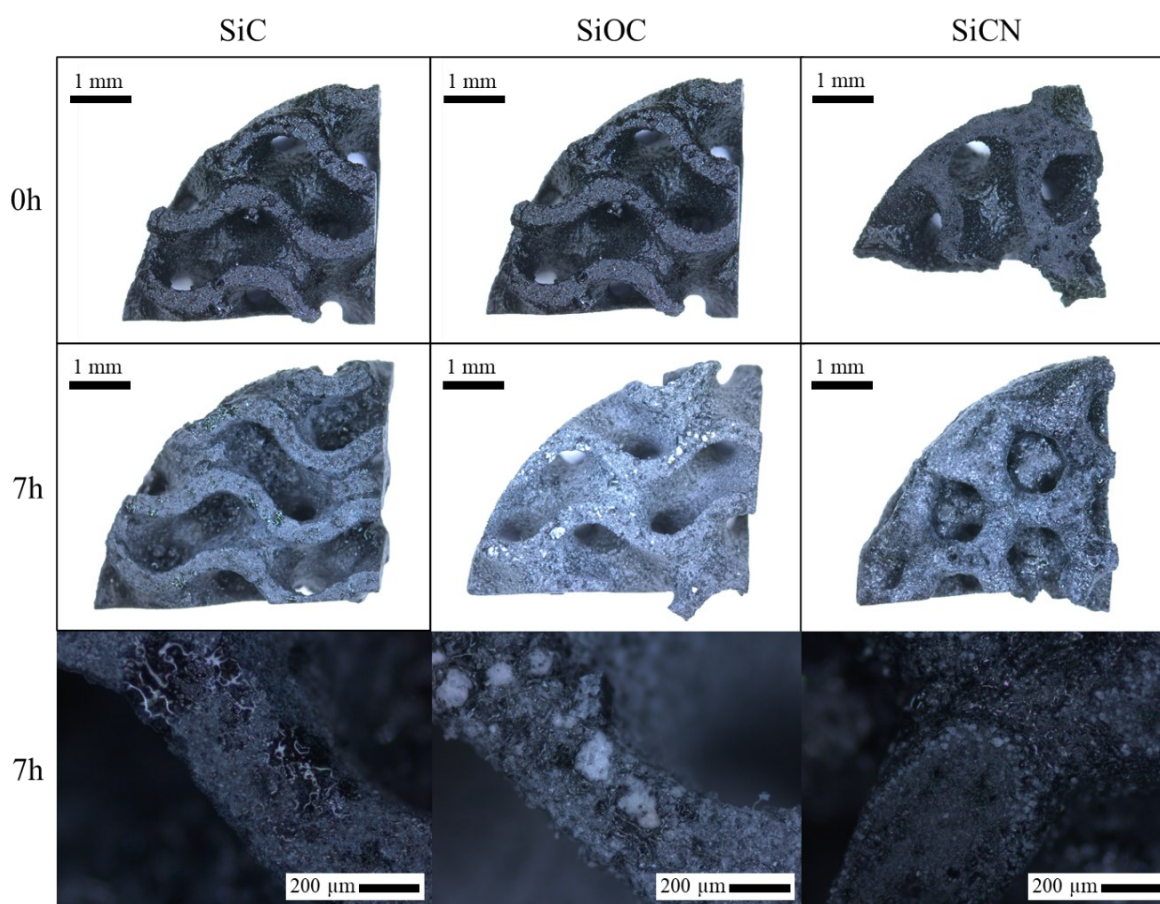
Figure 73. Optical images and micrographs of the polymer-derived ceramic samples before and after 7 hours of oxidation at high temperature.

4.4   Liquid Silicon Infiltration

The final densification was performed with liquid silicon infiltration at high temperature. Several preliminary LSI tests were performed using the same conditions presented in the paragraph 2.4.1. Non-complete infiltrations were obtained and then an optimization of the LSI treatment for processing complex-shaped architectures was performed. SiC ceramics after 4 PIP cycles were used for this experimental campaign.

4.4.1   Optimization of the thermal treatment

Three different parameters were varied to find the best thermal cycle for LSI:

- The maximum temperature was increased from 1600°C to 1800°C. The crystallization of the polymer-derived ceramics and its shrinking increase according to the temperature. Moreover, the SiOC decomposition can lead to higher porosity and the silicon infiltration could benefit. The temperature increasing does not affect the silicon because it melts at > 1414°C.

- The maximum temperature was hold for 1h and 3h, to see if the time at high temperature can have an influence on the microstructure (it is known from the literature that the infiltration takes place in seconds).

- The silicon grains mass was set to 100% and 120% of the sample weight.

Figure 74 shows the optical images of the RC and GY architectures produced using different parameters combination for the silicon infiltration thermal cycle. Higher magnifications of the red boxes are present in the center of the figure. Before LSI, a thermal treatment at the same temperature was performed for 1h to obtain the crystallization of the ceramics and to open the porosity for the subsequent silicon infiltration (paragraph 2.4.1 for details).
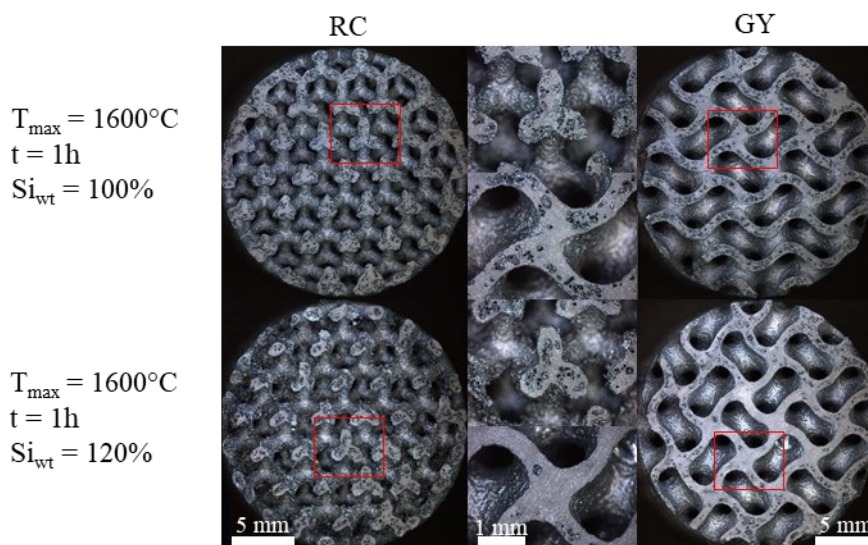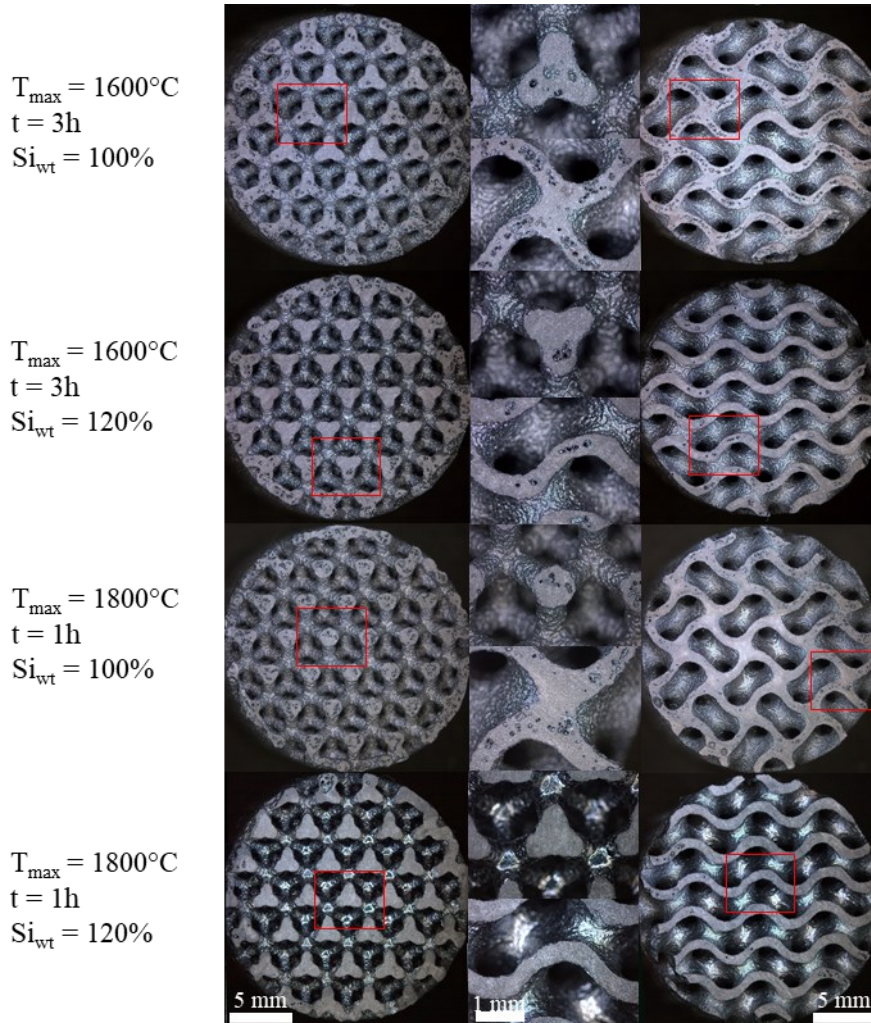
Figure 74. Optical images of the Si-infiltrated ceramic samples produced with different thermal cycles. T_{max} is the maximum temperature. t is the time at maximum temperature. Si_{wt} is the weight% of silicon grains used with respect to the samples weight.

The optical images showed no macrocracks formation for all the experiments. The first cycle (1600°C for 1h with 100%wt of Si) produced high level of porosity in the material both for RC and GY structures. An increase in the Si content produced a higher densification in the central zone, but not in the external regions, especially for the GY structure. The two methods were replicated with 3 hours of infiltrations at 1600°C resulting in an improvement, but not to a full densification of the materials. The tests at 1800°C for 1 hour with 100 and 120%wt of Si produced the best results. Especially with 120%wt of Si, the full densification of the materials was achieved for both the structures. This test campaign allowed to assess that the temperature increasing had the higher influence on the infiltration, allowing to open pores for the complete infiltration by the silicon. Also, the use of higher Si content with respect to the sample weight produced better results. Longer infiltration time did not appear to have a notable influence to justify such a long and onerous high-temperature treatment.

Figure 75 shows the same results obtained with the SEM analysis. The samples were fracture, incorporated with phenolic resin (large and dark gray areas) and then the surface was polished for the observation. The black areas are the pores not filled with the resin. The light grey area is the silicon, and the faceted grey shapes are the silicon carbide crystals.

The micrographs confirmed that the fully infiltrated material was obtained at 1800°C for 1 hour with 120%wt of Si. The expectation to observe smaller crystals at 1800°C has not been confirmed. Indeed, the size of the crystals appeared similar in all cases. This means that the increase in temperature does not have a direct effect on the shrinkage of the crystals. Rather it influenced the decomposition of the SiOC phase, indeed in the 1800°C case less ceramic phase was observed. Therefore, it can be said that the increase in temperature allowed the decomposition of more SiOC phase which produced more porosity useful for the silicon to fully infiltrate the part.
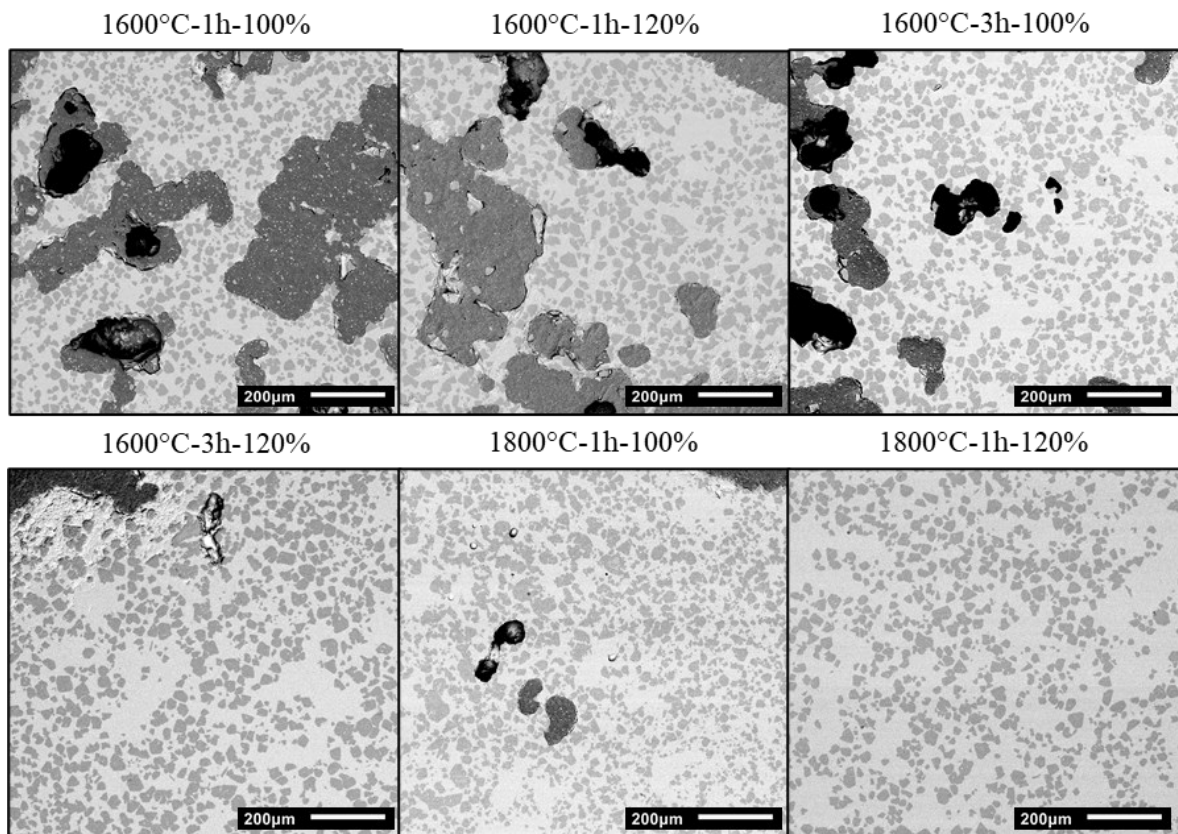
Figure 75. SEM micrographs of the Si-infiltrated ceramic samples produced with six different thermal cycle at high temperature. Samples were fractured, incorporated, and polished to observe the fracture surface. The light grey area is the silicon, and the faceted grey forms are the silicon carbide crystals. The large and dark gray area is the resin used to incorporate the parts and the black area is the porosity not filled by the resin.

The crystallization of the SiC phase at the two temperatures can be observed also with higher magnification thanks to Figure 76. The light grey area is the silicon, and the dark grey areas are the silicon carbide.

With the treatment at 1800°C, a greater uniformity in the size of the crystals was noted. The βSiC crystals were almost all the same size, while in the case of 1600°C, they had very different sizes. Moreover, a notable faceting of the crystal surfaces was observed with more regularity at 1800°C. As expected, this result indicated that the increase of the temperature allowed for higher crystallization. A common note seen in all micrographs was a sort of boundary of the crystals which was analyzed via EDX analysis in Figure 76-C. The analysis was repeated on several samples to avoid measurement and observation errors, such as reflections. An analysis of the content was performed along the blue line. The red lines show the content result respectively for carbon and silicon. As expected, in the SiC phase there was high presence of carbon and silicon, while in the Si phase there was almost only silicon. A gradient of the respective elements was observed in the boundary. This is probably due to the formation and precipitation of the SiC crystals into the silicon matrix, and to the non-completion of this process. No useful study was found in the literature; therefore, this effect will need to be better investigated in future work.
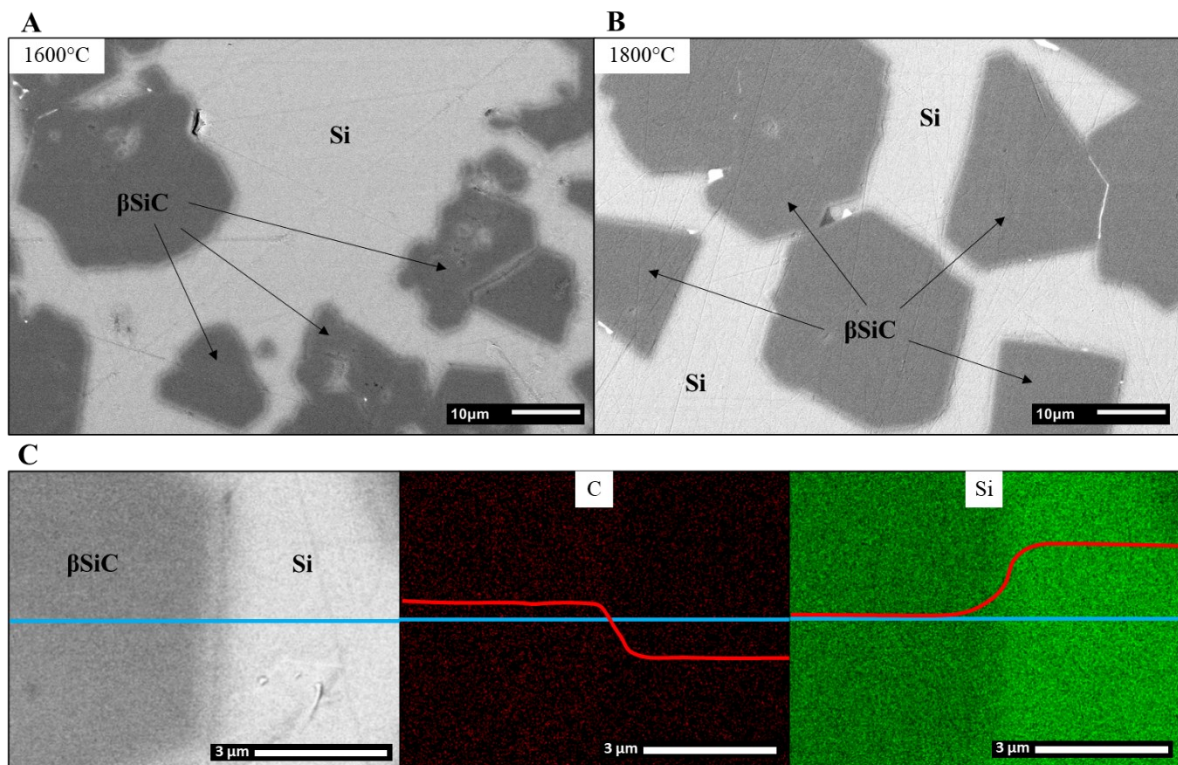
Figure 76. SEM micrograph with high magnification of the βSiC crystals into the Si matrix after thermal treatment at (A) 1600°C and (B) 1800°C. The light grey area is the silicon, and the dark grey areas are the silicon carbide. (C) EDX mapping of the boundary of a βSiC crystal after heating at 1800°C. Gradients in carbon and silicon content were detected.

The samples after the different thermal treatments were weighted and measured to evaluate the differences. The gain in weight was about 100-105% in any case, without significant correlations with the method. The diameter and height of the samples suffered a shrinkage of about 2-5%. Table 20 shows the results in terms of dimensions of the struts for the RC structure and thickness of the surface for the GY structures. In general, the struts and the surfaces suffered a thickening of 10%. A high concentration of Si was found in the boundary of the strut and surfaces, and therefore measurements were affected by the uneven surfaces. As expected, with the thermal treatment at 1800°C the struts and surfaces were thinner. This was probably due to the high phase shrinkage and SiOC decomposition which reduced the occupied volume. The effect was accentuated with the GY structure with suffered only a 2% thickening while the RC 10%, with respect to the initial sizes.

	RC – Strut diameter [mm]	GY – Surface thickness [mm]
SiC after 4 PIP	0.850 ± 0.012	0.773 ± 0.019
1600°C-1h-100% and 120%	0.955 ± 0.034	0.860 ± 0.021
1600°C-3h-100% and 120%	0.930 ± 0.010	0.875 ± 0.028
1800°C-1h-100% and 120%	0.940 ± 0.020	0.765 ± 0.049

Table 20. Measure of the strut and surface dimensions after silicon infiltration with different cycles.

Figure 74 shows the lateral-external surface of the cylindrical samples for both architectures produced with thermal treatment at 1800°C for 1 hour with 120%wt of Si. This cycle was selected as the optimum one for the final infiltrations. Despite the shrinking, the samples maintained their pristine shape and topology, with constant thicknesses and without macrocracks or defects.
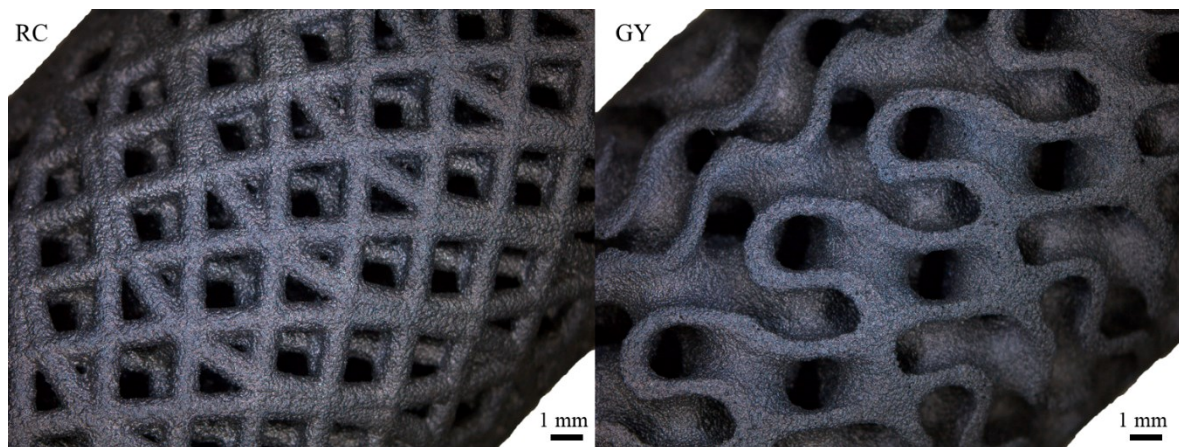
Figure 77. Optical images of the Si-infiltrated ceramic samples produced with silicon infiltration at 1800°C for 1h and with 120%wt of silicon.

4.4.2 Final densification

The final densification was performed via liquid silicon infiltration employing the optimized thermal cycle. Samples underwent two cycles at the same conditions: the first for the thermal treatment without silicon infiltration and the second one with the liquid silicon infiltration. A heating rate of 20°C/min was set from T_{amb} to 1500°C and then 15°C/min up to 1800°C. The final temperature was hold for 1h. The cooling to T_{amb} was set to 20°C/min. The pressure of the chamber was hold at 5 mbar (P_{abs}) and for safety reasons a slight argon flow rate of 1 L/min was imposed.

A further purpose of this stage was to increase the industrial interest of the materials in terms of density and mechanical strength. <u>The practical objective was to increase the SiC content in the material with respect to the Si phase</u>. Four different strategies were adopted to produce different Si-βSiC ceramics:

SiC + Si → SiC matrix was produced with 5 PIP cycles (p_{rel} = 0.841) of AHPCS, and then LSI was performed (the same method used for the discs).

C + Si → C matrix was produced with 3 PIP cycles (p_{rel} = 0.670) of FUR and then LSI was performed. The aim was to obtain βSiC by the reaction of the amorphous carbon generated by the PIP with the Si (called reaction bonded silicon carbide or RB-βSiC).

SiC + C + Si → SiC+C matrix was made by combining 4 PIP of AHPCS and 1 of FUR. 4 PIP (p_{rel} = 0.798) of AHPCS were performed to obtain the amorphous SiC matrix. A thermal treatment at 1800°C was done to crystallize the βSiC and to open the porosity (p_{rel} = 0.372). Then one PIP cycle (p_{rel} = 0.720) of FUR was performed to obtain free amorphous carbon into the βSiC matrix. The SiC+C ceramics was then infiltrated with molten silicon. The objective was to obtain two βSiC phases: one produced from the AHPCS and the other generated from the reaction of the free carbon with the Si (RB-βSiC).

SiC + Gr + Si → SiC+Gr matrix was produced with only 1 PIP cycle (p_{rel} = 0.501) with AHPCS and graphite powder (d90: 12.6 μm. d50: 6.2 μm. TIMREX KS 10, Imerys, Bodio, Switzerland). The graphite powder was mixed (13%wt) with the AHPCS liquid polymer and used for the infiltration of the 3D printed preform. The LSI was performed to obtain two βSiC phases: one produced from the AHPCS and the other generated from the reaction of the graphite powder with the Si (RB-βSiC). Graphite was chosen for its high reactivity with silicon.

Before LSI, all the materials were subjected to thermal treatment at 1800°C for 1h. The motivation for the thermal treatment were explained in the paragraph 2.4.1. Figure 78 shows the mercury intrusion porosimetry analysis of the architectures after 4 PIP cycles at 960°C (amorphous SiC, black curves), and the same architectures after the thermal treatment at 1800°C (βSiC, yellow curves). As expected, the thermal treatment produced a large increase of the material porosity. The large pores in the range of 100-10 μm were present in both microstructures in the same quantity and size. The clear difference is the generation of smaller pores due to the crystallization and shrinking of the βSiC phase, and to the SiOC decomposition (see paragraph 2.4.1). The microstructure was comprised by a prevalence of very small pores in the range of 0.3-0.05 μm. The total porosity of the SiC sample was of 20.2%, and the one of the βSiC samples was of 62.8% available for the subsequent silicon infiltration.
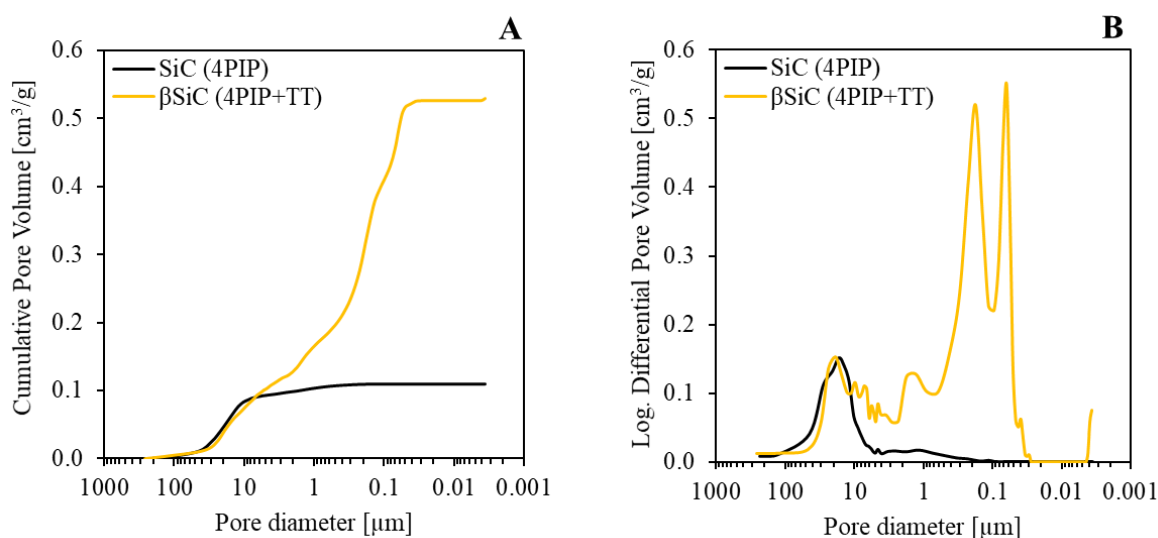
Figure 78. Mercury intrusion porosimetry of the SiC ceramic samples before (black curve, 4 PIP) and after heating at 1800°C for 1h (yellow curve, 4PIP+TT). Cumulative pore volume and log differential pore volume against the pore diameter.

Figure 79-A and -B show the optical images of the SiC architectures after the last PIP cycles compared with the Si-βSiC structure after LSI. The samples maintained their pristine shape and no macrocracks or distortion were observed. A linear shrinkage of about 2-5% was observed. Figure 79-C shows other two structures made by C+Si and SiC+C+Si, which showed no significant difference between each other and the SiC+Si. All the samples were dull grey. The SiC+Gr+Si ceramics showed an optical difference due to a shiny grey surface and a dimensional difference with much less thick strut and surfaces (see Figure 80 and Table 21). Figure 79-D shows the example of a βSiC gyroid architecture after the thermal treatment at 1800°C. The pristine shape of the sample was maintained and a linear shrinkage of 2.5% was observed. Also, a light grey/yellow surface color was visible. All the measurement of the produced Si-infiltrated ceramics are reported in Table 21.
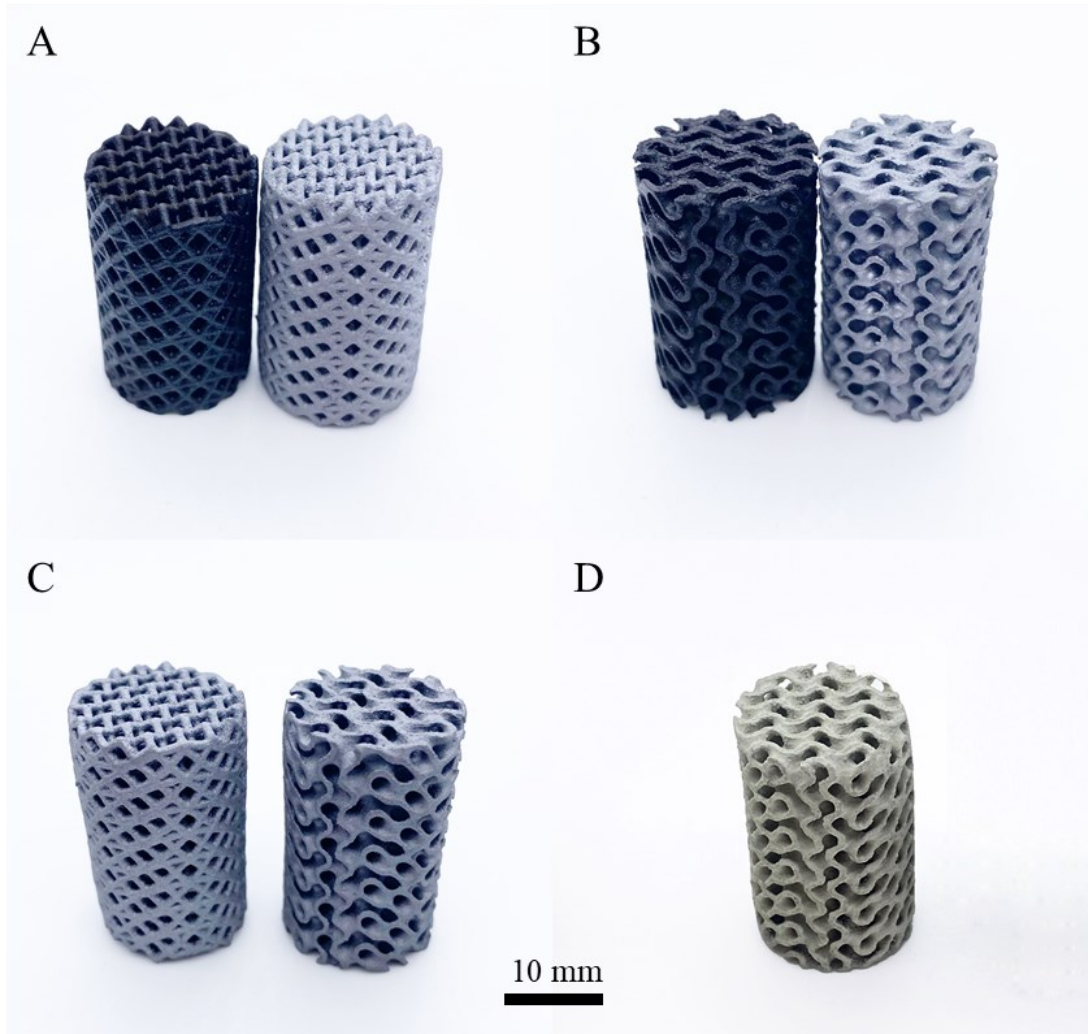
Figure 79. Optical images of the samples after LSI. (A-B) Comparison between the SiC sample after PIP with the Si-βSiC sample after LSI for the RC and GY respectively. (C) C+Si and SiC+C+Si samples showed no optical differences, and all were dull grey. SiC+Gr+Si difference is evaluated in Figure 80. (D) Example of a βSiC gyroid sample after the thermal treatment at 1800°C (4PIP+TT).

Figure 80 shows the micrographs of the SiC+Si and the SiC+Gr+Si ceramics architectures produced. The SiC+Si ceramics showed surfaces of the gyroid with a thickness of 0.765 ± 0.049 mm. The same value was measured in the cross-section surface (A) and in the external surface of the cylinder (B). The SiC+Gr+Si ceramics showed very different thickness of the gyroid surface. In the cross-section surface (C) the thickness was 0.475 ± 0.035 mm (53% lower). The surface thickness of the SiC+Gr+Si ceramics in the external surface of the cylinder (D) was 0.185 ± 0.022 mm (92% less than the original surface thickness). This difference could be attributed to a much higher porosity in the external surfaces of the lattice. The two materials had different surface thickness due to the different number of PIP cycle perform for the densification of the ceramic matrix before the LSI. The SiC+Si ceramics underwent 5 PIP cycles reaching a relative density of 0.841, while the SiC+Gr+Si ceramics underwent only one PIP cycle with a final relative density of only 0.501.

The <u>notable result</u> was the possibility to produce Si-βSiC with only one PIP cycle (AHPCS + graphite) followed by LSI, maintaining the pristine shape of the lattice (same diameter and height) but reducing the thickness of the surfaces from 53% to 92%. Furthermore, the SiC+Gr+Si ceramics had the higher relative density (0.957 ± 0.035) with respect to the other produced ceramics (see Table 21). This manufacturing approach, in addition to save time and production costs by reducing the number of PIP cycles, allows to produce complex Si-βSiC structures with wall thickness < 0.5 mm, which cannot be achieved with other AM techniques on the market (binder jetting and direct ink writing above all).
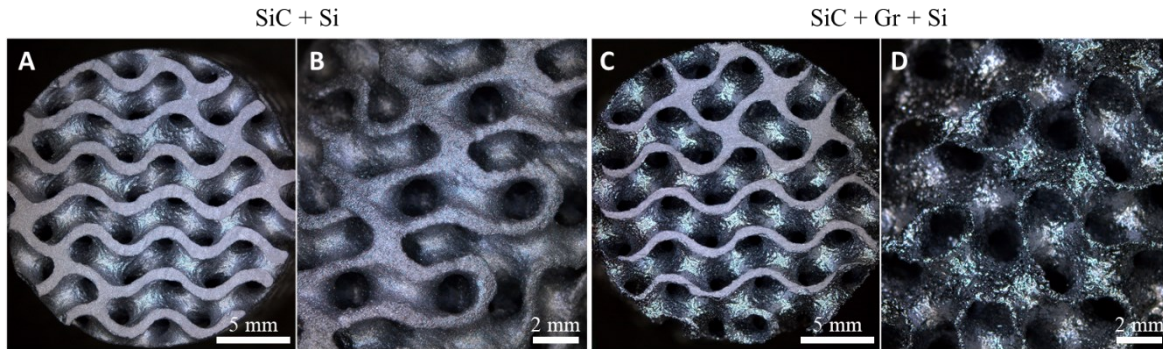
Figure 80. Micrographs of the SiC+Si samples (A-B) in comparison with the SiC+Gr+Si samples (C-D).

Table 21 reports the measurements of the produced ceramics after LSI. Helium pycnometry was used to assess their true density, apparent density, and relative density. Eight runs were carried out for each material.

		SiC + Si	C + Si	SiC + C + Si	SiC + Gr + Si
Weight	g	10.13 ± 0.72	11.00 ± 0.93	10.05 ± 0.34	8.07 ± 1.09
Gain in weight	%	102 ± 11	147 ± 17	80 ± 7	99 ± 19
Diameter	mm	19.26 ± 0.13	19.12 ± 0.13	18.23 ± 0.39	19.69 ± 0.49
Height	mm	31.92 ± 0.22	34.48 ± 0.17	32.58 ± 0.17	35.79 ± 0.20
Strut diam. of RC	mm	0.940 ± 0.020	0.918 ± 0.040	0.840± 0.010	0.575 ± 0.035
Surf. thick. of GY	mm	0.765 ± 0.049	0.835 ± 0.054	0.724 ± 0.089	0.475 ± 0.035
Linear shrink	%	2.45 ± 0.30	1.68 ± 0.38	4.99 ± 0.97	3.28 ± 1.29
True density	g/cm³	2.845 ± 0.050	3.005 ± 0.031	3.173 ± 0.022	2.686 ± 0.045
Apparent density	g/cm³	2.694 ± 0.112	2.519 ± 0.080	2.966 ± 0.047	2.571 ± 0.090
Relative density	-	0.947 ± 0.042	0.838 ± 0.032	0.935 ± 0.016	0.957 ± 0.035
Residual porosity	%	5.32 ± 4.16	16.19 ± 3.18	6.52 ± 1.58	4.26 ± 3.48
βSiC (from AHPCS)	vol%	0.59 ± 0.09	-	0.38 ± 0.03	0.24 ± 0.04
RB-βSiC	vol%	-	0.77 ± 0.03	0.58 ± 0.03	0.17 ± 0.04
Si (+C)*	vol%	0.41 ± 0.09	0.23 ± 0.03	0.04 ± 0.03	0.59 ± 0.04

Table 21. Comprehensive data of the experimental measurements on the produced Si-infiltrated ceramic samples.

* The estimation of the βSiC volume fraction was carried out using Eq. 17, and assuming that the density of the residual graphite and carbon was like the one of silicon (2.329 g/cm³). This means that the Si volume fraction can also include residual C and graphite, if present. The graphite has a density of 2.267 g/cm³, which is about the same of silicon. The polymer-derived amorphous carbon had a density of 1.921 g/cm³ after PIP (see Table 17), and the increase in temperature may have produced an increase in its density. Literature studies showed that a sort of polycrystalline graphite structure gradually can appear at temperatures above 1500°C[256–258]. Therefore, also the density of the residual carbon phase after LSI can be assumed similar to the one of silicon.

Figure 81-A shows the true density against the relative density of the produced ceramics, and Figure 81-B shows the volume fraction of βSiC and Si (+C). The higher true density value was obtained by the SiC+C+Si, meaning that the free C reacted very well with Si, producing an additional SiC phase. The total amount of βSiC was estimated of 96%. The C+Si ceramics produced a high true density despite the relative density was the lower. This can be attributed to the generation of βSiC from the reaction of C with Si, which during infiltration produced a clogging of the pore channels and left several pores inside the material. However, in the solid phase, the SiC content was of 77%. The SiC+Si ceramics resulted in similar true density, relative density and volume fractions of the same material of the discs (see paragraph 2.4.1). The lower true density and higher Si content was observed in the SiC+Gr+Si ceramics. This was due to the low content of SiC derived from only one PIP with AHPCS, and to the low amount of graphite added to the infiltrating solution, which not allowed to produce a considerable volume of additional SiC phase. However, this ceramic had the higher relative density.
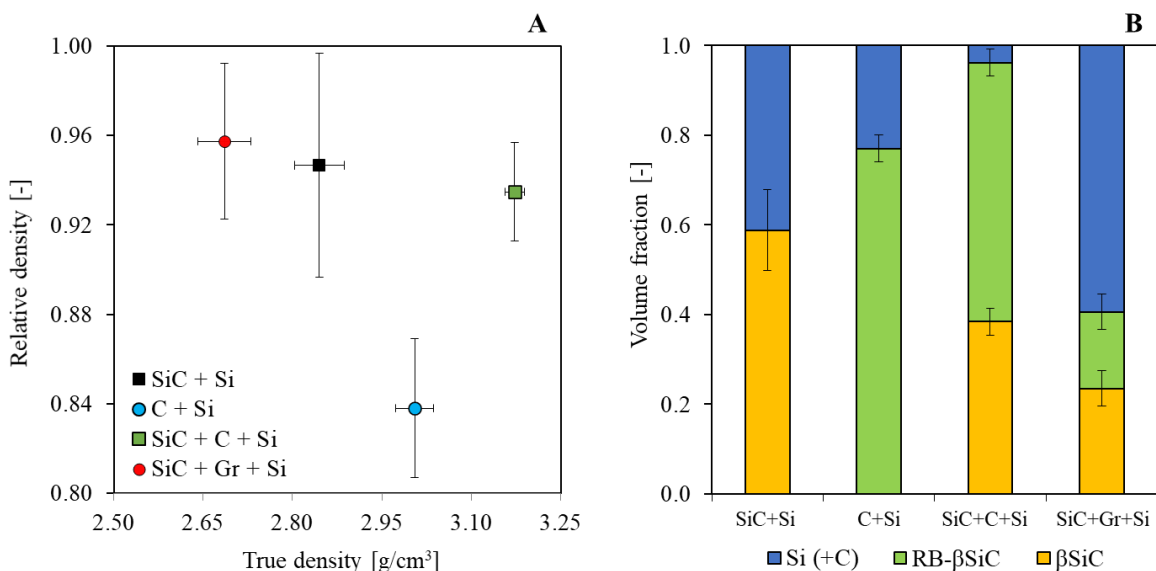
Figure 81. Measurements on the produced Si-infiltrated ceramic samples: (A) true density against the relative density measured with a helium pycnometry; (B) volume fraction of Si and βSiC.

4.4.3   Phases assessment

The phase assemblage of the Si-infiltrated ceramics was investigated on the sample powder, using an X-ray diffractometer with Cu(kα) radiation, from 10° to 80°, 0.05°/step, 2 s/step. The Match! *S*oftware package (Crystal Impact GbR, Bonn, Germany) was used for a semi-automatic phase identification, supported by data from the PDF-2 database (ICDD-International Centre for Diffraction Data, Newtown Square, PA, USA). Figure 82 shows the results obtained. The phase assemblage of the SiC+Si (black curve) showed the full crystallized βSiC and the presence of large quantity of Si, besides slight graphitic carbon. The amorphous SiC was eliminated from the sample after Si infiltration. The result confirmed the one obtained for the SiSiC discs (see Figure 42). The phase assemblage of the C+Si (blue curve) was comprised by the presence of lower amount of Si, much more graphitic carbon, and a different crystalline type of the βSiC (with respect to the SiC+Si ceramics). Probably, this was the difference between the βSiC derived from the AHPCS (SiC+Si case) and the RB-βSiC generated by the reaction between amorphous carbon and silicon (C+Si case). The higher magnification of Figure 82-B shows the additional SiC peaks at 34°, 36°, 38°, 44° and 58°. They are typical of an α-SiC, even if the formation temperature of this ceramic is higher than 2000°C, or they are due to stacking faults[259,260] produced by preceramic polymers conversion (βSiC-2 in Figure 82). As expected, the phase assemblage of the SiC+C+Si (green curve) was comprised by a very low amount of Si, slight graphitic carbon and both βSiC phases described above. The well crystallization of the βSiC and its large volume fraction is visible. The phase assemblage of the SiC+Gr+Si (red curve) comprised both βSiC phases, slight graphitic carbon, and a large amount of Si.
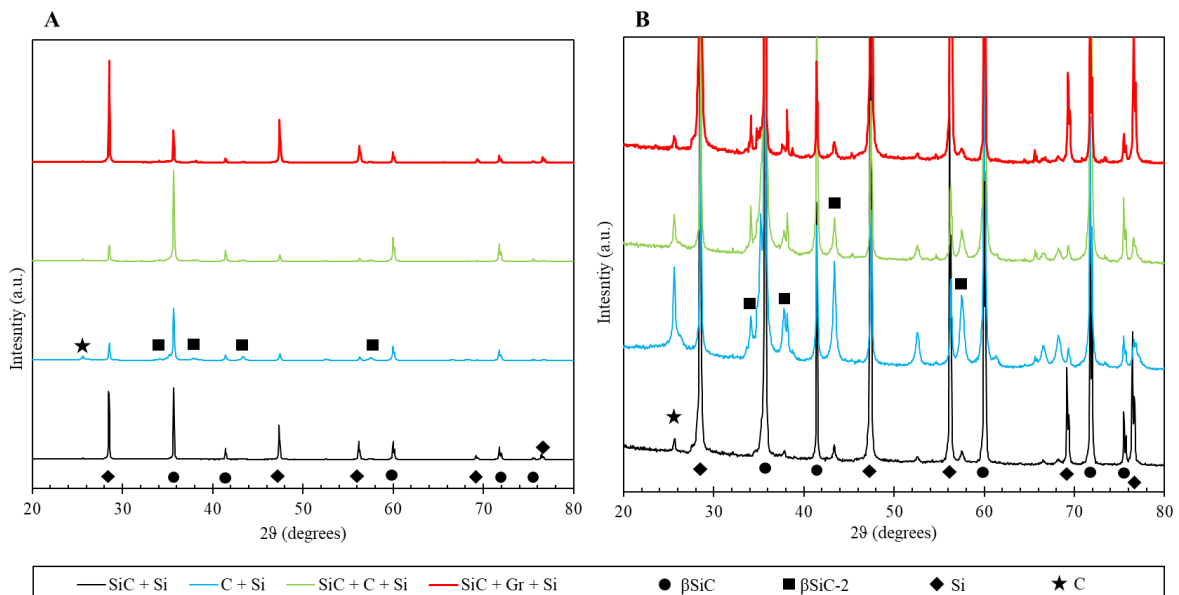
Figure 82. XRD analysis of the Si-infiltrated ceramic samples: SiC+Si (black curve), C+Si (blue curve), SiC+C+Si (green curve) and SiC+Gr+Si (red curve).

4.4.4 Microstructure characterization

Figure 83 shows the SEM analyses with different magnification of the produced Si-infiltrated ceramics. The samples were fracture and incorporated with phenolic resin. The surface was then polished for the observation with the microscope.
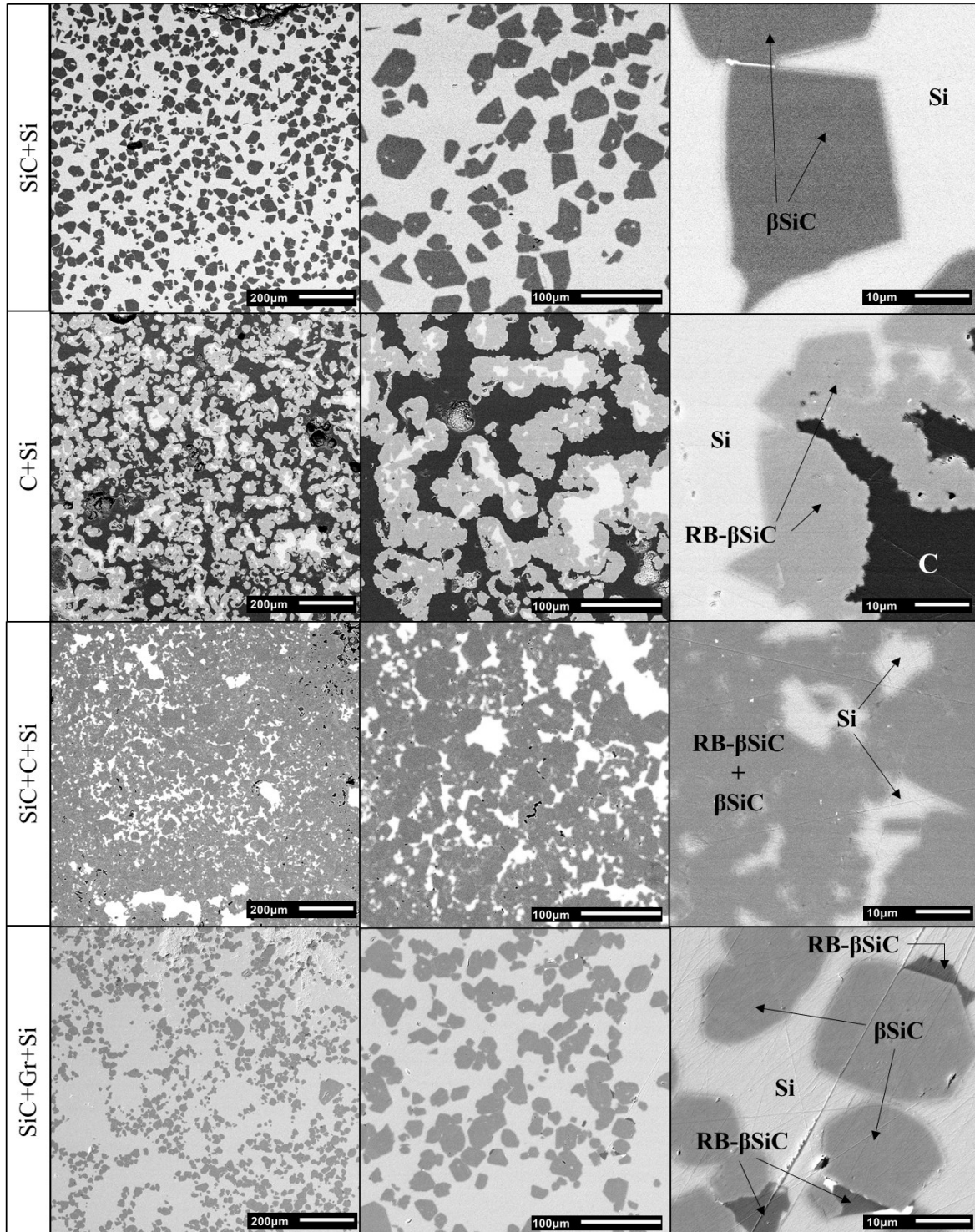
Figure 83. SEM micrographs with different magnifications of the produced Si-infiltrated ceramic samples.

The SiC+Si micrographs showed a nearly fully dense material with the only presence of silicon (light grey areas) and beta silicon carbide (dark grey areas) as expected. The high presence of silicon was visible. The full crystallization of the amorphous SiC matrix into the βSiC phase and the faceting of the crystals' boundary is visible. The volume fractions for βSiC and Si were of 59% and 41% respectively for this material.

The C+Si micrographs showed the presence of silicon (light grey area) and βSiC (dark grey area). The black area is the resin used to incorporate the material and an undistinguishable small amount of residual carbon. As expected, the residual silicon was always surrounded by the SiC phase. This demonstrates that during infiltration, the silicon reacted with the amorphous carbon and produced the reaction bonded βSiC, with a volume increase typical of this reaction. The silicon that could not reach the carbon surface became trapped into the formed SiC matrix (or SiC layer). Furthermore, 16% of porosity was trapped into the material leading to an incomplete infiltration. This was due to the clogging of the infiltration channels by the formed SiC on the C surface. In an ideal infiltration, all the silicon should react with all the carbon to form βSiC, and leave no residue and no porosity. The notable result was the possibility to obtain a continuous arrangement of crystals to form a sort of βSiC layered matrix, while in the SiC+Si case the crystals formed individually and separately. The micrographs showed that a large quantity of βSiC was produced during the infiltration. Figure 84 shows the EDX of the C+Si ceramics.
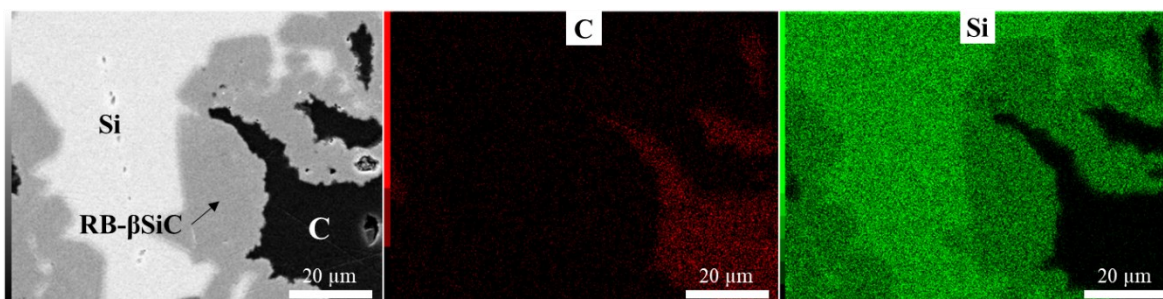
Figure 84. EDX mapping of the C+Si ceramic samples. Only carbon and silicon were present in the composition.

The SiC+C+Si micrographs showed a combined microstructure between the previous ones. In this case, the large amount of βSiC is visible (dark grey areas) with respect to the silicon phase (light grey areas). Two βSiC phases were formed: one βSiC directly derived from the preceramic polymer, and another derived from the reaction between the carbon and the silicon during infiltration (RB-βSiC). These two phases were not distinguishable with SEM. However, the notable result was the production of a nearly fully dense part with 96% of βSiC and only 4% of residual silicon.

The SiC+Gr+Si micrographs showed three phases: the high presence of residual silicon (light grey areas), the βSiC (dark grey areas) derived from the precursor and the RB-βSiC (black areas) derived by the reaction between the silicon and the graphite powder. In this case the high quantity of residual silicon (59%) was justified by the only one PIP cycle performed for this material. The ceramic before LSI had a porosity of about 50%. The notable result is that after LSI the porosity was only 4%, so the lowest obtained between the four cases. The βSiC formed by the AHPCS conversion was clearly visible in higher quantity (24%) with respect to the RB-βSiC (17%) which was probably covered by the high presence of silicon. The composition of the different SiC ceramics was assessed by EDX with points analysis as shown in Figure 85. No appreciable differences were observed between the two SiC produced in terms of composition.
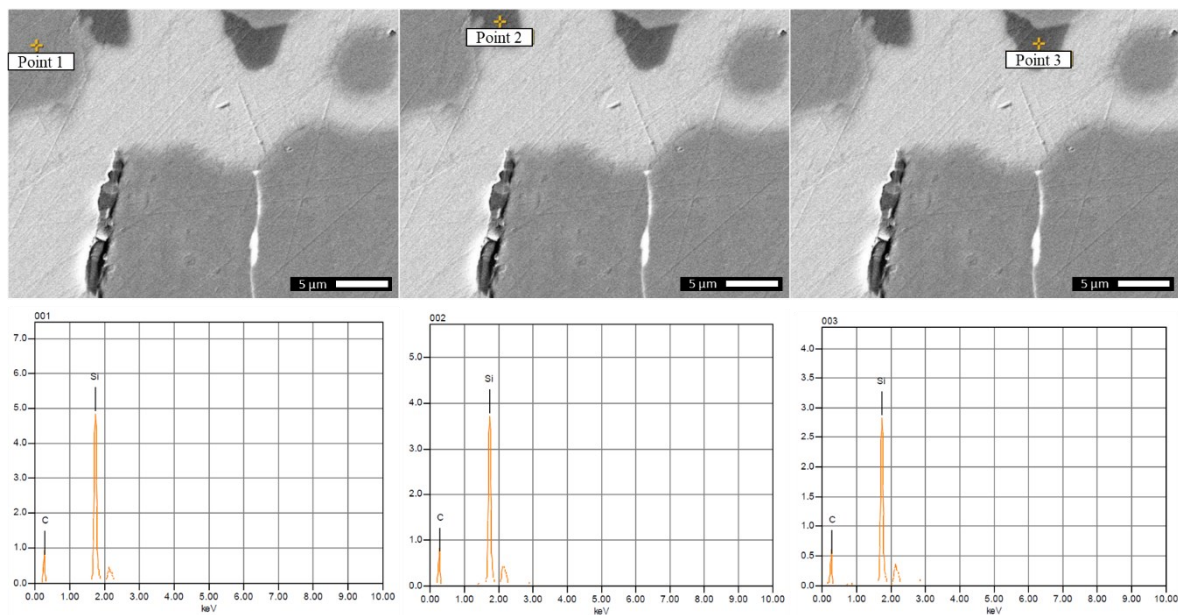
Figure 85. EDX analysis of the SiC+Gr+Si ceramic samples: assessment of the SiC phases by using points analysis.

Table 22 shows the composition of the SiC phases in terms of atom% of the three points analyzed in Figure 85.

Element	Point-1	Point-2	Point-3
-	Atom%	Atom%	Atom%
C	79.68	81.40	80.66
Si	20.32	18.60	19.34

Table 22. EDX points analysis of the SiC+Gr+Si ceramic samples: carbon and silicon atom% of the SiC phases.

4.4.5 Mechanical properties

The mechanical strength of the ceramic samples was evaluated through uniaxial quasi-static compression tests (Zwick Z050, Zwick GmbH & Co.KG, Ulm, Germany). Tests were performed at strain rate of 10^{-3} s^{-1} and a cell load of 50 kN (KAP-S, AST, Dresden, Germany) was used to record the reaction force. The cylindrical sample (~19 mm diameter and ~33 mm height) was placed at the center of the plates and pre-loaded with a force of 5 N. Ten samples were tested for each type. Before testing the top and bottom surfaces of the cylinders were machined for flattening. Figure 86 shows the resulting stress-strain curves of the four materials according to the two types of architecture.
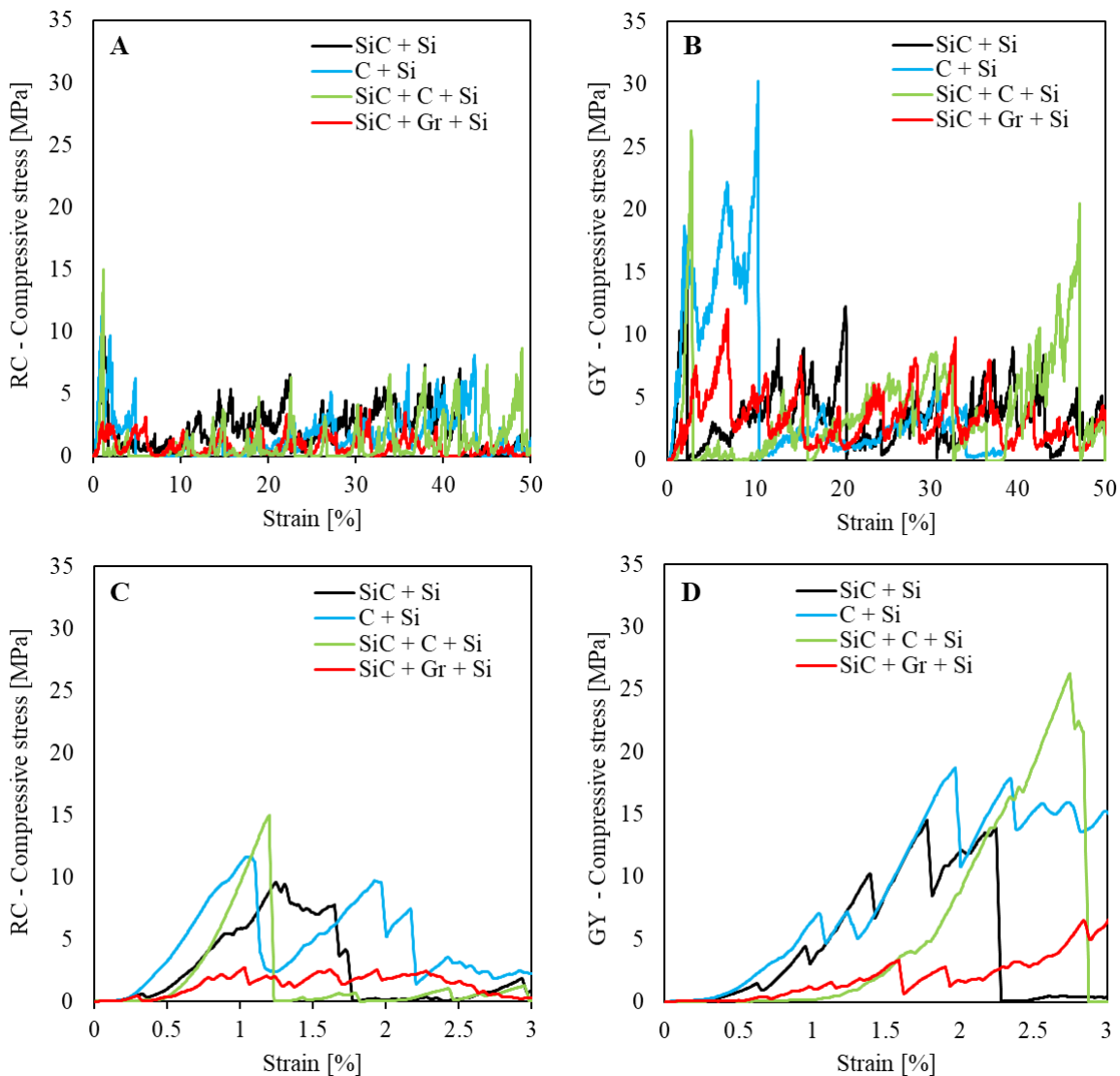
Figure 86. Mechanical compression tests results of the produced Si-infiltrated ceramic samples. (A-B) Stress-strain curves up to 50% deformation and (C-D) stress-strain curves with a magnification up to 3% deformation for the RC and GY structures respectively.

Figure 86-A and -B show that the stress-strain curves for the RC and GY had a similar trend but with different magnitude. At the very beginning of the tests (see higher magnification in Figure 86-C and -D), the maximum stress was reached for all the ceramics at a strain between 1% and %. Except for the SiC+Si ceramics which reached the maximum stress with a higher deformation (10%) than the other ceramics. In general, once the first major crack in the architecture was created, it propagated into the various cells of the lattice leading to a stepwise behavior. As for the PIP ceramics, the material did not collapse after the first fracture but continued to support the load thanks to its cellular structure. This can be seen from the continuous compressive stress that was sustained up to 50% deformation. Considering that between RC and GY of the same material there was no difference in terms of relative density, this allowed to directly compare the two geometries. In general, the geometry of the gyroid supported about twice as much load as the rotated cube. Furthermore, at large deformations (>20%) the GY structure offered greater strength, thus leading to a lower propagation of cracks than for the RC ones. Figure 87 helps to understand the fractur of the different architectures. Basically, the same behavior of the PIP ceramics was observed, but with higher strength reached. The RC lattice after the first fracture (45° oriented) continued to fragment with a crack propagation at an almost constant rate cell after cell. The crack propagated in the direction of the struts. Instead, the GY after the first fracture (also in this case 45° oriented) continued to support the load and proceeded with a slower crack propagation. In both cases, the collapse of the structure occurred by propagation of the initial crack through the cells of the structure, and indeed the cells remained intact in the opposite side.
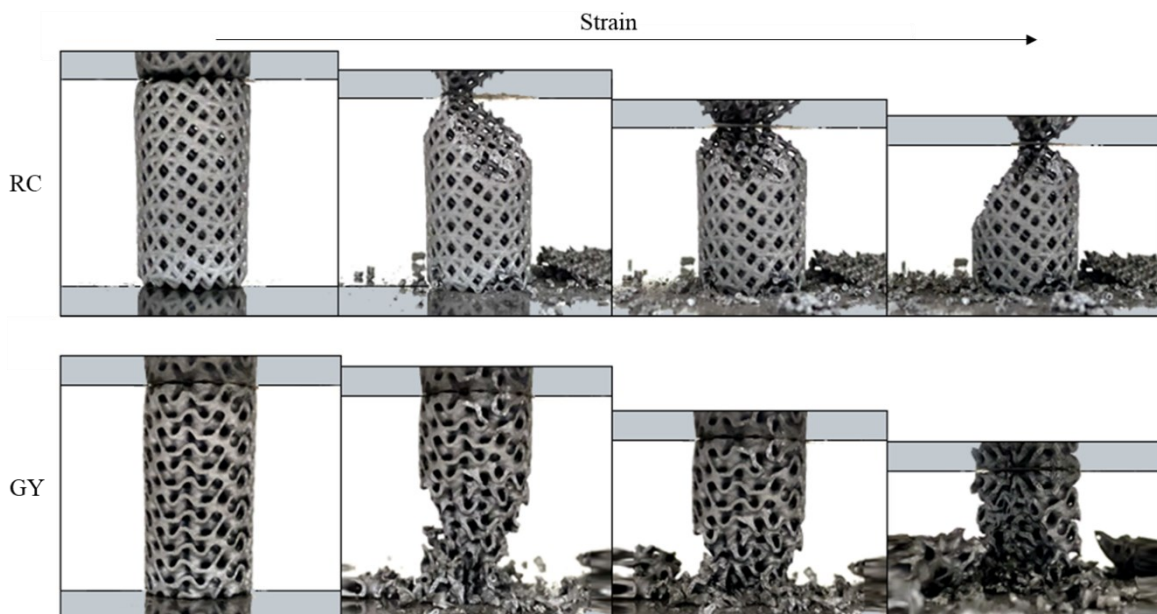
Figure 87. Optical views during the compression tests at increasing strain rate of the Si-infiltrated SiC ceramic samples of the RC and GY architectures.

Figure 88-A and -B show the comparison of the produced materials and structures in terms of maximum compressive strength against their true density and relative density. In general, and accordingly to the amorphous ceramics, the strength of the GY structures doubled that of the RC lattices. Results showed that there is a correlation between the compressive strength and the true density. As expected, the increase of the true density, which is related to the increase of the βSiC phase, leaded to an increase of the strength for both RC and GY structures. The SiC+C+Si ceramics had the higher strength (11.8 MPa and 24.7 MPa for RC and GY respectively) according to its higher βSiC content in Figure 81. The SiC+Gr+Si ceramics showed the lower strength due to the only one PIP cycle, and consequently less βSiC phase. Instead, the relative density showed no correlation with the strength. The C+Si and SiC+C+Si ceramics offered the higher strength despite the lower relative density.
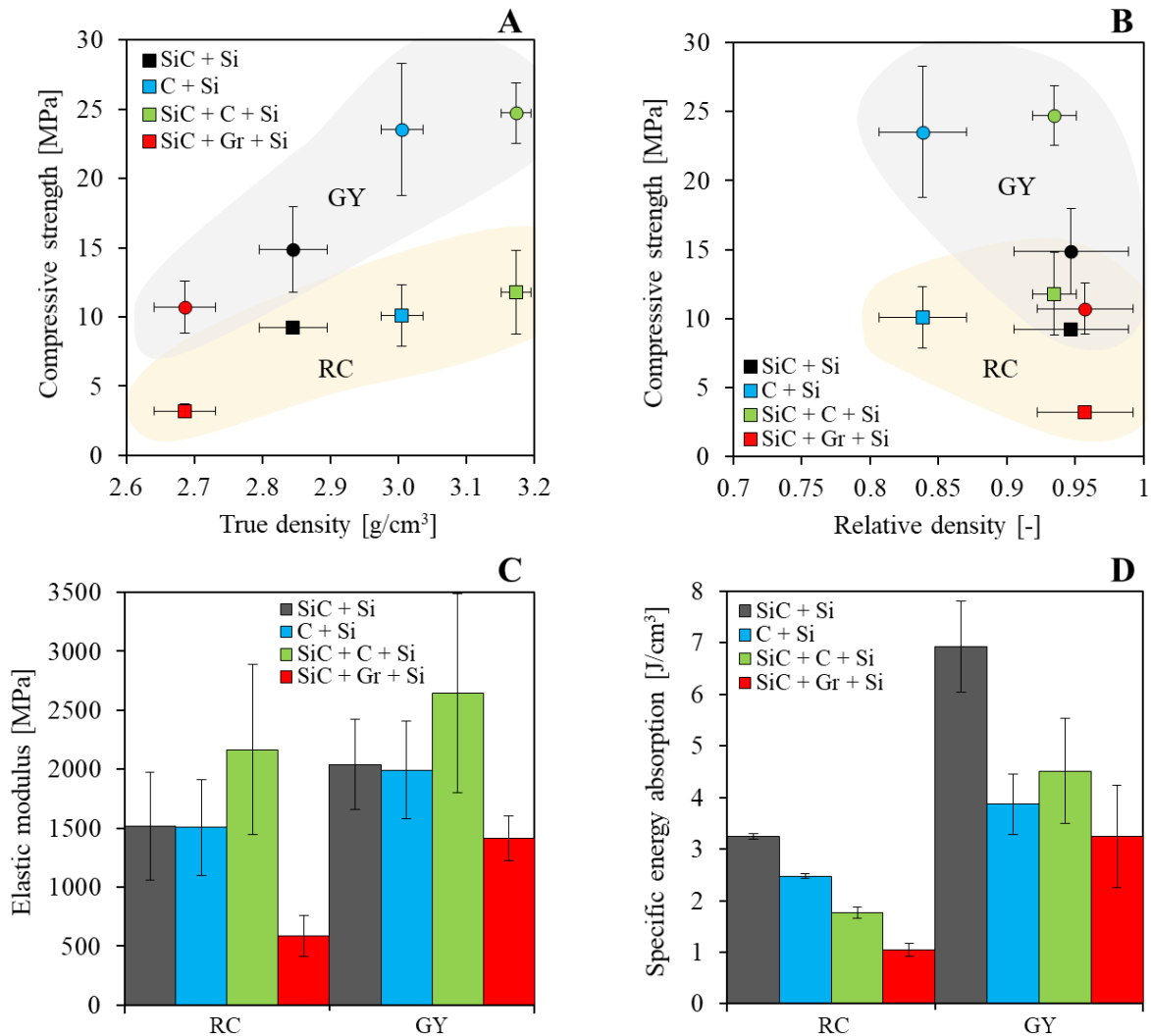
Figure 88. Mechanical compression tests results of the produced Si-infiltrated ceramic samples. (A-B) Maximum compressive strength against the true density and the relative density. (C-D) Estimated elastic modulus and specific energy absorption for the different materials and architectures.

Figure 88-C shows the estimation of the elastic modulus for the produced ceramics useful for comparing the architectures. The large error bars can be attributed to the random cracking of the lattice cells. The values of the elastic modulus had, to a great extent, a similar trend as that of the strength plot. In general, the modulus of the GY structures was higher than that of RC. Considering that the relative density is the same for the two architectures of the same ceramics, the results mean that the geometry of the lattice played an important role on the mechanical performance. The trend showed that the SiC+C+Si ceramics had the highest value of 2166 MPa and 2646 MPa for the RC and GY respectively. The SiC+Gr+Si showed the lowest values. SiC+Si and C+Si ceramics had about the same elastic modulus for both architectures.

Figure 88-D shows the specific energy absorption of the different materials and architecture. The calculation of the integral in the stress-strain curve was performed up to 50% of the strain. The large error bars can be attributed to the random cracking of the lattice cells and this behavior is more evident for the GY structures. As expected, in general the GY structure absorbed twice energy with respect to the RC of the same materials. The SiC+Gr+Si ceramics had the higher geometry influence on the energy absorbed with 310% times increase from RC to GY. This means that if the absorbed energy is crucial for an application, not only the material but also the geometry counts. The maximum specific energy of 6.933 J/cm^3 was absorbed by the SiC+Si gyroid.

Table 23 summarizes the data of the compression tests of the Si-infiltrated ceramic samples.

Arch.	Material	Maximum load	Compressive strength	Elastic modulus	Specific energy absorption (ε=50%)
[-]	[-]	[N]	[MPa]	[MPa]	[J/cm^3]
RC	SiC+Si	2629 ± 185	9.2 ± 0.4	1519 ± 458	3.238 ± 0.053
	C+Si	2843 ± 548	10.1 ± 2.2	1507 ± 408	2.474 ± 0.046
	SiC+C+Si	3026 ± 717	11.8 ± 3.0	2166 ± 722	1.769 ± 0.111
	SiC+Gr+Si	1047 ± 169	3.2 ± 0.5	584 ± 173	1.044 ± 0.119
GY	SiC+Si	4220 ± 949	14.9 ± 3.1	2040 ± 384	6.933 ± 0.883
	C+Si	6688 ± 784	23.5 ± 4.8	1992 ± 414	3.871 ± 0.585
	SiC+C+Si	6287 ± 697	24.7 ± 2.2	2645 ± 843	4.515 ± 1.021
	SiC+Gr+Si	3201 ± 548	10.7 ± 1.9	1412 ± 188	3.250 ± 0.993

Table 23. Comprehensive data of the compression tests results of the produced Si-infiltrated ceramic samples.

The compressive strength of the produced ceramics was compared with the performance of several SiSiC ceramic architectures from literature in the paragraph 4.5.1.

4.4.6 Oxidation tests

Because of its properties, Si-SiC is widely used in applications that involve exposure to combustion and high temperatures[255]. However, because of their employment in high temperature conditions (above 1400°C), their mechanical properties are strongly affected by oxidation[149]. If employed in a high temperature oxidizing environment, a layer of silicon dioxide forms on its surface. This process is called passive oxidation, it occurs at oxygen partial pressures around one bar (Eq. 30). The SiO_2 dense layer on the surface of Si-SiC acts as an anti-oxidation protective layer[248,249]. At pressures lower than one bar a loss of mass is observed (active oxidation in Eq. 31 and Eq. 32) due to the formation of a gaseous phase of both SiO[250] and CO[255]. As oxidation progresses, the core of the Si-SiC will be at low oxygen pressures[261]. This favor active oxidation and thus a dangerous inner material deterioration like the "corrosion pitting" in metals. Also, the presence of excess C can play an important role on the oxidation and mass loss according to Eq. 33.

$$2\ SiC\ (s) + 3\ O_2\ (g) \rightarrow 2\ SiO_2\ (s) + 2\ CO\ (g) \qquad Eq.\ 30$$

$$2\ SiC\ (s) + O_2\ (g) \rightarrow SiO\ (g) + CO\ (g) \qquad Eq.\ 31$$

$$Si + 0.5\ O_2 \rightarrow\ SiO(g) \qquad Eq.\ 32$$

$$C\ (s) + O_2\ (g) \rightarrow CO_2\ (g) \qquad Eq.\ 33$$
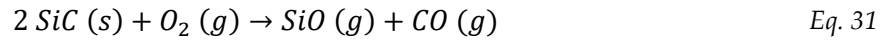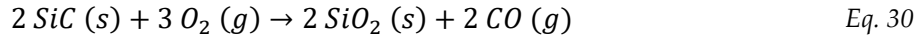
To investigate the performance of the produced Si-SiC ceramics, oxidation tests were performed at 1500°C in steady air in a standard furnace (LHT 08/18, Nabertherm GmbH, Germany) for 1, 2 and 4 hours cumulatively. The heating rate was 20°C/min. Between each oxidation cycle at high temperature, samples were weighted with a precision balance (0.1 mg resolution) to record mass variations. Figure 89 shows the test results in terms of weight change against the oxidation time.
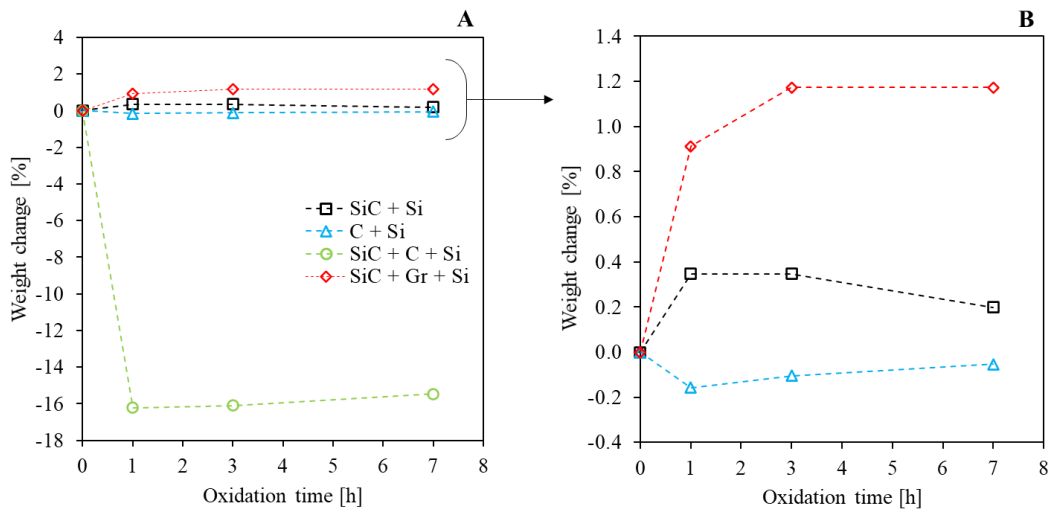
Figure 89. Oxidation tests of the Si-infiltrated ceramic samples at 1500°C for 1h, 2h and 4h cumulatively. (A-B) Weight change Vs. Oxidation time with two magnifications.

The results obtained were very different from the expected ones and from those found in the literature[262]. Indeed, the common oxidation of SiC at high temperature produces a large weight gain (more than 10%) due to passive oxidation which forms solid SiO_2.

In this study, very different oxidation behaviors were observed. The SiC+C+Si ceramics (green curve) suffered a mass loss of about 16% just after 1 hour at 1500°C. This huge loss can be attributed to the oxidation of the residual free carbon (according to Eq. 33), the SiC and Si (according to Eq. 31 and Eq. 32). Subsequent oxidation probably led to the formation of a SiO_2 layer and a gain in mass (according to Eq. 30). Similar behavior was observed for the C+Si ceramics (blue curve) due to the same nature of the polymer-derived C phase present in the material. However, in this case, a negligible mass change was detected. An unexpected result, because in the XRD analysis Figure 82-B a large amount of residual carbon was observed. Probably in this case the residual carbon was not on the surface and not accessible for the oxidation, due to the SiC layer formation during silicon infiltration on the C surface. The SiC+Si ceramics (black curve) showed the opposite behavior with a weight gain after 1 hour and subsequently weight loss, but also in this case the deviations were negligible. The SiC+Gr+Si ceramics (red curve) showed a 1.2% weight increasing after 3 hour and then no change until 7 hours. SiO_2 was formed and acted as an oxidation barrier.

Figure 90 shows the optical images and the micrographs of the Si-infiltrated ceramics between each oxidation cycle at high temperature. The optical images of the non-oxidated samples (0h) were taken from other fractured pieces and they are not the same as the oxidized ones. After high temperature oxidation, two main effects were macroscopically visible: surface glazing and Si exudation. The surface glazing was due to the external oxidation of silicon and SiC, leading to the formation of a SiO_2. Bead exudation was observed. This was related to reactions (Eq. 31 and Eq. 32) taking place inside the material (with lower oxygen partial pressures) and leading to the formation of gasses squeezing out the molten silicon. Indeed, the oxidation temperature intentionally exceeds the melting temperature of silicon (1414°C). SiC+Si and SiC+Gr+Si ceramics, which were the samples with the higher content of silicon, showed several silicon bead exudations on the surface. The change in the beads position over the surface means that during heating the Si melts and then with oxidation its exudates from other sites. Another important result was observed in the color of the samples. Especially for the SiC+C+Si ceramics, three different surface colors were observed after 1 hour (brown), 3 hours (green) and 7 hours (grey), probably showing different stages of oxidation. After 7 hours, its surface was characterized by 50-100 μm green chunks as shown thank to the magnification. This was SiO_2 and a very low quantity of silicon which had failed to form beads and therefore oxidized.

These very slight variations in mass can suggest a surprising resistance to oxidation of the materials produced (comparison with literature values is presented in the paragraph 4.5.1). This is due to the reaction products of Eq. 30, which formed an expanded silica barrier at the surface of the material. This barrier silica layer slowed diffusion of oxygen into the bulk and, therefore, inhibited oxidation from proceeding rapidly throughout the entire material. However, further investigations are needed to confirm these results, such as by using a larger mass of materials for testing (to increase the surface area for oxidation), XRD, SEM and Raman spectrometry before and after the oxidation to evaluate the oxidation products.
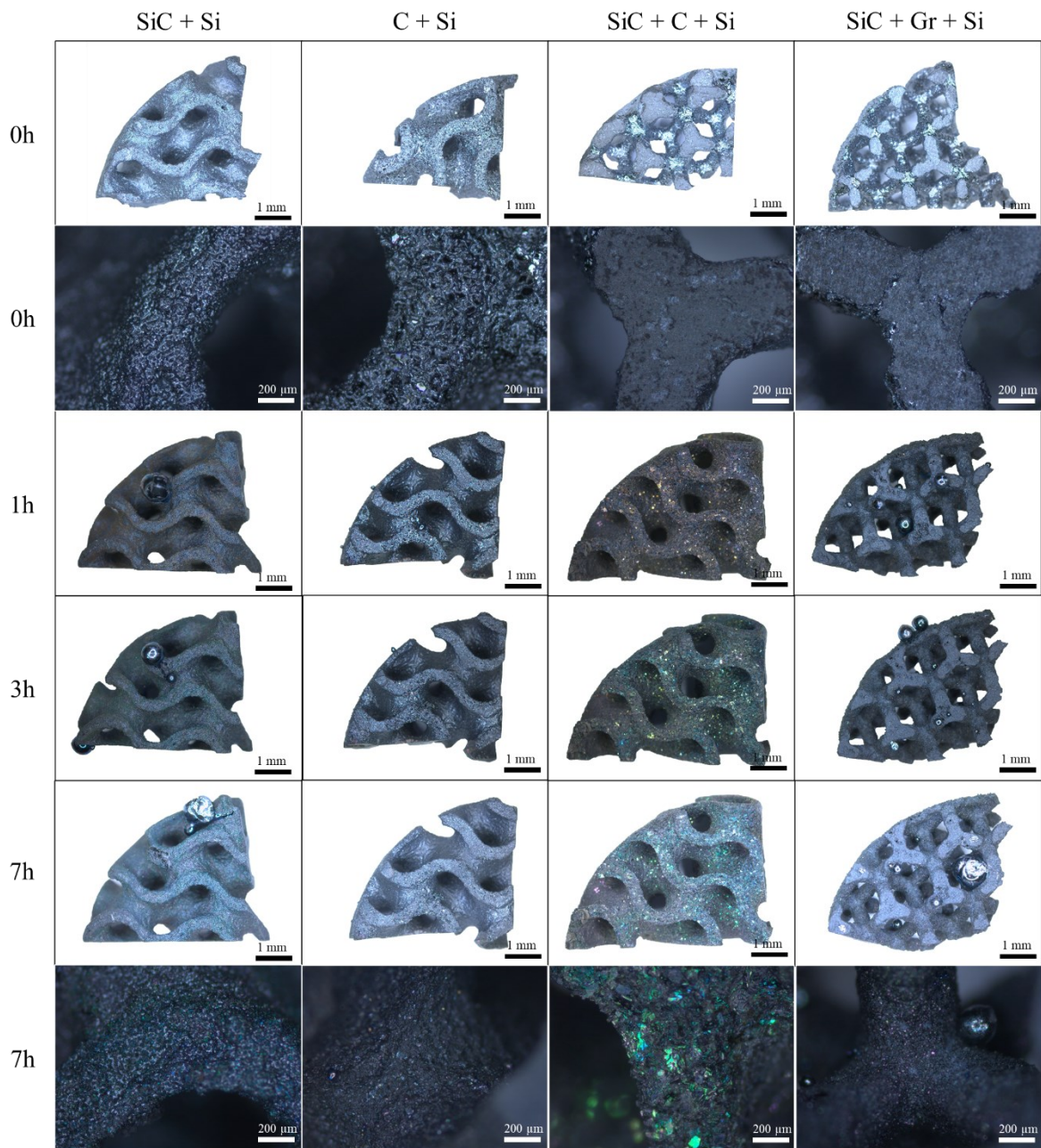
Figure 90. Optical images and micrographs of the Si-infiltrated ceramic samples between each oxidation cycle at high temperature.

4.5   Results summary and discussion

The novel fabrication approach based on hybrid additive manufacturing was successfully used to produce complex ceramic architectures. The topology of two complex structures was designed and 3D printed exploiting the selective laser melting of PA12 powders. The porous preforms were then converted into ceramics through few cycles of polymer infiltration and pyrolysis. The preceramic polymers of polycarbosilane, polycarbosiloxane, polysilazane and furanic resin were used for the fabrication of amorphous polymer-derived ceramics of silicon carbide (SiC), silicon oxycarbide (SiOC), silicon carbonitride (SiCN) and carbon C, respectively. A limited amount of SiOC phase derived from the PA12 was present in all the compositions. Despite the high linear shrinking (21-25%) during the first conversion, the parts kept their pristine shape, and no macrocracks or shape distortion were observed. After four PIP cycles, the SiOC ceramics had the higher relative density of 92.5% and the SiC ceramics had the higher compressive strength of 7.1 MPa. The final densification was achieved via liquid silicon infiltration of four different ceramic matrices: SiC ceramics, C ceramics, SiC+C ceramics and SiC+Gr (graphite) ceramics. During silicon infiltration at high temperature, the ceramic phase crystallizes and shrinks allowing for a full infiltration by molten silicon, producing the final Si-βSiC ceramic component without shape distortion. The notable result was obtained by the Si-infiltrated SiC+C ceramics (or SiC+C+Si) which was composed by crystalline βSiC, reaction bonded βSiC and Si with the volume fraction of 38%, 58% and 4%, respectively. The final nearly fully dense (>93%) ceramic part had a compressive strength of 24.7 MPa. Figure 91 summarizes the results of the produced polymer-derived ceramics and Si-infiltrated ceramics in terms of compressive strength, relative density, and volume fraction.
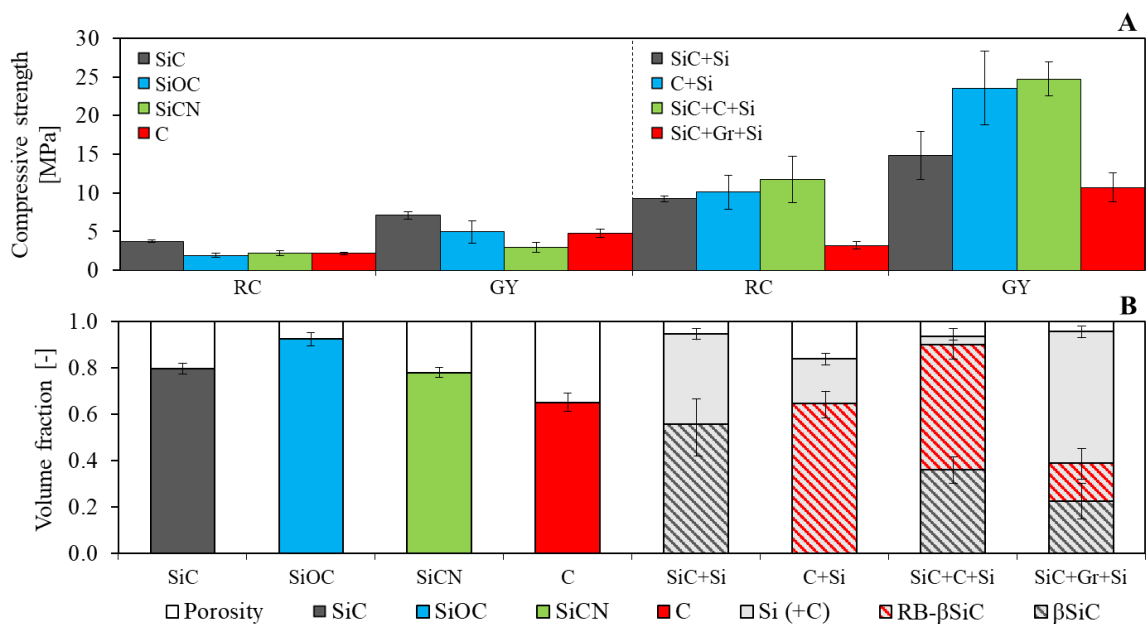
Figure 91. Summary of the results of the produced polymer-derived and Si-infiltrated ceramic samples in terms of (A) compressive strength for the two architectures and (B) relative density and volume fraction.

4.5.1 Comparison with literature in terms of density and performance

Table 24 shows the comparison between the density of SiSiC ceramics fabricated by different AM technologies combined with LSI. The Si-infiltrated ceramics produced in this work are compared with the literature ones. In general, the true density achieved with the proposed hybrid AM method were in line with the average values found in literature. The notable result was the very high values achieved with the C+Si and SiC+C+Si ceramics of 3.005 and 3.173 g/cm^3 respectively. The latter was the highest value found in literature for a SiSiC ceramics produced via AM followed by infiltration. Accordingly, the silicon content of 4% was the lowest. Despite that, the achieved relative densities were lower than the literature ones in all the cases, meaning that more PIP cycles are needed to increase the ceramics fraction and a further optimization of the LSI process is also needed to produce such complex architectures.

Fabrication method	Material	True density	Relative density	Si content	Ref.
-	-	g/cm^3	-	vol%	-
SLM+PIP+LSI	SiC+Si	2.845	0.947	41	This study
	C+Si	3.005	0.838	23	
	SiC+C+Si	3.173	0.935	4	
	SiC+Gr+Si	2.686	0.957	59	
iSLS + LSI	SiSiC	3.06	~1	16.4	[54]
iSLS + LSI	SiSiC	2.69	-	-	[70]
iSLS + LSI	SiSiC	2.73	0.99	54	[66]
iSLS + LSI	SiSiC	2.64	~1	65	[134]
ROB + LSI	SiSiC	2.94	0.979	22.9	[53]
BJ + LSI	SiSiC	2.49	0.91	41	[78]
iSLS+CIP+LSI	SiSiC	2.96	0.94	7	[62]
EFF + LSI	SiSiC	-	-	-	[59]
LOM + LSI	SiSiC	2.60	-	-	[86]
BJ + LSI	SiSiC	3.05	~1	15-25	[52]

Table 24. Comparison between the density of SiSiC ceramic samples fabricated by different AM technologies combined with LSI.

Figure 92 shows the Ashby chart (Granta EduPack 2022 R2, ANSYS, Pittsburgh, PA, USA) of the compressive strength against the density. It compares the mechanical properties of the ceramic architectures produced in this study, along with its dense ceramic and with other ceramic structures found in literature[7,66]. However, not many works concerning complex SiSiC structures tested in compression have been found in the literature.

Before analyzing the results, it is essential to observe the geometric characteristics of the different architectures. Table 25 shows the details of the data in the figure.

It must be remembered that the structures produced in this work had ~19 mm diameter and ~33 mm height and had a geometric porosity (that of the CAD model) of 67%. This means that the cross section available to withstand the compressive load was extremely small. Another important factor to consider is the topology of the lattice. The RC and GY structure are not suitable for compressive loads, as they do not have struts or surfaces aligned with the direction of the load. For example, a straight cubic structure (with vertical beams) would resist much more to compression.

Despite that, the produced ceramic architectures had superior compressive strength (more than double) with respect to ceramic structures of the same materials found in literature[7,66]. Also, the density achieved by the SiC+C+Si ceramics is much higher. A notable result found in literature was the different strength of rotated cube (RC) and straight cube lattices produced with the same materials and method[7]. The RC lattice have six-time lower compressive strength than the straight cube. This means that the strength of the material produced in this study could be even greater if a compression-optimized geometry were manufactured.
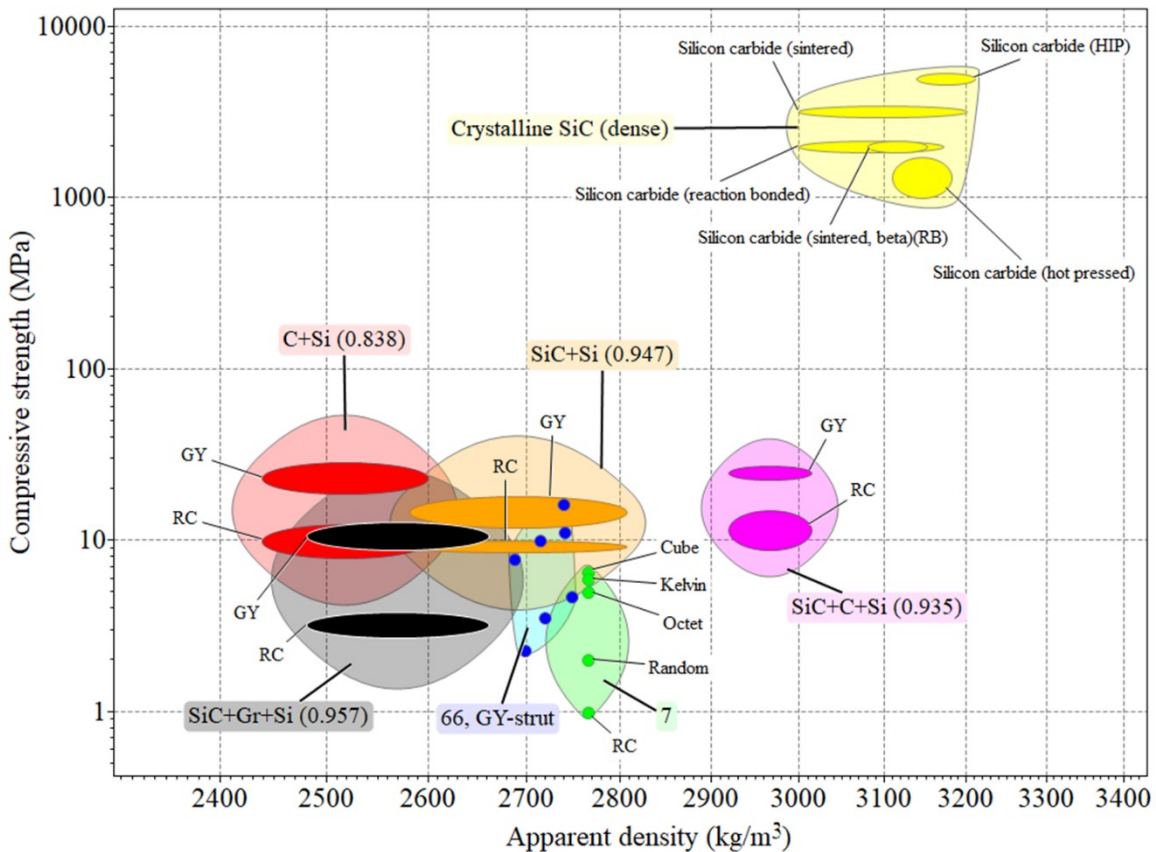
Figure 92. Ashby chart of the compressive strength against the density for SiSiC ceramic samples. The chart compares the fabricated complex architectures with other materials. Other groups of materials were taken from literature and reported in Table 25.

Table 25 shows the data comparison between the SiSiC ceramic architectures fabricated by different methods and tested with uniaxial compression as reported in Figure 92.

Fabrication method	Material	Architecture	Sample size mm³	Geometric porosity %	True density g/cm³	Apprent density g/cm³	Relative density	Si content content vol%	Strength MPa	Ref.
SLM+PIP+LSI	SiC+Si	RC	D19H33	67	2.845 ± 0.050	2.694 ± 0.112	0.947 ± 0.042	41 ± 9	9.2 ± 0.4	-
	C+Si			67	3.005 ± 0.031	2.519 ± 0.080	0.838 ± 0.032	23 ± 3	10.1 ± 2.2	This study
	SiC+C+Si			67	3.173 ± 0.022	2.966 ± 0.047	0.935 ± 0.016	4 ± 3	11.8 ± 3.0	
	SiC+Gr+Si			67	2.686 ± 0.045	2.571 ± 0.090	0.957 ± 0.035	59 ± 4	3.2 ± 0.5	
	SiC+Si	GY		67	2.845 ± 0.050	2.694 ± 0.112	0.947 ± 0.042	41 ± 9	14.9 ± 3.1	
	C+Si			67	3.005 ± 0.031	2.519 ± 0.080	0.838 ± 0.032	23 ± 3	23.5 ± 4.8	
	SiC+C+Si			67	3.173 ± 0.022	2.966 ± 0.047	0.935 ± 0.016	4 ± 3	24.7 ± 2.2	
	SiC+Gr+Si			67	2.686 ± 0.045	2.571 ± 0.090	0.957 ± 0.035	59 ± 4	10.7 ± 1.9	
iSLS+PIP+LSI	SiSiC	GY-strut	20x20x20	75	2.711	2.698	0.995	56	2.304	
				70	2.735	2.719	0.994	53	3.542	
				65	2.764	2.747	0.994	50	4.689	
				60	2.699	2.687	0.996	58	7.821	66
				55	2.732	2.714	0.993	54	10.037	
				50	2.757	2.74	0.994	51	11.104	
				45	2.747	2.739	0.997	52	16.267	
Replica	SiSiC	Random	35x35x35	80		-	-	-	2	2
		RC		85		-	-	-	1	1
		Cube		85	≈ 2.765	-	-	≈ 50	6.5	7
		Kelvin		85		-	-	-	6	6
		Octet		80		-	-	-	5	5

Table 25. Comparison between SiSiC ceramic samples fabricated by different AM technologies combined with LSI and tested with uniaxial compression.

Figure 93 shows the comparison between the oxidation test results of the Si-infiltrated ceramics produced in this work with similar materials found in literature[263]. The literature values are referred to a SiSiC ceramics produced with the replica method. Some parts were coated with a SiC nano powders slurry to protect the surface from the oxidation. Four different coating thicknesses were produced to investigate the influence on the oxidation: 10, 100, 200 and 300 µm. These materials were tested exactly at the same conditions of the ones tested in this work: maximum temperature of 1500°C (20°C/min of heating rate) in steady air for 1, 2 and 4 hours cumulatively.

The figure shows that the ceramic materials produced in the present thesis work had superior oxidation resistance with respect to the literature ones. Except for the SiC+C+Si ceramics (green curve) which suffered a 16% weight loss after 7 hours due to the oxidation of the free carbon present on the surface. The other produced ceramics suffered about 1% weight change. All the ceramics found in literature (orange curves with black dots) gained weight agreement with the literature on the oxidation of SiC[262]. Passive oxidation of SiC formed a solid SiO_2 barrier with grown parabolically. After 7 hour the coated samples (100 µm) gained 50% less mass than the uncoated ones.

The higher oxidation resistance of the SiC+Si, C+Si and SiC+Gr+Si ceramics can be attributed to a low content of residual free carbon or to a SiO_2 barrier on the surface which generated a more tortuous path for oxide species to diffuse. However, the oxidation effects occurred also deep into the substrate material where molten silicon tended to migrate toward the surface in forms of beads. The lower partial pressure of oxygen favored the active oxidation of both Si and SiC, which formed SiO gasses that pushed the liquid silicon outside.
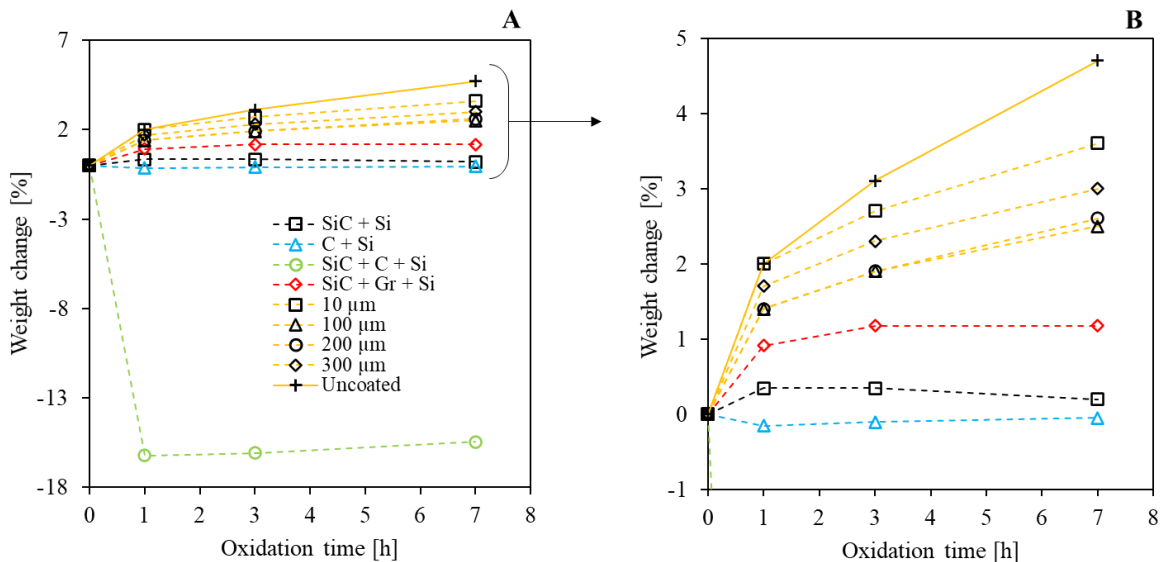
Figure 93. Comparison between the oxidation test results of the produced Si-infiltrated ceramic samples with the values found in literature for similar materials.

5

Conclusions and prospects

This chapter aims to conclude the thesis by summarizing the work carried out and underlying the major findings. A perspective on the needed next steps and further improvements is also given.

5.1 Summary

Figure 94 shows the optical image of the produced complex architectures during the three main phases of the proposed hybrid additive manufacturing process:

1. 3D printing of the porous polymeric preforms through the selective laser melting of PA12 powders. The optimized combination of the printing parameters allows the fabrication of complex-shaped parts with controlled relative density. The structure topology was designed with purpose-built parametric computational design tools developed into Grasshopper.

2. Polymer infiltration and pyrolysis was used for the conversion into amorphous ceramics and to increase the relative density. Despite the high shrinking of ~25%, the parts maintain their pristine shape without macrocracks or distortion. Any type of preceramic polymers can be used with this approach to produce a wide range of polymer-derived ceramics. The only constraint is that the preceramic polymer must crosslink at a temperature lower than the PA12's melting point (~155°C). Catalysts can be added to the preceramic solutions to promote their crosslinking.

3. Liquid silicon infiltration was used for the final densification to produce net-shape and nearly fully dense Si-βSiC ceramics, with the crystallization of the βSiC phase and low residual silicon content. The optimization of the infiltration process was performed, and notable results were achieved with the reactive silicon infiltrations. Superior density, superior compressive strength and superior oxidation resistance were assessed, with respect to other SiSiC ceramics produced with other additive manufacturing methods combined with silicon infiltration.
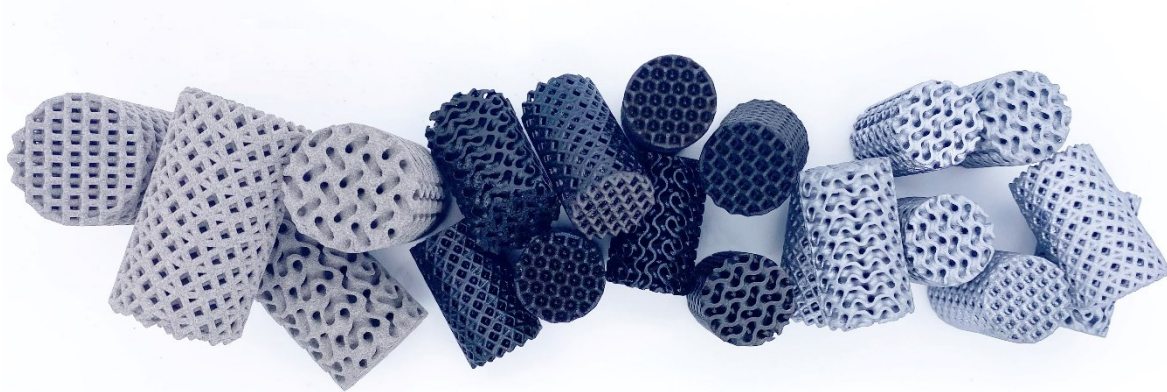
Figure 94. Optical image of the produced samples after the three main phases of the proposed process: 3D printing of the porous polymeric preforms, polymer infiltration and pyrolysis for the conversion into ceramics, and the final densification through liquid silicon infiltration to produce nearly fully dense Si-SiC ceramics.

For designing complex cellular architectures, several parametric computational design tools were developed by using Grasshopper. The algorithm contains a library of several purpose-built unit cells made up of lines, such as straight cube, rotated cube, hexagonal, kelvin, octet, and others. The desired lattice unit cell is selected and replicated in the space until filling the volume of the desired size and shape. The array of lines is then converted into a 3D triangular mesh and the final output is a STL file that can be processed immediately for 3D printing. Also, Voronoi (random) structure and multifunctional lattices can be generated with the produced tools. Furthermore, it allows the generation of triply periodic minimal surface-based structures. In conclusion, the developed computation design tools allow the generation of cellular structures of any shape, with a quick parametrization of the geometrical quantities: cells type, cells size, orientation, struts diameter, gradient for struts diameter, sample size and shape. The high control on the geometric parameters and on the 3D mesh allows to create very precise and smooth surface. Also, the complexity of the structure and the size of the details are a complete description of the operator, i.e., the more geometrically simple is a model, the less effort it will take to develop the code and the less time it will take to generate.

5.2   Major outcomes

The developed hybrid AM process allows the fabrication of complex cellular architectures made of Si-infiltrated polymer-derived ceramics with fine resolution and smaller unit cells than those produced with other ceramics AM approaches. The fabrication of parts with high complex geometry was achieved leading to (i) parts with much smaller features (e.g., pores) than those achievable using binder jetting and (ii) denser struts than those obtainable through the replica method of structures manufactured by digital light processing. This approach allows to overcome several processing problems that have been found in other AM techniques for ceramics. For example, powder-based methods have the difficulty of removing the support material after printing, especially when highly intricate structures with small pores are produced. For stereolithography the main drawback is the opacity of the powders, which does not allow high powder packing. Filament extrusion techniques currently do not allow sufficient geometric freedom to produce 3D highly intricate structures. Therefore, not all the ceramic AM techniques are best suited to produce complex cellular ceramic architectures. In addition, regardless of the used technology, the ceramic preforms are coarse in resolution with respect to the traditional approaches, coarse in the surface quality, low in mechanical strength and low in density.

The big advantage of the proposed method is the possibility of manufacturing nearly fully dense and net-shape ceramics directly from the preceramic precursor, without the need of ceramic powder. The significant advantage of this approach is associated to the maturity and cost of selective laser melting with thermoplastic powders with respect to ceramics. The process is very flexible in reference to the material to be produced. In principle, it is possible to produce any ceramic material starting from its preceramic polymer. It will be enough to infiltrate the 3D printed preform with the selected preceramic polymer to produce a wide variety of different ceramic materials. In this study polycarbosilane, polycarbosiloxane, polysilazane and furan resin were used for the fabrication of the polymer-derived ceramics of SiC, SiOC, SiCN and C respectively. An interesting result was achieved comparing the polycarbosilane with the polycarbosiloxane. It was confirmed that when processed inertly to high temperatures (> 1,000°C) the resulting ceramics always contain a certain amount of oxygen in the matrix. The assessed strength of the polycarbosilane-derived ceramics was 1.5 times higher with respect to polycarbosiloxane-derived ceramics, while the oxidation resistance is low in both cases. However, the cost of polycarbosiloxane (under $100 per kg) is 15 times lower than the one of polycarbosilane (over $1,500 per kg). Therefore, the polycarbosiloxane can be established as the material of choice over polycarbosilane use in several working industrial applications, if it is necessary to reduce costs.

The final densification through liquid silicon infiltration at high temperature produced very interesting results. Especially with the reactive silicon infiltration, the final Si-βSiC ceramics (SiC+C+Si) had a maximum true density of 3.173 g/cm^3, with apparent density of 2.966 g/cm^3 and a relative density of 0.935. The βSiC, RB-βSiC and Si composed the final material with 38%, 58% and 4% of volume fractions respectively. A maximum compressive strength of 25 MPa was achieved by these architected structures, which is more than twice than what found in literature. This was an impressive result considering that the structures were not optimized for compression. Furthermore, a superior oxidation resistance at high temperature was assessed with respect to several SiSiC ceramics found in literature.

Another notable result obtained with the reactive infiltration was the possibly to produce Si-βSiC ceramics with only one PIP cycle (AHPCS + Graphite) followed by silicon infiltration, maintaining the pristine shape of the lattice (same diameter and height) but reducing the thickness of the gyroid surfaces of 92%. In this project, gyroid surfaces of 1.0 ± 0.015 mm were 3D printed and then after LSI a surface thickness of 0.185 ± 0.022 mm was achieved. Furthermore, this ceramic (SiC+Gr+Si) had the higher relative density (0.957 ± 0.035) with respect to the other produced ceramics. This manufacturing approach, in addition to meaningful time saving and production costs saving by reducing the number of PIP cycles, allows to produce complex Si-βSiC structures with extremely thin walls, which cannot be achieved by any other AM techniques for non-oxide ceramics on the market.
This leads to two different uses of the developed process: (i) to perform many PIP cycles of densification to keep the thickness of the walls almost constant after the final LSI; or (ii) to perform only one (or few) PIP cycle to achieve a huge shrinkage of the walls after the LSI.

Regarding the computational work, the developed design tools allow to generate any type of geometry with very fine details. Compared to traditional CAD modeling and to other design methods found in literature, the tools have several advantages: (i) the generation time is much shorter with respect to the manual modelling of traditional CAD software; (ii) the tool is automated and, once the Grasshopper model is built, the operator only has to choose the parameter and the computer does the whole generation effort to reach the final solution; (iii) the very quick possibility to change the topology of the cellular structure, with respect to traditional CAD software, allows its coupling with the simulation of the component behavior (mechanical, thermal, fluid dynamic, etc.) to improve the performance with a trial-and-error approach.

5.3 Future developments

Although the developed process has led to remarkable results, it can be further optimized. There are several aspects that can be improved, including:

a) Equipment: using a 3D printer with a higher resolution (the actual in-plane resolution is 250 µm) will allow to produce a microstructure with finer details, leading to the possibility of generating polymer preforms with much higher microporosity. Consequently, the first PIP will generate a ceramic part with a relative density that is higher than the current 0.30. The total number of PIP cycles will be reduced, also reducing time and cost. A finer resolution will also lead to a higher control on the shape and to the production of cellular structures with more detailed parts, such as more and more small cells size, strut diameter and surface thickness. This can be also linked to the computational design task. Furthermore, a 3D printer with higher power laser will handle loaded powder beds (e.g., with polymer + SiC powders) thereby generating a preform already containing a high amount of crystalline SiC phase.

b) Process: the number of polymer infiltration and pyrolysis cycles must be reduced to save time and costs. This means that a relative density of about 0.85-0.90 must be achieved with fewer PIP cycles than the current ones (6-7 respectively). Stating that the infiltration technique is already being optimized, two strategies can be adopted: (i) by using a 3D printer with a higher resolution, because of the reasons explained above; (ii) by using raw materials with higher ceramic yield both for the 3D printed powder and for the preceramic polymers. Furthermore, as alternative approach, the direct 3D printing of the preceramic powders (if it can be produced) could be investigated. An interesting future development will be on investigating the influence of the PIP cycles number on the subsequent LSI: in this project, it was assessed that only one PIP cycle can be performed to obtain 92% shrinkage of the gyroid surface. It will be useful to evaluate the result as the number of cycles increases.

c) Material after PIP: the oxygen content produced in the first conversion could be reduced or eliminated. Several strategies could be adopted, such as drying the powder before printing, printing in an oxygen-free environment, drying the preform before processing, drying the infiltrated preform before each pyrolysis cycle, infiltrating the preform in an oxygen-free environment, or by using a polymer powder without oxygen content instead of PA12. However, a small amount of oxygen is produced by the conversion of preceramics in almost all cases.

d) <u>Material after LSI</u>: the volume fraction of the βSiC phase with respect to the residual Si phase has already been increased in this study, but residual silicon remained trapped in the material. Ideally it should be eliminated. The silicon could be removed by heating the part in an inert environment beyond the melting temperature of the silicon (>1414°C) and putting the part in contact with porous carbon, so that the silicon can be removed. Furthermore, other methods can be tried to increase the βSiC phase, such as by infiltrating the preform with AHPCS containing also SiC particles (especially for the first PIP cycle), or by printing a bed comprised of both PA12 and SiC particles thereby generating a preform already containing a high amount of crystalline SiC phase, or by testing other reactive infiltration methods. An interesting approach could be to perform dipping LSI.

e) <u>Multifunctionality</u>: the composition of the material can be tuned as desired to produce multifunctional ceramics for the required application. The process allows to perform PIP with different preceramic polymers to combine different types of polymer-derived ceramics in the same part. For example, polycarbosilane can be used for the first infiltration and polysilazane for the subsequent infiltration to obtain SiC/SiCN ceramics.

f) <u>Structure</u>: the optimization of the material was performed only on cellular structures. A further development will be to perform reactive infiltration on solid parts, such as discs and bars, and to compare their bending strength with the literature (Table 13). Regarding the cellular structures, the topology of the produced ceramic architectures was not optimized for compression. A further step forward will be to design and produce structures optimized for specific applications and loads, such as compression, bending and so on. Also, the addition of short fibers in the infiltrating solutions could be investigated. These optimizations combined with the impressive mechanical strength assessed in this work could open to new areas of application for advanced ceramics and to the production of new generation components with more detailed parts, such as porous supports for heat exchangers, heating elements for porous burners, and high-performance catalytic substrates. For example, it was assessed in this work that the specific surface area (see Table 9) of the SiC discs after the first pyrolysis exceeded the one of many catalytic supports in literature. In a future work could be interesting to produce catalytic supports by combining this fabrication method with surface coating, to increase reactivity during catalysis. In addition, the production of templates with high-geometric surface area (such as cellular architectures) could be a further advantage.

References

1. Belmonte, M. Advanced Ceramic Materials for High Temperature Applications. *Adv. Eng. Mater.* **8**, 693–703 (2006).

2. Krenkel, W. *Ceramic matrix composites: fiber reinforced ceramics and their applications*. (John Wiley \& Sons, 2008).

3. Sommers, A. *et al.* Ceramics and ceramic matrix composites for heat exchangers in advanced thermal systems-A review. *Appl. Therm. Eng.* **30**, 1277–1291 (2010).

4. Mason, T. O. (2016, November 3). advanced ceramics. Encyclopedia Britannica. https://www.britannica.com/technology/advanced-ceramics.

5. Santoliquido, O. *et al.* Structured Alumina Substrates for Environmental Catalysis Produced by Stereolithography. *Appl. Sci.* **11**, (2021).

6. Al-Ketan, O., Pelanconi, M., Ortona, A. & Abu Al-Rub, R. K. Additive manufacturing of architected catalytic ceramic substrates based on triply periodic minimal surfaces. *J. Am. Ceram. Soc.* **102**, 6176–6193 (2019).

7. Rezaei, E. E., Haussener, S., Gianella, S. & Ortona, A. Early-stage oxidation behavior at high temperatures of SiSiC cellular architectures in a porous burner. *Ceram. Int.* **42**, 16255–16261 (2016).

8. Pelanconi, M., Barbato, M., Zavattoni, S., Vignoles, G. L. & Ortona, A. Thermal design, optimization and additive manufacturing of ceramic regular structures to maximize the radiative heat transfer. *Mater. Des.* **163**, (2019).

9. Zhakeyev, A. *et al.* Additive manufacturing: unlocking the evolution of energy materials. *Adv. Sci.* **4**, 1700187 (2017).

10. Kosolapova, T. Y. *Carbides: properties, production, and applications*. (Springer Science \& Business Media, 2012).

11. Li, Q., Dong, S., Wang, Z. & Shi, G. Fabrication and properties of 3-D Cf/ZrB2-ZrC-SiC composites via polymer infiltration and pyrolysis. *Ceram. Int.* **39**, 5937–5941 (2013).

12. Yan, C., Liu, R., Cao, Y., Zhang, C. & Zhang, D. Ablation behavior and mechanism of C/ZrC, C/ZrC-SiC and C/SiC composites fabricated by polymer infiltration and pyrolysis process. *Corros. Sci.* **86**, 131–141 (2014).

13. Guo, W., Ye, Y., Bai, S., Zhu, L. & Li, S. Preparation and formation mechanism of C/C–SiC composites using polymer-Si slurry reactive melt infiltration. *Ceram. Int.* **46**, 5586–5593 (2020).

14. Delhaes, P. Chemical vapor deposition and infiltration processes of carbon materials. *Carbon N. Y.* **40**, 641–657 (2002).

15. Stinton, D. P., Caputo, A. J. & Lowden, R. A. Synthesis of fiber-reinforced SiC composites by chemical vapor infiltration. *Am. Ceram. Soc. Bull.* **65**, 347–350 (1986).

16. Macdonald, L. Facile Fabrication of SiC Matrix Composites Using Novel Preceramic Polymers. *Advanced SiC/SiC Ceramic Composites: Developments and Applications in Energy Systems* 87–95 at https://doi.org/https://doi.org/10.1002/9781118406014.ch7 (2006).

17. Dong, S. M., Katoh, Y., Kohyama, A., Schwab, S. T. & Snead, L. L. Microstructural evolution and mechanical performances of SiC/SiC composites by polymer

impregnation/microwave pyrolysis (PIMP) process. *Ceram. Int.* **28**, 899–905 (2002).

18. Kotani, M., Kohyama, A., Okamura, K. & Inoue, T. Fabrication of High Performance SiC/SiC Composite by Polymer Impregnation and Pyrolysis Method. *23rd Annual Conference on Composites, Advanced Ceramics, Materials, and Structures: B: Ceramic Engineering and Science Proceedings* 309–316 at https://doi.org/https://doi.org/10.1002/9780470294574.ch36 (1999).

19. Sreeja, R., Swaminathan, B., Painuly, A., Sebastian, T. V. & Packirisamy, S. Allylhydridopolycarbosilane (AHPCS) as matrix resin for C/SiC ceramic matrix composites. *Mater. Sci. Eng. B Solid-State Mater. Adv. Technol.* **168**, 204–207 (2010).

20. Sangsuwan, P., Orejas, J. A., Gatica, J. E., Tewari, S. N. & Singh, M. Reaction-bonded silicon carbide by reactive infiltration. *Ind. Eng. Chem. Res.* **40**, 5191–5198 (2001).

21. Qian, J. M., Wang, J. P. & Jin, Z. H. Preparation and properties of porous microcellular SiC ceramics by reactive infiltration of Si vapor into carbonized basswood. *Mater. Chem. Phys.* **82**, 648–653 (2003).

22. Wang, Y., Tan, S. & Jiang, D. The effect of porous carbon preform and the infiltration process on the properties of reaction-formed SiC. *Carbon N. Y.* **42**, 1833–1839 (2004).

23. Qian, J. M., Jin, Z. H. & Wang, X. W. Porous SiC ceramics fabricated by reactive infiltration of gaseous silicon into charcoal. *Ceram. Int.* **30**, 947–951 (2004).

24. Chen, Z. *et al.* 3D printing of ceramics: A review. *J. Eur. Ceram. Soc.* **39**, 661–687 (2019).

25. Travitzky, N. *et al.* Additive manufacturing of ceramic-based materials. *Adv. Eng. Mater.* **16**, 729–754 (2014).

26. Chartier, T. *et al.* Additive manufacturing to produce complex 3D ceramic parts. *J. Ceram. Sci. Technol.* **6**, 95–104 (2015).

27. Zocca, A., Colombo, P., Gomes, C. M. & Günster, J. Additive Manufacturing of Ceramics: Issues, Potentialities, and Opportunities. *J. Am. Ceram. Soc.* **98**, 1983–2001 (2015).

28. Moritz, T. & Maleksaeedi, S. 4 - Additive manufacturing of ceramic components. in (eds. Zhang, J. & Jung, Y.-G. B. T.-A. M.) 105–161 (Butterworth-Heinemann, 2018). doi:https://doi.org/10.1016/B978-0-12-812155-9.00004-9.

29. Lu, Z., Cao, J., Song, Z., Li, D. & Lu, B. Research progress of ceramic matrix composite parts based on additive manufacturing technology. *Virtual Phys. Prototyp.* **14**, 333–348 (2019).

30. O'Masta, M. R. *et al.* Additive manufacturing of polymer-derived ceramic matrix composites. *J. Am. Ceram. Soc.* **103**, 6712–6723 (2020).

31. Wang, W. *et al.* Additive manufacturing of fiber reinforced ceramic matrix composites: Advances, challenges, and prospects. *Ceram. Int.* **48**, 19542–19556 (2022).

32. Sun, J. *et al.* A review on additive manufacturing of ceramic matrix composites. *J. Mater. Sci. Technol.* (2022) doi:https://doi.org/10.1016/j.jmst.2022.06.039.

33. Schlier, L. *et al.* Macro-cellular silicon carbide reactors for nonstationary combustion under piston engine-like conditions. *Int. J. Appl. Ceram. Technol.* **8**, 1237–1245 (2011).

34. Scheithauer, U., Schwarzer, E., Moritz, T. & Michaelis, A. Additive Manufacturing of Ceramic Heat Exchanger: Opportunities and Limits of the Lithography-Based Ceramic Manufacturing (LCM). *J. Mater. Eng. Perform.* **27**, 14–20 (2018).

35. Laguna, O. H., Lietor, P. F., Godino, F. J. I. & Corpas-Iglesias, F. A. A review on

additive manufacturing and materials for catalytic applications: Milestones, key concepts, advances and perspectives. *Mater. Des.* **208**, 109927 (2021).

36. Cramer, C. L. *et al. Additive manufacturing of ceramic materials for energy applications: Road map and opportunities. Journal of the European Ceramic Society* vol. 42 (Elsevier Ltd, 2022).

37. Zhu, J. *et al.* Recent advances in 3D printing for catalytic applications. *Chem. Eng. J.* **433**, 134341 (2022).

38. Koyanagi, T., Terrani, K., Harrison, S., Liu, J. & Katoh, Y. Additive manufacturing of silicon carbide for nuclear applications. *J. Nucl. Mater.* **543**, 152577 (2021).

39. Halloran, J. W. Ceramic Stereolithography: Additive Manufacturing for Ceramics by Photopolymerization. *Annu. Rev. Mater. Res.* **46**, 19–40 (2016).

40. Shahzad, K., Deckers, J., Kruth, J. P. & Vleugels, J. Additive manufacturing of alumina parts by indirect selective laser sintering and post processing. *J. Mater. Process. Technol.* **213**, 1484–1494 (2013).

41. Rueschhoff, L., Costakis, W., Michie, M., Youngblood, J. & Trice, R. Additive Manufacturing of Dense Ceramic Parts via Direct Ink Writing of Aqueous Alumina Suspensions. *Int. J. Appl. Ceram. Technol.* **13**, 821–830 (2016).

42. Schwentenwein, M. & Homa, J. Additive Manufacturing of Dense Alumina Ceramics. *Int. J. Appl. Ceram. Technol.* **12**, 1–7 (2015).

43. Wu, H. *et al.* Fabrication of dense zirconia-toughened alumina ceramics through a stereolithography-based additive manufacturing. *Ceram. Int.* **43**, 968–972 (2017).

44. Melcher, R., Martins, S., Travitzky, N. & Greil, P. Fabrication of Al2O3-based composites by indirect 3D-printing. *Mater. Lett.* **60**, 572–575 (2006).

45. Barberi, J. *et al.* Robocasting of SiO2-Based Bioactive Glass Scaffolds with Porosity Gradient for Bone Regeneration and Potential Load-Bearing Applications. *Materials (Basel).* **12**, (2019).

46. Gómez-Gómez, A. *et al.* Highly-porous hierarchical SiC structures obtained by filament printing and partial sintering. *J. Eur. Ceram. Soc.* **39**, 688–695 (2019).

47. Du, W., Singh, M. & Singh, D. Binder jetting additive manufacturing of silicon carbide ceramics: Development of bimodal powder feedstocks by modeling and experimental methods. *Ceram. Int.* **46**, 19701–19707 (2020).

48. Liu, R. *et al.* Fabrication of Porous SiC by Direct Selective Laser Sintering Effect of Boron Carbide. *Metals (Basel).* **11**, 737 (2021).

49. Gianella, S., Gaia, D. & Ortona, A. High Temperature Applications of Si-SiC Cellular Ceramics. *Adv. Eng. Mater.* **14**, 1074–1081 (2012).

50. Ortona, A. *et al.* SiSiC Heat Exchangers for Recuperative Gas Burners with Highly Structured Surface Elements. *Int. J. Appl. Ceram. Technol.* **11**, 927–937 (2014).

51. Polozov, I. *et al.* Fabrication of silicon carbide fiber-reinforced silicon carbide matrix composites using binder jetting additive manufacturing from irregularly-shaped and spherical powders. *Materials (Basel).* **13**, (2020).

52. Zocca, A., Lima, P., Diener, S., Katsikis, N. & Günster, J. Additive manufacturing of SiSiC by layerwise slurry deposition and binder jetting (LSD-print). *J. Eur. Ceram. Soc.* **39**, 3527–3533 (2019).

53. Wahl, L., Lorenz, M., Biggemann, J. & Travitzky, N. Robocasting of reaction bonded

silicon carbide structures. *J. Eur. Ceram. Soc.* **39**, 4520–4526 (2019).

54. Meyers, S., De Leersnijder, L., Vleugels, J. & Kruth, J. P. Direct laser sintering of reaction bonded silicon carbide with low residual silicon content. *J. Eur. Ceram. Soc.* **38**, 3709–3717 (2018).

55. Ortona, A., Yoon, D. H., Fend, T., Feckler, G. & Smirnova, O. Tubular Si-infiltrated SiCf/SiC composites for solar receiver application – Part 2: Thermal performance analysis and prediction. *Sol. Energy Mater. Sol. Cells* **140**, 382–387 (2015).

56. Ortona, A. *et al.* Tubular Si-infiltrated SiCf/SiC composites for solar receiver application—Part 1: Fabrication by replica and electrophoretic deposition. *Sol. Energy Mater. Sol. Cells* **132**, 123–130 (2015).

57. Bianchi, G., Gianella, S. & Ortona, A. Design and additive manufacturing of periodic ceramic architectures. *J. Ceram. Sci. Technol.* **8**, 59–66 (2017).

58. Zhang, H. *et al.* Stereolithography-based additive manufacturing of lightweight and high-strength Cf/SiC ceramics. *Addit. Manuf.* **34**, 101199 (2020).

59. Zhang, H., Yang, Y., Liu, B. & Huang, Z. The preparation of SiC-based ceramics by one novel strategy combined 3D printing technology and liquid silicon infiltration process. *Ceram. Int.* **45**, 10800–10804 (2019).

60. Sergi, D., Camarano, A., Molina, J. M., Ortona, A. & Narciso, J. Surface growth for molten silicon infiltration into carbon millimeter-sized channels: Lattice–Boltzmann simulations, experiments and models. *Int. J. Mod. Phys. C* **27**, 1650062 (2015).

61. Bougiouri, V., Voytovych, R., Rojo-Calderon, N., Narciso, J. & Eustathopoulos, N. The role of the chemical reaction in the infiltration of porous carbon by NiSi alloys. *Scr. Mater.* **54**, 1875–1878 (2006).

62. Liu, K. *et al.* Laser additive manufacturing and homogeneous densification of complicated shape SiC ceramic parts. *Ceram. Int.* **44**, 21067–21075 (2018).

63. Jin, L., Zhang, K., Xu, T., Zeng, T. & Cheng, S. The fabrication and mechanical properties of SiC/SiC composites prepared by SLS combined with PIP. *Ceram. Int.* **44**, 20992–20999 (2018).

64. Wu, W.-J. *et al.* Effect of impregnated phenolic resin on the properties of Si–SiC ceramic matrix composites fabricated by SLS-RMI. *Ceram. Int.* (2022) doi:https://doi.org/10.1016/j.ceramint.2022.06.324.

65. Fu, H. *et al.* Effect of silicon addition on the microstructure, mechanical and thermal properties of Cf/SiC composite prepared via selective laser sintering. *J. Alloys Compd.* **792**, 1045–1053 (2019).

66. Wu, S., Yang, L., Wang, C., Yan, C. & Shi, Y. Si/SiC ceramic lattices with a triply periodic minimal surface structure prepared by laser powder bed fusion. *Addit. Manuf.* **56**, 102910 (2022).

67. Mearns, C., Potgieter, J., Dirven, S. & Le Guen, M. J. Experimental analysis of the effectiveness of current modelling methods for SLS parameter determination. *2017 24th Int. Conf. Mechatronics Mach. Vis. Pract. M2VIP 2017* **2017**-**Decem**, 1–5 (2017).

68. Ahlhelm, M., Richter, H. J. & Haderk, K. Selective laser sintering as an additive manufacturing method for manufacturing ceramic components. *J. Ceram. Sci. Technol.* **4**, 33–40 (2013).

69. Chen, X. *et al.* Effect of laser power on mechanical properties of SiC composites

rapidly fabricated by selective laser sintering and direct liquid silicon infiltration. *Ceram. Int.* **48**, 19123–19131 (2022).

70. Song, S. *et al.* Performance optimization of complicated structural SiC/Si composite ceramics prepared by selective laser sintering. *Ceram. Int.* **46**, 568–575 (2020).

71. Xu, T.-T., Cheng, S., Jin, L.-Z., Zhang, K. & Zeng, T. High-temperature flexural strength of SiC ceramics prepared by additive manufacturing. *Int. J. Appl. Ceram. Technol.* **17**, 438–448 (2020).

72. Grossin, D. *et al.* A review of additive manufacturing of ceramics by powder bed selective laser processing (sintering / melting): Calcium phosphate, silicon carbide, zirconia, alumina, and their composites. *Open Ceram.* **5**, (2021).

73. Deckers, J. P. *et al.* Shaping ceramics through indirect selective laser sintering. *Rapid Prototyp. J.* **22**, 544–558 (2016).

74. Terrani, K., Jolly, B. & Trammell, M. 3D printing of high-purity silicon carbide. *J. Am. Ceram. Soc.* **103**, 1575–1581 (2020).

75. Cramer, C. L. *et al.* Processing and properties of SiC composites made via binder jet 3D printing and infiltration and pyrolysis of preceramic polymer. *Int. J. Ceram. Eng. Sci.* **2**, 320–331 (2020).

76. Baux, A. *et al.* Synthesis and properties of macroporous SiC ceramics synthesized by 3D printing and chemical vapor infiltration/deposition. *J. Eur. Ceram. Soc.* **40**, 2834–2854 (2020).

77. Heisel, C. *et al.* Digital design and 3D printing of innovative SiC architectures for high temperature volumetric solar receivers. *Sol. Energy Mater. Sol. Cells* **232**, 111336 (2021).

78. Cramer, C. L. *et al.* Properties of SiC-Si made via binder jet 3D printing of SiC powder, carbon addition, and silicon melt infiltration. *J. Am. Ceram. Soc.* **104**, 5467–5478 (2021).

79. Fleisher, A. *et al.* Reaction bonding of silicon carbides by Binder Jet 3D-Printing, phenolic resin binder impregnation and capillary liquid silicon infiltration. *Ceram. Int.* **45**, 18023–18029 (2019).

80. Ziaee, M. & Crane, N. B. Binder jetting: A review of process, materials, and methods. *Addit. Manuf.* **28**, 781–801 (2019).

81. Lv, X., Ye, F., Cheng, L., Fan, S. & Liu, Y. Binder jetting of ceramics: Powders, binders, printing parameters, equipment, and post-treatment. *Ceram. Int.* **45**, 12609–12624 (2019).

82. Baux, A. *et al.* Complex geometry macroporous SiC ceramics obtained by 3D-printing, polymer impregnation and pyrolysis (PIP) and chemical vapor deposition (CVD). *J. Eur. Ceram. Soc.* **41**, 3274–3284 (2021).

83. Yang, Y., Kulkarni, A., Soraru, G. D., Pearce, J. M. & Motta, A. 3d printed sioc(N) ceramic scaffolds for bone tissue regeneration: Improved osteogenic differentiation of human bone marrow-derived mesenchymal stem cells. *Int. J. Mol. Sci.* **22**, (2021).

84. Kulkarni, A., Sorarù, G. D. & Pearce, J. M. Polymer-derived SiOC replica of material extrusion-based 3-D printed plastics. *Addit. Manuf.* **32**, 100988 (2020).

85. Kulkarni, A., Pearce, J., Yang, Y., Motta, A. & Sorarù, G. D. SiOC(N) Cellular Structures with Dense Struts by Integrating Fused Filament Fabrication 3D Printing with Polymer-Derived Ceramics. *Adv. Eng. Mater.* **23**, (2021).

86. Windsheimer, H., Travitzky, N., Hofenauer, A. & Greil, P. Laminated object

manufacturing of preceramic-paper-derived Si-SiC composites. *Adv. Mater.* **19**, 4515–4519 (2007).

87. He, R., Ding, G., Zhang, K., Li, Y. & Fang, D. Fabrication of SiC ceramic architectures using stereolithography combined with precursor infiltration and pyrolysis. *Ceram. Int.* **45**, 14006–14014 (2019).

88. Ding, G., He, R., Zhang, K., Zhou, N. & Xu, H. Stereolithography 3D printing of SiC ceramic with potential for lightweight optical mirror. *Ceram. Int.* **46**, 18785–18790 (2020).

89. Bai, X. *et al.* Stereolithography additive manufacturing and sintering approaches of SiC ceramics. *Open Ceram.* **5**, 100046 (2021).

90. Zanchetta, E. *et al.* Stereolithography of SiOC Ceramic Microcomponents. *Adv. Mater.* **28**, 370–376 (2016).

91. Wang, X. *et al.* Additive manufacturing of ceramics from preceramic polymers: A versatile stereolithographic approach assisted by thiol-ene click chemistry. *Addit. Manuf.* **27**, 80–90 (2019).

92. Schmidt, J. & Colombo, P. Digital light processing of ceramic components from polysiloxanes. *J. Eur. Ceram. Soc.* **38**, 57–66 (2018).

93. de Hazan, Y. & Penner, D. SiC and SiOC ceramic articles produced by stereolithography of acrylate modified polycarbosilane systems. *J. Eur. Ceram. Soc.* **37**, 5205–5212 (2017).

94. Tang, J., Chang, H., Guo, X., Liu, M. & Wei, Y. Preparation of photosensitive SiO 2 / SiC ceramic slurry with high solid content for stereolithography. *Ceram. Int.* (2022) doi:10.1016/j.ceramint.2022.06.306.

95. Cai, K. *et al.* Geometrically complex silicon carbide structures fabricated by robocasting. *J. Am. Ceram. Soc.* **95**, 2660–2666 (2012).

96. Feilden, E., Glymond, D., Saiz, E. & Vandeperre, L. High temperature strength of an ultra high temperature ceramic produced by additive manufacturing. *Ceram. Int.* **45**, 18210–18214 (2019).

97. McClain, M. S., Gunduz, I. E. & Son, S. F. Additive Manufacturing of Carbon Fiber Reinforced Silicon Carbide Solid Rocket Nozzles. in *AIAA Scitech 2019 Forum* (American Institute of Aeronautics and Astronautics, 2019). doi:doi:10.2514/6.2019-0408.

98. Held, A., Puchas, G., Müller, F. & Krenkel, W. Direct ink writing of water-based C–SiC pastes for the manufacturing of SiSiC components. *Open Ceram.* **5**, 100054 (2021).

99. Pierin, G., Grotta, C., Colombo, P. & Mattevi, C. Direct Ink Writing of micrometric SiOC ceramic structures using a preceramic polymer. *J. Eur. Ceram. Soc.* **36**, 1589–1594 (2016).

100. Huang, K., Elsayed, H., Franchin, G. & Colombo, P. Additive manufacturing of SiOC scaffolds with tunable structure-performance relationship. *J. Eur. Ceram. Soc.* **41**, 7552–7559 (2021).

101. Xiong, H. *et al.* Building SiC-based composites from polycarbosilane-derived 3D-SiC scaffolds via polymer impregnation and pyrolysis (PIP). *J. Eur. Ceram. Soc.* **41**, 1121–1131 (2021).

102. Kopeliovich, D. Fabrication of Ceramic Matrix Composites by Liquid Silicon

Infiltration. Substances & Technologies. at (2012).

103. Kopeliovich, D. Advances in the manufacture of ceramic matrix composites using infiltration techniques. in *Advances in Ceramic Matrix Composites* 79–108 (Elsevier, 2014).

104. Cornolti, L., Martinelli, S., Bianchi, G. & Ortona, A. Microwave heating controlled reactive melt infiltration for graphite-Si-SiC ceramics manufacturing. *J. Am. Ceram. Soc.* **102**, 2304–2315 (2019).

105. Naikade, M., Ortona, A., Graule, T. & Weber, L. Liquid metal infiltration of silicon based alloys into porous carbonaceous materials. Part I: Modelling of channel filling and reaction phase formation. *J. Eur. Ceram. Soc.* **42**, 1971–1983 (2022).

106. Naikade, M. *et al.* Liquid metal infiltration of silicon based alloys into porous carbonaceous materials. Part II: Experimental verification of modelling approaches by infiltration of Si-Zr alloy into idealized microchannels. *J. Eur. Ceram. Soc.* **42**, 1984–1994 (2022).

107. Naikade, M. *et al.* Liquid metal infiltration of silicon based alloys into porous carbonaceous materials Part-III: experimental verification of conversion products and infiltration depth by infiltration of Si-Zr alloy into mixed SiC/graphite preforms. *J. Eur. Ceram. Soc.* (2022) doi:https://doi.org/10.1016/j.jeurceramsoc.2022.09.036.

108. Caccia, M. & Narciso, J. Key parameters in the manufacture of SiC-based composite materials by reactive melt infiltration. *Materials (Basel).* **12**, (2019).

109. Tong, Y., Bai, S., Liang, X., Qin, Q. H. & Zhai, J. Reactive melt infiltration fabrication of C/C-SiC composite: Wetting and infiltration. *Ceram. Int.* **42**, 17174–17178 (2016).

110. Silverstein, R., Zok, F. W. & Levi, C. G. Vapor-mediated melt infiltration for synthesizing SiC composite matrices. *J. Am. Ceram. Soc.* **104**, 3833–3844 (2021).

111. Caccia, M. & Narciso, J. Production of sic materials by reactive infiltration. *Mater. Sci. Forum* **783–786**, 1863–1866 (2014).

112. Louis, E., Miralles, J. A. & Molina, J. M. Reactive infiltration: identifying the role of chemical reactions, capillarity, viscosity and gravity. *J. Mater. Sci.* **52**, 7530–7538 (2017).

113. Yang, Z. *et al.* Infiltration mechanism of diamond/SiC composites fabricated by Si-vapor vacuum reactive infiltration process. *J. Eur. Ceram. Soc.* **33**, 869–878 (2013).

114. He, R. *et al. Progress and challenges towards additive manufacturing of SiC ceramic. Journal of Advanced Ceramics* vol. 10 (2021).

115. Ainger, F. W. & Herbert, J. M. The preparation of phosphorus-nitrogen compounds as non-porous solids. *Spec. Ceram.* 168–182 (1960).

116. Chantrell, P. G. & Popper, P. Inorganic polymers and ceramics. *Spec. Ceram.* **67**, (1965).

117. Verbeek, W. Production of shaped articles of homogeneous mixtures of silicon carbide and nitride. at (1974).

118. Colombo, P., Mera, G., Riedel, R. & Sorarù, G. D. Polymer-derived ceramics: 40 Years of research and innovation in advanced ceramics. *J. Am. Ceram. Soc.* **93**, 1805–1837 (2010).

119. Bernard, S., Fiaty, K., Cornu, D., Miele, P. & Laurent, P. Kinetic modeling of the polymer-derived ceramics route: investigation of the thermal decomposition kinetics

of poly [B-(methylamino) borazine] precursors into boron nitride. *J. Phys. Chem. B* **110**, 9048–9060 (2006).

120. Vakifahmetoglu, C., Zeydanli, D. & Colombo, P. Porous polymer derived ceramics. *Mater. Sci. Eng. R Reports* **106**, 1–30 (2016).

121. Colombo, P., Schmidt, J., Franchin, G., Zocca, A. & Günster, J. Additive manufacturing techniques for fabricating complex ceramic components from preceramic polymers. By Paolo Colombo, Johanna Schmidt, Giorgia Franchin, Andrea Zocca, and Jens Günster. Retrieved from www.ceramics.orgbricatin.

122. Franchin, G. *et al.* Additive Manufacturing of Ceramics from Liquid Feedstocks. *Chinese J. Mech. Eng. Addit. Manuf. Front.* **1**, 100012 (2022).

123. Chaudhary, R. P. *et al.* Additive manufacturing of polymer-derived ceramics: Materials, technologies, properties and potential applications. *Prog. Mater. Sci.* **128**, 100969 (2022).

124. Ortona, A., D'Angelo, C., Gianella, S. & Gaia, D. Cellular ceramics produced by rapid prototyping and replication. *Mater. Lett.* **80**, 95–98 (2012).

125. Muth, J. T., Dixon, P. G., Woish, L., Gibson, L. J. & Lewis, J. A. Architected cellular ceramics with tailored stiffness via direct foam writing. *Proc. Natl. Acad. Sci.* **114**, 1832–1837 (2017).

126. Deshpande, V. S., Ashby, M. F. & Fleck, N. A. Foam topology: bending versus stretching dominated architectures. *Acta Mater.* **49**, 1035–1040 (2001).

127. Murr, L. E. *et al.* Next-generation biomedical implants using additive manufacturing of complex, cellular and functional mesh arrays. *Philos. Trans. R. Soc. A Math. Phys. Eng. Sci.* **368**, 1999–2032 (2010).

128. Wang, P., Li, J. B., Vafai, K., Zhao, L. & Zhou, L. Thermo-fluid optimization of a solar porous absorber with a variable pore structure. *J. Sol. Energy Eng.* **139**, (2017).

129. Wang, H., Chen, Y. & Rosen, D. W. A hybrid geometric modeling method for large scale conformal cellular structures. in *International Design Engineering Technical Conferences and Computers and Information in Engineering Conference* vol. 47403 421–427 (2005).

130. Babaee, S. *et al.* Metamaterials: 3D Soft Metamaterials with Negative Poisson's Ratio (Adv. Mater. 36/2013). *Adv. Mater.* **25**, 5116 (2013).

131. Kolken, H. M. A. & Zadpoor, A. A. Auxetic mechanical metamaterials. *RSC Adv.* **7**, 5111–5129 (2017).

132. Evans, A. G., Hutchinson, J. W. & Ashby, M. F. Cellular metals. *Curr. Opin. Solid State Mater. Sci.* **3**, 288–303 (1998).

133. Mayer, G. & Sarikaya, M. Rigid biological composite materials: structural examples for biomimetic design. *Exp. Mech.* **42**, 395–403 (2002).

134. Friedel, T., Travitzky, N., Niebling, F., Scheffler, M. & Greil, P. Fabrication of polymer derived ceramic parts by selective laser curing. *J. Eur. Ceram. Soc.* **25**, 193–197 (2005).

135. Wu, Z. *et al.* Experimental and numerical studies of the pressure drop in ceramic foams for volumetric solar receiver applications. *Appl. Energy* **87**, 504–513 (2010).

136. Esser, B. *et al.* Innovative thermal management concepts and material solutions for future space vehicles. *J. Spacecr. Rockets* **53**, 1051–1060 (2016).

137. Dimopoulos Eggenschwiler, P. *et al.* Ceramic foam substrates for automotive catalyst

applications: fluid mechanic analysis. *Exp. Fluids* **47**, 209–222 (2009).

138. Wu, Z., Caliot, C., Flamant, G. & Wang, Z. Numerical simulation of convective heat transfer between air flow and ceramic foams to optimise volumetric solar air receiver performances. *Int. J. Heat Mass Transf.* **54**, 1527–1537 (2011).

139. Ferrari, L., Barbato, M. C., Ortona, A. & D'Angelo, C. Convective heat transfer in cellular ceramic: A 3D numerical solution. in (2014).

140. Gibson, L. J. Cellular solids. *Mrs Bull.* **28**, 270–274 (2003).

141. Pelanconi, M., Rezaei, E. & Ortona, A. Cellular ceramic architectures produced by hybrid additive manufacturing: A review on the evolution of their design. *J. Ceram. Soc. Japan* **128**, (2020).

142. Pelanconi, M. & Ortona, A. Review on the Design Approaches of Cellular Architectures Produced by Additive Manufacturing BT - Industrializing Additive Manufacturing. in (eds. Meboldt, M. & Klahn, C.) 52–64 (Springer International Publishing, 2021).

143. Santoliquido, O., Colombo, P. & Ortona, A. Additive Manufacturing of ceramic components by Digital Light Processing: A comparison between the "bottom-up" and the "top-down" approaches. *J. Eur. Ceram. Soc.* **39**, 2140–2148 (2019).

144. Galante, R., Figueiredo-Pina, C. G. & Serro, A. P. Additive manufacturing of ceramics for dental applications: A review. *Dent. Mater.* **35**, 825–846 (2019).

145. Bhargav, A., Sanjairaj, V., Rosa, V., Feng, L. W. & Fuh YH, J. Applications of additive manufacturing in dentistry: A review. *J. Biomed. Mater. Res. Part B Appl. Biomater.* **106**, 2058–2064 (2018).

146. Santoliquido, O., Bianchi, G., Dimopoulos Eggenschwiler, P. & Ortona, A. Additive manufacturing of periodic ceramic substrates for automotive catalyst supports. *Int. J. Appl. Ceram. Technol.* **14**, 1164–1173 (2017).

147. Meng, Q.-L., Lee, C., Ishihara, T., Kaneko, H. & Tamaura, Y. Reactivity of CeO2-based ceramics for solar hydrogen production via a two-step water-splitting cycle with concentrated solar energy. *Int. J. Hydrogen Energy* **36**, 13435–13441 (2011).

148. König, R. *et al.* Micropollutant adsorption from water with engineered porous ceramic architectures produced by additive manufacturing and coated with natural zeolite. *J. Clean. Prod.* **258**, 120500 (2020).

149. Ortona, A. *et al.* Aging of reticulated Si-SiC foams in porous burners. *Adv. Appl. Ceram.* **109**, 246–251 (2010).

150. Papetti, V. *et al.* Additive Manufactured open cell polyhedral structures as substrates for automotive catalysts. *Int. J. Heat Mass Transf.* **126**, 1035–1047 (2018).

151. Felzmann, R. *et al.* Lithography-based additive manufacturing of cellular ceramic structures. *Adv. Eng. Mater.* **14**, 1052–1058 (2012).

152. Altun, A. A., Prochaska, T., Konegger, T. & Schwentenwein, M. Dense, strong, and precise silicon nitride-based ceramic parts by lithography-based ceramic manufacturing. *Appl. Sci.* **10**, 996 (2020).

153. Cai, K. *et al.* Geometrically Complex Silicon Carbide Structures Fabricated by Robocasting. *J. Am. Ceram. Soc.* **95**, 2660–2666 (2012).

154. Jana, P., Santoliquido, O., Ortona, A., Colombo, P. & Sorarù, G. D. Polymer-derived SiCN cellular structures from replica of 3D printed lattices. *J. Am. Ceram. Soc.* **101**,

2732–2738 (2018).

155. Radhika, N. & Sathish, M. A Review on Si-Based Ceramic Matrix Composites and their Infiltration Based Techniques. *Silicon* 1–31 (2022).

156. Vasquez, M., Haworth, B. & Hopkinson, N. Methods for quantifying the stable sintering region in laser sintered polyamide-12. *Polym. Eng. \& Sci.* **53**, 1230–1240 (2013).

157. Panwisawas, C. *et al.* On the role of thermal fluid dynamics into the evolution of porosity during selective laser melting. *Scr. Mater* **105**, 14–17 (2015).

158. Toth-Taşcău, M., Răduţă, A., Stoia, D. I. & Locovei, C. Influence of the energy density on the porosity of Polyamide parts in SLS process. *Solid State Phenom.* **188**, 400–405 (2012).

159. Stoia, D. I., Linul, E. & Marsavina, L. Influence of manufacturing parameters on mechanical properties of porous materials by selective laser sintering. *Materials (Basel).* **16**, (2019).

160. Kurzynowski, T. *et al.* Effect of scanning and support strategies on relative density of SLM-ed H13 steel in relation to specimen size. *Materials (Basel).* **12**, 239 (2019).

161. Salmoria, G. V. *et al.* Rapid manufacturing of polyethylene parts with controlled pore size gradients using selective laser sintering. *Mater. Res.* **10**, 211–214 (2007).

162. March, J. & others. Advanced organic chemistry. (1968).

163. Interrante, L. V, Whitmarsh, C. W. & Sherwood, W. Fabrication of SiC matrix composites by liquid phase infiltration with a polymeric precursor. *MRS Online Proc. Libr.* **365**, 139–146 (1994).

164. Interrante, L. V *et al.* Silicon-based ceramics from polymer precursors. *Pure Appl. Chem.* **74**, 2111–2117 (2002).

165. Sreeja, R., Swaminathan, B., Painuly, A., Sebastian, T. V & Packirisamy, S. Allylhydridopolycarbosilane (AHPCS) as matrix resin for C/SiC ceramic matrix composites. *Mater. Sci. Eng. B* **168**, 204–207 (2010).

166. Konegger, T., Patidar, R. & Bordia, R. K. A novel processing approach for free-standing porous non-oxide ceramic supports from polycarbosilane and polysilazane precursors. *J. Eur. Ceram. Soc.* **35**, 2679–2683 (2015).

167. Bruzzoniti, M. C. *et al.* Regenerable, innovative porous silicon-based polymer-derived ceramics for removal of methylene blue and rhodamine B from textile and environmental waters. *Environ. Sci. Pollut. Res.* **25**, 10619–10629 (2018).

168. Santhosh, B. *et al.* Effect of pyrolysis temperature on the microstructure and thermal conductivity of polymer-derived monolithic and porous SiC ceramics. *J. Eur. Ceram. Soc.* **41**, 1151–1162 (2021).

169. Sorarù, G. D., Tavonatti, C., Kundanati, L., Pugno, N. & Biesuz, M. Effect of the pyrolysis atmosphere on the mechanical properties of polymer-derived SiOC and SiCN. *J. Am. Ceram. Soc.* **103**, 6519–6530 (2020).

170. Kwon, D., Park, E., Ha, S. & Kim, N. Effect of humidity changes on dimensional stability of 3D printed parts by selective laser sintering. *Int. J. Precis. Eng. Manuf.* **18**, 1275–1280 (2017).

171. Zheng, J., Kramer, M. J. & Akinc, M. In situ growth of SiC whisker in pyrolyzed monolithic mixture of AHPCS and SiC. *J. Am. Ceram. Soc.* **83**, 2961–2966 (2000).

172. Schade, O. R., Kalz, K. F., Neukum, D., Kleist, W. & Grunwaldt, J.-D. Supported gold- and silver-based catalysts for the selective aerobic oxidation of 5-(hydroxymethyl) furfural to 2, 5-furandicarboxylic acid and 5-hydroxymethyl-2-furancarboxylic acid. *Green Chem.* **20**, 3530–3541 (2018).

173. Tapah, B. F., Santos, R. C. D. & Leeke, G. A. Processing of glycerol under sub and supercritical water conditions. *Renew. energy* **62**, 353–361 (2014).

174. Börger, A., Supancic, P. & Danzer, R. The ball on three balls test for strength testing of brittle discs: stress distribution in the disc. *J. Eur. Ceram. Soc.* **22**, 1425–1436 (2002).

175. Danzer, R. *et al.* The ball on three balls test—Strength and failure analysis of different materials. *J. Eur. Ceram. Soc.* **27**, 1481–1485 (2007).

176. Xu, T. T., Cheng, S., Jin, L. Z., Zhang, K. & Zeng, T. High-temperature flexural strength of SiC ceramics prepared by additive manufacturing. *Int. J. Appl. Ceram. Technol.* **17**, 438–448 (2020).

177. Ashby, M. F. & Johnson, K. *Materials and design: the art and science of material selection in product design*. (Butterworth-Heinemann, 2013).

178. Ashby, M. F., Shercliff, H. & Cebon, D. *Materials: engineering, science, processing and design*. (Butterworth-Heinemann, 2018).

179. Danzer, R., Lube, T., Supancic, P. & Damani, R. Fracture of ceramics. *Adv. Eng. Mater.* **10**, 275–298 (2008).

180. Chi, W., Jiang, D., Huang, Z. & Tan, S. Sintering behavior of porous SiC ceramics. *Ceram. Int.* **30**, 869–874 (2004).

181. Ozcivici, E. & Singh, R. P. Fabrication and characterization of ceramic foams based on silicon carbide matrix and hollow alumino-silicate spheres. *J. Am. Ceram. Soc.* **88**, 3338–3345 (2005).

182. Ding, S., Zeng, Y. P. & Jiang, D. In-situ reaction bonding of porous SiC ceramics. *Mater. Charact.* **59**, 140–143 (2008).

183. Li, J., Lin, H. & Li, J. Factors that influence the flexural strength of SiC-based porous ceramics used for hot gas filter support. *J. Eur. Ceram. Soc.* **31**, 825–831 (2011).

184. Lim, K. Y., Kim, Y. W. & Song, I. H. Low-temperature processing of porous SiC ceramics. *J. Mater. Sci.* **48**, 1973–1979 (2013).

185. Anwar, M. S., Bukhari, S. Z. A., Ha, J. H., Lee, J. & Song, I. H. Effect of Ni content and its particle size on electrical resistivity and flexural strength of porous SiC ceramic sintered at low-temperature using clay additive. *Ceram. Int.* **47**, 31536–31547 (2021).

186. Yun, S. Il, Nahm, S. & Park, S. W. Effects of SiC particle size on flexural strength, permeability, electrical resistivity, and thermal conductivity of macroporous SiC. *Ceram. Int.* **48**, 1429–1438 (2022).

187. D'Amico, G. C. *et al.* Oxidation Behavior at 1600 °C of Si-SiC-ZrB2 Composites Produced by Si Reactive Infiltration. *Adv. Eng. Mater.* **16**, 176–183 (2014).

188. Park, D. J., Jung, Y. Il, Kim, H. G., Park, J. Y. & Koo, Y. H. Oxidation behavior of silicon carbide at 1200 C in both air and water--vapor-rich environments. *Corros. Sci.* **88**, 416–422 (2014).

189. Sheehan, J. E. Oxidation protection for carbon fiber composites. *Carbon N. Y.* **27**, 709–715 (1989).

190. Wagner, C. Passivity during the oxidation of silicon at elevated temperatures. *J. Appl.*

Phys. **29**, 1295–1297 (1958).

191. Bois, L., Maquet, J., Babonneau, F. & Bahloul, D. Structural characterization of sol-gel derived oxycarbide glasses. 2. Study of the thermal stability of the silicon oxycarbide phase. *Chem. Mater.* **7**, 975–981 (1995).

192. Sorarù, G. D. *et al.* Chemical durability of silicon oxycarbide glasses. *J. Am. Ceram. Soc.* **85**, 1529–1536 (2002).

193. Kleebe, H.-J. *et al.* Evolution of C-rich SiOC ceramics. *Int. J. Mater. Res.* **97**, 699–709 (2006).

194. Saha, A. & Raj, R. Crystallization maps for SiCO amorphous ceramics. *J. Am. Ceram. Soc.* **90**, 578–583 (2007).

195. Stabler, C. *et al.* Thermal properties of SiOC glasses and glass ceramics at elevated temperatures. *Materials (Basel).* **11**, 279 (2018).

196. Narisawa, M. *et al.* Silicon carbide particle formation from carbon black—polymethylsilsesquioxane mixtures with melt pressing. *J. Ceram. Soc. Japan* **116**, 121–125 (2008).

197. Chase, M. W. & (US), N. I. S. O. *NIST-JANAF thermochemical tables*. vol. 9 (American Chemical Society Washington, DC, 1998).

198. Camacho, Y. S. M. *et al.* Development of a robust and efficient biogas processor for hydrogen production. Part 1: modelling and simulation. *Int. J. Hydrogen Energy* **42**, 22841–22855 (2017).

199. Camacho, Y. S. M. *et al.* Development of a robust and efficient biogas processor for hydrogen production. Part 2: Experimental campaign. *Int. J. Hydrogen Energy* **43**, 161–177 (2018).

200. Fend, T. High porosity materials as volumetric receivers for solar energetics. *Opt. Appl.* **40**, 271–284 (2010).

201. Szczurek, A. *et al.* Carbon periodic cellular architectures. *Carbon N. Y.* **88**, 70–85 (2015).

202. Klahn, C., Leutenecker, B. & Meboldt, M. Design strategies for the process of additive manufacturing. *Procedia Cirp* **36**, 230–235 (2015).

203. Giani, L., Groppi, G. & Tronconi, E. Mass-transfer characterization of metallic foams as supports for structured catalysts. *Ind. \& Eng. Chem. Res.* **44**, 4993–5002 (2005).

204. Lacroix, M. *et al.* Pressure drop measurements and modeling on SiC foams. *Chem. Eng. Sci.* **62**, 3259–3267 (2007).

205. Ortona, A. & Rezaei, E. Modeling the properties of cellular ceramics: from foams to lattices and back to foams. in *Advances in Science and Technology* vol. 91 70–78 (2014).

206. Kusner, R. & Sullivan, J. M. Comparing the Weaire-Phelan equal-volume foam to Kelvin's foam. *Forma* **11**, 233–242 (1996).

207. Georgiou, O., Richens, P. & Shepherd, P. Performance based interactive analysis. in *Computational Design Modelling* 115–122 (Springer, 2011).

208. Tedeschi, A. *Parametric architecture with Grasshopper®: primer*. (Le Penseur, 2011).

209. Willis, D., Braham, W., Muramoto, K. & Barber, D. *Energy accounts: Architectural representations of energy, climate, and the future*. (Routledge, 2016).

210. Stasiuk, D. Cocoon ADDON. Version 1.

211. Bourke, P. Polygonising a scalar field also known as:" 3D Contouring"," Marching

Cubes"," Surface Reconstruction". *http//astronomy. swin. edu. au/\~{} pbourke/modelling/polygonise/* (1994).

212. Fortune, S. Voronoi diagrams and Delaunay triangulations. *Comput. Euclidean Geom.* 225–265 (1995).

213. Boomsma, K., Poulikakos, D. & Ventikos, Y. Simulations of flow through open cell metal foams using an idealized periodic cell structure. *Int. J. Heat Fluid Flow* **24**, 825–834 (2003).

214. Boomsma, K. & Poulikakos, D. On the effective thermal conductivity of a three-dimensionally structured fluid-saturated metal foam. *Int. J. Heat Mass Transf.* **44**, 827–836 (2001).

215. Ferrari, L. *et al.* Sandwich structured ceramic matrix composites with periodic cellular ceramic cores: an active cooled thermal protection for space vehicles. *Compos. Struct.* **154**, 61–68 (2016).

216. Schoen, A. H. *Infinite periodic minimal surfaces without self-intersections.* (1970).

217. Michielsen, K., De Raedt, H. & Stavenga, D. G. Reflectivity of the gyroid biophotonic crystals in the ventral wing scales of the Green Hairstreak butterfly, Callophrys rubi. *J. R. Soc. Interface* **7**, 765–771 (2010).

218. Michielsen, K. & Stavenga, D. G. Gyroid cuticular structures in butterfly wing scales: biological photonic crystals. *J. R. Soc. Interface* **5**, 85–94 (2008).

219. Yu, S., Sun, J. & Bai, J. Investigation of functionally graded TPMS structures fabricated by additive manufacturing. *Mater. \& Des.* **182**, 108021 (2019).

220. Al-Ketan, O., Lee, D.-W., Rowshan, R. & Al-Rub, R. K. A. Functionally graded and multi-morphology sheet TPMS lattices: Design, manufacturing, and mechanical properties. *J. Mech. Behav. Biomed. Mater.* **102**, 103520 (2020).

221. Feng, J., Fu, J., Yao, X. & He, Y. Triply periodic minimal surface (TPMS) porous structures: from multi-scale design, precise additive manufacturing to multidisciplinary applications. *Int. J. Extrem. Manuf.* **4**, 22001 (2022).

222. Al-Ketan, O., Al-Rub, R. K. A. & Rowshan, R. The effect of architecture on the mechanical properties of cellular structures based on the IWP minimal surface. *J. Mater. Res.* **33**, 343–359 (2018).

223. Al-Ketan, O., Rowshan, R. & Al-Rub, R. K. A. Topology-mechanical property relationship of 3D printed strut, skeletal, and sheet based periodic metallic cellular materials. *Addit. Manuf.* **19**, 167–183 (2018).

224. Khan, K. A. & Al-Rub, R. K. A. Time dependent response of architectured Neovius foams. *Int. J. Mech. Sci.* **126**, 106–119 (2017).

225. Lee, D.-W., Khan, K. A. & Al-Rub, R. K. A. Stiffness and yield strength of architectured foams based on the Schwarz Primitive triply periodic minimal surface. *Int. J. Plast.* **95**, 1–20 (2017).

226. Abueidda, D. W. *et al.* Mechanical properties of 3D printed polymeric cellular materials with triply periodic minimal surface architectures. *Mater. \& Des.* **122**, 255–267 (2017).

227. Abueidda, D. W., Dalaq, A. S., Al-Rub, R. K. A. & Jasiuk, I. Micromechanical finite element predictions of a reduced coefficient of thermal expansion for 3D periodic architectured interpenetrating phase composites. *Compos. Struct.* **133**, 85–97 (2015).

228. Al-Ketan, O. *et al.* Microarchitected stretching-dominated mechanical metamaterials with minimal surface topologies. *Adv. Eng. Mater.* **20**, 1800029 (2018).

229. Al-Ketan, O., Soliman, A., AlQubaisi, A. M. & Abu Al-Rub, R. K. Nature-Inspired Lightweight Cellular Co-Continuous Composites with Architected Periodic Gyroidal Structures. *Adv. Eng. Mater.* **20**, 1700549 (2018).

230. Qureshi, Z. A., Elnajjar, E., Al-Ketan, O., Al-Rub, R. A. & Al-Omari, S. B. Heat transfer performance of a finned metal foam-phase change material (FMF-PCM) system incorporating triply periodic minimal surfaces (TPMS). *Int. J. Heat Mass Transf.* **170**, 121001 (2021).

231. Catchpole-Smith, S. *et al.* Thermal conductivity of TPMS lattice structures manufactured via laser powder bed fusion. *Addit. Manuf.* **30**, 100846 (2019).

232. Abueidda, D. W. *et al.* Effective conductivities and elastic moduli of novel foams with triply periodic minimal surfaces. *Mech. Mater.* **95**, 102–115 (2016).

233. Thomas, N. *et al.* 3D printed triply periodic minimal surfaces as spacers for enhanced heat and mass transfer in membrane distillation. *Desalination* **443**, 256–271 (2018).

234. Sreedhar, N. *et al.* Mass transfer analysis of ultrafiltration using spacers based on triply periodic minimal surfaces: Effects of spacer design, directionality and voidage. *J. Memb. Sci.* **561**, 89–98 (2018).

235. Sreedhar, N. *et al.* 3D printed feed spacers based on triply periodic minimal surfaces for flux enhancement and biofouling mitigation in RO and UF. *Desalination* **425**, 12–21 (2018).

236. Kapfer, S. C., Hyde, S. T., Mecke, K., Arns, C. H. & Schröder-Turk, G. E. Minimal surface scaffold designs for tissue engineering. *Biomaterials* **32**, 6875–6882 (2011).

237. Schwarz, H. A. *Gesammelte mathematische abhandlungen*. vol. 260 (American Mathematical Soc., 1972).

238. Du, Q., Faber, V. & Gunzburger, M. Centroidal Voronoi tessellations: Applications and algorithms. *SIAM Rev.* **41**, 637–676 (1999).

239. Pelanconi, M. *et al.* Application of Ceramic Lattice Structures to Design Compact, High Temperature Heat Exchangers: Material and Architecture Selection. *Mater. (Basel, Switzerland)* **14**, (2021).

240. Anand, R., Nayak, B. B. & Behera, S. K. Phase, nanostructure, and oxidation of precursor derived SiCN--TiO2 ceramic nanocomposites. *Ceram. Int.* **47**, 27822–27832 (2021).

241. Schiavon, M. A., Soraru, G. D. & Yoshida, I. V. P. Synthesis of a polycyclic silazane network and its evolution to silicon carbonitride glass. *J. Non. Cryst. Solids* **304**, 76–83 (2002).

242. Furtat, P., Lenz-Leite, M., Ionescu, E., Machado, R. A. F. & Motz, G. Synthesis of fluorine-modified polysilazanes via Si--H bond activation and their application as protective hydrophobic coatings. *J. Mater. Chem. A* **5**, 25509–25521 (2017).

243. Santhosh, B. *et al.* Processing and thermal characterization of polymer derived SiCN (O) and SiOC reticulated foams. *Ceram. Int.* **46**, 5594–5601 (2020).

244. Zambotti, A. *et al.* Synthesis and thermal evolution of polysilazane-derived SiCN(O) aerogels with variable C content stable at 1600 °C. *Ceram. Int.* **47**, 8035–8043 (2021).

245. Alghamdi, A. *et al.* Effect of additive manufactured lattice defects on mechanical

properties: an automated method for the enhancement of lattice geometry. *Int. J. Adv. Manuf. Technol.* **108**, 957–971 (2020).

246. Maconachie, T. *et al.* The compressive behaviour of ABS gyroid lattice structures manufactured by fused deposition modelling. *Int. J. Adv. Manuf. Technol.* **107**, 4449–4467 (2020).

247. Parisien, A., ElSayed, M. S. A. & Frei, H. Mechanoregulation modelling of stretching versus bending dominated periodic cellular solids. *Mater. Today Commun.* **33**, 104315 (2022).

248. Jorgensen, P. J., Wadsworth, M. E. & Cutler, I. B. Oxidation of silicon carbide. *J. Am. Ceram. Soc.* **42**, 613–616 (1959).

249. Auweter-Kurtz, M. *et al.* Investigation of oxidation protected C/C heat shield material in different plasma wind tunnels. *Acta Astronaut.* **45**, 93–108 (1999).

250. Harder, B., Jacobson, N. & Myers, D. Oxidation transitions for SiC part II. Passive-to-active transitions. *J. Am. Ceram. Soc.* **96**, 606–612 (2013).

251. Brewer, C. M., Bujalski, D. R., Parent, V. E., Su, K. & Zank, G. A. Insights into the oxidation chemistry of SiOC ceramics derived from silsesquioxanes. *J. sol-gel Sci. Technol.* **14**, 49–68 (1999).

252. Niu, M. *et al.* Oxidation behavior of dense SiOC monolithics: The oxide scale development. *Corros. Sci.* **163**, 108235 (2020).

253. Anand, R., Nayak, B. B. & Behera, S. K. Coarsening kinetics of nanostructured ZrO_2 in Zr-doped SiCN ceramic hybrids. *J. Alloys Compd.* **811**, 151939 (2019).

254. Riedel, R., Kleebe, H.-J., Schönfelder, H. & Aldinger, F. A covalent micro/nano-composite resistant to high-temperature oxidation. *Nature* **374**, 526–528 (1995).

255. Jacobson, N. S. Corrosion of silicon-based ceramics in combustion environments. *J. Am. Ceram. Soc.* **76**, 3–28 (1993).

256. Eom, Y. *et al.* Structure evolution mechanism of highly ordered graphite during carbonization of cellulose nanocrystals. *Carbon N. Y.* **150**, 142–152 (2019).

257. Sagues, W. J. *et al.* Are lignin-derived carbon fibers graphitic enough? *Green Chem.* **21**, 4253–4265 (2019).

258. Köhnke, J. *et al.* Electrically conducting carbon microparticles by direct carbonization of spent wood pulping liquor. *ACS Sustain. Chem. \& Eng.* **6**, 3385–3391 (2018).

259. Danko, G. A., Silberglitt, R., Colombo, P., Pippel, E. & Woltersdorf, J. Comparison of microwave hybrid and conventional heating of preceramic polymers to form silicon carbide and silicon oxycarbide ceramics. *J. Am. Ceram. Soc.* **83**, 1617–1625 (2000).

260. Niu, F., Wang, Y., Fu, S., Ma, L. & Wang, C. Ferrocene-assisted growth of SiC whiskers with hexagonal cross-section from a preceramic polymer. *Ceram. Int.* **43**, 12983–12987 (2017).

261. Aronovici, M. *et al.* Heat and Mass Transfer in Ceramic Lattices During High-Temperature Oxidation. *J. Am. Ceram. Soc.* **98**, 2625–2633 (2015).

262. Roy, J., Chandra, S., Das, S. & Maitra, S. Oxidation behaviour of silicon carbide-a review. *Rev. Adv. Mater. Sci.* **38**, (2014).

263. Bianchi, G., Di Mauro, A., Ferrari, L., Gianella, S. & Ortona, A. Si-SiC oxidation barrier coating on 3D printed Si-SiC strut-based architectures deposited by electrophoretic deposition. *J. Eur. Ceram. Soc.* (2022).

List of figures

List of tables

List of symbols

Latin symbols

AED	applied energy density	[J·mm^{-3}]
cp	specific heat capacity	[J·g^{-1}·°C^{-1}]
C_s	unit cell size	[mm]
C_t	unit cell type	[-]
D	sample diameter	[mm]
EMR	energy melt ratio	[-]
F	applied load	[N]
f	factor of disc geometry (B3B)	[-]
GSA	geometric surface area	[cm^2]
H	sample height	[mm]
h	thickness of the disc	[mm]
hf	enthalpy of melt	[J·g^{-1}]
HR	heating rate	[°C·s^{-1}]
Mi	initial weight	[g]
P	laser power	[W]
pf	packing factor	[-]
R	radius of the disc	[mm]
Ra	support radius	[mm]
Rb	radius of the support balls	[mm]
S	scan count	[-]
SGSA	specific geometric surface area	[1/m]
SP	specific power	[mW·mg^{-1}]
SSA	specific surface area	[m^2·g^{-1}]
t	strut diameter or surface thickness	[mm]
T_b	powder surface temperature	[°C]
T_m	melting onset temperature	[°C]
TME	theoretical melt energy	[J·mm^{-3}]
v	laser speed	[mm·s^{-1}]
v_p	poisson's ratio	[-]
V_s	solid volume	[cm^3]
V_{tot}	total volume occupied	[cm^3]
y	ceramic yield	[-]
y_h	scan hatching spacing	[mm]
z	layer thickness	[mm]

Greek symbols

α	alpha phase	[-]
β	beta phase	[-]
φ	micro porosity	[-]
φ_M	macro (or geometric) porosity	[-]
p	material true density	[g·cm^{-3}]
p_{rel}	relative density	[-]
p^*	apparent (bulk) density	[g·cm^{-3}]
σ	stress	[MPa]
σ_f	fracture strength	[MPa]
σ_f^*	apparent fracture strength	[MPa]
$\sigma_{f,rel}$	relative fracture strength	[-]
ε	strain	[%]

Subscripts

$*$	apparent value (referred to a bulk material)
a	amorphous
B	bending dominated
$bulk$	solid and porosity
$calc$	calculated value
max	maximum value
min	minimum value
MIP	value measured with porosimetry
$PA12$	polyamide
rel	relative value
S	stretching dominated

Acronyms

AED	applied energy density
$AHPCS$	allylhydridopolycarbosilane
AM	additive manufacturing
$B3B$	ball-on-three-balls
BJ	binder jetting
C	carbon
CAD	computer-aided design
CIP	cold isostatic pressing
CVD	chemical vapor deposition
CVI	chemical vapor infiltration
DoE	design of experiment

DSC	differential scanning calorimetry
EDX	energy dispersive X-ray analysis
EFF	extrusion free forming
EMR	energy melt ratio
FE	finite element
FUR	furanic resin
GSA	geometric surface area
HIP	hot isostatic pressing
HR	heating rate
LOM	laminated object manufacturing
LSI	liquid silicon infiltration
MIP	measured with porosimetry
PA12	polyamide (Nylon 12)
PCSO	polycarbosiloxane
PDC	polymer-derived ceramic
PIP	polymer infiltration and pyrolysis
PSN	polysilazane
RB-SiC	reaction bonded silicon carbide
RI	reactive infiltration
RMI	reactive melt infiltration
ROB	robocasting
RT	room temperature
SEM	scanning electron microscopy
SGSA	Specific geometric surface area
SiC	silicon carbide
SiCN	silicon carbonitride
SiOC	silicon oxycarbide
SiSiC	silicon infiltrated silicon carbide
SLM	selective laser melting
SLS	selective laser sintering
SP	specific power
SSA	specific surface area
TGA	thermogravimetry analysis
TME	theoretical melt energy
XRD	X-ray diffractometer

List of equations

Acknowledgments

Curriculum Vitae

Marco Pelanconi

Email:	marco.pelanconi.94@gmail.com
Date of birth:	April 14, 1994
Nationality:	Italian

Education

Oct. 2019 – Jan. 2023:	**Ph.D. in Industrial Engineering, Curriculum in Materials Engineering**
School:	Università degli Studi di Padova (UNIPD), Padua, Italy
Thesis:	Complex architectures of Si-infiltrated Polymer-Derived Ceramics: computational design and hybrid additive manufacturing
Oct. 2016 – Feb. 2019:	**Master of Science in Engineering, Industrial Technologies**
School:	University of Applied Sciences and Arts of Southern Switzerland (SUPSI), Lugano, Switzerland
Thesis:	Design, optimization and additive manufacturing of bio-inspired ultra-light sandwich structures
Sep. 2013 – Sep. 2016:	**Bachelor of Science in Mechanical Engineering**
School:	University of Applied Sciences and Arts of Southern Switzerland (SUPSI), Lugano, Switzerland
Thesis:	Additive design and manufacturing of porous ceramic structures for high temperature heat exchangers: a parametric study of the heat exchange
Sep. 2008 – Sep. 2013:	**Perito Industriale Capotecnico, Mechatronics**
School:	Istituto Statale di Istruzione Superiore "Isaac Newton" (ISIS), Varese, Italy
Thesis:	The progress

Work experience

Oct. 2019 – Present:	**Researcher Ph.D. Candidate**
Company:	Mechanical Engineering and Materials Technology Institute (MEMTi), SUPSI, Lugano, Switzerland
Description:	Computational design and hybrid additive manufacturing of complex ceramic architectures through novel methods, simulation, material characterization and testing.
Mar. 2017 – Oct. 2019:	**Research Assistant**
Company:	Mechanical Engineering and Materials Technology Institute (MEMTi), SUPSI, Lugano, Switzerland
Description:	Additive manufacturing of complex ceramic architectures: development of computational design tools, topology optimization, CFD simulation, manufacturing, material characterization and testing.

Journal publications

- Pelanconi, M., Bianchi, G., Colombo, P., & Ortona, A. (2022). **Fabrication of dense SiSiC ceramics by a hybrid additive manufacturing process**. Journal of the American Ceramic Society, 105(2), 786-793. https://doi.org/10.1111/jace.18134

- Pelanconi, M., Colombo, P., & Ortona, A. (2021). **Additive manufacturing of silicon carbide by selective laser sintering of PA12 powders and polymer infiltration and pyrolysis**. Journal of the European Ceramic Society, 41(10), 5056-5065. https://doi.org/10.1016/j.jeurceramsoc.2021.04.014

- Pelanconi, M., Ortona, A. (2021). **Review on the Design Approaches of Cellular Architectures Produced by Additive Manufacturing**. In: Meboldt, M., Klahn, C. (eds) Industrializing Additive Manufacturing. AMPA 2020. Springer, Cham, pp. 52–64. https://doi.org/10.1007/978-3-030-54334-1_5

- Santoliquido, O., Camerota, F., Pelanconi, M., Ferri, D., Elsener, M., Dimopoulos Eggenschwiler, P., & Ortona, A. (2021). **Structured Alumina Substrates for Environmental Catalysis Produced by Stereolithography**. Applied Sciences, 11(17), 8239. https://doi.org/10.3390/app11178239

- Pelanconi, M., Zavattoni, S., Cornolti, L., Puragliesi, R., Arrivabeni, E., Ferrari, L., ... & Ortona, A. (2021). **Application of ceramic lattice structures to design compact, high temperature heat exchangers: material and architecture selection**. Materials, 14(12), 3225. https://doi.org/10.3390/ma14123225

- Pelanconi, M., Rezaei, E., & Ortona, A. (2020). **Cellular ceramic architectures produced by hybrid additive manufacturing: A review on the evolution of their design**. Journal of the Ceramic Society of Japan, 128(9), 595-604. https://doi.org/10.2109/jcersj2.20071
- Pelanconi, M., & Ortona, A. (2019). **Nature-inspired, ultra-lightweight structures with gyroid cores produced by additive manufacturing and reinforced by unidirectional carbon fiber ribs**. Materials, 12(24), 4134. https://doi.org/10.3390/ma12244134
- Al-Ketan, O., Pelanconi, M., Ortona, A., & Abu Al-Rub, R. K. (2019). **Additive manufacturing of architected catalytic ceramic substrates based on triply periodic minimal surfaces**. Journal of the American Ceramic Society, 102(10), 6176-6193. https://doi.org/10.1111/jace.16474
- Pelanconi, M., Barbato, M., Zavattoni, S., Vignoles, G. L., & Ortona, A. (2019). **Thermal design, optimization and additive manufacturing of ceramic regular structures to maximize the radiative heat transfer**. Materials & Design, 163, 107539. https://doi.org/10.1016/j.matdes.2018.107539

Conference presentations

- "**How to produce a wide range of complex-shaped ceramic materials from selective laser melting of polymers**", 47th International Conference and Exposition on Advanced Ceramics and Composites, Daytona Beach, Florida, USA, January 2023
- "**Design and additive manufacturing of complex ceramic architecture by binder jetting on carbide-based powders**", SVMT Expert Group Powder Technology: Processing of nitride- and carbide-based ceramics and hardmetals, Lugano, Switzerland, December 2022
- "**Fabrication of dense SiC ceramics by a novel hybrid additive manufacturing process**", Young Ceramists Additive Manufacturing Forum, Barcelona, Spain, October 2022
- "**Additive manufacturing of Silicon Carbide complex structures**", Shaping 8, Zurich, Switzerland, September 2022
- "**Fabrication of dense SiC ceramics by a novel hybrid additive manufacturing process**", 46th International Conference and Exposition on Advanced Ceramics and Composites, Daytona Beach, Florida, USA, January 2022
- "**Review on the design approaches of cellular architectures produced by additive manufacturing**", Additive Manufacturing for Products and Applications Conference, Zurich, Switzerland, September 2020